About the Proton Conductivity of $BaFeO_{2.5+\delta}$ Epitaxial Thin Films in the Intermediate Temperature Range

TECHNISCHE UNIVERSITÄT DARMSTADT

Vom Fachbereich Material- und Geowissenschaften
der Technischen Universität Darmstadt

zur Erlangung des akademischen Titels
Doktor-Ingenieur (Dr.-Ing.)

genehmigte Dissertation
von
Dipl.-Ing. Alexander Benes
aus Eschborn

1. Gutachter:	Prof. Dr. Oliver Clemens
2. Gutachter:	Prof. Dr. Barbara Albert

Tag der Einreichung:	01. Februar 2019
Tag der Prüfung:	02. Mai 2019

Darmstadt 2019
D17

Abstract

Reduction of the operating temperature to an intermediate temperature range between 350 °C and 650 °C is a necessity to further increase the competitiveness of Solid Oxide Fuel/Electrolysis Cells (SOFC/SOECs) with existing energy conversion technologies. By lowering the operating temperature several high-temperature-related issues can be eliminated leading to lower costs. Motivated by the goal of lower operating temperatures the application of proton-conducting oxides has become an active and broad area of research. The incorporation of these proton-conducting materials entails problems such as ohmic resistances in the electrolyte as well as polarization resistances at the air electrode. To lower the air electrode polarizations, materials, which can be used as effective electrode catalysts on the air electrode, are required to conduct protons and electrons at the same time. Therefore, this thesis focuses on a thorough investigation of the proton conduction in the promising material system $BaFeO_{2.5+\delta}$ (BFO). The experiments are conducted on expitaxially grown $BaFeO_{2.5+\delta}$ thin films, deposited by pulsed laser deposition on (001)- and (111)-oriented Nb:$SrTiO_3$ substrates.

To monitor changes occurring to the thin films, they are examined before and after the electrochemical characterization: This investigation includes the analysis of structural and microstructural information by X-ray diffraction and scanning electron microscopy. Additionally, Mößbauer spectroscopy is used to determine the local coordination and oxidation state of Fe throughout the complete film. For the purpose of accounting for changes to the surface composition the films are furthermore examined using X-ray photoelectron spectroscopy.

For the characterization of the conductive properties Electrochemical Impedance Spectroscopy (EIS) is used, yielding a measurable protonic contribution. This protonic contribution can successfully be separated from the total conductivity by comparing measurements in wet and dry atmospheres (Ar or air, respectively). Thereby, the bulk proton conductivity of BFO can be estimated for the first time between 200 °C and 300 °C (3.6×10^{-6} S cm^{-1} at 300 °C). At temperatures above 300 °C the influence of oxidizing measurement atmosphere and water loss reveals a strong dependence on the conductivity.

For the goal of reducing the operating temperature to the intermediate temperature range it is not only important to find and employ well-suited electrode catalysts but furthermore essential to reduce ohmic resistances in the electrolyte. For this reason the search for possible deposition techniques, which enable the deposition of the respective proton conductors according to the required attributes, is subject of research efforts. Based on these grounds two deposition methods, which to date have not been used to synthesize Y-doped $BaZrO_3$ (one of the most promising proton conductors) thin films, were investigated in order to assess their potential of depositing high-quality films. In detail Laser-Assisted Chemical Vapor Deposition (LA-CVD) and Aerosol-Assisted Chemical Vapor Deposition (AA-CVD) are used for this purpose. The deposition parameters of the films are varied aiming to obtain stoichiometric smooth films with perovskite type structure. Both deposition methods present problems with relation to the required film attributes. The identified obstacles, for which solutions/workarounds are suggested, are based on thermodynamical as well as experimental facts.

Zusammenfassung

Die Reduzierung der Betriebstemperatur in einen intermediären Temperaturbereich zwischen 350 °C und 650 °C ist Voraussetzung, um die Wettbewerbsfähigkeit von Festoxidbrennstoff- und Festoxidelektrolysezellen gegenüber anderen Energiewandlungstechniken zu erhöhen. Durch das Senken der Temperatur können Probleme, die durch hohe Temperaturen verursacht werden, vermieden werden, was zu einer Verringerung der Kosten führt. Der durch das Ziel sinkender Betriebstemperaturen motivierte Einsatz von protonenleitenden Oxiden ist somit zu einem aktiven und breiten Forschungsfeld herangewachsen. Beim Einsatz dieser protonenleitenden Materialien ist neben im Elektrolytmaterial auftretenden ohmschen Widerständen vor allem der an der Luftelektrode auftretende Polarisationswiderstand problematisch. Um diese Polarisation zu verringern müssen Materialien, die als effektive Elektrodenkatalysatoren eingesetzt werden können, sowohl elektronische Leitfähigkeit als auch eine ausreichende Protonenleitfähigkeit aufweisen. Aus diesem Grund widmet sich diese Arbeit einer umfassenden Untersuchung der Protonenleitfähigkeit am vielversprechenden Materialsystem $BaFeO_{2.5+\delta}$ (BFO). Die Experimente werden an epitaktisch gewachsenen $BaFeO_{2.5+\delta}$ Dünnschichten, welche per Laserstrahlverdampfen (Pulsed Laser Deposition) auf (001) und (111)-orientierte Nb:$SrTiO_3$ Substrate abgeschieden sind, durchgeführt.

Um Veränderungen an den Dünnschichten zu beobachten, werden die Filme sowohl vor als auch nach der elektrochemischen Charakterisierung eingehend untersucht: Dazu gehört die Auswertung struktureller und mikrostruktureller Informationen mittels Röntgenbeugung und Rasterelektronenmikroskopie. Zusätzlich wird mittels Mößbauer Spektroskopie die lokale Umgebung und der Oxidationszustand von Fe über das komplette Volumen des Films untersucht. Um auch Änderungen der Zusammensetzung der Oberfläche zu verfolgen wird weiterhin Röntgenphotoelektronenspektroskopie eingesetzt. Für die Charakterisierung der Leitfähigkeit wird die elektrochemische Impedanzspektroskopie verwendet, wobei ein rein protonischer Anteil messbar ist. Dieser protonische Anteil kann erfolgreich von der Gesamtleitfähigkeit separiert werden, indem die Messungen in feuchten und trockenen Atmosphären (Ar oder Luft) verglichen werden. Dadurch ist es zum ersten Mal möglich, eine Volumenprotonenleitfähigkeit von BFO zwischen 200 °C und 300 °C (3.6×10^{-6} Scm^{-1}) abzuschätzen. Bei Temperaturen über 300 °C zeigt die Leitfähigkeit einen starken Einfluss von oxidierender Atmosphäre sowie Wasserverlust.

Für das Ziel der Reduzierung der Betriebstemperatur in einen intermediären Temperaturbereich ist es nicht nur wichtig, gut geeignete Elektrodenkatalysatoren einzusetzen, sondern weiterhin auch die ohmschen Widerstände im Elektrolytmaterial gering zu halten. Aus diesem Grund ist die Suche nach möglichen Abscheidetechniken, die es ermöglichen, dünne Schichten der entsprechenden Protonenleiter mit dem benötigten Anforderungsprofil abzuscheiden, Gegenstand der aktuellen Forschung. Darauf aufbauend wurden in dieser Arbeit zusätzlich zwei Dünnschichtabscheidemethoden, die bisher nicht für Y-dotiertes $BaZrO_3$ (einer der vielversprechendsten Protonenleiter) verwendet wurden, auf ihr Potential hin untersucht, hochwertige Filme abzuscheiden. Hierzu werden Laser-gestützte Chemische Gasphasenabscheidung (Laser-Assisted Chemical Vapor Deposition) und Aerosol-gestützte Chemische Gasphasenabscheidung eingesetzt. Die Abscheideparameter werden

variiert um stöchiometrische und glatte Filme in der Perovskitstruktur zu erhalten. Beide Abscheidetechniken weisen Probleme bei der Erfüllung der geforderten Filmcharakteristika auf. Die identifizierten Problematiken der Herstellungsrouten, für welche abschließend Abhilfen bzw. Lösungsansätze vorgeschlagen werden, beruhen sowohl auf thermodynamischen als auch auf experimentellen Gegebenheiten.

Table of contents

1. Introduction

Due to the rising energy consumption worldwide [1] a transition from fossil fuels to renewable energy sources has become necessary and has boosted research in technologies such as wind, solar and geothermal energy production [2]. This “energy revolution” goes hand in hand with many technological and infrastructural modifications as well as new political perspectives in a broader sense.

In 2010 the German government installed an expert committee, which has developed the so called “Energiekonzept 2050” [3]. The report presents a vision for a sustainable energy concept until the year 2050 based on 100 % renewable energy sources and energy efficiency. Although not in detail, the report presents the technological components and transformation processes, which are required to provide exclusive supply by renewable energies in a sustainable and cost-effective way [3]. In the context of renewable energy sources the well-known fluctuation in electricity production and the entailed limited capability to store electrical energy are addressed by presenting possible alleviations. Therein especially chemical energy carriers such as hydrogen and methane are considered as suitable candidates [3]. In this sense the term “hydrogen economy” is used to describe a system, which uses hydrogen and the conversion of water to hydrogen (by electrolysis) in order to supply energy. Although a uniquely hydrogen-based economy is still futuristic, the systematic integration of hydrogen-based technologies is of great potential and importance [3].

The groundwork for the fundamental basis of a hydrogen-based economy began with the discovery of the concept of water electrolysis as early as 1802 by Humphry Davy and eventually led to the development of the first hydrogen fuel cell by William Grove in 1839. However, while Grove’s discovery only rekindled interest about 100 years later, it would prove to be very important for today’s fuel cell technology. Since the development of the first fuel cell the vision of hydrogen as an energy carrier has gained tremendous significance, mainly because excess electrical energy can be stored chemically as hydrogen with high conversion efficiency (Figure 1.2). On demand the stored hydrogen can be converted back to electrical energy using fuel cells. Different types of fuel cells and electrolyzers have been developed to different extents and are available commercially or on a laboratory scale [4]. These devices can be categorized with respect to their electrolyte and their operating temperature. The classification into different temperature regimes is especially useful in terms of thermodynamics. The total energy demand ΔH, which can be expressed as

$$\Delta H = \Delta G + T\Delta S \tag{1.1}$$

where ΔG is the electric energy demand and $T\Delta S$ is the heat demand, varies for different temperature regimes [5]. The respective components of the thermodynamic data for water electrolysis are shown in Figure 1.1a. Due to the energy required to transform water from the liquid into the gaseous state a sudden drop in the total energy demand (ΔH) can be observed above 100 °C. In addition ΔG decreases with the compensation of thermal energy ($T\Delta S$) at higher temperatures. Therefore electrolysis cells operating at high temperatures consume less electricity and the required heat could (at least partially) be provided by an external source (e.g. waste heat).

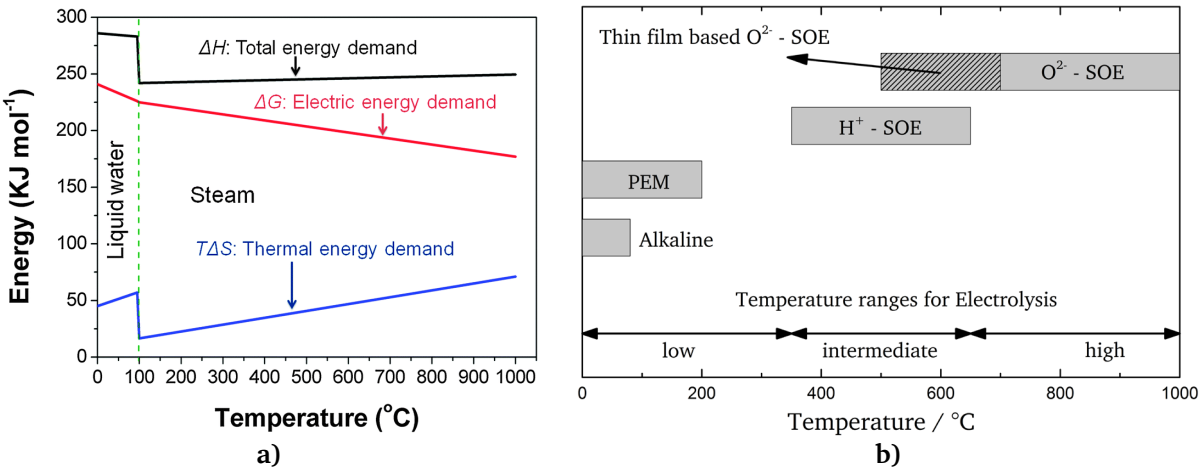

Figure 1.1. a) Electric, thermal and total energy demand for H_2O electrolysis as a function of temperature (at 1atm steam pressure). The electric energy demand decreases, while at the same time the thermal energy demand increases with working temperature. (Reprinted with permission from Royal Society of Chemistry: Chemical Society Reviews [5], © 2014) b) Temperature ranges for electrolysis including the main electrolysis technologies: Alkaline electrolyzers, Polymer-electrolyte membrane (PEM) electrolyzers, proton conducting solid oxide electroylzers (H^+ - SOE) and oxygen ion conducting solid oxide electrolyzers (O^{2-} - SOE).

However, the commercialization of these high temperature cells is impeded by high manufacturing costs, long start-up and shut-down times as well as high material degradation rates. For these reasons the most suitable temperature range for electrolysis is between 350 °C and 650 °C. Since they operate in the targeted temperature range (Figure 1.1b), possess a high conversion efficiency as well as fuel flexibility Solid Oxide Fuel Cells (SOFCs) and their reversely operated counterparts Solid Oxide Electrolysis Cells (SOECs) are promising candidates within the fuel cell family for producing electrical energy and hydrogen fuel, respectively [5,6]. Solid oxide fuel/electrolysis cells in the simplest description are galvanic cells, i.e. electrochemical cells, which convert chemical energy to electrical energy via redox reactions, which are taking place spontaneously within the cell.

Since no reaction involving the conversion of heat energy is taking place the processes in SOFCs are not limited to the Carnot theorem [7], to which all heat engines are bound. However, it is important to carefully analyze the impact of temperature on the efficiency. For this purpose Figure 1.2 shows the change of efficiency with increasing temperature for a heat engine according to the Carnot theorem and a fuel cell [8]. The efficiency of electrolyzers is described as the ratio of electrical energy ΔG produced by the cell to the heat (enthalpy of formation of gaseous water ΔH_f), which is created when burning the fuel [9]. Figure 1.2 shows that with increasing temperature the electrolyzer efficiency decreases and the efficiency of a Carnot engine (cold reservoir 25 °C) increases. At around 900 °C the efficiencies overlap. However it has to be taken into account that the real efficiency of an engine is much lower due to e.g. friction and usually does not surpass 40 %. Evidently the above considerations suggest that the best range of operation for these devices is the intermediate temperature range (Figure 1.1b).

For this reason, the main goal in SOFC/SOEC research is to decrease the operating temperature to an intermediate temperature regime below 600 °C. The two main constraints, which are limiting device operation only to high temperatures, are the insufficient ionic conductivity of the electrolyte at lower temperatures and polarization losses, occurring predominantly at the air electrode (cathode in fuel cell mode) [10]. There are different approaches about how to tackle these problems. Minimizing the ohmic losses in the

electrolyte can be realized by decreasing its thickness or by employing new material systems with higher ionic conductivity.

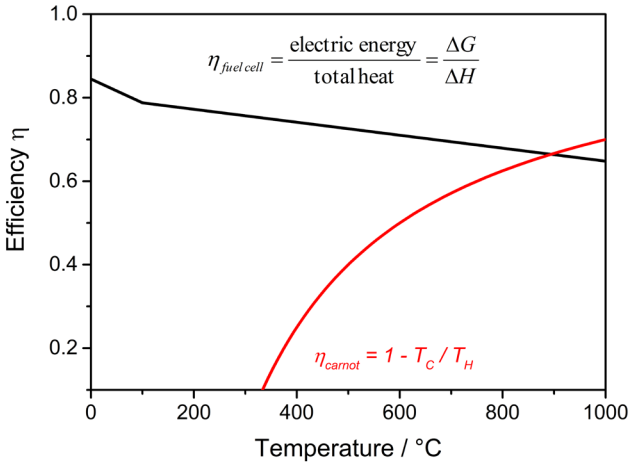

Figure 1.2. Comparison of the efficiency of a heat engine (red) and a fuel cell producing water vapor (black) as a function of temperature. The heat engine operates between a variable hot source and a fixed cold reservoir at room temperature (25 °C).

Since most SOFCs use oxygen ion conductors these new material systems are based on the idea of changing the diffusing species (O^{2-}) to a smaller ion (H^+), which has a lower activation energy (as a rule of thumb: $\frac{3}{2}E_{a,\,proton} \approx E_{a,\,oxide}$). In this respect proton-conducting electrolytes such as doped $BaCeO_3$ or $BaZrO_3$ have become a prominent area of research [11]. Proton migration pathways are most often characterized by lower activation barriers within solid oxides as compared to oxygen ions (protons possess smaller mass, lower radius, have no electron cloud and their transport behavior can be roughly described via a Grotthuss-related mechanism [12]) and therefore proton-conducting materials can in principle show increased ionic conductivity especially at intermediate temperatures [6,13]. Additionally, devices, employing proton conductors, have attracted attention due to potentially higher electrical efficiency [14–16]. A limiting factor for the application of these electrolytes is the lack of suitable electrode catalysts, which are conductive for both electrons and protons.

As opposed to oxygen ion-conducting devices, the rate-limiting steps at the air electrode for proton-conducting devices depend on the proton transfer and subsequent proton migration to the electrolyte [5]. There are very few reports on a single-phase air electrode materials enabling both adequate protonic (H^+) and good electronic (e^-) conductivity [17,18]. In principle, a single-phase material offering simultaneous conduction of all three charge carriers (O^{2-}, H^+ and e^-), which are involved in the electrochemical processes occurring at the air electrode, can even further enhance the catalytic activity (towards the oxygen reduction reaction in SOFC mode) as has been shown in recent reports [19,20]. Since to date there are only a few of such materials known and the determination of the individual conductivities in combination with the correct temperature range remains a scientific challenge, more research is needed. However, most of the time, one ionic charge carrier dominates the ionic conductivity: at low temperatures protons can dominate due to their higher mobility, but at higher temperatures (>600 °C) protonic transport is usually suppressed since protons cannot be stabilized within the lattice.

1.1. Objectives of this Thesis

The objectives of this thesis were motivated by the announcement of new guidelines concerning the federal promotion and funding for research of materials related to the "energy revolution" (issued in april 2013 by the Bundesministerium für Bildung und Forschung). These guidelines provide a framework for the "Energiekonzept 2050", which is based on energy efficiency and 100 % renewable energies. One of the research objectives suggested the investigation of new material systems, which could potentially be used in proton conducting solid oxide fuel cells to ultimately lower the operating temperature to an intermediate temperature range of 350 °C to 650 °C. More specific, on the basis of these guidelines, two main goals were defined with relation to this thesis.

On the one hand the problem of air electrode polarization, which is mainly caused by the lack of adequate materials providing (simultaneous) protonic and electronic conductivity (in analogy to oxygen ion and electronic conductivity in electrodes for oxygen ion conducting SOFCs), is addressed. To tackle this issue from a new perspective an extensive investigation of the material system, $BaFeO_{2.5+\delta}$ (BFO), which has shown interesting properties in terms of protonic and electronic conductivity in recent reports [21–23], is conducted in the first part of this thesis. Therein the examination is conducted on thin epitaxially grown films of $BaFeO_{2.5+\delta}$ with special focus on the behavior of the bulk proton conductivity in inert and oxidizing atmospheres. The milestones of this first goal are listed below:

- Deposition of epitaxially grown BFO films using pulsed laser deposition (PLD).
- Confirmation of the suitability of the deposited films (sufficiently reduced strain in through-plane direction, single phase structure, stoichiometric film composition) for further electrochemical investigation by electrochemical impedance spectroscopy (EIS).
- Determination of the conductive properties (bulk proton conductivity, capacitances of respective processes, activation energy) in inert and oxidizing atmospheres (in wet and dry state) to prompt a deeper understanding of the structure-property relationships and enable a comparison to current proton conductors.

The second goal, which was defined in the scope of this thesis, directly addresses the main problem of SOFC research: Lowering the temperature of operation to an intermediate temperature range. Since it had previously been shown that the ohmic resistance can be reduced by employing thin films as solid electrolytes (deposited on hydrogen electrode substrates) [5], the focus was set to the deposition of such films using new deposition techniques. In this thesis CO_2 laser-assisted chemical vapor deposition (LA-CVD) and pressurized spray deposition (PSD) are investigated to reveal their potential for the fabrication of thin films of Y-doped $BaZrO_3$ (BZY). The milestones for the second goal are defined in the following:

- Establishing the influence of the basic experimental setup parameters for the deposition of BZY thin films by LA-CVD and PSD.
- Exploration of the feasibility to deposit BZY via LA-CVD and PSD in terms of homogenous dense films with stoichiometric, controllable Y_2O_3 content.
- Assessment of the suitability of these films to be investigated electrochemically and to have potential for large scale depositions.

1.2. Thesis Structure

Chapter 2 provides an introduction to the basic theoretical fundamentals, which are necessary to understand the results, conclusions and assumptions found and made throughout this thesis. Therefore this chapter focuses on the principles and concepts of ionic and especially proton transport in oxide materials as well as on properties related to the deposition and structural characteristics of thin films.

Chapter 3 presents an introduction to the basic principles and concepts for the two most intensively used characterization methods, namely X-ray diffraction (XRD) and electrochemical impedance spectroscopy (EIS). Additionally, all the experimental information for the other material characterization methods (X-ray photoelectron spectroscopy- XPS, scanning electron microscopy – SEM, conversion electron Mößbauer spectroscopy – CEMS and atom probe tomography – APT) is provided.

Chapter 4 contains descriptions of the different experimental setups and sample preparation methods, which were used within this thesis. In addition a description of the custom-built setup for EIS measurements and the integrated ultra-high vacuum (UHV) system called Darmstadt Integrated System for Battery Research (DAISY-Bat) is presented.

Chapter 5 covers an in-depth analysis of $BaFeO_{3-\delta}$ epitaxial thin films in terms of their structure, morphology, oxidation state of Fe and surface composition. This information is then used to analyze and explain the conductive properties, which are observed in different atmospheres. The results are then put into a larger context, comparing the obtained conductivities to other leading proton conductors.

Chapter 6 introduces the key features of LA-CVD and PSD deposition techniques. Both techniques are subsequently used to optimize the deposition parameters of BZY thin films. The techniques are assessed in terms of their general applicability to the deposition of BZY. For this purpose the problems, which occurred during the deposition processes, were analyzed in detail applying thermodynamic considerations.

Chapter 7 summarizes the conclusions, which were drawn from the results of chapters 5 and 6. Additionally an outlook on further research is presented.

After more extensive subchapters, a brief preliminary summary of the results is provided and highlighted by a black frame.

2. Theoretical Fundamentals

2.1. Perovskite Materials

As the materials, which are investigated in this thesis, crystallize in a perovskite or perovskite-related structure, a short introduction to the perovskite structure will be given at this point. A comprehensive elaboration on structure and structure-property relationships can be found elsewhere [24,25]. The characteristic crystal structure of the mineral $CaTiO_3$ was first named perovskite-type structure. However, as is the case for many minerals the name was later applied to a family of compounds (Perovskites), which have the general formula close to or derived from a general composition ABX_3. Therein A is usually a large cation (usually alkaline earth metal or lanthanide), which is similar in size to the anion, B a medium-sized cation (usually a transition metal) and X an anion (O^{2-}, F^-, Cl^-, I^-). Although $BaTiO_3$ with its valuable ferroelectric and dielectric properties was the initial discovery, which highlighted the importance of perovskites, this group of materials has since proven to possess very useful physical and chemical properties [24]. These properties include ionic (proton and oxygen ion) and electronic conductivity, as well as thermal, optical, magnetic and dielectric properties. The variety of properties is caused in great parts due to the flexibility of the perovskite structures to substitute A, B and X sites.

The aristotype (idealized) perovskite structure is adopted by $SrTiO_3$ at room temperature and presents in a cubic modification with space group *Pm*-3*m* (No 221) and a lattice parameter of a=3.905 Å. The atomic positions are listed in Table 1 and the corresponding unit cell is shown in Figure 2.1. The A-site cation (Sr) is 12-fold coordinated by oxygen and the B-site cation (Ti) is six-fold coordinated (octahedral coordination) by oxygen as shown in Figure 2.1b.

Table 1. Atom positions for $SrTiO_3$ with space group Pm-3m (No. 221) at room temperature.

Atom	Wyckoff position	Coordinates
Sr	1*a*	(0, 0, 0)
Ti	1*b*	(½, ½, ½)
O	3*c*	(½, ½, 0) (½, 0, ½) (0, ½, ½)

In the ideal case the lattice parameter a is geometrically related to the ionic radii r_A, r_B and r_X of cations A, B and the anion X (in ABX_3), respectively. This relationship is described in equation (2.1)

$$a=2(r_B + r_X) = \sqrt{2}(r_A + r_X) \tag{2.1}$$

The ratio of these two expressions for the lattice parameter is called the Goldschmidt tolerance factor G. The tolerance factor is based on the assumption of purely ionic bonding but can also be used as an indication for compounds with a high degree of ionic bonding. Equation (2.2) shows the ratio, by which the tolerance factor is described.

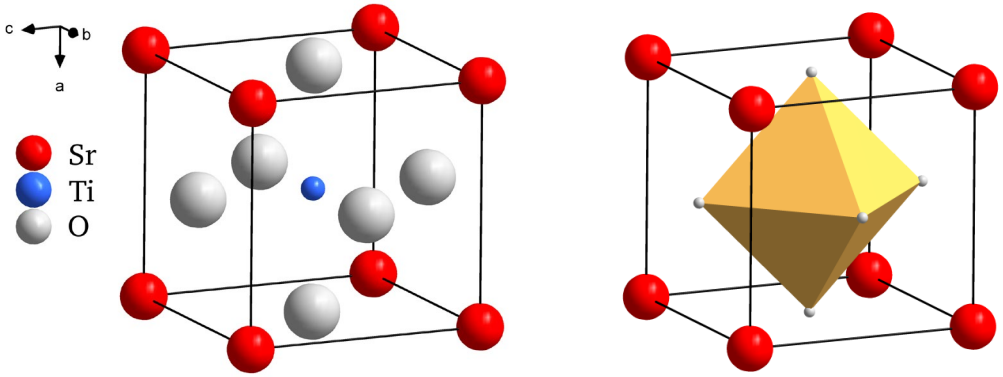

a) b)

Figure 2.1. a) Unit cell representation of the idealized perovskite structure of $SrTiO_3$ with Sr^{2+} cations at the origin. b) Unit cell of $SrTiO_3$ with TiO_6 coordination polyhedron.

$$G = \frac{r_A + r_X}{\sqrt{2}(r_B + r_X)} \tag{2.2}$$

Using the tolerance factor the existence of structure distortions or deviations from a ccp stacking of AX_3 layers can often be predicted in a simple and straightforward way. For G=1 the ideal cubic perovskite structure can be expected but it has been shown empirically that also for 0.9<t<1.0 the cubic perovskite structure is a reasonable assumption. For G>1 (due to a large A or a small B ion) a partial hexagonal stacking of AX_3 layers can be expected leading to the formation of a hexagonal phase with face-sharing BX_6 octahedra (Figure 2.2a). In the case of 0.7<G<0.9 the structure distorts and results in a lowering of the crystal symmetry from cubic, which is caused by tilting of the BX_6 octahedra (Figure 2.2b).

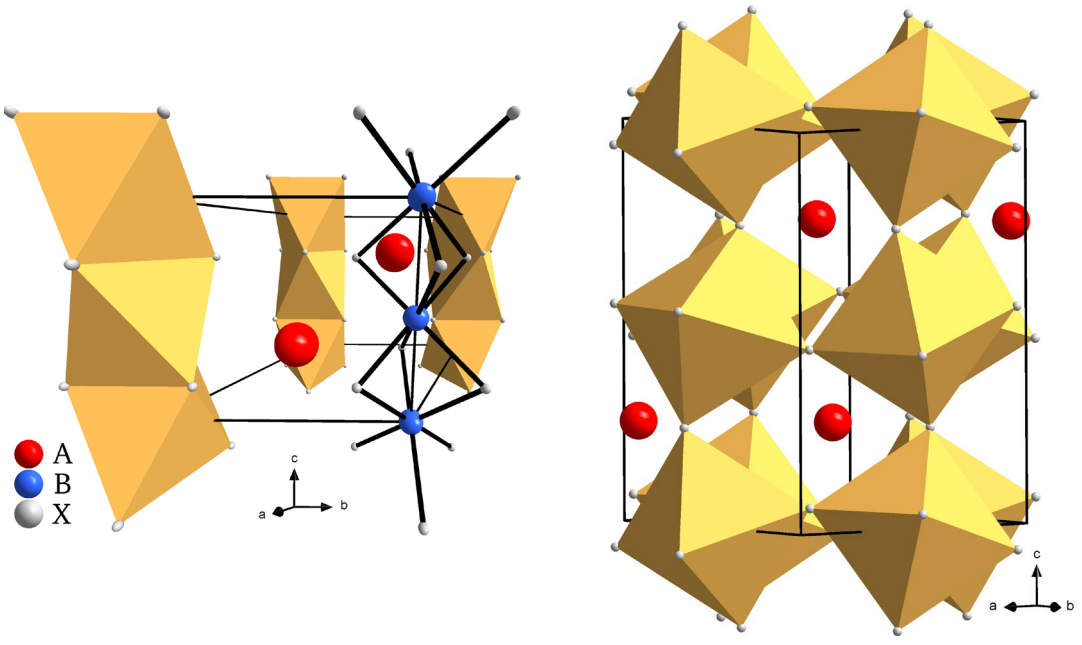

a) b)

Figure 2.2. a) High values of the Goldschmidt tolerance factor (G>1) can lead to the formation of hexagonal variants of the perovskite structure with face sharing BX_6 octahedra. For the purpose of clarity one column of octahedra is not shown. Instead, the bonds between the B and X atoms are displayed. b) Low values of G (0.7<G<0.9) will lower the symmetry of the structure and cause tilting of the octahedra.

The BX_6 octahedra (Figure 2.1b) play an important role for many important physical properties of the perovskites, such as ferroelectric and magnetic responses to external fields or for ionic conduction. Several factors, including the relatively small cation size, the impact of the surrounding anions and the flexibility of the valence state (not always), are responsible for the importance of the B-site cation. The A-site cations are mostly less influential in terms of chemical manipulation since they tend to be larger, closed-shell ions with a fixed valence (e.g. Sr^{2+}, Ba^{2+}, Ca^{2+}). There are mainly three structural responses, which characterize the deviations from the perfect octahedral configuration shown in Figure 2.1b.

The simplest change includes a displacement of the B-site cation away from the center of the octahedron (symmetry lowering), which can give rise to pyroelectric, ferroelectric and antiferroelectric effects. A second structural response, which maintains the nearly perfect octahedral geometry, is the rotation or tilt of the complete octahedron. Similar to the aforementioned cation displacement this tilt or twist also causes a symmetry lowering. A third structural response includes the distortion (elongating or flattening) of the octahedra. This can be caused as a result of interactions between the cation orbitals and the surrounding anions (Jahn-Teller effect), by cation valence changes or by stress and strain. Further deviations from cubic symmetry can arise due to vacancy ordering for anion deficient perovskites, which is discussed in more detail on the BFO system in chapter 2.1.1.

In this thesis the focus of investigation is on the topic of ionic conduction in thin films, which experience large stresses and strains, due to various reasons (e.g. lattice mismatch, change in valence state). As the resulting deviations from the structure of the parent bulk compound can be large for such films, it can be convenient for comparison to relate the structures of the film and bulk materials to each other by calculating a so-called pseudocubic lattice parameter $a_{ps.cub}$. It is calculated from the volume per ABX_{3-y} formula unit $V_{f.u.}$ by taking the cube root $\sqrt[3]{V_{f.u.}}$.

2.1.1. The Material System $BaFeO_{2.5+\delta}$

$BaFeO_{3-\delta}$ exists over a wide compositional range of oxygen stoichiometry, extending from $BaFeO_{2.5}$ to $BaFeO_3$. An assumption to vaguely predict the deviation from a ccp stacking arrangement in BFO can be made using G from equation (2.2). The resulting value (G>1 for Fe^{4+}) points towards hexagonal stacking and indeed the phases, which have been observed in literature confirm that hexagonal modifications exist over a wide range of oxygen stoichiometry (see also Table 6 in chapter 5.1). Figure 2.3 provides an overview of the modifications and synthesis parameters of BFO. To better understand and simplify the different modifications the nomenclature according to Jagodzinski is used throughout this thesis [26] and introduced in the following paragraph.

The perovskite structure (ABO_3) can be described in terms of close-packed AO_3 layers stacked one over another [27] with the B-cations occupying octahedral sites (represented as BO_6 octahedra). When the stacking sequence is all cubic (ccc sequence – adjacent layers both differ from the middle one, i.e. ABCABC) the octahedra around the B-cations all share corners as displayed in Figure 2.1 (3C-type). On the other hand, when the stacking is all hexagonal (hhh sequence – adjacent layers are the same but differ from the middle one, i.e. ABAB) the BO_6 octahedra share opposite faces thereby forming infinite chains extending parallel to the hexagonal c-axis as displayed in Figure 2.2a. A stacking sequence in between both terms hhh and ccc, can therefore describe mixed stacking arrangements, which form polytypes with larger periodicities. E.g. the arrangement cchcch (6H) of AO_3 layers is common for $BaFeO_{3-\delta}$ and formed over wide ranges of synthesis conditions (Table 6 in chapter 5.1). The 6H-type structure is displayed in Figure 2.3 showing that two octahedra sharing faces are linked by octahedra sharing corners. Another stacking arrangement, which is termed 12H-type, can be obtained under high oxygen pressures. The stacking sequence for the 12H-type arrangement is $(cchh)_3$ and corresponds to a succession of two compact hexagonal planes and two cubic planes leading to the formation of three oxygen octahedra units, which share faces. These groups are linked by a fourth octahedron by corner sharing (Figure 2.3).

For the case of high oxygen deficiency a different vacancy-ordered modification can be obtained for a composition of $BaFeO_{2.5}$ [28,29]. Structurally it can be derived from the cubic aristotype perovskite structure. The complex vacancy ordering in this modification has been subject in several investigations and is thoroughly presented in [28]. In addition, the hydration behavior of this monoclinic phase of $BaFeO_{2.5}$ has been investigated by Knöchel et al. [21]. Two different phases, namely $BaFeO_{2.33}(OH)_{0.33}$ and $BaFeO_{2.25}(OH)_{0.5}$ were found to occur depending on the hydration temperature. The structure of $BaFeO_{2.33}(OH)_{0.33}$ is displayed in Figure 2.3 (no detailed structural model could be determined for $BaFeO_{2.25}(OH)_{0.5}$) including the likely location of protons (indicated by orange clouds). For a detailed description and explanation of the protonated structure the reader is referred to [21]. The high water uptake was correlated with the electrical conductivity showing that the activation energy was in good agreement with a protonic contribution [21]. However, since Knöchel et al. used non-sintered pellets (sintered pellets cracked due to strong volume increase during hydration) for their conductivity measurements the obtained values are assumed to be lower than for sintered pellets. Furthermore, the influence of grain boundaries could not be reliably separated during the analysis of impedance data. Therefore, the proton conductivity and hydration behavior of thin epitaxial (grain-boundary-free) films of BFO are examined in this thesis (indicated by “???” in Figure 2.3) with the goal of determining the bulk proton conductivity and the influence of different measurement atmospheres.

Although the modifications of BFO, which are described above, represent the majority of investigated phases, Hayashi et al. succeeded in synthesizing fully oxidized $BaFeO_3$ (using O_3 as an oxidant at low temperatures) with a cubic cell parameter of a=3.97 Å (Figure 2.3).

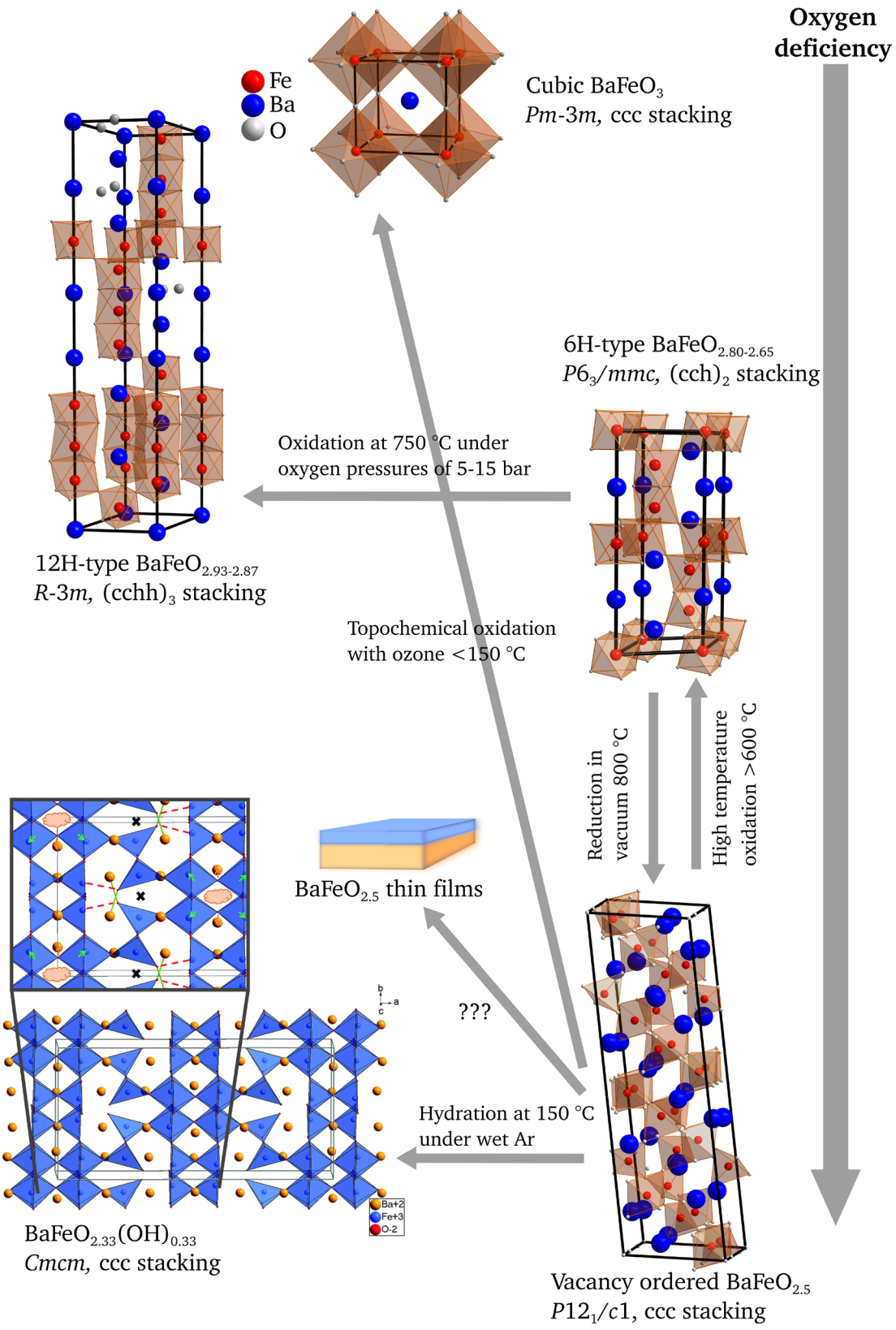

Figure 2.3. Overview of different BFO modifications with respect to oxygen stoichiometry and synthesis parameters. $BaFeO_{2.5}$ thin films are indicated with "???" because they are investigated in this thesis. The structure of $BaFeO_{2.33}(OH)_{0.33}$ is reprinted with permission from Royal Society of Chemistry: Journal of Materials Chemistry A [21], © 2016.

2.2. Ionic Conduction in Solids

As opposed to the conductivity in metals or semiconductors, the charge in ionic conductors is transported by ions instead of electrons and holes. The electrical conductivity σ is defined as the ratio of current density j and electric field E

$$\frac{j}{E} = \sigma = \sum_i c_i \, \mu_i Z_i q \tag{2.3}$$

where c_i is the charge carrier density (number/cm^3), μ_i the mobility (cm^2/Vs) and $Z_i q$ the charge of the respective ith charge carrier [30]. When the charge carriers are reduced to ions only, c is the number of ions per unit volume that can change their lattice position under the influence of an electric field. In order for ions to have ionic mobility within a crystal lattice two conditions have to be fulfilled. The first requirement is that an adjacent nearly energetically equivalent lattice site is vacant and can thereby accommodate a diffusing ion. In this respect the conductivity in (2.3) depends directly on the vacancy concentration in the crystal. Secondly, in order to complete a jump to the next lattice site, the ion is required to possess a sufficient amount of energy to overcome the barrier separating both lattice sites. The energy, which is necessary to overcome the barrier, is termed activation energy E_a and the distance between the lattice sites d.

Figure 2.4a displays the schematic energy landscape of a crystal lattice with an ion jumping to an adjacent vacant lattice site. In this case no preferential direction of motion exists, so that the ions will jump to the left or right randomly. This condition without external forces acting on the ions and no prevailing concentration gradient is referred to as Brownian motion. In the case of an existing concentration gradient a net movement, which is termed diffusion, from a region of higher concentration to a region of lower concentration can be observed. If however a uniform external force (such as e.g. electrical potential, temperature or stress) is applied to the crystal the activation energy is lowered towards one and increased towards the other direction, as shown in Figure 2.4b. The result is a preferential motion of the ions, termed migration [31].

Diffusion and migration of ions can both be described by an activated jump process [30], for which the diffusion coefficient D is temperature dependent and can be described by (in the absence of an external force)

$$D = D_0 e^{-\frac{E_a}{k_B T}} \tag{2.4}$$

where D_0 is a pre-exponential factor, which depends on the vibrational frequency and the jump distance of the ions. The diffusion coefficient is in turn directly related to the mobility of ions, through the Einstein relation (also known as Nernst-Einstein equation [32])

$$\mu_{ion} = \frac{ZqD}{k_B T} \tag{2.5}$$

This expression can be used to estimate the flux of ions by migration as well as the electrical conductivity of a crystal. By combining equations (2.3), (2.4) and (2.5) the following relationship is obtained:

$$\sigma = c\frac{Z^2q^2}{k_BT}D_0e^{-\frac{E_a}{k_BT}} \tag{2.6}$$

Using an Arrhenius plot equation (2.6) can be used to determine the activation energy for the process under investigation (used in chapter 5.7). In principle both cations and anions are capable of migrating simultaneously when for example an electric field is applied. However, not only the size of the respective ion is of importance but for a noticeable ion flux to occur vacancies have to be present. From (2.6) it is in turn apparent that the number of vacancies influences the conductivity. The intrinsic vacancy concentration in a crystal is temperature dependent in the form of a Boltzmann distribution. Since charge neutrality has to be maintained whenever vacancies are created no single ion can be removed from the crystal. Instead a possible mechanism of vacancy formation is the creation of an interstitial pair (Frenkel pair). The most common way to extrinsically introduce anion vacancies into a crystal is the doping with differently charged impurity atoms (aliovalent doping, see chapter 2.3.2). This is for example the case in Y-doped $BaZrO_3$, which is investigated in this thesis.

As a consequence of the above elaborations it might be concluded that in polycrystalline materials the grain-boundaries could act as preferred paths for migration, thus enhancing the conductivity. However a contrary impact is also possible. For Y-doped $BaZrO_3$ this is not the case since on the contrary the grain boundaries cause low conductivity. This effect has recently been explained by the space charge model [33], which assumes that charged defects segregate to the structurally distorted region near the grain boundary plane (grain-boundary core). The resulting charge at the core induces an electrostatic potential barrier and thereby a depletion of mobile charge carriers of the same polarity in close proximity of the space charge layers [33].

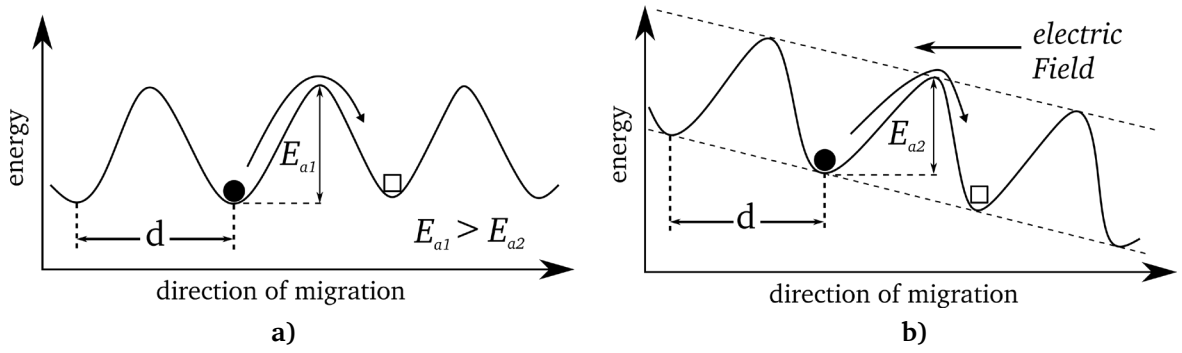

Figure 2.4. Schematic representation of an energy landscape, which an ion has to overcome to swap sites with a vacancy. a) Without the influence of an external electric field and b) with an applied external electric field. d represents the distance between two adjacent lattice sites and Ea the activation energy.

2.3. Proton Conduction in Oxides

2.3.1. Overview of Proton-Conducting Oxide Materials

Proton conduction in solid oxides was first observed for (Ba,Sr)$CeO_{3-\delta}$ based perovskite materials in hydrogen containing atmospheres [34]. Following this discovery a multitude of perovskite and perovskite-related materials was found to show similar protonic conductivity. One of the best proton conductors with the highest proton conductivity to date is $BaCeO_3$. Unfortunately, the very low stability of cerates has impeded the practical application tremendously. The main problems are that cerates are only slightly stabilized with respect to the decomposition into binary oxides [35], the tendency to react with low levels of CO_2 (to form carbonates) [36] and to form alkaline earth hydroxides at high water activities [37]. Therefore Y-doped $BaZrO_3$, which shows slightly lower proton conductivity but much higher stability, has found increased application, either pure or in solid solution with $BaCeO_3$. Except for in these materials, proton conductivity has been observed and investigated in several other oxides. Table 2 provides an overview of selected proton conducing oxide materials classified according to their structure type.

Table 2. Overview of classes of proton conductors (oxide materials). In addition, the proton conductivity values at 600 °C are listed.

Structure Type	Materials	σ_{600} / Scm^{-1}
II-IV perovskite $A(M_x,B_{1-x})O_3$	$A(Zr,M)O_3$ (A=Ba, Ca; Sr)	10^{-3}-10^{-2} [38,39]
		$>10^{-1}$ (bulk) [40]
	$A(Ce,M)O_3$ (A=Ba, Sr)	10^{-3}-10^{-2} [34,41]
	$BaBO_3$ (B=Th, Tb, Pr)	0.1 [42,43]
	Dopants M=Y, Sc, Yb, In, Ga, Gd, Nd	
Layered perovskite $A_2B'_{1+x}B''_{1-x}O_{6-\delta}$	$Ba_3(Ca_{1.18}Nb_{1.82})O_9$	10^{-3} [44]
Perovskite-type oxide	$A_{1-x}Ca_xScO_{3-\delta}$ (A=La, Nd, Sm, Gd)	1-5•10^{-5} [45]
	$LaSc_{1-x}Mg_xO_{3-\delta}$	
K_2NiF_4 type	$La_{1-x}Sr_{1+x}AlO_{4-\delta}$	2•10^{-5} [46]
	$La_{1-x}Ba_{1+x}GaO_{4-\delta}$	3•10^{-4} [47]
	$Sr_2Ti_{1-x}In_xO_{4-\delta}$	10^{-3} [48]
Perovskite related	$Sr_6M_2O_{11}$ (M=Nb, Ta)	10^{-4}-10^{-3} [49,50]
Brownmillerite-type	$Ba_2In_2O_5$	10^{-4} [51]
	$Ba_2YSnO_{5.5}$	10^{-3} [52]
Fluorite	$La_{5.8}WO_{11.7}$	2•10^{-3} [53]
	$La_{3-x}Sr_xNbO_{7-\delta}$	2•10^{-4} [46]
Aragonite	$LaBO_3$ (Sr-doped)	10^{-6}-10^{-5} [53,54]
Pyrochlore	$A_2Zr_{2-x}Y_xO_{7-\delta}$ (A=La, Nd, Gd, Sm)	4•10^{-4} [55]
Monazite	$RE_{1-x}M_xPO_4$ and $RE_{1-x}M_x(PO_3)_3$	10^{-5}-10^{-4} [56–58]
	RE=La, Y	
	M = Ca, Sr, Ba	
Fergusonite	$RE_{1-x}M_xNbO_4$ and $RE_{1-x}M_xTaO_4$	10^{-4} [59]
	RE=La, Nd, Gd, Tb	
	M= Ca	

2.3.2. Formation of Protonic Defects and Defect Chemistry

A proton (positively charged hydrogen ion) possesses no electron cloud and for this reason interacts strongly with electron clouds in its close proximity. In nonmetallic compounds such as oxides, a proton can interact with a single or two of its nearest neighbors. When connected to a single oxygen atom the bond length is around 100 pm [60]. Considering that the ionic radius of an oxygen ion is 140 pm [60], the proton in its equilibrium position is embedded into the valence electron cloud of oxygen (Figure 2.5a). In the case of two oxygen atoms as nearest neighbors, their distance influences the equilibrium position of the proton. If the average distance between the oxygen atoms is between 250 pm to 280 pm [60] an asymmetric hydrogen bond is formed as shown in Figure 2.5b with a short strong bond and a longer weak bond. However if the distance between the oxygen atoms is shorter (around 240 pm [60]) a symmetrical hydrogen bond is possible (Figure 2.5c). In that case the proton shares two equivalent bonds.

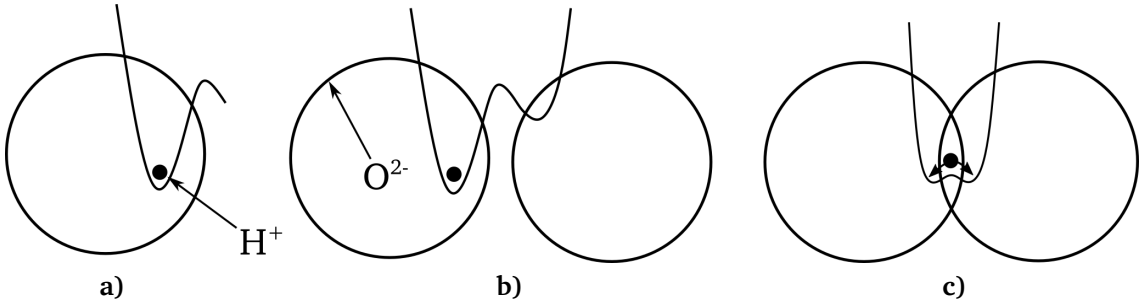

Figure 2.5. Different cases of proton binding are schematically represented in the environment of an oxide material. The proton is coordinated to one or two oxygen ions. The potential surfaces correspond to the electronic structure of the indicated proton location. a) The proton has its equilibrium position embedded in the valence electron density of the oxygen. b) Asymmetric hydrogen bond with directional character. c) Hydrogen is involved in two equivalent bonds. This figure has been adopted and modified from [60].

The hydrogen, which is dissolved in oxide materials, is present as protons leading to positive charge defects. These defects can be described in two different ways using the Kröger-Vink-Notation. The first possibility depicts the protons on an interstitial lattice site, nearby a regular oxygen ion on its regular lattice site. Since the protons are not free in the crystal lattice but rather dwell in the electron cloud of an oxygen ion, the second way of describing the proton in the lattice is more common. The protons are described as a substituting hydroxyl group on an oxygen lattice site $OH_O^{\bullet}$. It has to be kept in mind that both descriptions depict the same actual situation. Throughout this thesis the hydroxyl group is chosen for the representation of protonic defects.

There are two ways, which lead to the formation of these hydroxyl defects. Either hydrogen or water can be incorporated into the crystal lattice of an oxide. The simplest way is the incorporation of hydrogen, which is described by the following reaction equation in Kröger-Vink-Notation and displayed schematically in Figure 2.6d:

$$H_2(g) + 2O_O^x \Leftrightarrow 2OH_O^{\bullet} + 2e' \tag{2.7}$$

During this process the hydrogen molecule splits into two protons and two electrons. The protons, together with two lattice oxygen ions on oxygen lattice sites, form two hydroxyl defects, while the electrons form two defect electrons. The most important reaction, leading to the incorporation of protonic defects into perovskite oxides is the dissociative adsorption of

H_2O, which in turn requires the presence of oxygen ion vacancies. These vacancies may either be formed intrinsically by variation of the main constituents (such as in e.g. $Ba_2YSnO_{5.5}$) or by employing reducible B-site cations, which can form vacancy-ordered superstructures on the anion lattice (e.g., $BaFe^{IV}_{1-x}Fe^{III}_{x}O_{3-x/2}$) by heat treatment in reducing/oxidizing atmospheres. Alternatively the variable oxygen stoichiometry of perovskites can further be influenced by introducing charge compensating defects in the form of aliovalent B-site substitions such as e.g., Y in $BaZr_{1-x}Y_xO_{3-x/2}$ (acceptor-doped oxides). The partial substitution of a B site cation with a trivalent dopant such as Y^{+3} leads to the formation of oxygen vacancies, which compensate the negatively charged dopant-ion lattice sites Y'_{Zr}.

$$2Zr^x_{Zr} + O^x_O + Y_2O_3 \Leftrightarrow 2Y'_{Zr} + V^{\bullet\bullet}_O + 2ZrO_2 \tag{2.8}$$

In order to take up protons into the crystal structure water molecules (usually from the gas phase) have to dissociate into a proton, which then forms a covalent bond with a lattice oxygen, and into a hydroxyl ion, which subsequently fills an available oxygen vacancy.

$$H_2O(g) + V^{\bullet\bullet}_O + O^x_O \Leftrightarrow 2OH^{\bullet}_O \tag{2.9}$$

Since protons in oxides are not part of the structure but rather hydroxyl defects in the host lattice, the concentration is variable. The concentration can vary depending on the host lattice and depending on the surrounding atmosphere.

In terms of the host lattice the oxygen vacancy concentration is of crucial importance. For acceptor doped perovskite structures the oxygen vacancy concentration correlates directly with the doping concentration and therefore the available sites for proton incorporation. The influence of atmosphere depends on the partial pressures of oxygen, hydrogen and water as well as the temperature.

Figure 2.6 displays a simplified image of the defect chemistry occurring in a perovskite-type acceptor doped structure under different atmospheres using Kröger-Vink notation to describe each condition. It is evident that depending on the atmosphere and the partial pressures respectively several processes occur, which are examined in more detail. At a given temperature and a given ratio of partial pressures of p_{O_2} to p_{H_2} and p_{H_2O} respectively, a specific ratio of oxygen vacancies to hydroxyl defects exists in the crystal as is can easily be deduced when (2.9) and (2.10) are brought in relation.

$$H_2(g) + O_2(g) \overset{K}{\Leftrightarrow} H_2O(g) \quad K = \frac{a_{H_2O}}{a^{1/2}_{O_2} a_{H_2}},\ a_i = \frac{p_i}{p_0} \tag{2.10}$$

In a dry atmosphere (respectively at low water partial pressure) the negatively charged defects caused by acceptor doping are compensated by oxygen vacancies as expressed in (2.8). In wet atmosphere, corresponding to higher water partial pressure, these defects are compensated by hydroxyl defects as is shown by (2.9). Since (2.10) is an exothermic reaction and determines the amount of water present in the gas phase, the equilibrium will shift towards the educts (according to Le Chatelier's principle) with increasing temperature. Accordingly the concentration of oxygen vacancies will increase and the concentration of hydroxyl defects in the lattice will decrease at high temperatures.

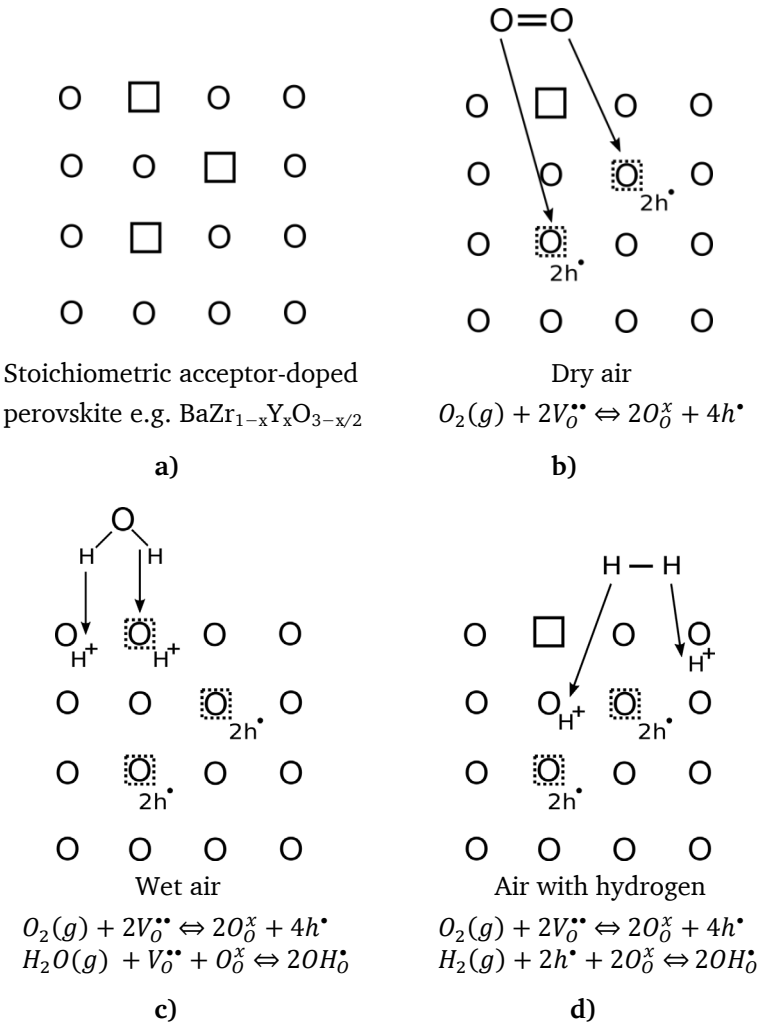

Figure 2.6. Schematic representations of a) a stoichiometric acceptor-doped perovsikte structure and the defect equilibria occurring b) dry air, c) wet air and d) air mixed with hydrogen.

The temperature up to which the protons are stable in the crystal lattice varies from material system to material system as well as with different dopants. Kreuer et al. postulated that hydroxyl defects are easier stabilized in basic oxides [61] (cerate-> zirconate -> stannate -> niobate -> titanate). The factors, which influence the basicity predominantly in oxides, are atomic radius and electronegativity. A different empirical correlation between the hydration enthalpy and the difference in electronegativity was suggested by Norby et al. stating that the hydration enthalpy tends to become more exothermic with decreasing difference in electronegativity of the cations A and B (ΔX_{B-A}) [62]. Therefore, especially the electronegativity of the B site cation is relevant because it can vary to some extent and in that way influence the water/proton uptake greatly. Another factor, which influences the hydration enthalpy, is the dopant concentration. Conclusively the highest hydration enthalpies are predicted for closely packed basic oxides with low ΔX_{B-A}. However, the exact influence of structural and chemical parameters on the hydration enthalpy still remains a topic of controversy and no physio-chemical concepts have been presented so far.

2.3.3. Proton Transport Mechanisms

The elementary processes and reactions dominating the mobility of protonic defects have been subject to detailed investigation, experimentally but also theoretically, using numerical simulations. In principle there are three possible proton transport mechanisms in solid oxides. Out of these three, two are usually discussed and compared, while the third mechanism, tunneling, can be anticipated to be of negligible influence [60]. The first mechanism discussed here, is the so-called vehicle mechanism, which suggests the hopping transport of a proton together with a larger molecule in the form of e.g. NH_4^+, H_3O^+ or OH^- where H_2O, NH_3 and O^{2-} are the vehicles [63]. Although the vehicle mechanism mainly occurs in liquids it has been suggested to play a role, especially at elevated temperatures [60]. Other studies indicate that a vehicle transport is limited to oxides with open structures (e.g. channels, layers), which enable the transport of large ions and molecules. For this reason it is suggested that the vehicle process in oxides can only become a dominating transport mechanism, if it occurs via interstitial lattice sites [64]. In the case of vehicle transport the electroneutrality balance is maintained by the counterdiffusion of non-protonated species (e.g. O^{2-}) or vacancies, creating a net transport of protons (Figure 2.7a). The rate limiting step of this type of proton transport is the molecular diffusion of the vehicle [60].

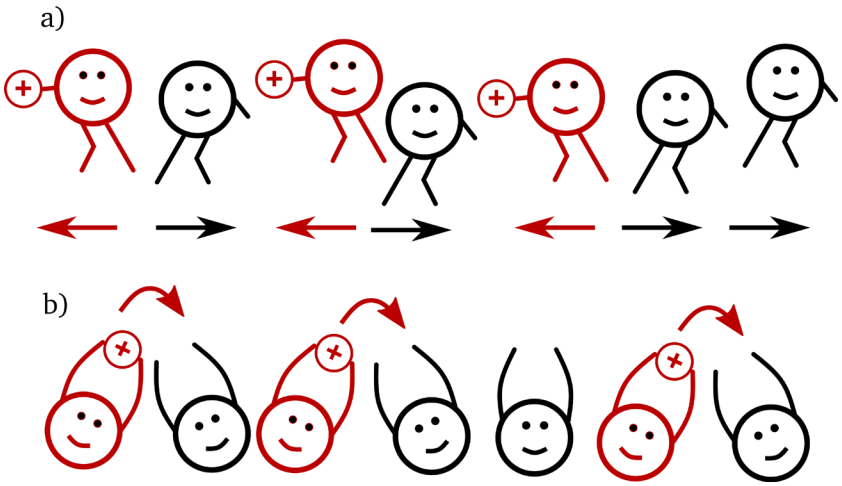

Figure 2.7. Schematic representation of proton transport through an oxide material according to a) the vehicle mechanism with couterdiffusing "empty vehicles" and according to b) the Grotthuss mechanism.

The second mechanism, often referred to as Grotthuss mechanism, includes a rotational diffusion of the protonic defect and proton transfer toward a neighboring oxide ion (Figure 2.7a). When protons are incorporated into an oxide material, they reside close to an oxide ion and exhibit thermal rotational diffusion and stretching vibrations (Figure 2.8). The stretching vibrations, which can also be described as a phonon-activated hopping process, are the rate limiting steps for the proton migration [65].

The activation energy for the rotational motion around the host oxide ion is fairly low, but does not lead to any long-range proton migration [66]. Energetically the protons may be located in one of several local energy minima around the host oxide ion, depending on the nearest neighboring oxide ion. During the rotation temporary hydrogen bonds with neighboring oxide ions in the form of OH-O may be created, which in turn leads to a decrease in O-O distance and slightly affects the lattice structure by polarization. These temporary hydrogen bonds, caused by the stretching vibrations, may lead to a jump to the next oxide

ion. The O-O distance and thereby the related activation energy influence whether or not a stretching vibration leads to a jump (which can be assisted by a tunneling event).

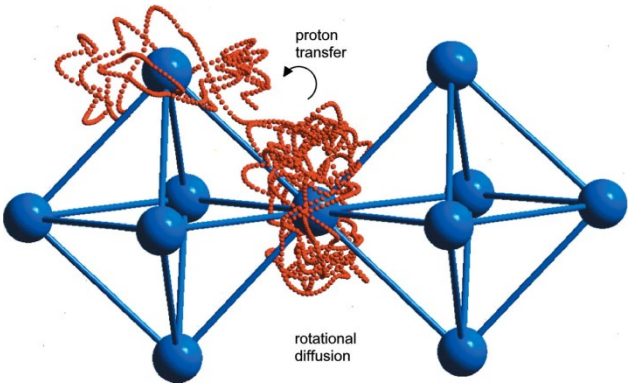

Figure 2.8. Quantum-MD simulation of the proton motions in cubic $BaCeO_3$ (Grotthuss mechanism), displaying the proton trace with rotational diffusion and proton transfer (Reprinted with permission from Annual Reviews: Annual review of materials research [61], © 2003)

The reason for this correlation is the drop in electron density and the increase of the potential barrier in between the oxide ions. The activation energy, which is associated with overcoming the potential barrier between the oxide ions, will therefore be higher in stiff and unpolarizable lattices and lower in softer and wider lattices, especially during stretching vibrations of the anion lattice when the O-O distance decreases. For this reason, wider structures with "soft" anion sublattices (dynamics of oxygen sublattice) such as $BaMO_3$ (M=Zr, Ce, Sn…) perovskites, show high proton mobilities with low activation energies (0.5±0.1 eV) for proton migration. The considerable proton mobility and low activation energy in perovskites can be explained by the large polarizable A-site cations, which allow substantial lattice dynamics of the BO_6 octahedra. Close packed, rigid structures on the other hand such as for e.g. α-Al_2O_3 exhibit very low proton mobility and larger activation energy (~1 eV) [67,68] (polarization effects of different cations may play an additional role), despite the shorter O-O distances. The conductivity of protons in cubic perovskites is higher as compared to less symmetrical crystal structures (e.g. high symmetry in $BaCeO_3$ versus reduced symmetry in $SrCeO_3$), which can be explained by the oxide ion lattice sites being equivalent [61,69].

The above explanations lead to the conclusion that stretching vibrations (phonons) are essential to enable proton transfer from one oxide ion to another [60]. Although oxide ions temporarily move in closer proximity to one another, they only partly penetrate the potential barrier, which in the case of a jump to a neighboring vacancy would have to be fully overcome. The proton on the other hand can jump or tunnel across the remainder of the potential barrier, once its oxide host ion has already overcome part of the potential barrier. Proton conductivity has therefore been rationalized by phonon-assisted jumps and can be interpreted as a polaron-activated process (small polaron) [70]. The activation energy for oxide ion migration is therefore larger (as a rule of thumb: $\frac{3}{2}E_{a,\,proton} \approx E_{a,\,oxide}$) than that for proton diffusion [71].

2.4. Deposition Mechanisms from Liquid Solutions

The chemical reactions, which provide the basis for standard chemical vapor deposition (CVD) in chapters 6.3 and 6.4.1, are the thermal decompositions of the precursor materials. Following the process of decomposition the oxidation of remaining materials leads to the formation of the desired products. Since the decomposition reaction should occur in close proximity of the substrate surface it is necessary that the precursors are kept below their decomposition temperature until arriving at the substrate. A solution to the preliminary precursor decomposition is to use Aerosol-Assisted CVD (AA-CVD), which as opposed to regular CVD does not require high temperatures for thermal precursor evaporation. This modified spray pyrolysis technique implies three processing steps:

1) Dissolution of the respective precursor materials and subsequently atomizing this solution into droplets using pressurized air, ultrasonic or electrostatic techniques
2) Droplet transport (aerosol) to the heated substrate surface by a carrier gas
3) Decomposition of the precursor to initiate film growth

By using a solvent as means of transport the precursor materials are kept below their decomposition temperature. Ideally the droplets are transported to the substrate and the solvent vaporizes just as it reaches the substrate. Since the exact vicinity of the vaporization depends on the droplet size, the parameters have to be well adjusted. However, during the droplet generation a distribution of droplet sizes cannot be avoided thereby leading to different deposition processes occurring at the same time. To clarify and visualize the droplet evolution, of which more than one are inevitably prone to occur simultaneously, a schematic of the different processes is depicted in Figure 2.9.

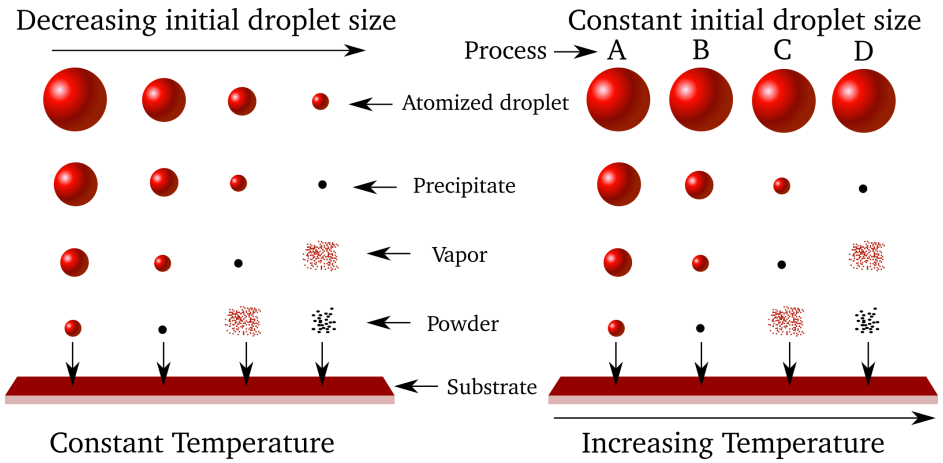

Figure 2.9. (a) Droplet evolution during transport from the atomizer towards the substrate, due to the effect of changing droplet size and increasing temperature [72].

During **Process A** the aerosol droplet size is too large causing the droplet to still contain solvent when reaching the substrate. Therefore, once the droplet reaches and spreads on the substrate the remaining solvent evaporates leaving a dry precipitate on the surface, which subsequently decomposes. As a consequence of the solvent evaporation the substrate temperature is changed locally and thereby influences the reaction kinetics. Consequently, process A leads to rough surfaces.

In **Process B** the entire solvent evaporates before the droplet reaches the surface in the form of precipitates. The non-uniform distribution on the surface not only causes irregular decomposition but also local re-evaporation of particles, resulting in local temperature drops similar to process A (although to a lower extent).

The conditions during **Process C** are ideal so that the classical chemical vapor deposition process can occur, thereby leading to optimal film quality [73]. The solvent completely evaporates similar to process B so that a dry precipitate is left over. However as opposed to process B there is enough time for the precipitate to heat up and vaporize and undergo the stages of chemical vapor deposition [74]:

a) Diffusion of reactant molecules to the surface
b) Adsoption of the molecules at the surface
c) Chemical reaction on the surface (including surface diffusion)
d) Desorption of product molecules from the surface

Process D finally describes the case where the complete evaporation of the solvent occurs at a distance from the substrate. Thereafter the precipitates vaporize as in process C but instead of being adsorbed to the substrate surface the molecules (to form the desired material) already react in the vapor phase. The reacted material then deposits in the form of microcrystallites, which accumulate to a powdery precipitate on the substrate. This powder hinders the formation of a dense high-quality thin film.

Summing up it can be concluded that mainly process C is desirable for the deposition of thin films and that the conditions must be very precise in order for the majority of the droplets to undergo this process.

2.5. Structural Classification of Thin Films

Thin films can be divided into different states of structural order. Therein it is important to distinguish between order of atoms in a crystal or crystallite (grain) and the orientation of grains with respect to each other. The adjacent areas between grains (grain boundaries) are not considered in the following categories. Ideally there are four basic types of order in crystals:

- **Amorphous** thin films possess only a short range order of atoms and no distinguishable grains.
- **Polycrystalline** thin films possess a long range ordering of the atoms (ions) within individual grains and a statistical ordering of the grains with respect to each other and the substrate.
- **Textured** thin films also have a long range order of atoms (ions) within the grains but as opposed to polycrystalline films the grains also have a preferential orientation with respect to each other and to the substrate. Several preferential directions are possible (depending on the exact definition textured materials can also be defined as epitaxial).
- **Epitaxial** thin films show long range ordering with a defined orientation of the grains towards each other and towards the substrate. Ideally only one orientation exists.

For inhomogeneous layers a mixture of the above listed types of ordering is possible. In many cases film deposition on single crystalline substrates can lead to epitaxial growth, if the process parameters are well adjusted. A more comprehensive description of epitaxial growth is presented in the following.

2.6. Epitaxial Growth and Growth Mechanisms

Generally, the oriented growth of a crystalline material on the surface of a single crystal or single crystalline substrate (different material) is called epitaxy [75]. Miller indices of crystal planes and directions are commonly used to describe the epitaxial orientation of thin films. The epitaxial growth and growth mode are defined by the strength and nature of the chemical bonds of substrate and film, and by the difference in lattice parameters. The difference in lattice parameters is called lattice mismatch m and is defined as

$$m = \frac{a_{substrate} - a_{film}}{a_{film}} \tag{2.11}$$

where a_{film} and $a_{substrate}$ are the lattice parameters of the epilayer and substrate material. For many applications nearly matched lattices are desired to minimize defects. However, for larger lattice mismatches the film material is strained laterally (tensile or compressive) to accommodate the lattice structure of the substrate. During the initial stages of film formation the deposit grows fully strained (Figure 2.10b) with a lattice constant matched to the one of the substrate (pseudomorphic growth) until a critical thickness is reached. When the critical thickness is surpassed the strain energy is larger than the energy of formation for defects. The layer will start to relax by plastic deformation involving the formation of misfit dislocations (Figure 2.10c), provided that sufficient stresses are present in the film to cause both nucleation and movement of dislocations. Below the critical thickness the formation of defects

is energetically unfavorable. Figure 2.10a shows this case where a thin film with a_{film} and a substrate with a_{sub} are joined in theory. Since $a_{film} > a_{substrate}$ the resulting lattice parameter $a_{film,\ in\text{-}plane}$ and $a_{film,\ out\text{-}of\text{-}plane}$ adjust accordingly ($a_{film,\ in\text{-}plane} < a_{film}$ and $a_{film,\ out\text{-}of\text{-}plane} > a_{film}$).

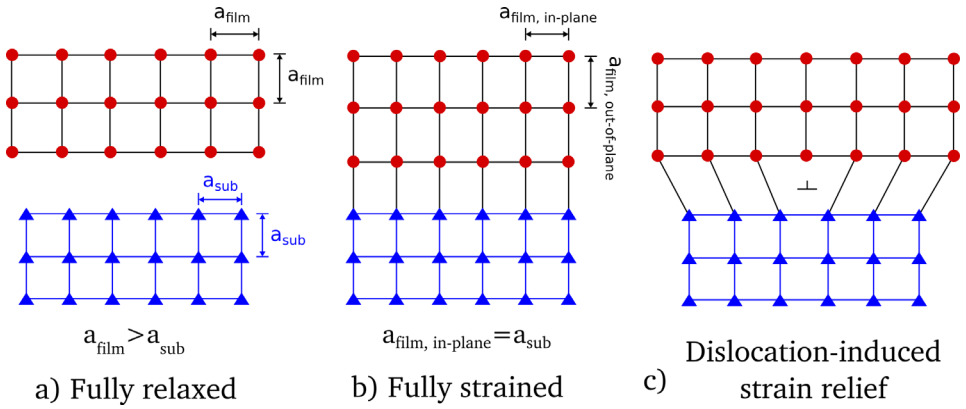

Figure 2.10. a) Cross-section of a theoretically separated film and substrate, b) a pseudomorphically grown film under compression and c) a relaxed film with misfit-induced dislocations.

According to Royer epitaxial growth can only occur when the difference in lattice parameters does not exceed 15 % [76]. The growth itself can be governed by one of three different growth modes. When layer-by-layer growth (Frank-Van der Merve - Figure 2.11a) is occurring these layers grow in a pseudomorphic manner, if the lattice mismatch is not too high (usually <10 %). During this type of growth complete monolayers grow on top of each other until the pseudomorphic growth is no longer energetically favorable. The criterion for layer-by-layer growth is based on surface energy considerations, involving the surface energy of the substrate γ_s, the surface energy of the film γ_f and the interfacial energy γ_i:

$$\gamma_f - \gamma_s + \gamma_i \leq 0 \tag{2.12}$$

The Frank-Van der Merwe growth results in smooth films with a low density of defects. However, if equation 2.12 is not fulfilled, isolated 3-dimensional nuclei (islands) are formed (Volmer-Weber type growth - Figure 2.11b), provided a sufficiently high diffusion coefficient for the atoms across the substrate surface is given. Different islands are characterized by different growth rates, leading to a rough surface. Depending on the lattice mismatch the initial nuclei might grow pseudomorphic. At some point the islands start to coalesce and the deposition is preferential in surface voids. During the coalescence additional imperfections are introduced, because the lattice mismatch introduces small shifts between the lattices of neighbouring islands. The third and final growth mode (Stranski Krastanow – Figure 2.11c) initially exhibits layer-by-layer and subsequently island growth. This type of growth is commonly explained by strain relief, which occurs during the island formation.

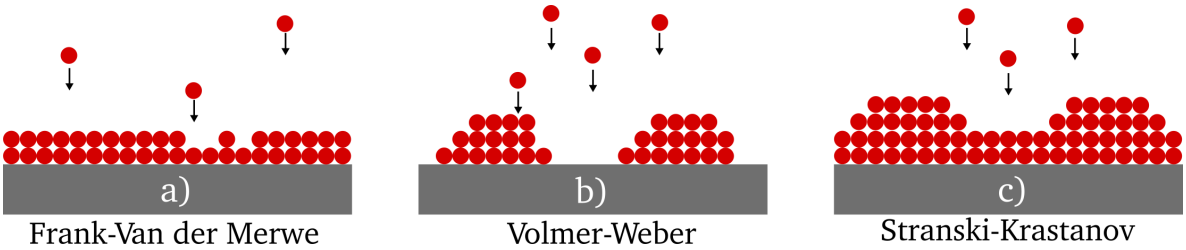

Figure 2.11. The main epitaxial growth modes including a) layer-by-layer (Frank-Van der Merwe), b) island (Volmer-Weber) and the combination layer-then-island (Stranski-Krastanov) growth.

If nucleation and growth of the thin film on the substrate are favorable, the crystal lattices bond perfectly resulting in grain boundary-free regions. This is usually the case during homoepitaxial growth when film and substrate consist of the same material. However during heteroepitaxial growth, when film and substrate material are different, some of the nuclei are misaligned resulting in low energy, low-angle domain boundaries. The implication is that the crystal does not extend in a perfect periodicity across the complete thickness but is instead comprised of small building blocks, which exhibit small variations in orientation, with respect to a reference orientation. This concept is known as mosaicity and was introduced by Darwin in order to describe the microstructure in single crystals [77]. The standard deviations in block tilts Δ are usually considered as equal to the full width at half maximum (FWHM) of x-ray rocking curves (ω-scans). A single crystal is regarded as ideally perfect when the FWHM of a reflection and thereby $\Delta=0$. For example, wavers of GaAs show values of about 10 arsec (1 arcsec = $1/3600^{th}$ part of 1°) [78].

3. Methods for Material Characterization

3.1. Electrochemical Impedance Spectroscopy

3.1.1. Basic Principles

Electrochemical impedance spectroscopy is a powerful technique, which can serve to characterize electrochemical systems such as batteries and fuel cells. The essential concept is based on the fact that when a small perturbation is applied to a system in equilibrium condition, a response, which is completely determined by the initial signal, is triggered. Given that the system in its initial condition is at equilibrium it should return to its original state after the perturbation is stopped. An electrical perturbation (current or voltage) will induce a change of the electrochemical processes around their equilibrium conditions, meaning that the generated response contains the information related to the perturbation and the equilibrium state. The perturbation signal in electrochemical impedance spectroscopy has a sinusoidal form of small amplitude (small signal stimulus), which can be produced by both current and potential. Analogous to direct current measurements, which determine the ohmic resistance, the alternating signal, which is applied in EIS measurements, uses the concept of impedance. Unlike resistance, impedance is based in the (angular) frequency ($\omega=2\pi f$) domain and thus the impedance $Z(\omega)$ of an electric circuit is determined by the ratio of the voltage $V(\omega)$ and the current $I(\omega)$, which are also frequency dependent. Equation (3.1) shows how the ratio of voltage and current are defined using complex exponentials

$$Z(\omega) = \frac{V(\omega)}{I(\omega)} = \frac{V_0 \cdot e^{-i\cdot\omega\cdot t}}{I_0 \cdot e^{-i\cdot(\omega\cdot t+\varphi)}} = \frac{V_0}{I_0} \cdot e^{i\cdot\varphi} \tag{3.1}$$

where t and φ are time and phase angle respectively . The phase shift φ between voltage and current is 0°, +90° and -90° for an ideal resistor, inductor and capacitor, respectively. Instead of complex exponentials the impedance can also be transformed using Euler's formula (according to $e^{ix} = cosx + isinx$) according to

$$Z(\omega) = |Z| \cdot e^{i\varphi} = |Z| \cdot (cos\varphi + i \cdot sin\varphi) = Z' + i \cdot Z'' \tag{3.2}$$

with |Z|, Z' and Z" being the absolute value, real part, imaginary part of the complex impedance, respectively. In this form the impedance can be displayed as a vector in the complex impedance plane as shown in Figure 3.1. When a (usually sinusoidal) excitation voltage or current is applied and the frequency is swept over the desired range, so called Nyquist or Cole-Cole plots are obtained. In these plots the negative imaginary part is plotted as a function of the real part of the impedance. This convention is used for convenience since capacitors, which have a negative imaginary component, occur more often than inductances. A drawback of this mode of representation is that the frequency dependence is not directly displayed. Therefore, so-called Bode plots, which explicitly show the frequency dependence of phase angle and magnitude, are used as complementary sources of information. To interpret the impedance data equivalent model circuits, consisting of resistances, impedances and capacitors, are constructed. The representations of the individual elements in the complex

plane are shown in Figure 3.1, together with the respective impedances of these circuit elements. The impedance of an ideal resistor does not depend on ω and coincides with the real axis, while the impedances of an ideal capacitor and an ideal inductor can be identified by a straight line parallel to the Z" axis.

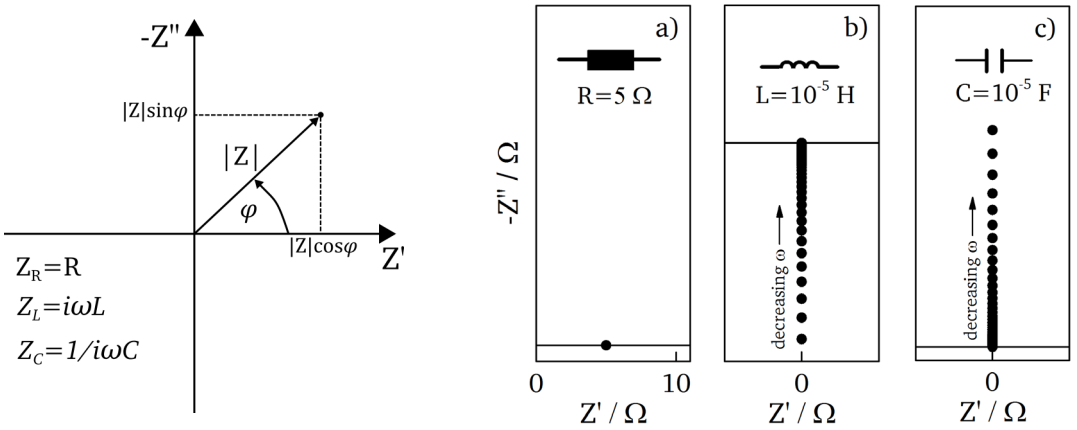

Figure 3.1. The impedance of all elements can be represented in the complex plane: The impedance Z can be separated into its real Z' and into its imaginary Z'' part. Alternatively the impedance can be described using the impedance's phase angle φ and magnitude |Z|. The impedances of the respective phase elements are listed, showing that inductor and capacitor have purely imaginary contributions and a resistor has a purely real contribution. Representations of the basic most common equivalent circuit elements with their Nyquist plots of a a) single resistor, b) a single inductor and c) a single capacitor.

One of the simplest and also most often encountered combinations is a circuit consisting of a resistor and a capacitor in parallel (Figure 3.2). This electrical circuit provides the equivalent model to the impedance response for a single specific relaxation phenomenon (Table 3) within the sample. One example would be a single faradaic electrochemical reaction. Such a reaction can for example take place at the interface of an electrode in combination with another material (e.g. electrolyte), where R_0 is the electrolyte or ohmic resistance (impedance), R_1 is the charge-transfer resistance and C_1 is the double-layer capacitance of the faradaic reaction (polarization region near the electrode).The impedance of such an RC element is described by

$$Z_{RC}(\omega) = \frac{R_1}{1 + i\omega R_1 C_1} \tag{3.3}$$

and yields the Bode plot displayed in Figure 3.2 [79].

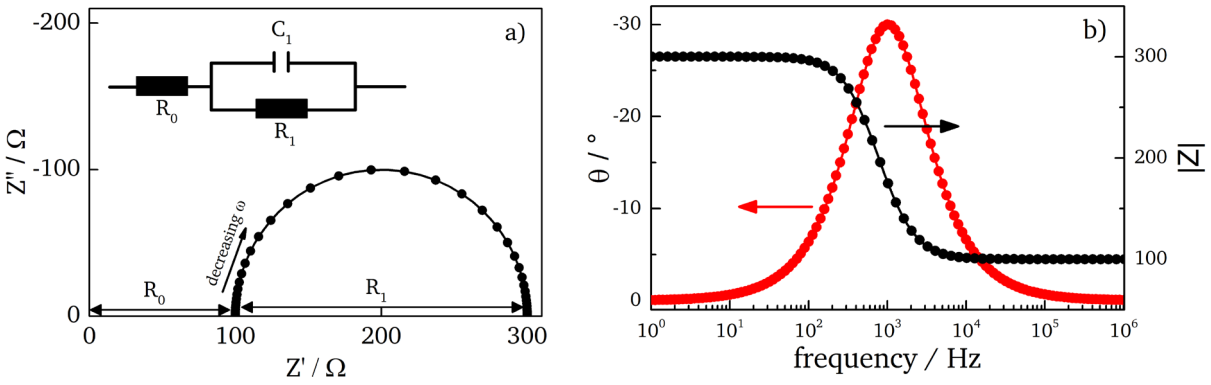

Figure 3.2. a) Simulated impedance spectrum of one RC element in series with a resistor (R_0=100 Ω, R_1=200 Ω and C_1=2·10^{-6} F) in Nyquist plot and b) in the respective Bode plot representation.

The parameter, which can be extracted from such a semicircle, is the time constant τ specific to the faradaic reaction. The parameters of the equivalent circuit are related according to

$$\omega_{max} = \frac{1}{\tau} = \frac{1}{R_1 C_1} \tag{3.4}$$

where ω_{max} is the angular frequency at the highest point of the semicircle and τ is the time constant of the RC element. It is therefore obvious that each reaction, which is represented by a semicircle in a Nyquist plot, possesses a time constant and a capacitance specific to the relaxation (resonance) process of the RC element. Therefore the capacitance values can be used to identify different RC elements and to assign them to different regions of a sample. Since the assignment is based on the magnitudes of the capacitances the influence of the sample geometry is also of concern. As the capacitance of a parallel plate capacitor with area A and plate separation d is defined according to

$$C = \varepsilon_0 \varepsilon_r \frac{A}{d} \tag{3.5}$$

with ε_0 and ε_r being the permittivity of free space and the permittivity of the material, a direct comparison of different samples (with different sample geometries) is only possible when the values are normalized to A/d. Typical normalized capacitance values for different phenomena are listed in Table 3 [80].

Table 3. Typical capacitance values and their possible interpretations for thin films [80]. The capacitances are normalized by A/d.

Capacitance / Fcm^{-1}	**Phenomenon responsible**
10^{-12}	Dielectric relaxation in bulk material
10^{-11}	minor, second phase
10^{-11} - 10^{-8}	Grain boundary polarization in a polycrystalline material
10^{-9} - 10^{-7}	surface layer
10^{-7} - 10^{-5}	sample-electrode interface
10^{-4}	surface layer

Most commonly the tested systems are more complex so that several phenomena occur simultaneously. If the time constants of these phenomena differ by at least two orders of magnitude or more, several semicircles will be measured. The semicircle with the shorter time constant will be the one closest to zero on the x-axis. Figure 3.3 shows the case where two RC elements with two time constants, display two well-separated semicircles with two well-defined phenomena. However the impedance response of most real measurements does not render this ideal behavior. The more frequently obtained impedance response of polycrystalline samples reflects a distribution of time constants instead of a well-defined semicircle caused by deviations from ideal behavior. These variations in reactivity can manifest along or normal to a surface, in current or potential. The occurrence of such behavior may be caused by a number of different phenomena. One physical explanation, which is frequently used, relies on electrode/surface roughness. For a rough surface the

surface dimension is fractal between 2- (flat surface) and 3-dimensional (3-dimensional nature of surface/interfaces) so that a dispersion of capacitances is caused [79,81].

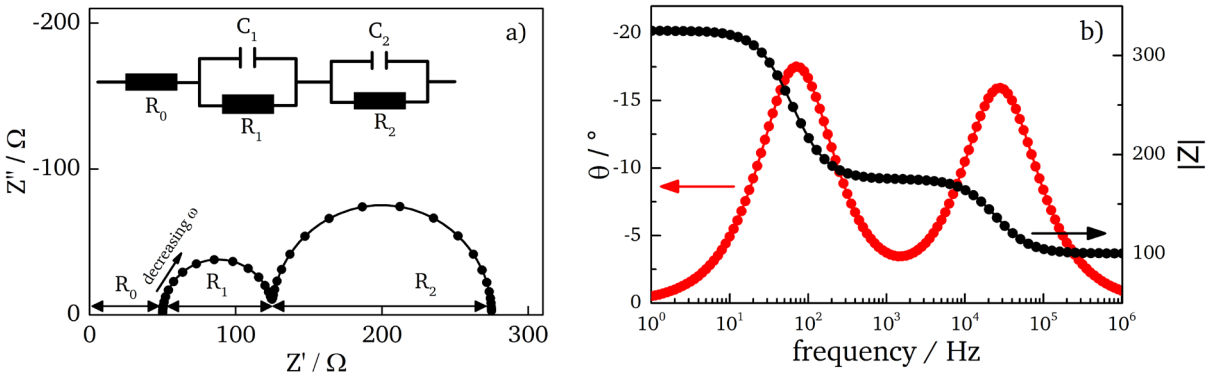

Figure 3.3. a) Simulated impedance spectrum of two RC elements in series with a resistor (R_0=50 Ω, R_1=75 Ω and C_1=1·10^{-7} F, R_2=150 Ω and C_2=2·10^{-5} F) in Nyquist plot and b) in the respective Bode plot representation.

Alternative explanations include local inhomogeneities of the materials such as varying thickness or composition [79,82]. The varying response across or normal to a surface must therefore include additive contributions from each part of the surface/material. Both cases (across and normal to a surface) can be represented by the so called constant phase element CPE, which consists of an infinite number of RC elements in series (surface inhomogeneities) or in parallel (variation of properties normal to the surface such as varying thickness or composition), depending on the geometrical distribution of the phenomenon in question [83]. Although the particular theories may not give exact CPE behavior it has to be pointed out that experimental data will be well fitted, because the deviations are completely hidden by experimental noise and uncertainties [79]. As the complexity of a system increases this becomes increasingly true. Therefore, a CPE can be a useful modeling element even if the exact physical nature of the system is not completely understood. For this reason any fitting procedure needs a careful evaluation of the measurement data and a considerable review of the obtained results in order to validate the chosen model system.

The impedance for a normal distribution of time constants associated with a simple faradaic reaction without diffusion can be expressed in terms of a CPE as

$$Z_{R-CPE}(\omega) = \frac{R}{1 + QR(i\omega)^{\alpha}} \tag{3.6}$$

where α is the constant phase element exponent related to the deviation of a straight capacitive line. The CPE itself can be considered to represent a circuit parameter, for which the limiting behavior represents different circuit elements.

$$Z_{CPE}(\omega) = \frac{1}{Q(i\omega)^{\alpha}} \tag{3.7}$$

In the case of $\alpha = 1$, Q has the units of a pure capacitor and represents the film capacitance. For a value of $\alpha = 0$ the frequency dependence is eliminated and the element behaves like a resistor. If α = -1 or $\alpha = 0.5$ the element behaves like an inductor or a Warburg impedance (diffusion-limited) respectively. This demonstrates the flexibility of the fitting parameter and also highlights why the exact physical meaning of this element is not straightforward. Both α and Q are independent of frequency. The effect of a constant phase exponent on a

measurement ($0.5 < \alpha < 1$) is displayed in Figure 3.4a. The smaller the exponent the more depressed appears the semicircle. Figure 3.4b shows how the arc of such a depressed semicircle can be extended to a full semicircle in a clockwisely rotated hypothetical coordinate system and in what way the constant phase element exponent is a measure of this rotation.

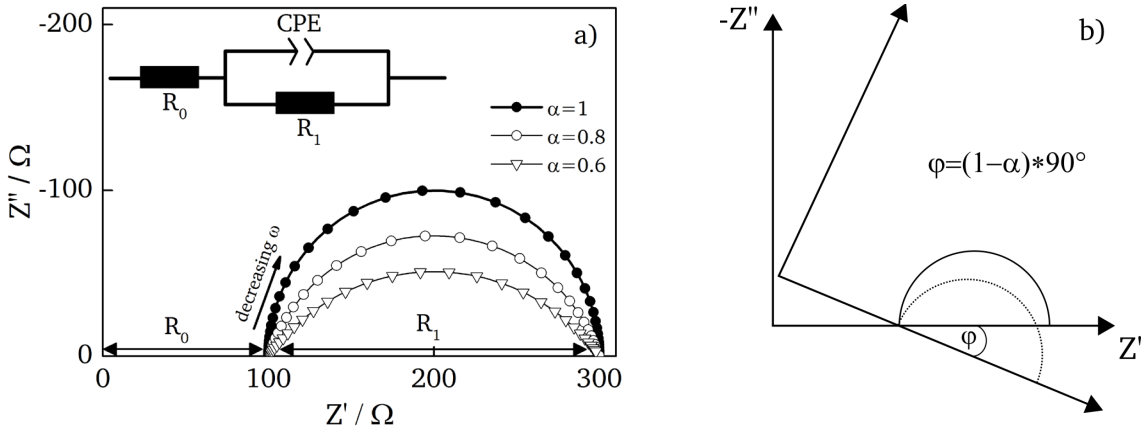

Figure 3.4. a) Sample geometry for EIS measurements of BFO thin films in 'through-plane' geometry; b) equivalent circuit model used for data fitting.

By using a fitting software (ZView [84]), the parameters α and Q can be extracted from respective impedance measurements and the true (or effective) capacitance of the corresponding electrochemical reaction can be calculated, according to a formula presented by Hsu and Mansfeld [85]:

$$C_{eff} = Q^{1/\alpha} R_1^{(1-\alpha)/\alpha} \tag{3.8}$$

Since in most cases experimental results agree well with the R-CPE equivalent circuits, this approach is widely-used as an empirical model, although the exact physical nature and meaning (of a constant phase element) is still a topic of discussion [86]. In addition to the sometimes poorly understood physical basis a depressed semicircle can also result from two or more RC elements, which are connected in series and whose underlying phenomena have comparable time constants. Therefore it is of essence that the process of fitting data to equivalent circuit models is conducted with careful consideration of physical processes, occurring in the sample. A sound understanding of the system under investigation is required to account for all processes and to start with a suited initial fitting model. Since the time constants depend on the experimental conditions such as partial pressures and temperature, systematic studies can separate the impedance responses of the different processes. In this thesis a model, which is commonly accepted in literature for epitaxial thin films is used. The model and the experimental setup, which was used for the impedance measurements is described in detail in chapter 3.1.2.

3.1.2. Experimental Details

Electrochemical Impedance Spectroscopy (EIS) measurements were used to analyze the conducting properties of BFO films as a function of temperature and measurement atmosphere. For this purpose circular Au electrodes, with a diameter of 5 mm, were sputtered on both sides of the samples. The samples were then clamped in between two point contacts (Figure 3.5d) corresponding to a through-plane measurement geometry (Figure 3.5b). A custom build measurement setup as is shown in Figure 3.5c and d was used to control temperature and atmosphere. A schematic of the setup is shown in Figure 3.5a. The shown tube, containing the sample in a controlled atmosphere, was introduced into a furnace to control the temperature. The impedance data were recorded using a frequency response analyzer (Solartron 1260, AMETEK, Berwyn, PA, USA) in the range of 1 MHz to 1 Hz with an excitation AC voltage of 20 mV.

All impedance data was fitted using two conventional Constant Phase Elements in parallel to resistors accounting for film (CPE1-R1) and sample-electrode interface contributions (CPE2-R2) respectively, as shown in Figure 3.5b. An additional resistor (R0) was assumed in series to the R/CPE elements, accounting for the resistance of the measurement setup given by electrodes, wires, leads and Nb:STO substrate (which is typically in the order of 1–3 Ω at elevated temperatures). To account for residual inductance caused by the leads (Figure 3.5a and b) an inductance (L0) was added in series to the equivalent circuit fit model Figure 3.5b), so that the high frequency range (100 kHz–1 MHz) could be described correctly.

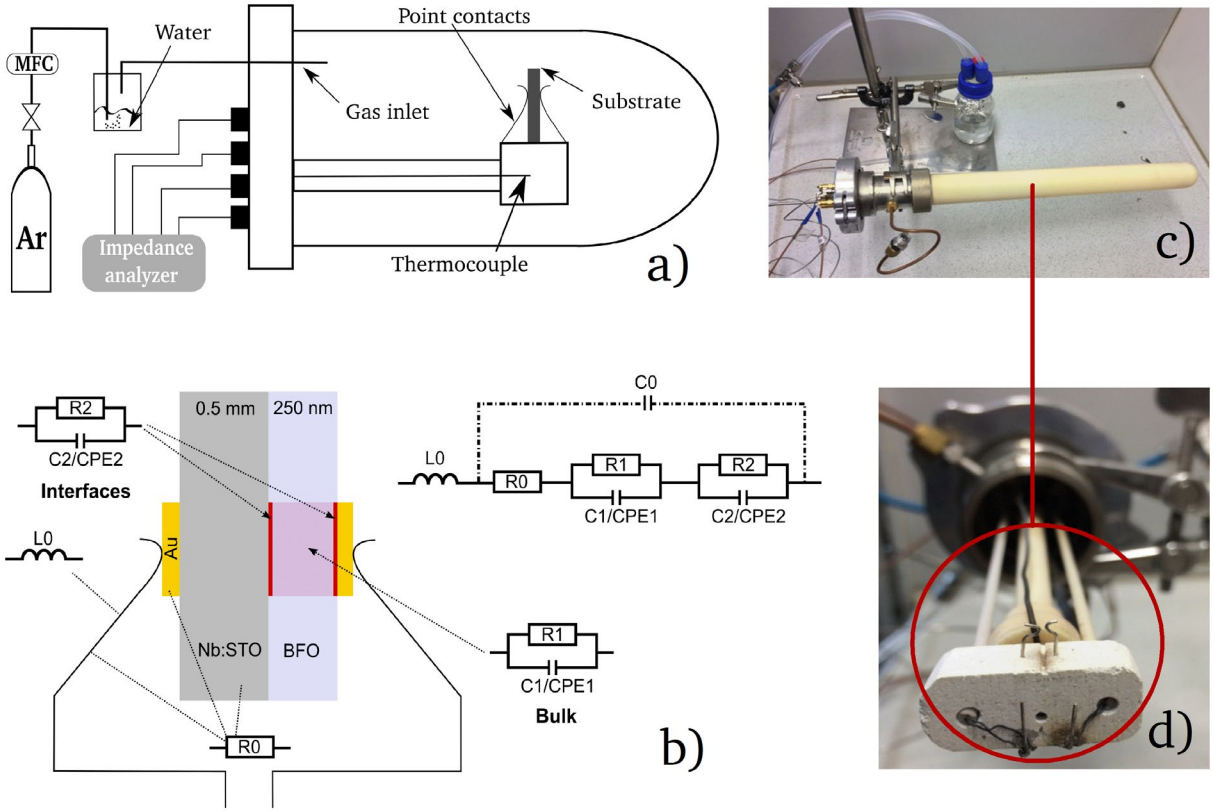

Figure 3.5. a) Schematic representation of the custom-build EIS setup and b) the substrate-film configuration including the individual equivalent circuit elements and their origin. In addition the equivalent circuit model, which was used for the analysis of the thin films, is depicted. c) and d) display photographs of the actual experimental setup and a magnification of the point contacts inside of the alumina tube.

The residual capacitance of the measurement setup (C0) was determined by connecting a resistor (10 MΩ) in place of the substrate/film configuration, meaning in parallel to the other circuit elements. The Nyquist and Bode plots of this configuration as well as the equivalent circuit is shown in Figure 3.6a) and b). The capacitance value of the setup is ~1.2 pF, which is about 5 orders of magnitude lower than the capacitances in question. Therefore this capacitance can and has been neglected in the calculations and equivalent circuit considerations. The intrinsic impedance of the substrate (clean substrate with sputtered Au electrodes) was measured in the temperature range from 200 °C to 500 °C in Ar atmosphere. The measurements from 200 °C to 300 °C are shown in Figure 3.6c). At 200 °C a resistance of 4Ω could be estimated, which is small compared to the film resistance at this temperature (2 orders of magnitude higher), and could therefore be assumed to not influence the measurements significantly.

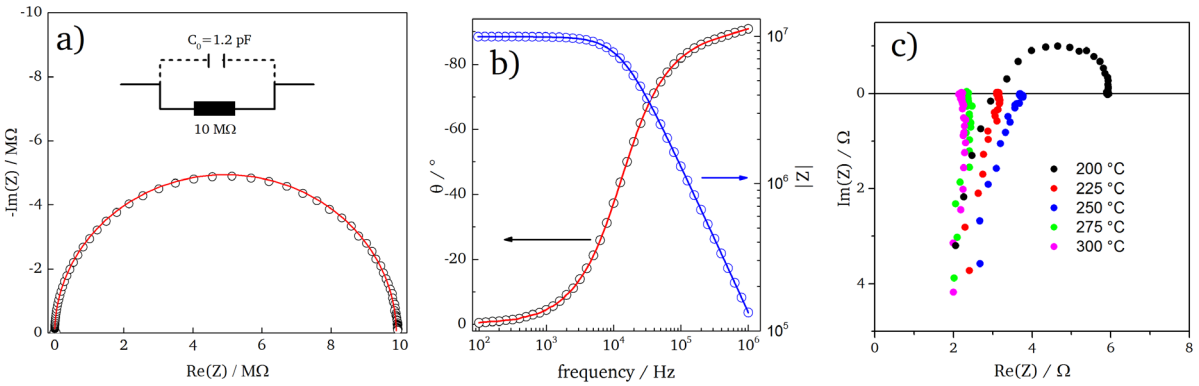

Figure 3.6. a) Nyquist plot showing the measurement and fit of the equivalent circuit model when instead of the substrate film configuration only a single resistor (10 MΩ) is connected. b) The Bode plot corresponding to the single resistor measurement. c) Substrate-only (with sputtered Au contacts) measurements performed in Ar atmosphere.

At temperatures higher than 200 °C the resistance of the substrate is too small to be determined. Solely the residual inductance of the leads could be observed. Figure 3.6c shows the Nyquist plots of the "substrate-only" measurements in the temperature range from 200 °C to 300 °C. The temperature range from 300 °C to 500 °C is not displayed, since it does not contain any additional information. The impedance spectra were fitted and evaluated using the software ZView3.4 [84]. All samples were measured during heating in the temperature range of 200 °C to 550 °C in steps of 25 °C. A continuous flow of Argon/synthetic air was used during the measurement and regulated by a Mass Flow Controller (MFC - MKS Instrument 647B). The hydrated samples were measured in the respective wet atmosphere by bubbling the gas through a water-containing closed beaker (Figure 3.5a) at room temperature (~3% H_2O).

Figure 3.7 displays two characteristic Nyquist plots of measurements in air and Ar at 400 °C, including the fits. The frequency over phase-angle plots (Figure 3.7b) show two distinct maxima, indicating that the fit model is suitable to fit data with two semi-circles. The fitting parameters, which were obtained from the CPEs, were converted to effective capacitances C_{eff} according to equation (3.8) presented by Hsu and Mansfeld [85]. The effective capacitance values of the second semicircle were normalized to the contact area A confirming capacitance values for typical sample-electrode interface reactions (~8.1×10^{-6} F cm^{-2}). The same procedure was applied to the capacitance values of the first semicircle whereas those were normalized to a geometrical factor (f = electrode area/film thickness) and resulted in

capacitance values C_{eff}^{*} typical for bulk contributions corresponding to the film properties [80].

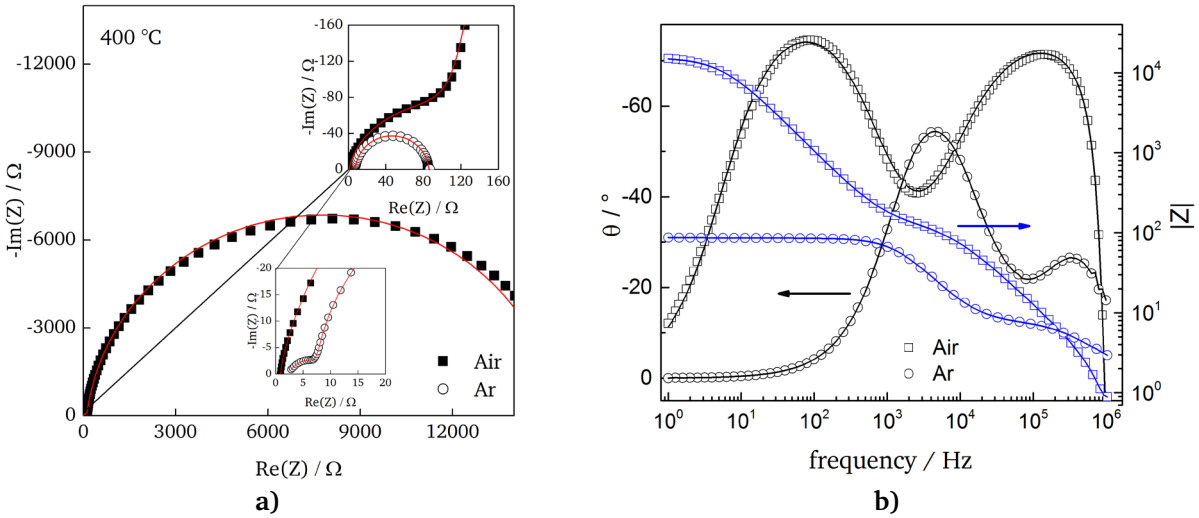

Figure 3.7. a) Characteristic Nyquist plots for a measurements in Air and Ar, including Zview fits (using the model in Figure 3.5b) with the corresponding b) Bode plots for a measurement at 400 °C (Ar atmosphere).

3.2. X-Ray Diffraction

3.2.1. Basic Principles

One of the most versatile methods for the structural characterization of crystalline materials is X-Ray Diffraction. Because of their short wavelengths in the order of hundreds of picometers [87], X-rays are particularly well-suited to interact with crystalline materials, which have lattice dimensions in the same order of magnitude. When X-Rays interact with matter, they can get scattered, reflected, absorbed, refracted or transmitted. The scattering can be coherent or incoherent. Incoherent scattering (Compton scattering) refers to the case, in which the wavelength of the scattered beam increases due to partial loss of photon energy (inelastic) caused by collisions [87]. Incoherent scattering is not relevant because its phase is only randomly related to that of the incident beam. It is therefore usually neglected, when the interaction of X-rays with crystal lattices is of concern. However, if the scattering is coherent, the scattered beam has the same frequency and wavelength as the incident beam, since there is a definite relationship between the phases of both beams. This type of scattering is elastic and shows a scattering angle dependent intensity distribution. Since the effect was first worked out by J. J. Thomson, this type of scattering from a single electron is also called Thomson scattering [87]. Conversely, even though the Thomson theory only assumes free electrons the agreement with experiments is very good, when used to calculate scattering amplitudes and cross sections. When an X-ray beam encounters an atom, each electron scatters part of the radiation coherently. Constructive interference can occur when the waves are scattered elastically (X-rays) from the crystal planes of a lattice, under the condition that Bragg's law is fulfilled. This type of scattering is called diffraction and is described by Bragg's equation [87]

$$n\lambda = 2dsin\theta \tag{3.9}$$

with λ being the X-ray wavelength, d the spacing between lattice planes, θ the scattering angle between sample surface and incident X-rays and n an integer (n=1,2,3..). The Bragg equation basically states, that the phase shift of the coherently scattered waves needs to be an integer multiple of λ to result in constructive interference. A set of parallel equally spaced lattice planes can be summed up as a family (or series) of lattice planes defined by the Miller indices h, k and l. For each family of lattice planes the Miller indices can be obtained by using the reciprocal intercepts of the planes with the lattice vecors in real space. A specific family is then defined by d_{hkl} and the orientation of the lattice plane normal.

The visualization and interpretation of experimental results can be simplified by using the concept of reciprocal space, rather than direct space. By definition the lattice spacing in reciprocal space is called g. For an orthorhombic crystal system the relationship between Miller indices and lattice spacing is as follows

$$g = \frac{1}{d} = \sqrt{\frac{h^2}{a^2} + \frac{k^2}{b^2} + \frac{l^2}{c^2}} \tag{3.10}$$

with a, b and c being the lattice parameters [88,89]. The lattice parameters can be calculated if the reflection, which is observed in a diffractogram, can be assigned to specific Miller indices. In reciprocal space all families of planes are represented by reciprocal lattice points,

as indicated in Figure 3.8. In reciprocal space the incoming X-rays are represented by a propagation vector $\vec{k}_{in}$. Therefore an equivalent formulation of Bragg's law for diffraction can be visualized using the Ewald sphere construction [87]. The absolute value of the incident wave defines the radius of the Ewald sphere by the reciprocal wavelength $|\vec{k}_{in}| = 2\pi/\lambda$. The center of the Ewald sphere is set to be the origin of $\vec{k}_{in}$ with $\vec{k}_{in}$ ending at the origin of the reciprocal lattice (000). Similar to the incident wave vector the scattered outgoing wave is characterized by $\vec{k}_{out}$. Combining $\vec{k}_{in}$ and $\vec{k}_{out}$ yields the scattering vector $\vec{g}$ (Laue condition), which is perpendicular to the scattering plane, according to [89]

$$\vec{g} = \vec{k}_{out} - \vec{k}_{in} \text{ with } |\vec{g}| = \frac{2\pi}{d_{hkl}} \tag{3.11}$$

In the Ewald-Sphere construction Bragg's law is only satisfied when a reciprocal lattice point intercepts the surface of the Ewald sphere. The principle of diffraction in reciprocal space is displayed in Figure 3.8 where the scattering vector connects the origin (000) to the (001) diffraction maximum. For ideal crystals the size of the reciprocal lattice points is inversely proportional to the dimensions of the crystal. If however one dimension of the crystal is strongly decreased (e.g. during surface diffraction due to limited crystal dimension) the points in reciprocal space extend along the shortened dimension (crystal truncation rods) [87].

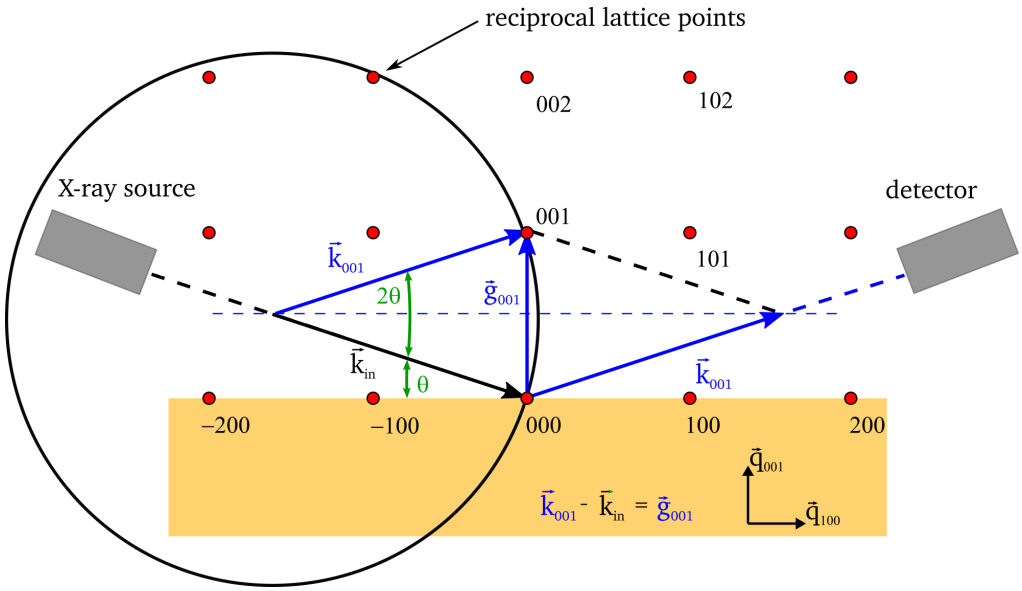

Figure 3.8. Schematic representation of the geometrical relationships between source, detector and diffraction in reciprocal space. The Ewald sphere is projected onto the $\vec{q}_{100}$ - $\vec{q}_{001}$ plane to visualize the diffraction condition, which is fulfilled for the (001) reflection.

X-ray diffraction can be used in a variety of measurement geometries to structurally analyze thin films and bulk materials. Since the measurements in this thesis were mostly performed on epitaxial thin films, the setup and subsequently the most common types of scans will be discussed in the following sections. The sample was mounted onto a goniometer head, which could be moved into x, y and z direction, as displayed in Figure 3.9. Additionally the goniometer head could be rotated around the indicated angle ϕ and tilted around an axis within the measurement plane (angle χ). The measurement plane is defined by the X-ray source, the detector and the sample. The angle between the incoming X-ray and the sample

surface is defined as θ and the sum of entrance and exit angle as 2θ. A schematic setup for the investigation of epitaxial thin films is shown in Figure 3.9. The optics before and after the sample, include Göbel mirrors, monochromator, slits and Soller slits. These optics are necessary to parallelize and narrow down the used wavelength of the x-rays. Depending on the above described angles different types of scans were conducted to investigate the thin films structurally. The scan types used in this thesis comprise the coupled 2θ-θ scan, the rocking curve measurement (ω-scan) and the azimuthal scan (ϕ-scan). For a better understanding the different types of scans are described in the following. Further types of scans, which are not described in detail are the measurement under grazing incidence and X-ray reflectometry.

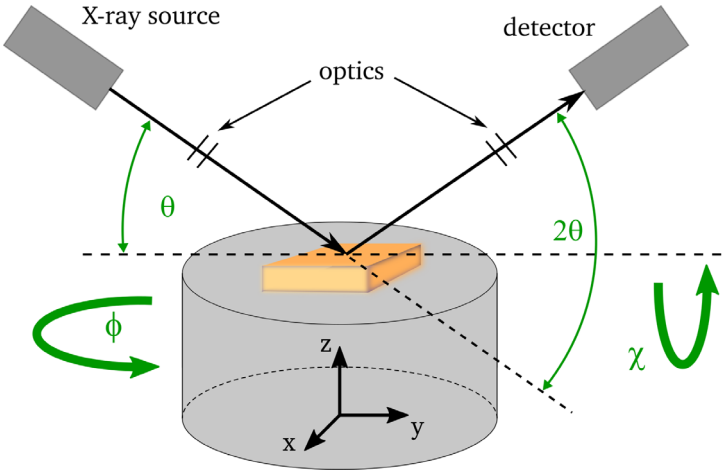

Figure 3.9. Schematic representation of the geometrical setup during the measurement on thin epitaxial films. The sample is fixed to a goniometer head and can thereby be moved into x, y and z direction as well as rotated around ϕ and tilted around χ.

3.2.2. Coupled θ-2θ Scan

One of the most common arrangements, which is often used to determine orientation, crystallinity, stress state, thickness and lattice parameters of epitaxial thin films, is the coupled θ-2θ scan. In order to carry out this measurement, the samples first have to be positioned correctly with respect to the X-ray beam, which is done by adjusting all angles with respect to the substrate lattice (see Figure 3.9). Thereafter a symmetrical scan, in which source and detector are moved in the same way, can be performed. The schematic representation of this type of scan in reciprocal space is displayed in Figure 3.10. It shows two different diffraction spots being in the Bragg condition, under different scattering angles and therefore highlights how a coupled symmetric θ-2θ measurement manifests in reciprocal space. The scattering vector q is moving in the out-of-plane direction and the Ewald sphere is rotating around the origin. During a θ-2θ scan all reflexes of parallel lattice planes can be detected and thereby offers the possibility to establish epitaxial relationships for heteroepitaxial films. Furthermore it is possible to determine the lattice constants a, b and c by measuring along the according directions h, k and l.

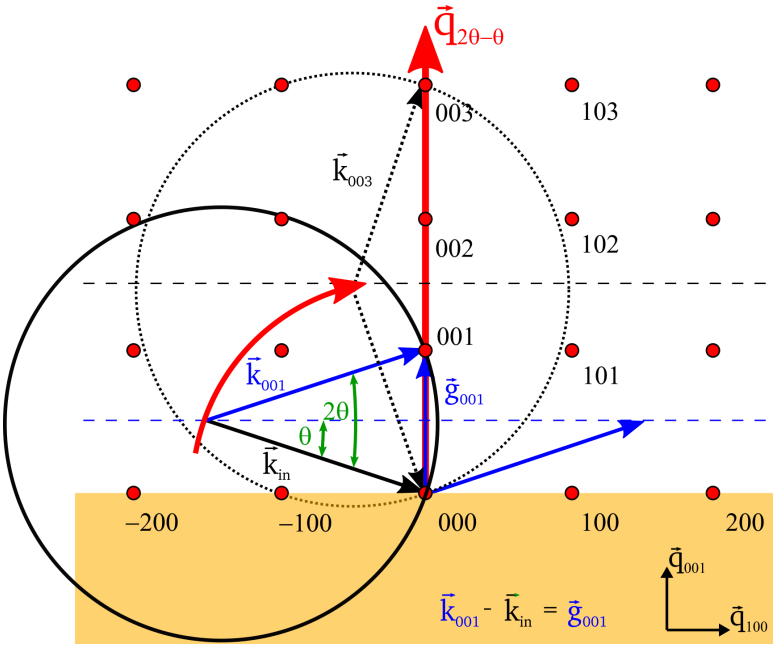

Figure 3.10. Projection of the diffraction relationships in reciprocal space during a θ-2θ scan onto the [100]-[001] plane. $\vec{q}_{100}$ and $\vec{q}_{001}$ relate to the directions of [100] and [001] in reciprocal space. $\vec{q}_{2\theta-\theta}$, which is displayed in red describes the direction of the measurement across the (00l) reflections. The wave vectors of two specific situations, namely (001) and (003), where the Bragg condition is fulfilled are displayed. The red arrow indicates the movement of the center of the Ewald sphere during a θ-2θ measurement. The Ewald sphere rotates around the origin.

3.2.3. Rocking Curve (ω-Scan)

Ideally the nucleation and epitaxial film growth on a substrate would occur without creating any grain-boundaries, implying that the grown crystals would meet and bond perfectly. However, in reality the nucleation and crystal growth takes place with a certain degree of misalignment so that the crystal lattice does not extend in perfect periodicity from one crystal face to the opposite one. Instead the concept of mosaicity regards a single crystal or an epitaxially grown film to be comprised of small building blocks with small variations in their orientation, which results in low-angle and low-energy domain boundaries. Usually, no voids exist between the individual domains but instead a series of dislocations accommodate the misorientation. These structural variations can be expressed by an orientation distribution function and is quite often given in the form of a Gaussian distribution with a standard deviation Δ, expressing the degree of tilt. A perfect crystal would yield a standard deviation of Δ=0. The so-called rocking curve measurement is usually employed to determine the degree of misorientation in a film. For this type of scan the incident angle θ as well as the exit angle 2θ are kept constant and only the sample is "rocked" by an angle ω so that lattice planes with equal lattice spacing are detected. In this way the tilts of lattice planes can be examined as is shown in Figure 3.11b. By rocking around the maximum intensity (+/-Δω) at θ, the broadening caused by the misorientation is made visible. In reciprocal space the mosaic structure can be explained by the broadened shape of a lattice point. The full width at half maximum can usually be used to compare mosaicities (see also 2.6) and thereby the quality of films. A single crystal is regarded as ideally perfect when the FWHM of a reflection and thereby Δ=0. For example, wavers of GaAs show values of about 10 arsec (1 arcsec = 1/3600th part of 1°) [78]. At a magnitude of Δ > 0.3-0.5 ° a distinction is usually made to separate highly textured films from the single crystalline films with mosaicity. However, this distinction is not explicit and the transition region between texture and mosaicity varies in literature.

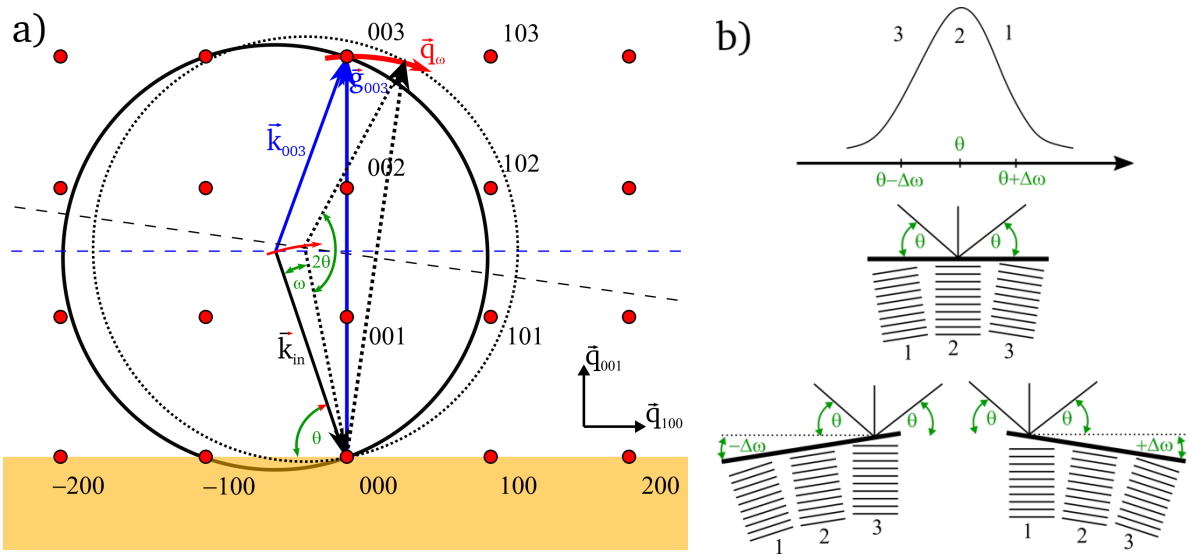

Figure 3.11. Projection of the diffraction relationships in reciprocal space during a 2θ-θ scan onto the [100]-[001] plane. $\vec{q}_{100}$ and $\vec{q}_{001}$ relate to the directions of [100] and [001] in reciprocal space. $\vec{q}_\omega$ describes the measurement direction in which the spread-out of a certain reflection is measured. The motion of the center of the Ewald sphere is again indicated by a red arrow.

3.2.4. Azimuthal Scan (ϕ-Scan)

While a coupled θ-2θ scan can determine, whether the crystallites within a film have one unit cell axis oriented perpendicular to the substrate, thereby forming an epitaxially grown layer, and the ω-scan can determine the degree of tilt of these crystallites, no information is gained about the azimuthal orientation of the crystallites. Since the azimuthal misorientation of the crystallites is also a critical feature the in-plane orientation can be investigated by azimuthal scans (ϕ-scans). Such a scan is performed under set conditions of a particular asymmetric Bragg diffraction peak e.g. (202), which includes an in-plane direction. The 2θ-angle of that particular reflection is kept constant while the azimuth angle ϕ is varied (rotation around the surface normal). Figure 3.12a shows the initial diffraction relationships at the beginning of the ϕ-scan after the sample has been aligned with respect to the (202) reflection for a specimen with fourfold rotational symmetry. Figure 3.12b shows the schematic rotation of scattering vector $\vec{g}_{202}$ around the sample normal during the ϕ-scan. The resulting measurement displays reflections according to the in-plane symmetry (in this case four). If this type of scan is performed for substrate and epilayer reflections the in-plane orientational relationship can be determined. In other words, the number of reflections is indicative for the in-plane crystal symmetry and can reveal details about film growth such as domains or rotations of the in-plane stacking.

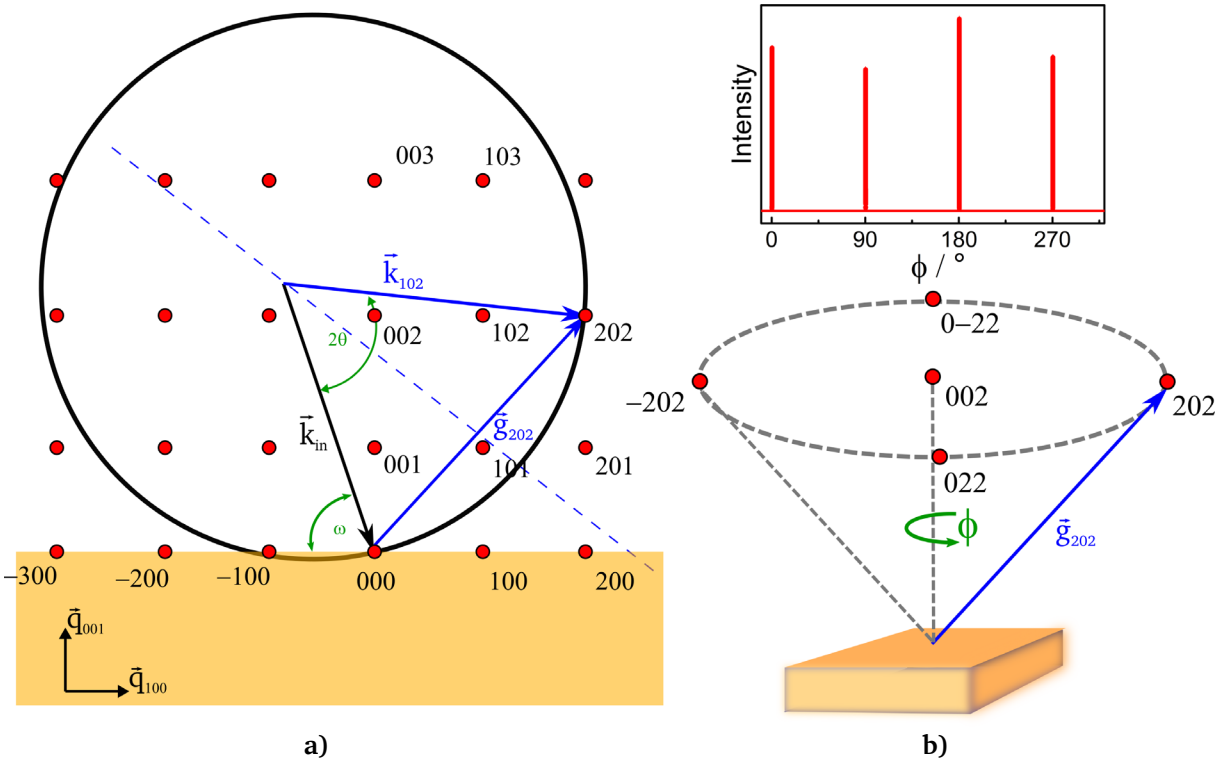

Figure 3.12. a) Projection of the diffraction relationships in reciprocal space at the beginning of a ϕ-scan onto the [100]-[001] plane. $\vec{q}_{100}$ and $\vec{q}_{001}$ relate to the directions of [100] and [001] in reciprocal space. b) Rotation of the the scattering vector $\vec{g}_{202}$ around the surface normal by an angle ϕ. Additionally, the measurement of a specimen with fourfold rotational symmetry is shown.

3.2.5. Experimental Details

- Epitaxial films

  XRD measurements (θ–2θ geometry) were performed using a Rigaku SmartLab X-ray diffractometer employing Cu K_α radiation ($\lambda_{K\alpha}$=0.154 nm) and a Ge[220] 2-bounce monochromator on the primary side operating in reflection parallel beam geometry (170 mA, 45 kV). Some XRD measurements were performed using a Bruker D8 diffractometer (Cu K_α radiation) in a high resolution setup, with 40 mA and 40 kV. The setup consisted of a Göbel mirror and a 4-bounce Ge[022] monochromator in parallel beam geometry. The measurements were performed in a 2θ range from 15° to 115°. The step size was 0.01° and the scan speed 1 s per step.

  The ϕ-scans ('in-plane' structure) were recorded with a STOE 4 circle diffractometer using a Cu anode and a 2-dimensional X-ray mirror on the primary side. On the secondary side a slit system, a Ni filter and an energy dispersive detector were used to separate the Cu K_α line (40 mA, 35 kV).

- Polycrystalline films

  The diffraction patterns of the polycrystalline films, which are discussed in chapter 6, were recorded using a Bruker D8 diffractometer (Cu K_α radiation) in Bragg-Brentano geometry. A Ni filter was installed in order to remove K_β radiation The structure refinements and quantitative phase determinations of the diffraction patterns were carried out using the Rietveld method [90]. For this purpose the software TOPAS 5.0 was employed. The instrumental broadening of measurement data was determined using scans of LaB_6 powder (NIST 660a) as reference.

3.3. Additional Characterization Methods Used in this Thesis

3.3.1. X-Ray Photoelectron Spectroscopy

The integrated ultra-high vacuum system Daisy-Bat (Darmstadt integrated System for Battery research) consists of several sample preparation chambers for thin films as well as a Physical Electronics 5000 Versaprobe XPS/UPS analysis unit. The system is operated by three different research groups, which use different deposition techniques such as CVD, RF-magnetron sputtering and PLD. In this thesis only the LA-CVD setup and the XPS unit were used. The samples were deposited using the indicated chambers in Figure 5.5 (LA-CVD and Deposition, for details see 4.2) and subsequently transferred to the XPS unit for surface analysis.

The base pressure of the LA-CVD setup is $< 10^{-2}$ mbar and increases to around 1-5 mbar during the deposition process and during the deposition process (described in chapter 4.2). Therefore after the deposition process is completed the samples first have to be transferred into a buffer chamber, where the pressure is reduced to $\sim 10^{-7}$ mbar. Hereafter a transfer to the XPS and other chambers of the system is possible, because the base pressure of the system is $\sim 10^{-9}$ mbar. In this way the thin films can be analyzed in-situ without breaking the vacuum. Therefore the electronic surface properties and the surface compositions can be determined in-situ.

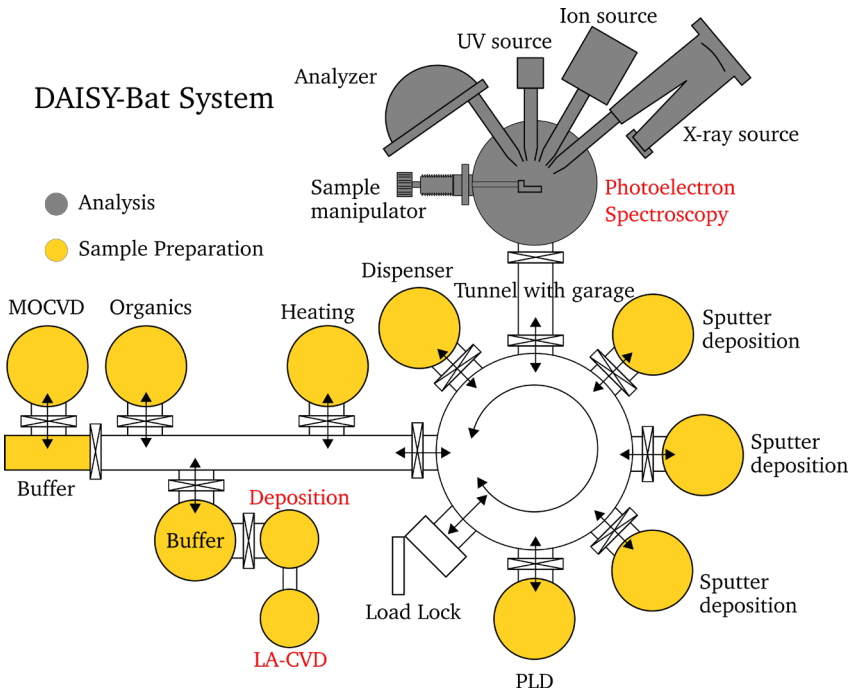

Figure 3.13. Schematic representation of the DAISY-Bat system. Several different deposition techniques (PLD, Sputtering, CVD and thermal evaporation) in combination with UV and XP spectroscopy for analysis. The chambers marked in red were used for deposition and analysis in the current thesis. A more detailed representation of the LA-CVD and deposition chamber can be found in Figure 4.3.

The surface composition and oxidation states were examined by ex-situ X-ray photoelectron spectroscopy (XPS) analysis using a Physical Electronic VersaProbe XPS unit (PHI 5000 spectrometer) with Al Kα radiation (1486.6 eV) under an electron escape angle of 45°. The spot size of 200 µm was chosen for all measurements. All detail spectra were recorded with 50.6 W, a step size of 0.1 eV and a constant pass energy of 23.5 eV. Whenever not mentioned specifically, the binding energies were calibrated with respect to the carbon 1s

(C 1s) emission line at 284.8 eV. To determine the integral intensity and the exact binding energies of the emission lines, the spectra in chapter 5.5 are background-corrected according to Shirley [91]. The atomic sensitivity factor method was used to perform a chemical analysis of the surface [92]. Atomic Sensitivity Factors (ASF) were provided by the Physical Electronics Handbook of XPS [93]. For the determination of the relative atomic concentrations (quantitative analysis) the software PHI MultiPak Version 9 was used [94]. The emission lines were fit using pseudo Voigt functions, which are linear combinations of Gaussian line shapes (related to e.g. the broadening due to the spectrometer) and Lorentzian line shapes (related to e.g. the intrinsic life-time broadening). Since no standards could be used the described method yields semiquantitive results with 10 – 20% accuracy [93].

3.3.2. Scanning Electron Microscopy

For the analysis of the film morphology and microstructure scanning electron microscopy (SEM) was used to characterize the deposited films. A Philips XL30 equipped with a field emission gun was used for all measurements. In order to prevent electrical charging thin conductive films of Au were sputtered onto the samples using a Quorum Q300T (30 s, 30 mA) sputter coater.

3.3.3. Conversion Electron Mößbauer Spectroscopy

Conversion electron ^{57}Fe Mößbauer spectra of Ar annealed thin films before and after hydration were measured with a custom designed proportional counter at room temperature working with a He-CH_4 (6 %) gas mixture. Due to the low ^{57}Fe concentration and the presence of several magnetically split subspectra the data acquisition time was in the order of several weeks. The Mößbauer drive is operated in linear acceleration mode and the data was fitted with the WIN Normos software package (R. A. Brand, WissEl GmbH). All Isomer shift IS are given relative to α-Fe at RT. The Mößbauer fitting parameters for the samples investigated in chapter 5.4 can be found in the Appendix (Table A 1 and Table A 2).

3.3.4. Atom Probe Tomography

Atom probe tomography (APT) sample preparation was performed employing a FEI Strata 400 STEM and a Zeiss Auriga 60 FIB. Prior to the lift-out, a platinum protection layer (150 nm) was deposited over the area of interest to protect the sample surface from Gallium (Ga) ion beam milling damage or sample degradation. Annular milling was used to create needle shaped morphology with an end diameter smaller than 100 nm. More details about the FIB milling process can be found elsewhere [95,96]. The APT analysis was carried out using a Cameca-LEAP 4000X HR instrument in laser pulsing mode (wave length 355 nm, pulse frequency 100 kHz, pulse energy 60 pJ, evaporation rate 0.50%) at 50 K. Data processing was achieved with the CAMECA Integrated Visualization and analysis software (IVAS-version 3.6.1), incorporating standard reconstruction algorithms, allowing the extraction of three-dimensional nanoscale chemical distribution of all detected atoms in the analysis volume.

4. Sample Preparation and Treatments

4.1. Pulsed Laser Deposition and Post-Deposition Treatments

For the deposition of BFO films pulses from a KrF excimer laser (Coherent COMPexPro 205) with a wavelength of 248 nm were focused on a BFO target material over an area of around 5 mm^2. The target for ablation was prepared by solid state synthesis using stoichiometric amounts $BaCO_3$ and Fe_2O_3 [28]. During film deposition the target was rotated (30 rpm) and toggled at the same time to ensure an even ablation of the material. To set the temperature of the substrate holder a diode laser, with a wavelength of 940 nm, was used. The temperature was controlled using a narrow band pyrometer as displayed in Figure 4.1. Silver paste provided the necessary thermal contact between the sample and substrate holder. The film deposition was conducted at 700 °C with a fluence of ~2 J/cm^2 and a repetition rate of 2 Hz, leading to a deposition rate of about 3.18 nm/min (0.53 Å/s). The film growth rate was estimated using X-ray reflectrometry on a Si substrate and then confirmed by Secondary Electron Microscope micrographs. The background oxygen pressure was maintained at 0.018 mbar and the substrate-target separation was set to a distance of 40 mm. All films were deposited on electronically conductive (001)-oriented Nb-doped $SrTiO_3$ (0.5 wt. % Nb, Nb:STO) substrates with dimensions of 5 × 10 × 0.5 mm (width × length × thickness). The cooling rate for all deposited films was 50 K/min, while maintaining an oxygen pressure of 0.018 mbar. For a few films the growth process was monitored via Reflection High Energy Electron diffraction Diffraction (RHEED). A schematic representation of the PLD setup is depicted in Figure 4.1.

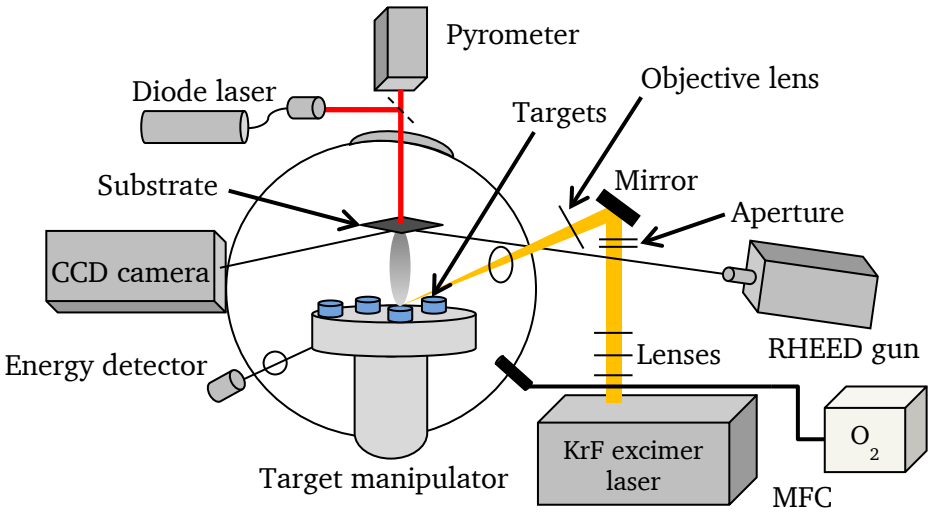

Figure 4.1. Schematic representation of the pulsed laser deposition setup, used for the deposition of $BaFeO_{2.5}$ films. The setup, located at the Institute of Nanotechnology (Karlsruhe Institute of Technology, Karlsruhe), was connected to an additional UHV chamber. This chamber was used for storing substrates as well as other targets and served as transfer chamber to insert and extract samples into the UHV system.

After the deposition the thin films were annealed at 700 °C in a tube furnace and under flowing argon for 15 h in order to minimize the Fe^{4+} contents. To observe and compare the effects of oxidation some samples were heated under flowing oxygen at 500 °C for 15 h.

Subsequently a hydration process was performed using a wet (water of American Chemical Society (ACS) reagent grade for ultratrace analysis) stream of Argon at 900 mbar and 150 °C. The setup was adopted from an ultrasonic spray pyrolysis setup. In the atomization chamber the water is nebulized using a transducer (TDK, NB series, Japan). When a high frequency electric field is applied the transducer vibrates (resonance frequency F=1.6 – 1.75 MHz) and causes the formation of fine droplets [97]. The droplets are subsequently transported to the substrate by a constant Ar gas flow (4 slm), which is regulated using a mass flow controller (MKS Instruments 1179A) and a gas controller (MKS Instrument 647B). The vacuum was created using a vacuum pumping unit (PC 3010 Vario, Vacuubrand, Germany) in combination with a butterfly valve. The substrate is located midway into an aluminum oxide tube with a diameter of 20 mm (Degussit Al23, Friatec, Germany), which was in turn placed into a 45 cm long horizontal tube furnace (CTF 1200, Carbolite, UK).

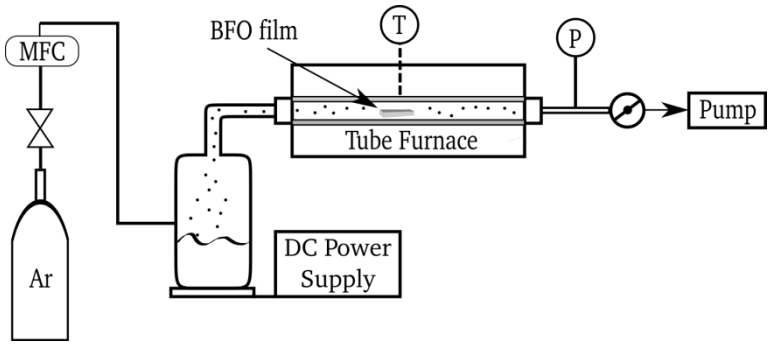

Figure 4.2. Schematic representation of the modified ultrasonic spray pyrolysis setup, used to hydrate the substrate. Temperature of the substrate and pressure are measured at the location indicated with T and P, respectively.

4.2. Laser-Assisted Chemical Vapor Deposition (LA-CVD) Setup

The LA-CVD setup was custom build in the framework of the DaISy-Bat integrated system (see chapter 3.3.1). The setup consists of two UHV stainless steel vacuum chambers. The vacuum chamber to the left in Figure 4.3 is used to introduce the precursor powders into the system as well as to evaporate the solid precursor using the CO_2 laser flash evaporator. The second vacuum chamber on the right-hand side is the cold wall deposition chamber, which contains the sample holder and substrate. The vacuum chambers are connected using an Al_2O_3 tube (Degussit AL23, Friatec AG) with an inner diameter of ~19 mm. The principle of operation and usage is explained in the following. Before introducing them into the left UHV chamber, the metal-organic precursor powders are mixed inside of a glove box under inert atmosphere (O_2 and H_2O levels usually below 1 ppm). When the precursors are poured into the chamber, the powder falls into a metal groove, positioned on a revolving metal plate. The circular motion is enabled by a stepper motor at an adjustable velocity (usually set to 12 s/revolution).

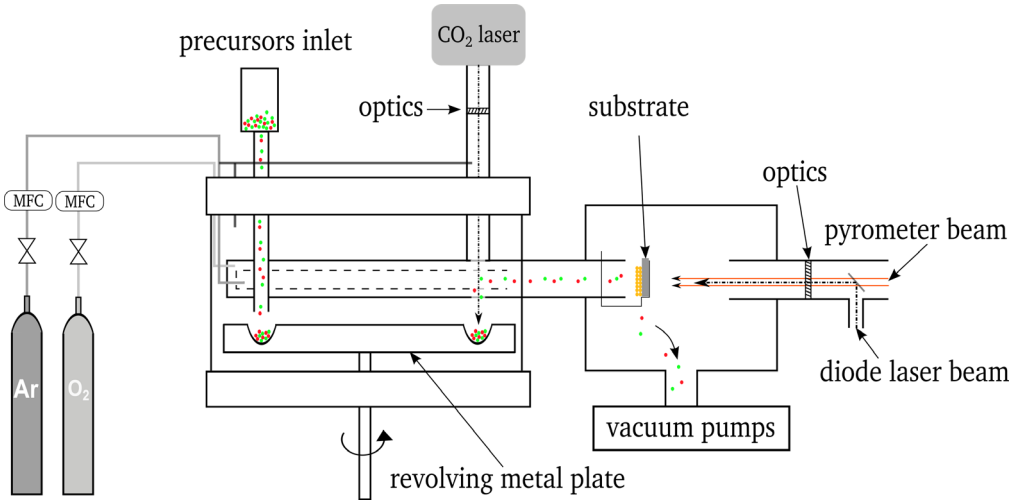

Figure 4.3. Schematic representation of the experimental LA-CVD setup. Both chambers are integrated into the DAISY-Bat system as shown in Figure 3.13.

The CO_2 laser enters the vacuum chamber through a ZnSe window and the spot size is adjusted by passing the laser beam through a plano-concave lens. The spot size is widened to 10 mm, when hitting the bottom of the groove, where the precursor materials are evaporated. The CO_2 laser power can be regulated continuously up to ~100 W. In that way the evaporation rate and the partial pressure of the precursors can be adjusted. After the precursors are evaporated, they are transported to the substrate by a heated carrier gas (Ar, purity ≥ 99.998 %, Air Liquide), which is fed into the inner metal tube (dotted line). O_2 (purity ≥ 99.998 %, Air Liquide) is used as a reaction gas and is introduced into the outer shell of the double-wall tube. The gas flow of each inlet is controlled using mass flow controllers and can be adjusted in the range from standard cubic centimeters per second (sccm) to standard liters per minute (slm). Before reaching the substrate, transport and reaction gas are well mixed. The substrate is heated using a diode laser (Jenoptik JOLD-140-CPXF-2P) with a wavelength of λ=938 nm. The diode laser can heat the substrate up to a maximum temperature of 1200 °C. The deposition temperature is monitored by a narrow band pyrometer (Metis MI16, Sensortherm). The pressure inside the reactor chamber is set using rotary vane pump (ComiLine WU232, Pfeiffer Vacuum) in combination with a butterfly valve (MKS type 253B) and a Baratron manometer (MKS type 626B) coupled to a pressure controller (MKS type 651C).

4.3. Pressurized Spray Deposition Setup and Precursors

In general the process of pressurized spray deposition consists of three stages. First the precursor solution is atomized using ultrasonic, electrostatic or air blast techniques. Secondly the droplets are transported in the form of an aerosol to the heated sample surface. As a third and last step the decomposition of the precursor commences initializing the film growth. In this thesis a setup with a pressurized air gun was used (Badger 150 air brush). A schematic representation of the setup is depicted in Figure 4.4 together with a photograph of the actual setup. The substrate temperature is controlled using a thermocouple, which is embedded into a steel plate to ensure adequate thermal contact. The temperature determined by the thermocouple was used to adjust the temperature of the heating plate (SLR Schott Instruments GmbH, Germany).

The precursor solution, which was prepared by mixing the stoichiometric precursor amounts, was pumped into the spray nozzle using a syringe pump (with the solution pressure being determined by the pump rate). At the needle tip the precursor solution and the pressurized air (above atmospheric pressure ~2 bar) merged to create droplets. The air pressure was controlled using a simple control unit (PR4000, MKS Instruments Inc, USA), which was connected to a mass flow controller. Increasing the air pressure directly leads to a decrease of the mean droplet diameter, while on the other hand increasing the precursor solution pressure directly causes an increase in the generated mean droplet diameter [98]. Furthermore it was also found that the size of the produced droplets is not related to the fluid properties of the precursor solution but rather depends on the charge density level of the fluid [99].

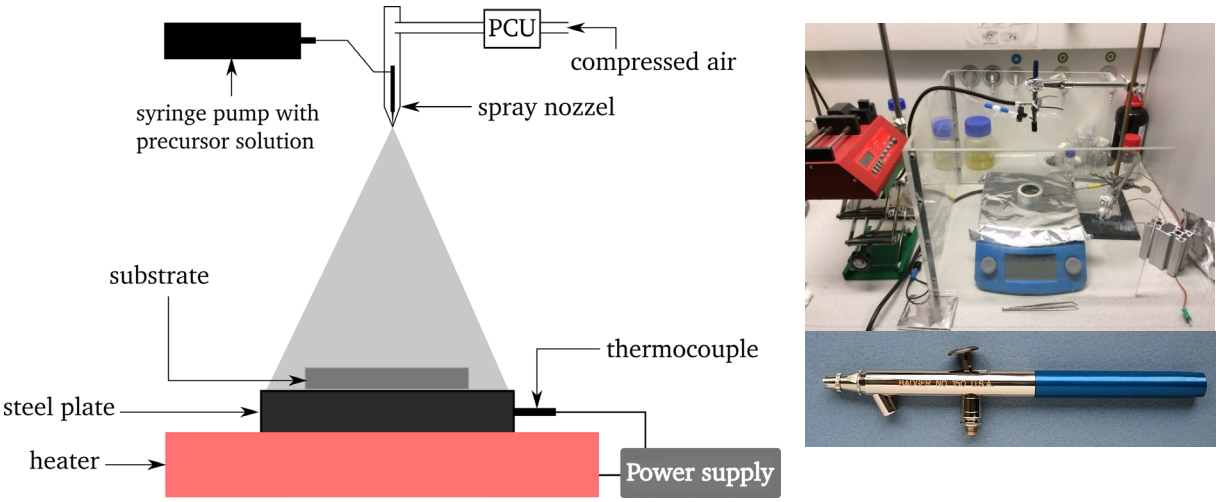

Figure 4.4. a) Schematic representation and b) a photograph of the pressurized spray deposition setup. In addition the Badger 150 air brush is shown in a close-up view.

Therefore different sets of precursors, which were dissolved in different ratios of distilled water and butyl carbitol, were tested. Both fluids have proven to be adequate solvents with their difference in boiling point enabling control of the evaporation temperature of the droplets. Within the mixture of solvents destilled water is the liquid with the low boiling point (100 °C) and butyl carbitol component with the high boiling point (231 °C). Using these solvents the different precursor classes were tested in terms of their solubility as listed in Table 4. The solubility of the precursors was tested for different molar concentrations. If a

precursor is said to be soluble a minimum molar concentration of 0.005 mol/l could be achieved (clear solution with no sedimentation). Since all material classes listed below (β-Diketonate, chlorides, nitrates and acetates) have previously been used in spray pyrolysis or CVD all of them were tested. Since Zirconium acetate is not available as a pure salt it was omitted. Similarly $Zr(NO_3)_4$ was not tested. The different precursors were grouped according to their material classes (i.e. chlorides with chlorides), as listed in Table 4. The different sets were subsequently dissolved in destilled water and butyl carbitol.

Table 4. Tested precursor materials for Ba, Zr and Y. The solubility that is indicated below is only qualitatively relevant for the required concentrations in this thesis and always refers to the dissolution in the pure solvent (e.g. $Ba(NO_3)_2$ in water). No solubility limits were determined. The precursors are grouped in the sets, which were used together.

Precursors	Purity / %	Supplier	Class	Soluble in	Grouped in
$Ba(acac)_2 \bullet 2H_2O$	98.0	Sigma-Aldrich	β-Diketonate	Methanol	Set C
$BaCl_2 \bullet 2H_2O$	99.9	Sigma-Aldrich	Chloride	Methanol, Water	Set A
$Ba(NO_3)_2$	99.0	ABCR	Nitrate	Water	Set D
$Ba(acetate)_2$	99.0	Sigma-Aldrich	Acetate	Water	Set B
$Zr(acac)_4$	97.0	Sigma-Aldrich	β-Diketonate	Butyl Carbitol, Ethanol, Methanol	Set A/B/C/D
$Y(acac)_3 \bullet H_2O$	99.9	Sigma-Aldrich	β-Diketonate	Ethanol, Methanol	Set C
$YCl_3 \bullet 6H_2O$	99.99	Sigma-Aldrich	Chloride	Water	Set A
$Y(acetate)_3 \bullet H_2O$	99.9	Sigma-Aldrich	Acetate	Water	Set B
$Y(NO_3)_3$	99.9	ABCR	Nitrate	Water	Set D

The respective precursors were first dissolved in the best suited medium for dissolution and stirred for 15 h (i.e. $Ba(acetate)_2$ and $Y(acetate)_3 \bullet H_2O$ in distilled water and $Zr(acac)_4$ in butyl carbitol). Thereafter the butyl carbitol solution was heated to 60 °C and stirred for 1 h to render a clear solution. Both distilled water and butyl carbitol solution were then mixed and heated for one more hour at 60 °C. The results of these tests are listed in Table 5. Only Set B and Set D were subsequently used to deposit thin films, because they showed full solubility and a clear mixture over an extended period of time. In addition to the ratio of the precursor solutions and the precursor type a number of other parameters are of importance. The needle tip size was chose to be the finest (smallest droplet diameter) and the needle to substrate distance was found to be best suited at a distance of 20 cm (homogeneous distribution pattern).

In the following the process of a typical deposition, using the experimental setup in Figure 4.4, is described. First the precursor solution was prepared as described above with the respective precursor materials. The substrate was heated to the desired temperature and the spray deposition was conducted for 30 min. During this time the flow rate of the precursor solution was set to 0.42 ml/min. To end the deposition a shutter was used to cut off the material transport to the substrate. At the same time the temperature was gradually decreased using a cooling rate of about 10 °C/min. Since after the deposition XRD showed unreacted

precursors in addition to the desired $BaZr_{1-x}Y_xO_{3-\delta}$ phase all films were subsequently annealed. The annealing was conducted in air at 1200 °C with a heating and cooling rate of 3 °C/min.

Table 5. The different sets of materials, which were described in Table 4, were tested in terms of sedimentation related to the ratio of destilled water and butyl carbitol

Set	Destilled water / vol%	Butyl Carbitol / vol%	Molarity / mol/l	Solubility
Set A	30	70	0.08	sedimentation
	40	60	0.08	Sedimentation
	50	50	0.08	Sedimentation
Set B	60	40	0.08	Clear, no sedimentation
	50	50	0.08	
	40	60	0.08	
Set C	60	40	0.08	Solution not clear
	50	50	0.08	
	40	60	0.08	
Set D	30	70	0.08	Clear, no sedimentation
	40	60	0.08	
	50	50	0.08	

4.4. Solid State Synthesis

For the investigation of $BaZr_{1-x}Y_xO_{3-\delta}$ films reference powders and subsequently pellets were synthesized as discussed in 6.2. The synthesis procedure will be briefly described here. $BaCO_3$ (Sigma-Aldrich, ACS reagent >99 %), ZrO_2 (Sigma-Aldrich) and Y_2O_3 (Sigma-Aldrich) were used as starting materials. The precursors were mixed in stoichiometric ratios and initially ground for 4 h at 200 rpm using a ball mill with steel jar and balls. The subsequent calcination was conducted at 1300 °C for 12 h with a heating and cooling rate of 5 °C (HTF 18/4, Carbolite, UK). Following the calcination procedure the powder was again ground for 4 h at 200 rpm (with rotation inversion every 30 min) to loosen the grains and obtain a finer microstructure. Thereafter pellets were pressed at 20 kN using an 8 mm die and an uniaxial press. Finally the sintering was conducted at the temperatures indicated in chapter 6.2, for 15 h and a heating/cooling rate of 5 °C (HTF 18/4, Carbolite, UK).

5. Investigation of $BaFeO_{2.5+\delta}$

Major parts of this chapter have been published in [100] and have been modified in the framework of this thesis. Namely, large sections in 5.2.1, 5.4, 5.5 and 5.7.1 have been taken from [100] although alterations and additions have been applied to fit the passages into the larger context.

5.1. Introduction and Motivation

Since perovskite-type and perovskite related materials find their use in many different applications including ferroelectrics [101], electrode and electrolyte materials (e.g. in fuel cells) [102], multiferroics [103] and many more, increasing efforts have been dedicated to the investigation of such materials. The structure of anion-deficient perovskites deviates from the aristotype cubic perovskite structure leading to more complex arrangements by vacancy ordering on the anion sublattice (e.g. brownmillerite structure $BaInO_{2.5}$). $BaFeO_{3-\delta}$ (BFO) is another example of such a compound possessing a variable oxygen stoichiometry, which can be altered by changing the B-site oxidation state and is therefore better described as $BaFe^{3+}_{1-\beta}Fe^{4+}_{\beta}O_{3-y}$ $(y = \frac{1-\beta}{2})$. The fact of having vacancies on the anion sublattice and especially the possibility of varying the vacancy distribution enables the use of BFO in a multitude of possible applications. The reason is that various material properties such as ionic conductivity (oxygen, proton), electronic conductivity (induced by mixed valence states of Fe) and magnetic ordering are strongly influenced by the anion sublattice. Depending on the oxygen stoichiometry and correlatively the oxidation state of Fe, BFO was found to exist in a variety of different polymorphs.

The occurring phase and ratio of Fe^{3+}/Fe^{4+} largely depends on the sample preparation and thermal treatments (temperature and O_2 pressure). Following extended research over decades the thermodynamically stable phases of BFO listed in Table 6 were analyzed in literature and correlated with the oxygen content in terms of Fe^{4+} rate for bulk samples.

Table 6. Different thermodynamically stable phases examined in literature. The oxygen stoichiometry depends on the oxidation state of Fe (rate of Fe^{4+} is represented by τ).

Composition	Fe^{4+} rate	Structure phase
$BaFeO_3$	$\tau=1$	cubic phase [105,106]
$BaFeO_{2.93\text{-}2.87}$	$0.74\leq\tau\leq0.86$	hexagonal 12H-type phase [29]
$BaFeO_{2.80\text{-}2.65}$	$0.30\leq\tau\leq0.60$	hexagonal 6H-type phase [107]
$BaFeO_{2.57\text{-}2.51}$	$0.02\leq\tau\leq0.14$	“cubic-type” phase [29]
$BaFeO_{2.5}$	$\tau=0$	monoclinic phase [108,109]

Although the different phases were extensively studied, the complex superstructure of monoclinic $BaFeO_{2.5}$ was only recently completely explained [28] revealing its complex anion vacancy ordering pattern and local coordination of Fe^{3+} cations. In addition the symmetry relationship to the cubic aristotype was shown. Since for SOFC/SOEC applications a cubic perovskite or perovskite-related structure (ccp packing of BaO_3 layers) with high symmetry favors high conductivities [61], such a structure was the basis of the work established in this

chapter. From a structural perspective the films examined in this chapter can be attributed to reduced $BaFeO_{2.5}$ with a pseudocubic perovskite-type crystal structure [104], in which the vacancy ordering is broken by the epitaxial growth. The desired composition of the $BaFeO_{2.5}$ thin films, which for bulk samples can be obtained under inert gas atmosphere, was obtained by PLD as described in the experimental section 4.1. From other reports it is known that this structure can be transformed into a RT- stable cubic phase of $BaFeO_3$ (making it a good electronic conductor) using low temperature (200-450 °C) oxidation in O_2/ozone [105], which is subsequently reversible under reducing conditions at temperatures of ~700 °C. To date most investigations concerning BFO have focused their research on structural aspects and oxygen non-stoichiometry of the different polymorphs. In addition the magnetic and electronic properties are of importance and have been studied accordingly in numerous publications [104,105,110–112].

However, recently another material property, the proton conductivity, has sparked interest, after the material's hydration behavior was analyzed in more detail [21]. A large water uptake was observed for $BaFeO_{2.5}$ and prompted the discovery of two new hydrated phases of BFO. The first report on these new hydrated phases, namely $BaFeO_{2.33}(OH)_{0.33}$ and $BaFeO_{2.25}(OH)_{0.5}$, highlighted the material's ability of incorporating significant amounts of water and therefore protons [21]. As was already highlighted in 2.3 the mechanism of water incorporation in oxides can take place in the presence of oxygen vacancies thereby leading to charge carrier (proton) loading according to equation (2.9). The fact that oxygen vacancies enable water incorportation suggests that anion deficient perovskite-type structures such as BFO are viable candidates for proton transport. Combining both, the possibility to be a good electronic as well as a good proton conductor, makes BFO an interesting material, which could find application as an air electrode in proton conducting SOFCs/SOECs.

As opposed to other proton conductors, for which the oxygen stoichiometry is influenced by introducing charge compensating defects in the form of aliovalent B-site substitutions (Y in $BaZr_{1-x}Y_xO_{3-x/2}$) the reducible/oxidizable B-site (Fe) in BFO is the cause for the formation of vacancy-ordered superstructures on the anion lattice. This implies that the oxygen stoichiometry and thereby the number of vacancies is strongly influenced, when the material is exposed to an oxidizing or reducing atmosphere at elevated temperatures. To draw meaningful conclusions from any conductivity or transport measurements it is therefore a necessity that the oxygen stoichiometry is well known. In this respect all films, which were examined in this chapter, were annealed under Ar prior to the impedance measurements to be in the same initial state containing only Fe^{3+} (see section 4.1).

In general, when examining the transport phenomena in polycrystalline samples by Electrochemical Impedance Spectroscopy two contributions (namely bulk and grain boundary) are of interest. Since grain boundaries can have detrimental effects on the total proton conductivity, as has been shown to be the case for similar perovskite-related oxides (e.g., $BaZr_{1-x}Y_xO_{3-x/2}$ [113]) the investigations focus on the bulk properties of BFO and a clear distinction of both contributions is necessary. A study, which was previously conducted by Knöchel et al., on compacted hydrated powders of BFO did not allow for a clear distinction of both effects [21]: Attempts to study the hydration behavior of dense ceramics (minimizing grain boundary contributions by sintering) were unsuccessful since during hydration of dense sintered pellets cracking and breaking occurred due to a high volume increase [21]. Such volume increases are not only limited to BFO, but were also found for the hydration of $BaInO_{2.5}$, which can take up even higher amounts of water under the formation of $BaInO_2(OH)$ [114]. These large volume increases result from additional repulsive forces of the

lattice cations and the incorporated protons, causing internal expansive strain (see also Figure 5.4) [21]. Clearly, the distinction between bulk and grain boundary can be challenging, especially when the grain boundary contribution cannot be minimized easily (e.g. by sintering). The most elegant solution to this problem is the investigation of single crystals, which by definition are grain-boundary free. Following this reasoning, epitaxially grown ultrathin films (~20 nm) of BFO were studied by Sukkurji et al. in order to eliminate grain boundary contributions and understand the process of hydration in more detail at ambient temperatures [115]. However, the results indicated that conductivity was prevalent due to electronic charge carriers, created by partial Fe oxidation as well as lattice strain effects, which were assumed to strongly reduce protonic contributions to the total conductivity. Therefore the determination of the bulk proton conductivity within BFO still remained an open question and thus is investigated in the following.

In this chapter the previously conducted investigations on ultra-thin BFO films are extended by studying the conductivity processes, occurring in thicker epitaxial films (250 nm) of BFO grown onto single-crystal Nb:STO substrates, as a function of different measurement temperatures (in the 200–550 °C range) and gas atmospheres (wet and dry air/Ar). In addition to the epitaxial films deposited on (001)-oriented Nb:STO, epitaxial films were also deposited on (111)-oriented Nb:STO so that the conductivity along different crystallographic directions could be compared and the preferential crystallographic orientation for proton transport could be determined. Furthermore polycrystalline films were deposited on (001)-oriented Nb:STO in order to examine the influence of grain boundaries and thereafter be correlated to the results obtained from the epitaxial films. The results for the epitaxial films on (001)-oriented Nb:STO indicate that due to the increased film thickness the lattice strain caused by the mismatch of film and substrate was reduced (with increasing distance from the interface) and in that way provided a more relaxed structure, which resembled more to the strain condition in individual crystallites found in bulk powder of BFO. For this reason an approximation of the temperature dependent bulk proton conductivity of BFO on (001)-oriented Nb:STO could be determined, which was not possible within the study of thinner films (~20 nm) reported previously [115].

5.2. Structural Analysis of BFO Films

5.2.1. Epitaxial Film Growth on (001)-Oriented Nb:STO Substrates

Table 7 contains the samples examined in this chapter, also listing the post-deposition treatments and EIS measurement conditions. BFO1 to BFO4 were also measured after their respective EIS measurements to account for changes in lattice parameter, caused by oxidation.

Table 7. Summary of all samples examined in this chapter including post-deposition treatments and EIS measurement conditions

Sample Name	Annealing	Hydration	EIS Measurement Conditions
BFO1	Ar (700 °C)	No	Dry Ar
BFO2	Ar (700 °C)	Yes	Wet Ar (~3% H_2O)
BFO3	Ar (700 °C)	No	Dry Air
BFO4	Ar (700 °C)	Yes	Wet Air (~3% H_2O)
BFO5	O_2 (500 °C)	No	none

The crystalline structure of as-deposited, annealed and hydrated BFO films was investigated by X-ray Diffraction (XRD) analysis. Figure 5.1 shows the θ–2θ high resolution XRD pattern of a 250 nm thick as-deposited BFO film on (001)-oriented Nb:STO. All films were grown epitaxially along the (00l) direction. Since the a and b lattice (in-plane) parameter is different to the c lattice (out-of-plane) parameter c_{out} [115,116], this induces at least a symmetry lowering to a tetragonal perovskite structure (highest possible symmetry *P*4/*mmm*). Since the out of plane lattice parameters of the BFO film and the cubic perovskite substrate differ significantly, the reflections are clearly separable and can be easily identified as indicated in Figure 5.1. The inset in Figure 5.1 shows the ω rocking curve with a FWHM of 0.16° for the (002) reflection of the BFO thin film. The narrow FWHM indicates a high degree of crystallinity and confirms a low mosaic spread throughout the film.

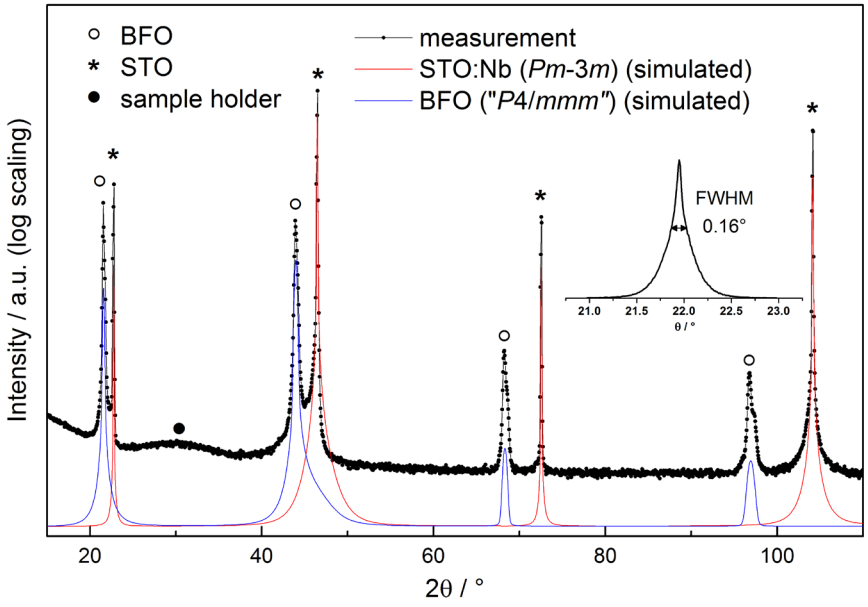

Figure 5.1. High resolution X-ray diffractogram of an as-deposited BFO film on (001)-oriented Nb:STO(highest possible symmetry *P*4/*mmm* due to epitaxial growth in combination with straining), showing film, substrate and sample holder reflections; the inset shows the rocking curve of the (002) reflection. Additionally, simulated intensities from structural data were added for (00l) reflections.

Table 8 lists the out-of-plane lattice parameters (c_{out}) of an as-deposited sample and of samples after various post-deposition treatments, determined from the diffractograms shown in Figure 5.1 and Figure 5.2. The diffractograms ranging from 10° to 115° include the $(001)_c$, $(002)_c$, $(003)_c$ and $(004)_c$ Nb:STO Bragg reflections and clearly show that all films are grown heteroepitaxially in a single domain without traces of any secondary or impurity phases. The changes in c_{out} correlate with the changes in unit cell volume and can be observed as a shift of the film reflections. To further examine and emphasize the effect of these shifts a magnified range around the (003) reflection is shown in Figure 5.2.

Table 8. Out-of-plane lattice parameter after different post-deposition treatments (±0.001 Å).

Post-Deposition Treatment	c_{out} /Å
as-deposited	4.110
Ar annealed	4.110
O_2 annealed	3.990
Ar annealed and hydrated	4.125

It is well known that reversible changes in the unit cell volume (increase and decrease) are associated with a change in oxidation state and a change in oxygen vacancy concentration, respectively. Furthermore volume changes can be induced by the incorporation of ions such as e.g. protons or fluoride ions [117]. These volume changes are referred to as chemical expansion of the crystal lattice to distinguish between thermally and chemically induced expansion [118]. In addition to strains induced by chemical expansion so called misfit strains, which will be discussed later on, are present at the near interface region. Since the misfit strain in combination with chemical and thermal expansion can add up to very large stresses (in the order of GPa [119]) especially during EIS measurements, micrographs of all film surfaces were recorded (see section 5.3) after the post-deposition treatments as well as after EIS measurements.

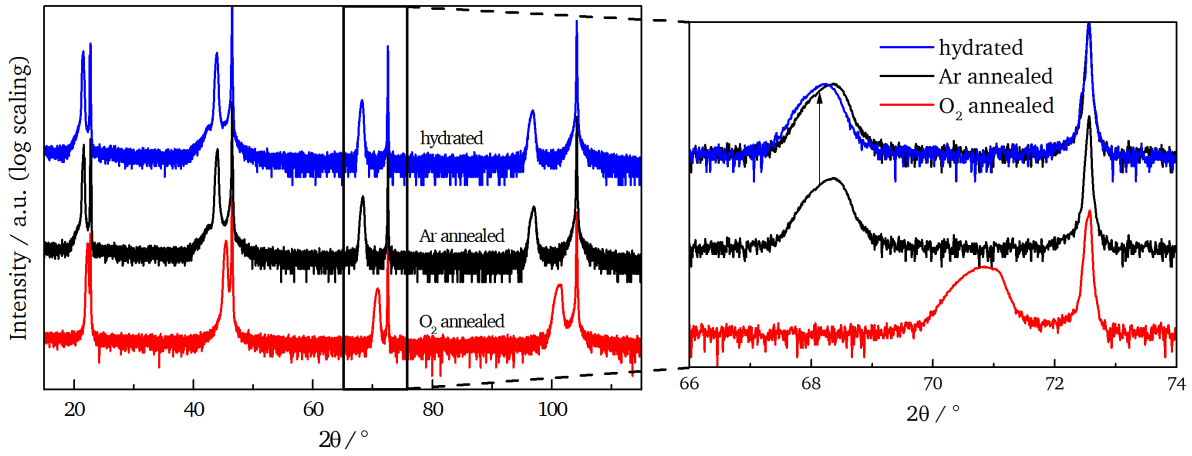

Figure 5.2. a) High resolution X-ray diffractogram of an O_2 annealed (red), an Ar annealed (black) and a hydrated (blue) BFO film. Shift of the (003) reflection due to different sample treatments. To emphasize the change in lattice parameter upon hydration the (003) reflection after Ar annealing is shifted up as indicated.

In the following section the chemical expansion is analyzed using c_{out} as a primary indicator. Subsequently a comparison with other types of samples of $BaFeO_{2.5}$ is conducted in terms of volume per $BaFeO_{2.5}$ formula unit ($V_{f.u.}$). The annealing treatment does not alter c_{out}

as compared to the as-deposited film. The effect of O_2 annealing on the other hand causes a decrease down to 3.990 Å, indicating that oxidation of Fe^{3+} to Fe^{4+} is taking place [105]. The ionic radius of Fe^{3+} (~64.5 pm) decreases when oxidized to Fe^{4+} (~58.5 pm) [120]. This trend is also reflected in the lattice parameters, respectively the cube root of the volume per $BaFeX_{3-y}$ formula unit ($a_{pseudo-cubic}$) of $BaFeO_{2.5}$ ($a_{pseudo-cubic}$ = 4.075 Å) containing only Fe^{3+} [21] and $BaFeO_3$ (a = 3.97 Å, *Pm*-3*m*) containing only Fe^{4+} [105]. This volume decrease is well-known for bulk powders of Fe systems [28,29], for ultra-thin films and was also observed in the present work for 250 nm thick films of BFO.

By creating mixed Fe^{3+}/Fe^{4+} oxidation states an additional electronic conductivity component might be induced (small polaron hopping), in addition to reducing the concentration of the protonic charge carriers, which is why an investigation into the conducting properties, depending on atmosphere and temperature was performed and analyzed in section 5.7 [22]. To illustrate the process of creating mixed Fe^{3+}/Fe^{4+} in $BaFeO_{2.5}$ in more detail the following equilibrium reaction in Kröger-Vink notation can be used

$$V_O^{\bullet\bullet} + \frac{1}{2}O_2 + 2Fe_{Fe}^{x} \Leftrightarrow O_O^{x} + 2Fe_{Fe}^{\bullet} \tag{5.1}$$

where Fe_{Fe}^{x} represents Fe ions in the 3+ valence state and $Fe_{Fe}^{\bullet}$ denotes Fe ions in the 4+ valence state (similar to holes), both on Fe lattice sites. Equations (2.9) and (5.1) are in equilibrium and thereby influence each other, leading to a decrease of the proton concentration when the equilibrium in Equation (5.1) shifts towards the right side. In oxygen containing atmospheres this equilibrium can affect the conductivity and lead to a deviation of Arrhenius-like behavior. Furthermore, hydration of the film induces an expansion of c_{out} to 4.125 Å (see Figure 5.4) thus proving water uptake [115]. The magnification in Figure 5.2 displays the (003) reflection for the samples listed in Table 8. The trend of change in lattice parameter due to oxidation and hydration follows what was previously observed in ultrathin films and for bulk powders [18,21].

The 'in-plane' structure of the films was probed by performing ϕ-scans around the (202) asymmetric reflection (Figure 5.3a). For a tetragonal BFO film there are there are three further planes, which are equivalent to (202) and have the same inclination from the (001) plane (Figure 5.3b). Therefore a 360° ϕ-scan should render four peaks in 90° intervals, owing to the four-fold rotational symmetry of the structure. Similarly this is also true for a cubic structure, which implies that when probing the substrate reflections a similar pattern should appear. The results of a ϕ-scan (similar results for other samples) are displayed in Figure 5.3 confirming an epitaxial film with four-fold symmetry as is expected for a cubic (or tetragonal from symmetry lowering due to epitaxial strain) system. The projections of the (202) lattice plane normals onto the surface plane are parallel to the in-plane lattice parameters and as the ϕ-scans in Figure 5.3 show the directions are the same for substrate and film. This result indicates that the in-plane orientation is [100] $BaFeO_{2.5}$ (001) // [100]] Nb:$SrTiO_3$ (001), with one domain. The reflections vary in intensity, which results from the miscut of the substrate or a slightly improper setting of the investigated (202) reflection.

The in-plane lattice parameter $c_{in-plane}$ was estimated previously for ultrathin films by TEM (4.04–4.05 Å) [115] and for thicker (85 nm) films by RSM (4.04 Å) [116] using the (103) reflections. Due to the low thickness (~20 nm) the ultrathin films were highly strained, while still being close to the pseudomorphic growth regime.

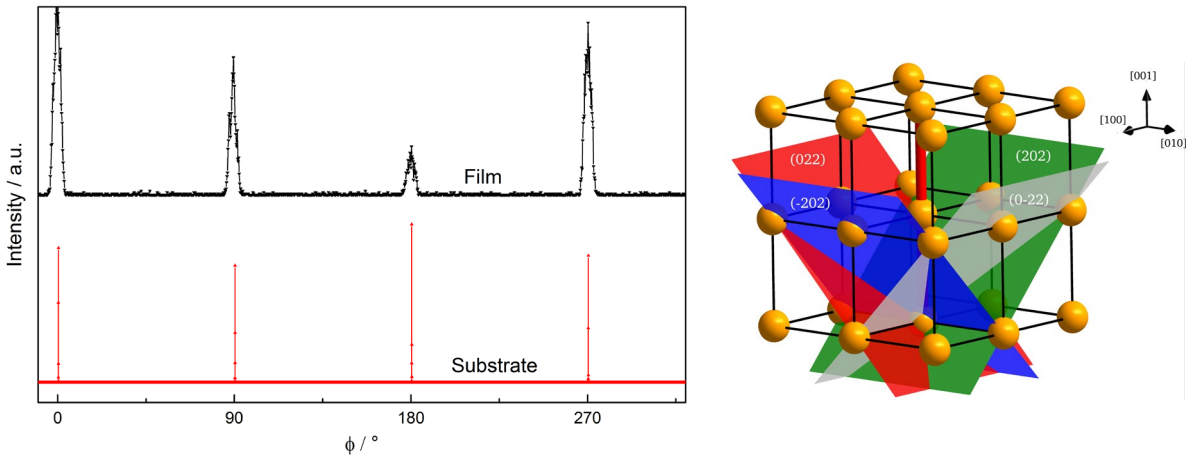

Figure 5.3. a) ϕ-scan of an Ar-annealed film around the (202) reflection, showing four-fold symmetry. b) Schematic representation of a cubic lattice structure with the four measured {202} equivalent lattice planes, which are measured in the ϕ-scan. The inclination of the planes normal vector towards the [001] direction (indicated as red bonds) is 45°. The sample rotation occurs around the red axis.

The reason for these large strains is that during deposition onto a substrate with a different crystal structure or lattice parameter (heteroepitaxial growth) the mismatch has to be compensated. The system accomplishes this compensation by inducing large misfit strains in the deposited film (chapter 2.6). Once the strain reaches a critical thickness (usually in the order of tens of nanometers) the strain energy is sufficiently large to be released by generating defects such as (misfit) dislocations. Following further growth relaxation of the film's crystal structure takes place. The films in this study are sufficiently thick so that the crystal structure can be assumed to have relaxed and the relief of strain is large enough so that the strain conditions in the film resemble to the one observed in individual crystallites within a bulk powder. Due to the impact of oxidation and hydration on the lattice parameter (only in out-of-plane direction, also see Figure 5.4), samples BFO1 to BFO4 were measured after each EIS measurement (Table 9). While the measurement in wet Ar causes an increase in c_{out}, the measurement in wet air slightly reduces the lattice parameter. Since oxidation and hydration have opposite effects on the lattice parameter this behavior is to be expected. Surprisingly the measurement in dry air does not show a decrease in c_{out} to the extent, which would be expected for oxidation at elevated temperatures.

Table 9. Lattice parameters c_{out} for samples BFO1-4 after EIS measurement (±0.001 Å).

EIS Measurement Condition	Out-of-Plane Lattice Parameter (after EIS) / Å
Dry Ar (BFO1)	4.110
Wet Ar (BFO2)	4.122
Dry Air (BFO3)	4.105
Wet Air (BFO4)	4.095

From the characterization shown here it is concluded that hydration and oxidation reactions show similar trends on the general change of the lattice parameter c_{out} as compared to changes of the pseudo-cubic lattice parameter $\sqrt[3]{V_{f.u.}}$ for bulk powders, although the overall magnitude still remains different [21]. Furthermore, after impedance measurements the films in air tend to show a significant oxidation, whereas the films, treated in Ar possess the same c_{out} measured before the impedance measurement. In comparison to ultra-thin films of BFO,

which were investigated previously [115], the out of plane lattice parameter of as-deposited and hydrated films is significantly shorter (4.110 Å as compared to 4.150 Å for the as-deposited and 4.125 Å as compared to 4.178 Å for the hydrated films, respectively). As mentioned above this is an indication that due to the increased film thickness the lattice strain caused by the lattice mismatch of film and substrate is reduced sufficiently so that the strain condition resembles more to the one found in individual crystallites in bulk powder of BFO. In that way it can be assumed that the films are well suited to accurately display ionic conduction in a similar manner, which would be observed in the bulk of a single crystal. However since in thin films the process of water uptake has a different effect on the lattice parameter than in bulk samples some further considerations are needed. As displayed in Figure 5.4 bulk crystallites can theoretically experience isotropic expansion of the lattice in all three dimensions. For thin films the bond between film and substrate causes a lateral clamping effect, which leads to a confinement of the lattice parameter in two dimensions (in-plane).

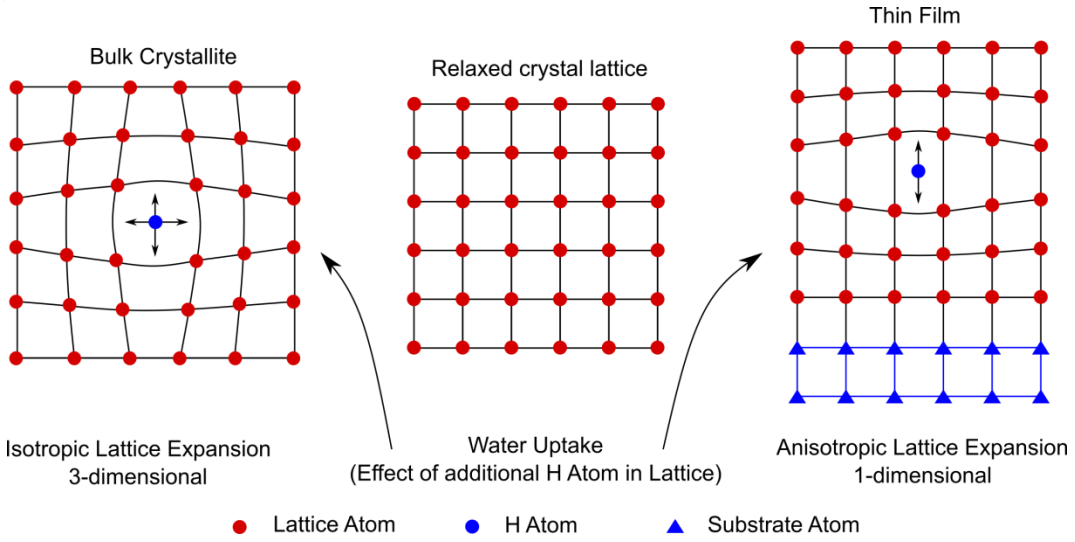

Figure 5.4. Schematic effect of proton incorporation upon water uptake (chemical expansion) on the lattice parameters in a bulk material compared to a thin film.

Therefore, upon water uptake of the film a lattice expansion is limited to the out-of-plane direction. Due to this anisotropic lattice expansion the water uptake and thereby the proton concentration can significantly vary in bulk samples, thin films and ultrathin films. Table 10 lists the changes in $V_{f.u.}$ before and after hydration for different types of samples.

Table 10. Comparison of different sample types and the corresponding volumes per formula unit $V_{f.u.}$ in the dry and hydrated state. To estimate the $V_{f.u.}$ for the films in the present work the in-plane lattice parameter was assumed to be the same as for ultrathin films (4.045 Å).

Type of Sample	$V_{f.u.}/Å^3$	Hydrated $V_{f.u.}/Å^3$	Change in $V_{f.u.}$ upon Hydration/$Å^3$
Thin film (250 nm)	67.25	67.49	0.24
Ultra-thin film (20 nm) [115]	67.90	68.36	0.46
$BaFeO_{2.5}$ powder ($P2_1/c$) [21]	67.67	70.96 ($BaFeO_{2.33}(OH)_{0.33}$) 71.84 ($BaFeO_{2.25}(OH)_{0.5}$)	3.29 4.17

As was already suspected due to the possibility of greater 3-dimensional lattice expansion, the bulk sample shows a significantly larger change in volume after hydration for

both the low water $BaFeO_{2.33}(OH)_{0.33}$ ($\Delta V_{f.u.}$~14x larger) and high water $BaFeO_{2.25}(OH)_{0.5}$ ($\Delta V_{f.u.}$~17x larger) modification. Additionally, bulk samples always contain grain-boundaries and larger near surface areas, which are usually hydrated before the bulk. The ultrathin films, although showing a much lower change in $V_{f.u.}$ upon hydration than bulk samples, experience roughly double the change of $V_{f.u.}$ as compared to the 250 nm thin films deposited in this work. The difference between the 250 nm thin films and the 20 nm ultrathin films can likely be attributed to the fact that the lattice parameters differ (due to the different strains) significantly. In this way, it is assumed that the strained ultra-thin films provide substantially more free volume for the incorporation of water.

In general physical properties, such as electrical, proton and thermal conductivity, of a material can be significantly influenced without changing the composition: The alteration of material properties can be induced e.g. by structural and morphological changes (porosity, grain size), by creating an interface between two materials (with properties that none of the individual parent materials possess) or by creating lattice distortions in the form of strain. An approximate idea of the stress state can be helpful in drawing conclusions related to the physical properties of materials. As was mentioned before the misfit strain in combination with chemical and thermal expansion can induce very large stresses. Based on the out of plane lattice parameters, which were discussed in detail, an estimation of the occurring stresses will be presented in the following.

Lattice distortions in a crystal have great impact since they change bond lengths, bond angles and thereby the electron density and bond strengths, which can lead to a variety of altered properties such as electronic band gap [121], catalytic properties [122], thermal conductivity [123] and charge transport [124]. Regarding the crystal structure, stress and the induced lattice strain lead to a change of lattice parameters and to a change in symmetry, if the applied stress has a symmetry, which differs from the symmetry of the influenced materials. The heteroepitaxial films, which are presented in this chapter would have a theoretical lattice mismatch *m*, which is in the order of

$$m = \frac{a_s - a_b}{a_b} = 2\% \tag{5.2}$$

with a_s being the lattice parameter of the substrate (3.905 Å for STO) and a_b being the bulk lattice parameter (3.971 Å for cubic $BaFeO_3$ [*Pm*-3*m*]). A lattice mismatch of m≤1-2 % can normally be completely accommodated into the thin film. However the BFO films, which were examined in this work are deposited so that the composition can be summarized as $BaFeO_{2.5}$ (with Fe being in the 3+ oxidation state) and therefore have a larger cell volume per formula unit. Since $BaFeO_{2.5}$ usually does not form in a cubic perovskite structure, when prepared as a bulk powder but rather forms a monoclinic perovskite-type related structure (P21/c) [28], there is no bulk cubic lattice parameter (a_b) and instead the pseudo-cubic lattice parameter of $BaFeO_{2.5}$ can be used here ($a_{p.c.}$=4.075 Å [21], see also p. 54). This is a reasonable assumption since the value of $a_{p.c.}$ is between the out-of-plane lattice parameter, which was determined in the present work and the in-plane lattice parameter, which was determined for ultra-thin films of BFO ($a_{in\text{-}plane} < a_{p.c.} < c_{out}$). The theoretical lattice mismatch for the films in this work can therefore be estimated to be 4 % using $a_{p.c.}$. In terms of epitaxial growth, for which an upper limiting misfit of about 15 % cannot be exceeded, 4 % is still considered an adequate value [76].

The lattice strain in the thin films, which were examined in this chapter, is biaxial along the two in-plane directions (due to the described clamping of the substrate), while in the out-of-plane direction the lattice can expand freely. In this respect the lattice strain along the in-plane (ε_x and ε_y) and out-of-plane (ε_z) directions may be expressed using a and c , which are the measured in-plane and out-of-plane c_{out} lattice parameters, respectively. Since in this work only c_{out} was measured the strain can only be directly computed in this direction according to [125,126]

$$\varepsilon_z = \frac{c_{out} - a_{p.c.}}{a_{p.c.}} \tag{5.3}$$

The determined lattice strains ε_z for the respective films are listed in Table 11. Since the composition of the film after annealing in O_2 can be assumed to be $BaFeO_3$ the lattice strain for BFO5 was calculated using the above mentioned bulk lattice parameter for $BaFeO_3$ (3.977 Å) instead of the pseudo-cubic lattice parameter $a_{p.c.}$.

The 4 rank stiffness tensor for an isotropic elastic material with cubic symmetry (which is assumed here), is displayed below [127]. Therein σ and ε are the stresses and strains along the principal axes and τ and γ are the shear stress and shear strains along the respective directions. The matrix shows that in this system there is no coupling between shear stress τ and strain ε. Therefore the shear strains are equal to zero. Furthermore the matrix contains the material properties *E* and *ν*, which are Young's modulus (185 GPa) and the Poisson's ratio (0.235), respectively [128].

$$\begin{pmatrix} \Sigma_x \\ \Sigma_y \\ \Sigma_z \\ \tau_{xy} \\ \tau_{yz} \\ \tau_{xz} \end{pmatrix} = \frac{E}{(1+\nu)(1-2\nu)} \begin{pmatrix} 1-\nu & \nu & \nu & 0 & 0 & 0 \\ \nu & 1-\nu & \nu & 0 & 0 & 0 \\ \nu & \nu & 1-\nu & 0 & 0 & 0 \\ 0 & 0 & 0 & \frac{1-2\nu}{2} & 0 & 0 \\ 0 & 0 & 0 & 0 & \frac{1-2\nu}{2} & 0 \\ 0 & 0 & 0 & 0 & 0 & \frac{1-2\nu}{2} \end{pmatrix} \begin{pmatrix} \varepsilon_x \\ \varepsilon_y \\ \varepsilon_z \\ \gamma_{xy} \\ \gamma_{yz} \\ \gamma_{xz} \end{pmatrix} \tag{5.4}$$

In the present situation where the film can grow/expand freely along the z direction (meaning that $\Sigma_z = 0$ GPa), a relation between ε_x, ε_y ($\varepsilon_y = \varepsilon_x = \varepsilon$ due to biaxial equal strain) and ε_z can easily be established, using the stiffness tensor above:

$$\varepsilon = \frac{(\nu - 1)}{2\nu}\varepsilon_z \tag{5.5}$$

Having calculated ε and ε_z the stresses along Σ_x and Σ_y ($\Sigma_x = \Sigma_y = \Sigma$) can be calculated according to

$$\Sigma = \frac{E}{(1+\nu)(1-2\nu)}[(1-\nu)\varepsilon + \nu\varepsilon + \nu\varepsilon_z] \tag{5.6}$$

Herein the sign of stress is defined as positive for tensile and as negative for compressive. As expected (based on Figure 5.4) the Ar annealed and hydrated film experiences the largest

lattice strain and stress. The O_2 annealed film on the other hand shows the lowest lattice strain and stress, due to the drastic reduction of the lattice parameter as compared to the films with high Fe^{3+} content (relaxation occurring).

Table 11. Lattice strains and stresses determined for films under different post-deposition treatments. For the films with the composition $BaFeO_{2.5}$ $a_{p.c.}$ was used for a_b.

Post-Deposition Treatment	c_{out} / Å	a_b / Å	ε_z / %	Σ / GPa
as-deposited - $BaFeO_{2.5}$	4.110	4.075 [21]	0.86	-3.38
Ar annealed - $BaFeO_{2.5}$	4.110	4.075 [21]	0.86	-3.38
Ar annealed and hydrated - $BaFeO_{2.5}$	4.125	4.075 [21]	1.22	-4.82
O_2 annealed (BFO5) - $BaFeO_3$	3.990	3.971 [105]	0.47	-1.88

The stresses and strains, which are calculated and listed in Table 11 are merely an estimation and include assumptions such as e.g. that the strained films have similar elastic material properties as an unstrained bulk sample. In some cases strained films have been found to have very different elastic properties [129] but in other cases these have matched quite well with data found in literature [130]. Furthermore no strain relaxation models such as e.g. surface roughening or the formation of cracks and dislocations have been taken into account. However, since in this work no stress analysis or monitoring techniques such as ellipsometry, RHEED or curvature-based techniques were employed, the above considerations yield a reasonable idea of the general stress state of the films, after deposition. A schematic (exaggerated for purposes of visualization) of the above determined stress condition is shown in Figure 5.5. The film with the bulk in-plane lattice constant (a_b) is joined from a theoretical freestanding state with the substrate (a_s). The lattice mismatch is compensated by reducing a_b to $a_{in\text{-}plane}$ and thereby creating compressive stresses along the in-plane directions of the film. Consequently as was constituted above c_{out} expands along the out-of-plane direction, producing a decreasing strain profile, away from the substrate.

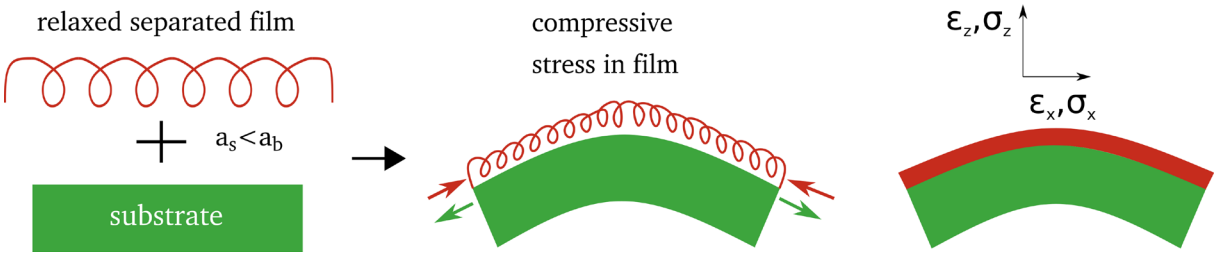

Figure 5.5. Schematic effect of stresses arising due to lattice mismatch between substrate (a_s) and bulk of the film (freestanding film a_b). The film is represented by a spring, which in the case of $a_s<a_b$ is squeezed together exerting compressive stress, as indicated by the red arrows.

As was already mentioned above the strains and stresses for the different films, which are listed in Table 11, can affect the physical properties of the material. Fluri et al. have shown that strain engineering can enhance the proton conductivity by as much as a factor of 2 in Y-doped $BaZrO_3$ [131]. The essential effect causing changes in proton conductivity are the creation of energetically different oxygen sites. In the aristotype cubic perovskite structure ABO_3 (Figure 5.6a) the BO_6 octahedra are highly symmetric with the oxygen positions all being equal. In this structure hydrogen bonds can only be formed within the octahedra and interoctahedral transfers are not possible. However when stress is applied to the structure (Figure 5.6b) the vertex separations between the O1 sites (shortest distance between grey

oxygen atoms) are shortened leading to energetically different oxygen sites and thereby new interoctahedral proton transfer pathways (t_2). These are present in addition to the preexisting intraoctahedral transfer pathways (t_1).

Another effect that stress and strain can have on the crystal structure is octahedral tilting, which is schematically displayed in Figure 5.6c. The deviations from the cubic perovskite structure, which is caused by the tilted BO_6 octahedra results in either shortened or elongated vertex separations. Along the shortened vertex separations between the same oxygen sites (grey only or red only) faster proton diffusion can occur 1-dimensionally. This reduction in dimensionalty from 3-dimensional to 1-dimensional diffusion paths can however lead to a lower overall conductivity, especially if the paths are interrupted by defects. For example, for $SrCeO_3$ it was suggested that the octahedral tilting may be caused by increased energy barriers for hydrogen reorientation and that the transfer between O1 and O2 oxygen sites may be the rate limiting step in the proton transport [132]. In light of the above described situations, there are clearly several possibilities of how the strain and stress in the here deposited films can influence the conductive properties. Therefore although the effects of stress and strain cannot be entirely predicted, these influences have to be considered upon investigating the EIS in 5.7.1.

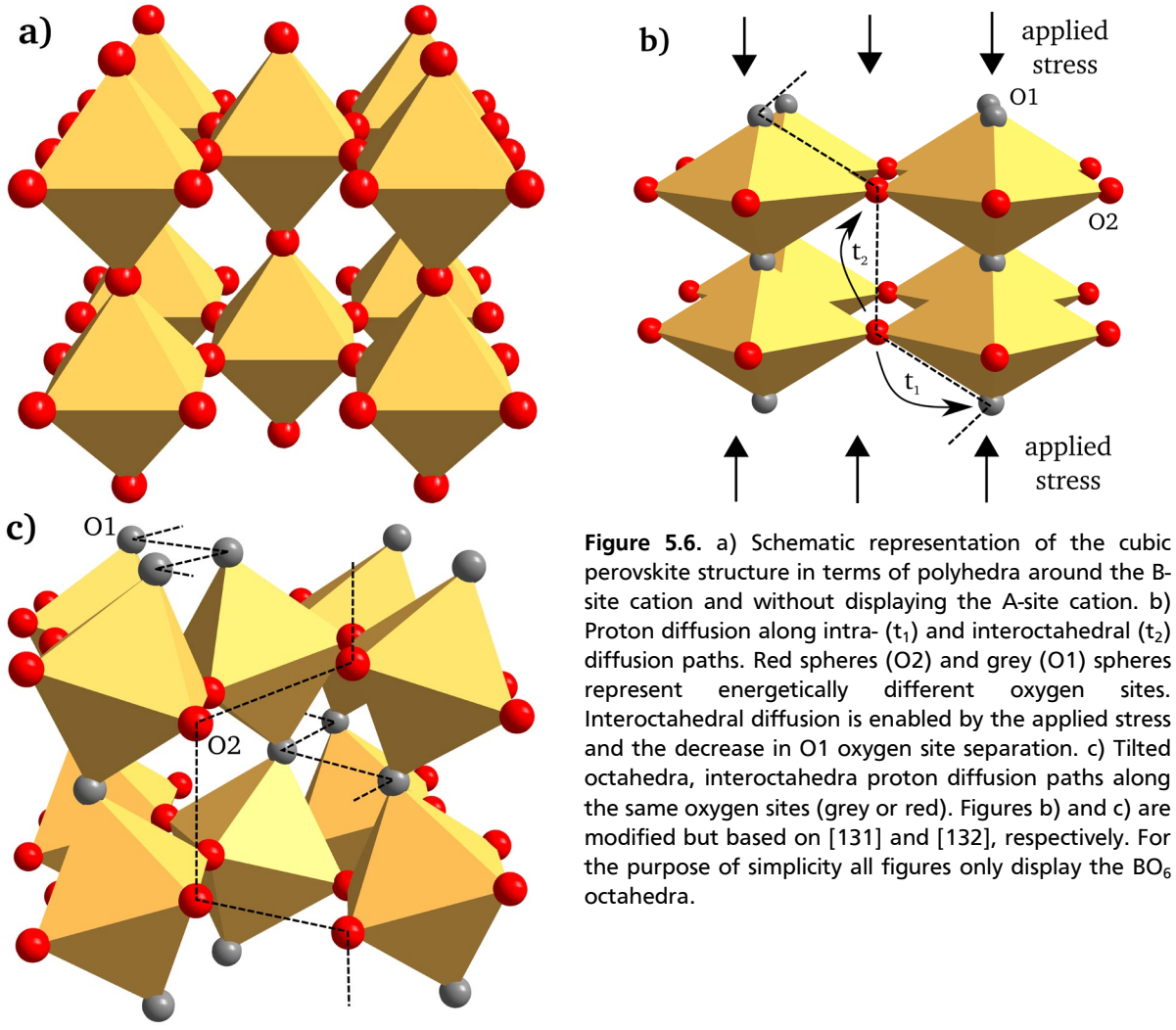

Figure 5.6. a) Schematic representation of the cubic perovskite structure in terms of polyhedra around the B-site cation and without displaying the A-site cation. b) Proton diffusion along intra- (t_1) and interoctahedral (t_2) diffusion paths. Red spheres (O2) and grey (O1) spheres represent energetically different oxygen sites. Interoctahedral diffusion is enabled by the applied stress and the decrease in O1 oxygen site separation. c) Tilted octahedra, interoctahedra proton diffusion paths along the same oxygen sites (grey or red). Figures b) and c) are modified but based on [131] and [132], respectively. For the purpose of simplicity all figures only display the BO_6 octahedra.

Short summary of structural results for BFO films deposited on (001)-oriented Nb:STO

The films were found to be epitaxially grown with a relatively low mosaicity of 0.16 °, which is adequate for a thickness of 250 nm and a lattice mismatch of about 4 %. The θ/2θ scans revealed a growth along the out-of-plane [001] direction with a tetragonal perovskite structure (from symmetry lowering). The ϕ-scan around the (202) asymmetric reflection revealed an in-plane orientation relationship of [100] BFO (001) // [100] STO:Nb (001) with cube-on-cube growth. Post-deposition treatments such as annealing and hydration indicated moderate stresses and strains, which could influence the proton conductivity positively or negatively as schematically displayed in Figure 5.6. In addition the clamping effect of the substrate (Figure 5.4), which is only allowing 1-dimensional anisotropic lattice expansion upon hydration (as opposed to isotropic lattice expansion in individual crystallites), is suggested to limit the incorporation of water when compared to bulk powders. These factors are taken into consideration in 5.7.1, where the proton conductivity is investigated.

5.2.2. Epitaxial Film Growth on (111)–Oriented Nb:STO Substrates

In addition to the previously examined films, which were deposited on (001)-oriented Nb:STO, BFO films were also deposited on (111)-oriented Nb:STO substrates, with the purpose of comparing both in terms of crystal structure and electrochemical behavior. The two samples examined in this chapter are listed in Table 12 including the post-deposition treatments and EIS measurement conditions. Sample BFO7 was annealed, hydrated, measured in different EIS conditions and annealed again. After each step a diffractogram was recorded.

Table 12. Summary of all samples examined in this chapter including post-deposition treatments and EIS measurement conditions

Sample Name	Annealing	Hydration	EIS Measurement Conditions
BFO6	O_2 (500 °C)	No	none
BFO7	Ar (700 °C) →	Yes →	Wet Ar (~3% H_2O) ↓ Dry Ar (~ 3% H_2O) ← Ar (700 °C)

Similarly as for the (001)-oriented films X-ray Diffraction analysis was performed on as-deposited, annealed (in Ar and O_2) and hydrated BFO films. Figure 5.8 shows the θ–2θ scan of an as-deposited BFO film on a (111)-oriented substrate. In addition to the substrate reflections, reflections of the BFO film are visible at lower 2θ angles. The XRD measurements are used to determine whether the film was deposited in a hexagonal or cubic-type crystal structure. For a better understanding of the film growth on the (111)-oriented STO substrate some structural and crystallographic considerations, describing the hexagonal stacking in perovskites, are necessary. For this reason an overview of the different BFO phases and a description of the stacking notation (according to Katz and Ward [27]) is presented in chapter 2.1.

In the present case the film was grown on the (111)-oriented Nb:STO, which could in principle lead to a partial hexagonal growth along the $[001]_{hex}$ direction (corresponds to the [111] direction in the cubic crystal system). At the same time a cubic-type growth with (111) orientation of the film is possible. Since the BaO_3 layers are stacked along [111] direction of the substrate the resulting crystal structure depends on the stacking sequence. For a purely cubic growth the θ–2θ scan of the epitaxial film would result in only two peaks as is shown Figure 5.7b. For a 6H-type stacking the resulting diffractogram of an epitaxial (00l)-oriented film would display more than two reflections as is shown in Figure 5.7d. The reflections in Figure 5.7d are of lower intensity than the main peak (006) but should still be visible, especially since the intensity in Figure 5.8 is plotted on a logarithmic scale. In the same way a 12H-type stacking (Figure 5.7e) would display an even higher number of reflections and can therefore also be excluded.

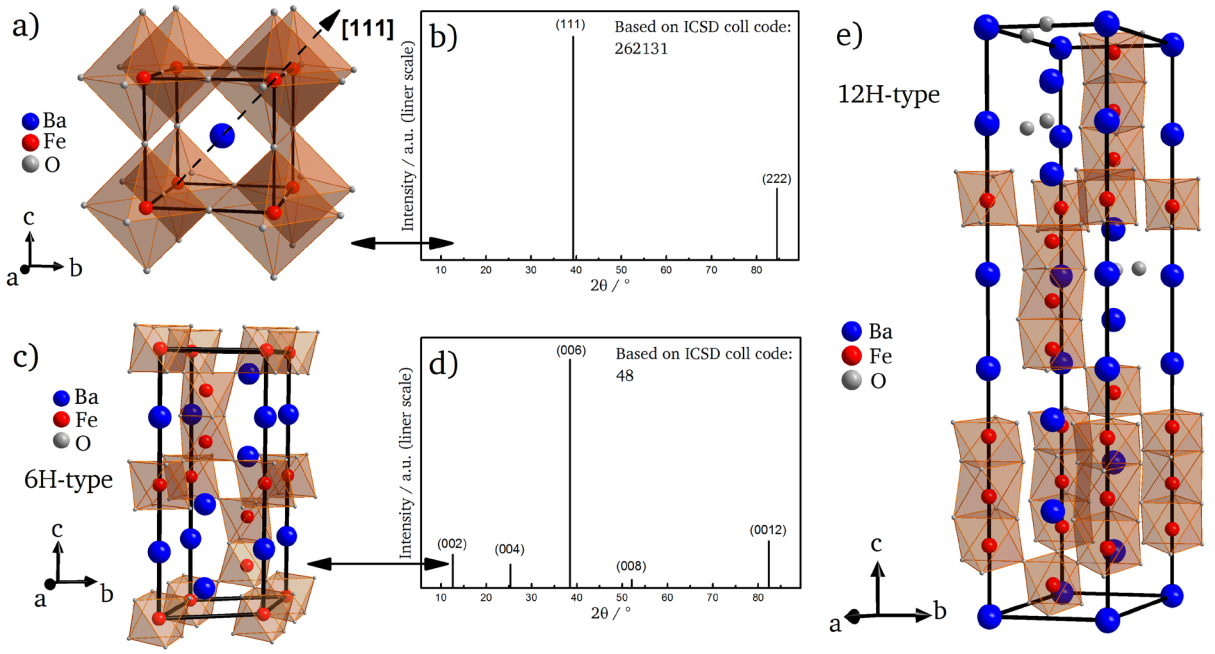

Figure 5.7. Crystal structures of a) 3C-type $BaFeO_3$ (Pm-3m), c) 6H-type $BaFeO_{3-\delta}$ ($P6_3/mmc$) [133] and e) 12H-type $BaFeO_{3-\delta}$ (R-3m) with indicated unit cells and polyhedral around the Fe-cations. The $[111]_{cubic}$-direction is indicated in a). In c) and e) the $[001]_{hex}$-direction, which is equivalent to the $[111]_{cubic}$-direction, lies along the c-axis. The diffractograms in b) and d) show reflections, which should theoretically be visible, when measuring epitaxial films of 3C-type $(111)_{cubic}$-oriented BFO and 6H-type $(001)_{hex}$-oriented BFO, respectively.

Previous reports have claimed that upon depositing BFO films on (111)-oriented Nb:STO substrates (with the same deposition parameters) a hexagonal crystal structure can be observed [104]. However this assumption was only supported by a single diffraction peak indexed (0006). No lower indexed reflection such as e.g. (0004) and no in-plane measurements were shown to confirm the growth of a hexagonal crystal structure and in-plane epitaxial relationship. The long range measurement, which is shown in Figure 5.8 only indicates two film reflections, with no indication of foreign phase and other oriented grains. Considering the logarithmic scaling of the y-axis in Figure 5.8 it is unlikely that any other lower-indexed reflections are present but could not be observed due to low intensity. This in combination with the above considerations suggests an epitaxial film growth, following the cubic [111] direction of the Nb:STO substrate. The rocking curve measurement (ω-scan) was performed on the (111) reflection and is shown in the inset of Figure 5.8. The full width at half maximum obtained from the rocking curve measurement, is 1.5 ° indicating high mosaicity, which is an order of magnitude higher than for the films deposited on (001)-oriented Nb:STO substrates. The reason for the high mosaic spread is that the deposition parameters were not optimized, due to time constraints.

The range magnifications (35 ° - 43 ° and 77 ° - 90 °), depicted in Figure 5.8, clearly show a peak splitting of the film reflections. Conclusively two lattice spacings, namely $d_{111,\ low\ angle}$=2.376 Å and $d_{111,\ high\ angle}$=2.353 Å can be extracted. The peak splitting could be caused by a single low symmetry phase with different oxygen stoichiometry. However, as was already suggested by Callender et al. (based on extended in-plane characterization of $BaFeO_{3-\delta}$ thin films), it is more likely that two pseudocubic phases with slightly different lattice spacing [112] are present, due to differently strained regions in the crystal lattice. The phenomenon of diffraction peak splitting due to differently strained regions is not uncommon in thin films and has for example been observed in epitaxial $La_{1-x}Sr_xMnO_3$ thin films [134]. Previous investigations showed that ultra-thin films ($c_{out,\ strained}$=4.15 Å [115] for 22 nm thickness)

exhibit large lattice strain and that this strain can be reduced by increasing the thickness ($c_{out,\ red.\ strain}$=4.11 Å for 250 nm thickness). For none of these films peak splitting was observed although the thicker films displayed a broadened peak shape, which is suggested to be caused by a distribution of out-of-plane lattice parameters, due to the gradual relaxation with increasing film thickness. In contrast, the films deposited on the (111)-oriented substrates show two clearly separated peaks in the XRD pattern, for which the one at lower diffraction angles can be attributed to a region of the film, which is more strained ($d_{111,\ low\ angle}$= $d_{111,\ strained}$=2.376 Å) and the one at higher diffraction angles to the more relaxed part of the film ($d_{111,\ high\ angle}$=$d_{111,\ relaxed}$=2.353 Å). Since both diffraction peaks are separated, it can be assumed that no gradual change in lattice parameter is occurring but instead, when a critical thickness is reached, defects are formed in the crystal lattice and the remaining part of the film is almost completely relaxed (in the out-of-plane direction).

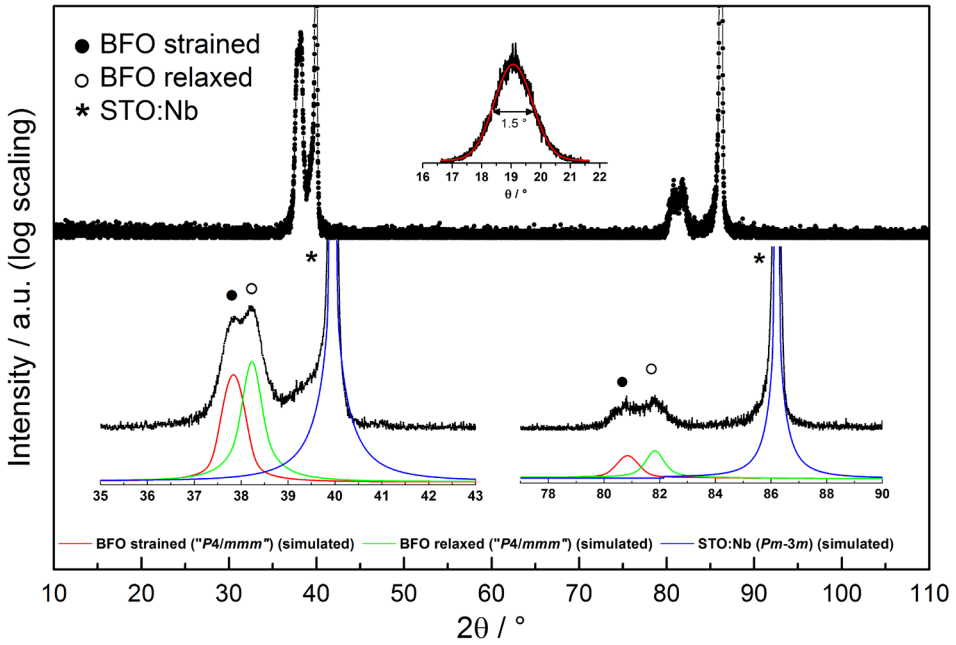

Figure 5.8. High resolution X-ray diffract gram of an as-deposited BFO film on (111)-oriented Nb:STO(highest possible symmetry *P*4/*mmm* due to epitaxial growth in combination with straining), showing film and substrate reflections; The diffraction angle ranges around the reflections are magnified and simulated intensities from structural data are added; the inset shows the rocking curve of the (111) reflections.

The effects of annealing and hydration on the BFO films, which are displayed in Figure 5.9, demonstrate different behavior as compared to the BFO films on (001)-oriented Nb:STO in chapter 5.2.1. Figure 5.9a displays a magnified range between 35° and 42° to emphasize the changes occurring during the different post-deposition treatments. The strained and relaxed components, which were introduced in Figure 5.8 are indicated by vertical lines. In addition to these reflections the Ar-annealing treatments induce another reflection around 36°. The long range measurements in Figure 5.9b show that there are several other reflections, which are clearly visible and which emerge at higher diffraction angles. These additional reflections are marked by ♦ in Figure 5.9. There are theoretically two ways how these reflections can be indexed and explained. The first option, which is simply accounting for the angular positions of the reflections, suggests that reflections could in principal be assigned to a hexagonal phase (PDF# 01-089-4613 – 6H-type). Such a hexagonal phase can be reversibly changed between cubic and hexagonal crystal structures (as is known for bulk powders of BFO) by employing different annealing treatments [105]. However, in epitaxial films this transition has not been

observed to date. Based on Figure 5.9 the observed reflections belong to planes, which are not parallel to the $(00l)_{hex}$ planes would be expected for the formation of a hexagonal phase from a cubic-type film grown along the [111] direction. Instead the peak positions would rather coincide with the $(h00)_{hex}$ reflections. This reasoning would entail a loss of epitaxy as well as a structural rearrangement, which would require a lot of energy, and is therefore unlikely to occur. An investigation by transmission electron microscopy could have been helpful in this respect but was not conducted due to time constraints.

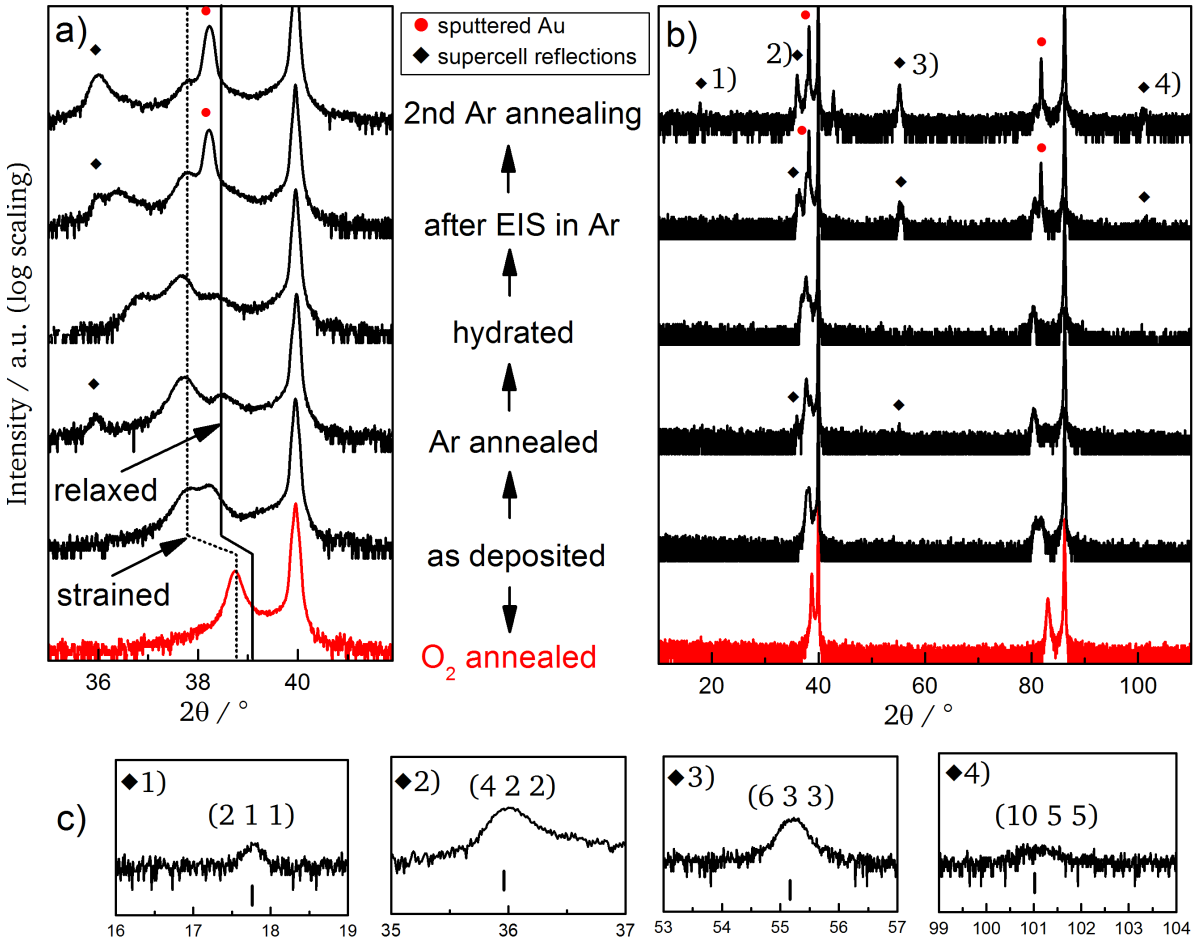

Figure 5.9. a) High resolution X-ray diffractograms of BFO films after various post deposition treatments. One film (red) was O_2 annealed (15 h at 500 °C). The second film (black) was subject to a sequence of Ar annealing → hydration → EIS measurement and again Ar annealing (15 h 700°C). b) Full range HRXRD measurements. Au reflections (sputtered Au) are indicated with ●. Reflections assigned to the superstructure are indicated with ♦. c) Magnifications of the superstructure reflections are shown with an indication of the respective calculated angles.

Therefore, since the formation of the additional reflections seems to be favored by high temperatures in Ar containing atmospheres it is more likely that the films are subject to relaxation processes. The reason for the need to minimize energy in a structural way is that Ar annealing at high temperatures causes a reduction of the oxidation state in Fe and thereby minimizes the content of Fe^{4+} in the structure. The consequence is an increase in unit cell volume and lattice parameter. As was already elaborated in 5.2.1 the increase is caused by the larger radius of Fe^{3+} (~64.5 pm) as compared to Fe^{4+} (~58.5 pm) and leads to stresses within the film. To accommodate these stresses during Ar annealing at high temperatures relaxation is taking place, causing the appearance of the reflections in Figure 5.9. The relaxation process is unlikely to involve large structural changes such as would have to occur

for the formation of the hexagonal phase, which was mentioned above. Therefore the second option that was found to account for the occurrence of the additional reflections is the relaxation of parts of the lattice to bring a slightly differently orientated set of lattice planes into the diffraction condition. The matching set of lattice planes could be attributed to the (211) lattice planes of a 3x3x3 superstructure, assuming that the growth of the thin film occurred along the $[111]_{cubic}$ direction (see azimuthal scan in Figure 5.11 and subsequent elaboration). In terms of the original unit cell these planes would correspond to the (⅔ ⅓ ⅓) lattice planes and to (211) in terms of the superstructure. Figure 5.10 schematically depicts how the (211) diffraction peaks of the 3x3x3 superstructure are suggested to arise during lattice relaxation (involving slight tilting) in certain parts of the film.

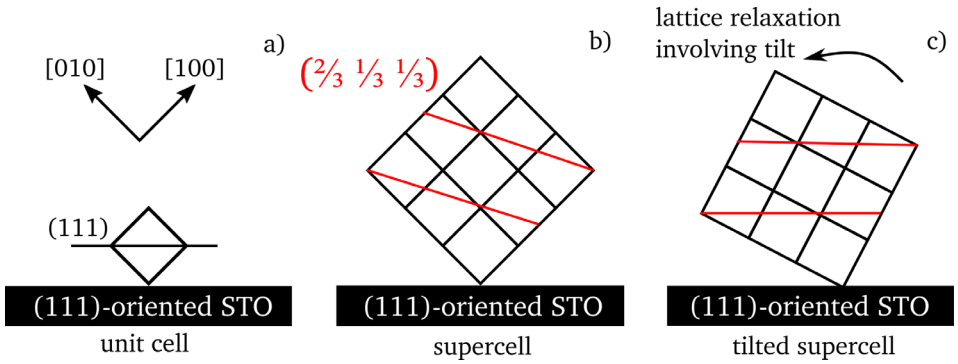

Figure 5.10. a) Individual unit cell, oriented along the $[111]_{cubic}$ direction according to the substrate orientation. b) 3x3x3 supercell of the assumed superstructure, which is only causing visible reflections in the diffractograms c) after relaxation and tilting (caused by Ar annealing) have taken place. The relaxation and tilting bring the (211) lattice planes of the superstructure into the Bragg condition and cause additional reflections in Figure 5.9.

This assumption enables that the additional reflections at 17.8°, 36.0°, 55.2° and 101.1° in Figure 5.9 can be assigned to the (211), (422), (633) and (1055) lattice planes of the superstructure. The intensity of these reflections increased during all post-deposition steps, except for during hydration of the film. In the diffractogram of the hydrated film all reflections, which had previously emerged during Ar annealing, completely disappeared. This indicates that the incorporation of water not only impedes further stress-induced film relaxation but also reverses the previously induced changes. Although the reflections pertaining to the (211) orientation of the superstructure are no longer observed after hydration, another reflection around 37° emerges after hydration, which could not be identified. The appearance of this reflection is undoubtedly related to the incorporation of water (especially because it disappeared again after the water was removed) but is unlikely caused by a simple lattice expansion as described in 5.2.1. The potential role and effects of this additional reflection are further elaborated in 5.7.4.

Since the film is grown along the $[111]_{cubic}$ direction no out-of-plane lattice parameters can be compared directly. Instead the d_{111} lattice spacings can be used to compare the strains and stresses, which occur due to the different post deposition treatments. The lattice spacings in combination with the lattice spacings of the bulk unstrained materials ($d_{111,\ bulk}$) are used to calculate the strain along the out-of plane direction (z-direction) of the films, using equation (5.3). The stresses along the in-plane directions (x-and y-direction) were accordingly calculated using equations (5.5) and (5.6) and under the same assumptions as in 5.2.1.

The two reflections in Figure 5.8, were already assigned to two differently strained regions, but the calculated strains and stresses in Table 13 confirm the assumption. The reflection, which was attributed to a more relaxed region of the film ($d_{111,\ relaxed}$=2.353 Å), yields strain

and stress values close to zero (for an as-deposited film). The reflection, which was attributed to the strained region of the film ($d_{111,\ strained}$=2.376 Å) on the other hand shows strain (1.02 %) and stress (-4.01 GPa) values, which are higher than for the film deposited on (001)-oriented Nb:STO. This difference between the as deposited films on (111) and (001)-oriented Nb:STO indicates that the film growth could be more favorable on a (001)-oriented substrate. The film growth on (001)-oriented Nb:STO occurs in a single less strained region and the film's integrity (structurally) remains intact throughout all post-deposition treatments. Films deposited on (111)-oriented Nb:STO on the other hand have to relieve increasing stress and strain during Ar-annealing, which causes the additional (211) reflections to emerge. Additionally the remaining stresses and strains, calculated from the lattice spacings after Ar-annealing and after hydration, show drastic increases compared to the as-deposited film. The diffractogram of the O_2-annealed film does not show two film reflections but rather a single peak is observed. Whereas the strain and stress of the O_2-annealed film on (001)-oriented Nb:STO decreased (0.47 %, -1.58 GPa), it increased for the deposition on (111)-oriented STO (1.26 %, -4.97 GPa). In general the growth of BFO on (111)-oriented Nb:STO appears to be less favorable than on (001)-oriented Nb:STO because the strains and stress are higher.

Table 13. (111) lattice spacings d_{111} of samples examined after different post-deposition treatments (±0.001 Å). From the experimental d_{111} and the (111) lattice spacing for bulk powders $d_{111,\ bulk}$ the out-of-plane strain ε_z and in-plane stress σ were calculated using equations 5.5 and 5.6. "s" and "r" stand for the reflections, which were attributed to "strained" and "unstrained" regions in the film, respectively.

Post-Deposition Treatment	d_{111} / Å		$d_{111,\ bulk}$ / Å	ε_z / %		Σ / GPa	
	s	r		s	r	s	r
as-deposited - $BaFeO_{2.5}$	2.376	2.352	2.352 [21]	1.02	0	-4.01	0
Ar annealed - $BaFeO_{2.5}$	2.384	2.338	2.352 [21]	1.36	-0.60	-5.35	2.34
Ar annealed and hydrated - $BaFeO_{2.5}$	2.387	2.345	2.352 [21]	1.48	-0.29	-5.85	1.17
O_2 annealed (BFO5) - $BaFeO_3$	2.322	-*	2.293 [105]	1.26	-	-4.97	-

*reflection was of no significant intensity

In addition to the d_{111} lattice spacing the epitaxial orientation of an as-deposited film was probed by performing ϕ-scans around the $(110)_{cubic}$ asymmetric reflection. The ϕ-scan measurements of both film and substrate are shown in Figure 5.11. The threefold azimuthal symmetry, which is observed for the substrate is consistent with the perovskite crystal structure. In order to assure that no other trigonal phase could display threefold symmetry and therefore be accidentally left unconsidered, the (hkl) planes of hexagonal and rhombohedral polytypes are examined in the following. For that purpose the (110) equivalent planes in the cubic crystal system, were converted to the trigonal crystal system, using the following transformation matrix

$$\begin{pmatrix} h_{trig} \\ k_{trig} \\ l_{trig} \end{pmatrix} = \begin{pmatrix} 1 & -1 & 0 \\ 0 & 1 & -1 \\ n/3 & n/3 & n/3 \end{pmatrix} \begin{pmatrix} h_{cubic} \\ k_{cubic} \\ l_{cubic} \end{pmatrix} \tag{5.7}$$

with n being an integer, representing the number of closest packed layers along the c-axis of the trigonal unit cell (e.g. n=15 for a 15R-perovskite modification). The details of this evaluation are attached in the Appendix (Table A 3). For example the $(110)_{cubic}$ reflection would correspond to the $(012)_{trig}$ for n=3 (see also Table 14).

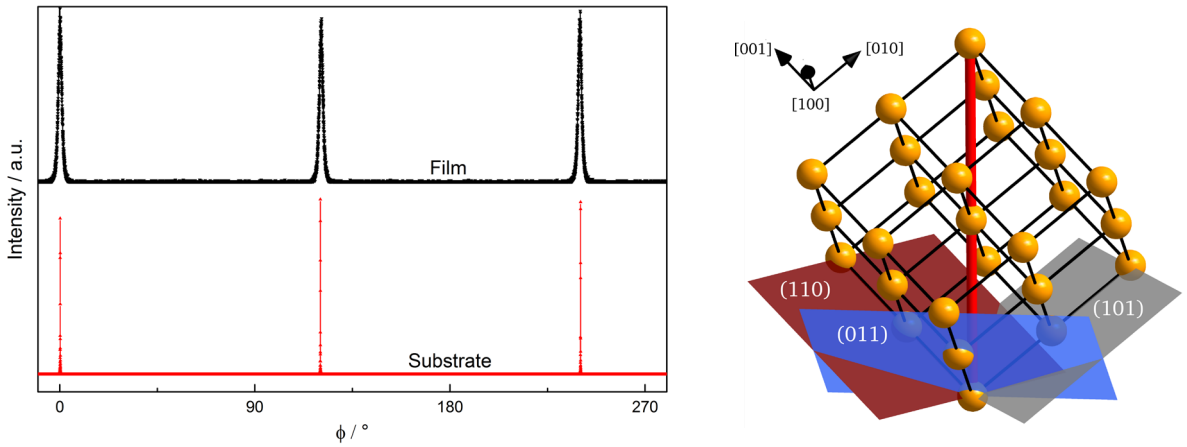

a) b)

Figure 5.11. ϕ-scan of an Ar-annealed film around the (110) reflection, showing three fold symmetry. b) Schematic representation of a cubic lattice structure with the three measured {110} equivalent lattice planes, which are measured in the ϕ-scan. The inclination of the planes normal vector towards the [111] direction (indicated as red bonds) is 35.2 °. The rotation of the sample occurs around the red axis.

The results of the examined trigonal polytypes are summarized in Table 14, showing that only when the number of closest packed layers n is a multiple of 3, reflections can be observed (n=3N, with N=integer). Therefore all other stacking arrangements of closest packed layers (n≠3N), in the hexagonal or rhombohedral structure type, can be excluded to represent the reflections in Figure 5.11. Additionally since for 3N-H polytypes the number of equivalent lattice planes amounts to 6 the simple hexagonal polytypes can be completely ruled out. Only 3N-R polytypes present the threefold symmetry, which is displayed by the ϕ-scan of the as-deposited film. However the diffractograms (θ/2θ scans) of these structures should also display more reflections than are observed in Figure 5.8 (as exemplified in Figure 5.7c and d for the 6H-modification). Therefore the ϕ-scan of the as-deposited BFO film emphasizes the previous assumption of cubic-type as opposed to hexagonal/rhombohedral growth following the $[111]_{cubic}$ direction.

Table 14. Visible reflections based on the number # of closest packed layers in the unit cell. H and R stand for hexagonal and rhombohedral, respectively

# of closest packed layers in unit cell along the x-axis	# of symmetry equivalent planes in reflection and under correct inclination observable via ϕ-scan		hkl indices corresponding to a $(110)_{cubic}$ reflection
	H-type	R-type	
3	6	3	{012}
4	-	-	-
5	-	-	-
6	6	3	{014}
7	-	-	-
8	-	-	-
9	6	3	{016}
10	-	-	-
11	-	-	-
12	6	3	{018}

Short summary of structural results for BFO films deposited on (111)-oriented Nb:STO

Based on the above elaborations related to the θ/2θ scans and the in-plane ϕ-scan it can be concluded that films on (111)-oriented Nb:STO were grown heteroepitaxially along the [111] direction, following the structure of the substrate in a pseudocubic perovskite-type structure (trigonal crystal structures can be excluded). This result in combination with the ϕ-scan suggests that the in-plane orientation relationship is [110] BFO (111) // [110] Nb:STO (111) with a "cube-on-cube" growth. Similar to the films deposited on (001)-oriented Nb:STO the BFO films on (111)-oriented Nb:STO were grown epitaxially but with a higher mosaicity and two differently strained regions. Post-deposition treatments, such as annealing and hydration, were found to cause film relaxation and the occurrence of a 3x3x3 superstructure in the form of (211) reflections (superstructure notion) in the diffractograms. However, further investigations by transmission electron microscopy would have to be conducted, in order to confirm this assumption. The different strains and stresses, which are present in the films were approximated after different post-deposition treatments and showed increased values as compared to the films grown on (001)-oriented Nb:STO. Considering all aspects the film growth of epitaxial BFO appears to be more favorable on (001)-oriented Nb:STO substrates. However, also the films on (111)-oriented Nb:STO are suitable to be characterized and compared by EIS. The examination and analysis of these films by EIS is treated in section 5.7.2.

5.2.3. Investigation of Polycrystalline BFO on (001)–Oriented Nb:STO

Since it is well known that grain boundaries can have detrimental effects on ionic (e.g. proton conduction in $BaZr_{1-x}Y_xO_{3-d}$ [11]) and electronic (e.g. electronic conduction in $Nb:SrTiO_3$ [135]) conduction processes an investigation of polycrystalline BFO films was conducted.

Table 15. Summary of all samples examined in this chapter including post-deposition treatments and EIS measurement conditions

Sample Name	Annealing	Hydration	EIS Measurement Conditions
BFO8	Ar (700 °C)	No	none
BFO9	Ar (550 °C)	Yes	Wet Ar (~3% H_2O) ↓ Dry Ar

To achieve polycrystalline film growth the deposition temperature was reduced. However films deposited at growth temperatures of 25 °C and 450 °C, did not display polycrystalline growth. The θ/2θ scan only displayed STO substrate reflections as shown in Figure 5.11. Therefore grazing incidence XRD was used to probe only the film surface.

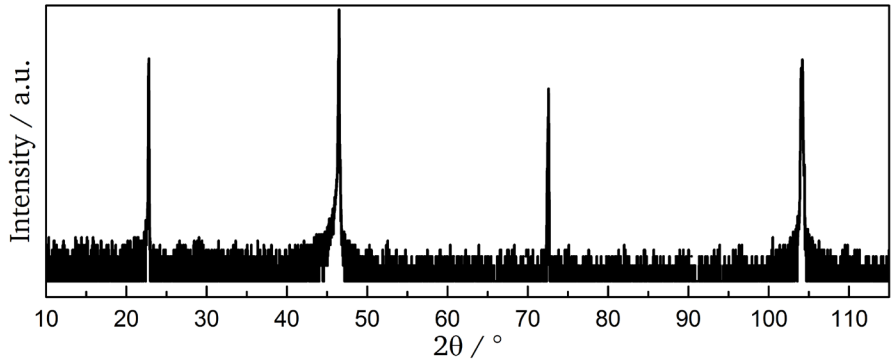

Figure 5.12. a) Diffractograms of amorphous BFO film deposited at 450 °C (black), Ar annealed BFO film (at 700 °C) showing cracks in optical and SEM micrographs, as well as Ar annealed BFO film (at 550 °C)

The diffraction patterns all showed a broad diffraction pattern, as shown in Figure 5.13 for a film deposited at 450 °C, indicating amorphous film growth. Due to time and material constraints no further films were deposited at higher temperatures. Instead the films deposited at 450 °C were annealed at 700 °C (BFO8) and 550 °C (BFO9).

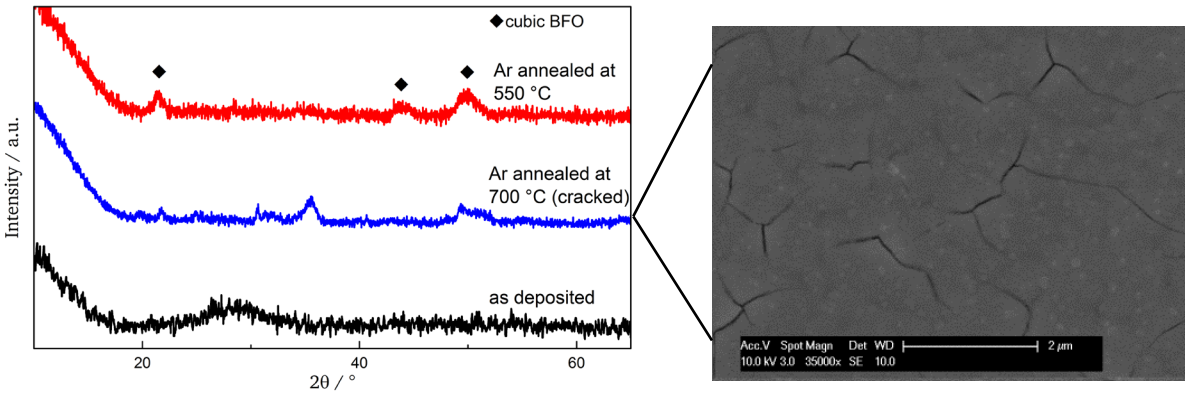

Figure 5.13. a) Diffractograms of amorphous BFO film deposited at 450 °C (black), Ar annealed BFO film (at 700 °C) showing cracks in optical and SEM micrographs, as well as Ar annealed BFO film (at 550 °C)

Figure 5.13 shows the grazing incidence X-ray diffractograms of the films after deposition and after the different annealing treatments. Due to the low incident angle during GIXRD the penetrated volume of the thin film is small and the intensities are low but still clearly visible. Figure 5.13 also displays an SEM micrograph after annealing at 700 °C. The SEM image clearly confirms crack formation during the crystallization, which is the reason why the film could not be used for further electrochemical testing. Instead the film annealed at 450 °C, which experienced no cracking, was selected to be compared to the epitaxial films examined in chapters 5.2.1 and 5.2.2. The diffraction pattern, which is depicted in Figure 5.13a shows 3 distinctive reflections that can be attributed to the (001), (002) and (021) crystal planes in the cubic crystal structure and indicates that a film with several crystallographic orientations was deposited, even though many reflections are missing, which would have to be present for a perfectly polycrystalline film.

5.3. Influence of Post-Deposition Treatments on Microstructure

In chapter 5.2 the BFO films were examined in terms of their crystal structure, which yielded insights pertaining to the post-deposition treatments and measurements. In addition to the structural analysis the changes of morphology and microstructure were monitored and are discussed in the following.

Figure 5.14 shows the cross-sectional and surface micrographs of an as-deposited (before any annealing or post-deposition treatment) epitaxial BFO film on (001)-oriented STO. Using the cross-sectional micrograph a film thickness of 251.2 nm could be measured, which coincides well with the film thickness, estimated from X-Ray Reflectometry (XRR) on Si substrates (film growth rate was determined to be 3.18 nm/min (0.53 Å/s). The micrographs in Figure 5.14 present no discernible features and the cross-section reveals homogenous film growth with a flat smooth surface in the same way as we previously observed by RHEED analysis for thinner films [115]. The relatively large feature (not part of the film), which can be seen in Figure 5.14b was solely used to make sure the micrograph was recorded in focus. All thin films deposited on (001)-oriented Nb:STO (BFO1 through BFO5) are comparable in terms of surface and cross-section of the film (in an as-deposited state) and therefore are not presented here. This constitutes that not only the crystal structure of the films but also the morphology and microstructure were consistently good in quality, even though the fluence of the laser slightly varied (between 1.9 and 2.0 J/cm^2), due to the condition of the experimental setup.

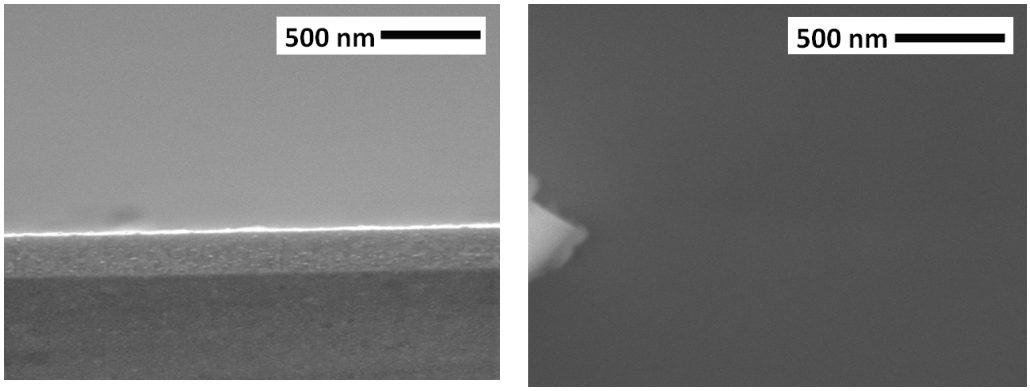

Figure 5.14. a) SEM micrographs of an as-deposited epitaxial BFO film on (001)-oriented STO showing the film's a) cross-section and b) surface (with a relatively large feature, used for focusing).

However, the surface morphology shows noticeable changes after EIS measurements were performed in Ar at elevated temperatures. Figure 5.15 displays the surfaces of BFO1 to BFO4, after EIS measurements in dry and wet Ar (BFO1,BFO2) and in dry and wet O_2 (BFO3/BFO4), respectively. It is apparent that, as opposed to the as deposited film, the surfaces of the measured films feature a multitude of grain-like forms in the range below 150 nm. Whereas BFO1 mostly features a fine and dense grain structure with only a few larger outgrowths of particles, the surface of BFO2, which was exposed to wet Ar, displays structures with distinct facets and edges. The outgrowths of BFO2 are in the range of 250 to 300 nm and are evenly distributed across the whole surface and embedded in a finer grained matrix. These changes, especially for BFO1 are surprising, since under inert Ar atmosphere no surface reactions are expected and the temperature during EIS measurements was lower than during deposition (max. of 550 °C as compared to 700 °C). In Figure 5.15c and d the micrographs after the measurement in air are displayed. Since the samples were measured in air, oxidative reactions

are possible, as was found during the analysis of the impedance data (section 5.7) and the surface composition in X-ray Photoelectron Spectroscopy Analysis (section 5.5). The shapes of the outgrowths show similar round features as are observed on the surface of BFO1. BFO3, which was measured in dry air, presents a broader distribution of grain sizes ranging from grains below 100 nm up to 350 nm. The grain-like features of BFO4 are smaller in size but higher in quantity. Although all of the above films deposited on (001)-oriented Nb:STO developed differently shaped outgrowths the films remained dense and crack-free. Furthermore the structure analysis in 5.2.1 showed that the epitaxy remained intact. Independently of the measurement atmosphere samples BFO1 through BFO4 developed structures on the surface after being measured by EIS, which is an indication for reactions taking place on the surface and most likely also within the film. The composition of the surface and the bulk is examined in more detail by XPS (5.5) and APT (5.6) respectively.

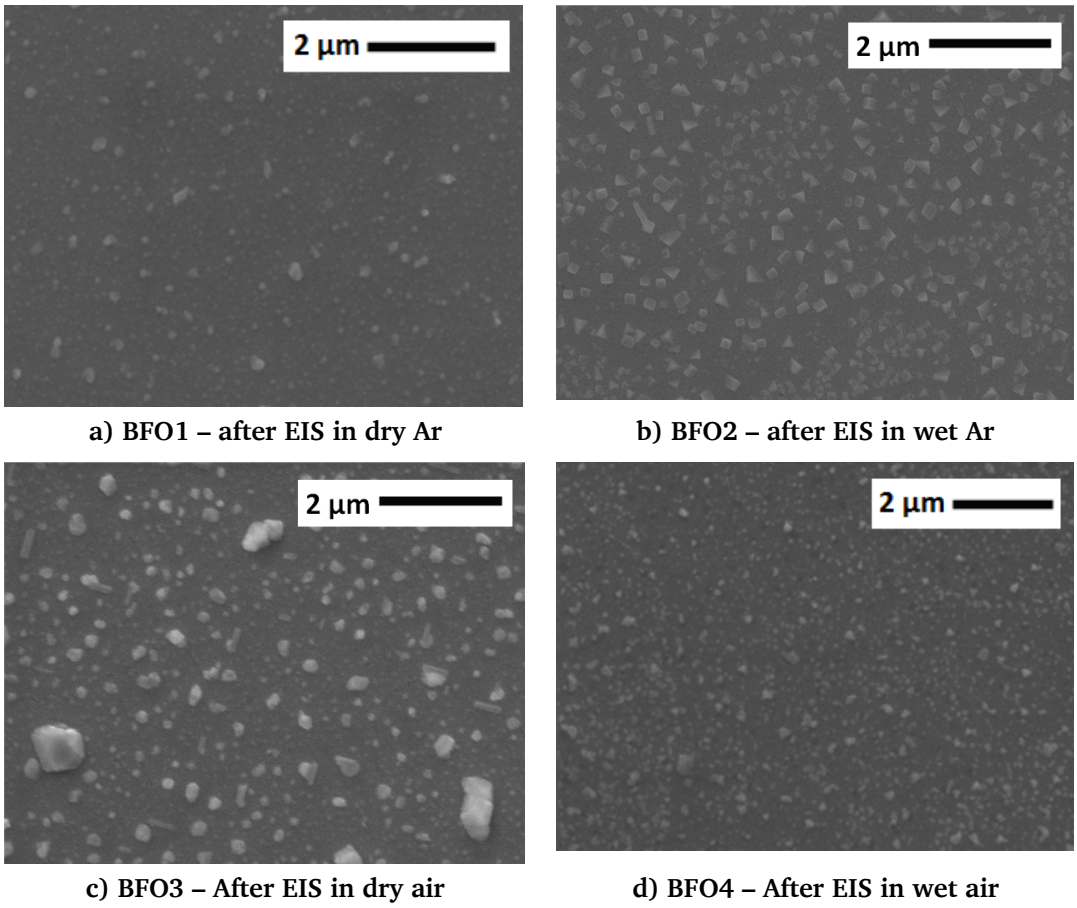

a) BFO1 – after EIS in dry Ar **b) BFO2 – after EIS in wet Ar**

c) BFO3 – After EIS in dry air **d) BFO4 – After EIS in wet air**

Figure 5.15. SEM micrographs of thin films on (001)-oriented STO after EIS measurement in a) dry and b) wet Ar as well as in c) dry and d) wet Air

Similarly to the above examined samples BFO1-BFO4, the microstructure of the films deposited on (111)-oriented STO, whose structure was analyzed in 5.2.2, is analyzed in the following. Figure 5.16 displays sample BFO7 after deposition and after annealing in Ar at 700 °C. The surface of the as-deposited film on (111)-oriented Nb:STO (BFO7) is comparable to the as-deposited film on (001)-oriented Nb:STO (Figure 5.14b) presenting no discernable features and a homogenous smooth surface. A dirt particle was again used to ensure that the surface was in focus during recording. The grains, which are visible in Figure 5.16b after annealing in Ar, are larger than the ones observed in Figure 5.15a but similar in shape. The conclusion is therefore that Ar annealing has a similar effect on the films deposited on (111)-

oriented Nb:STO as it has on the epitaxial films deposited on (001)-oriented Nb:STO. Lastly the microstructure of the films deposited on (001)-oriented STO at lower temperatures is shown below. Figure 5.17 shows sample BFO8 after deposition at 450 °C.

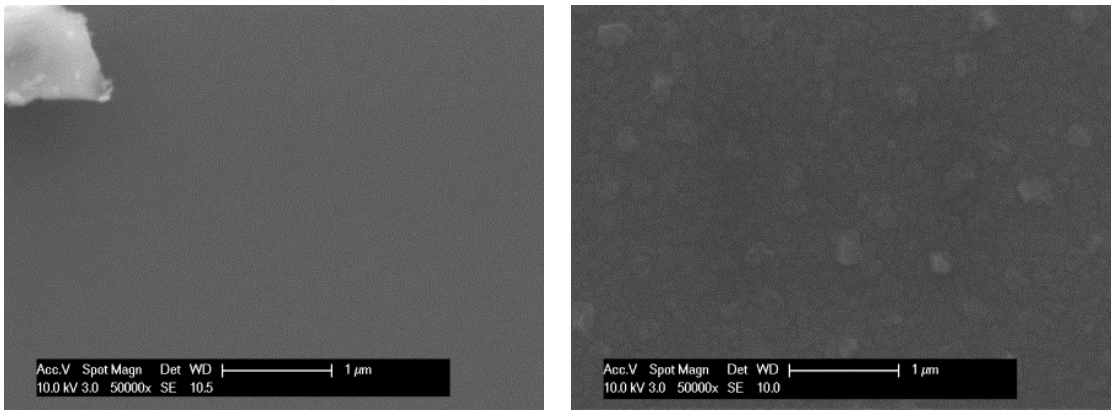

a) BFO7 – as-deposited **b) BFO7 – Ar annealed**

Figure 5.16. SEM micrograph of a) an as-deposited thin film on (111)-oriented STO and b) after annealing in Ar.

As was found in 5.2.3 the deposition at 450 °C caused the film to adopt an amorphous state. The difference between the micrograph of the as-deposited film (450 °C) in Figure 5.17a and the other as-deposited samples is apparent. While the other as-deposited samples did not present any surface features, BFO8 has a different microstructure. The surface pattern appears wavy and as opposed to annealed samples does not show any outgrowths or grains, which are distinguishable from the rest of the surface. After BFO8 was deposited the annealing in Ar led to cracking of the film. The cracking could be observed macroscopically as well as microscopically, as shown in Figure 5.17b. Since the transition from amorphous to crystalline state (e.g. closest packed) with long range order usually involves a reduction of volume, the formation of cracks is most probably caused by the crystallization process and the associated volume reduction. The formation of grain boundaries and the rearrangement of atoms is occurring too quickly at the chosen annealing temperature of 700 °C so that cracking is the easiest way for the film to quickly relieve stress. In addition to the emerging cracks the wavy pattern is reduced and small grains below 150 nm are visible in the pattern. Although XRD analysis revealed a structure with more than one crystallographic orientation after annealing, the cracks rendered the film useless in terms of EIS analysis.

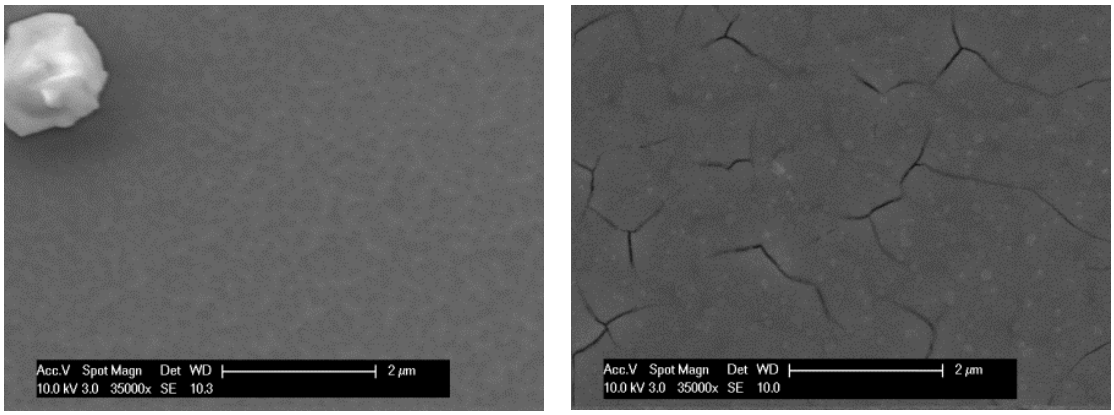

a) BFO8 – as-dep. low temp. **b) BFO8 – after annealing at 700 °C.**

Figure 5.17. SEM micrograph of an as-deposited thin film (450 °C) on (001)-oriented STO and after annealing at 700 °C.

To avoid the formation of cracks, sample BFO9 was annealed at a lower temperature of 450 °C. By employing the lower annealing temperature it can be assumed that the crystallization process occurred slower and without the visible formation of cracks. According to the diffraction pattern in Figure 5.12, crystallization occurs after annealing. Therefore and due to the fact that the diffraction pattern displayed several crystallographic orientations after annealing, BFO9 was examined by EIS analysis in 5.7.3.

5.4. Local Coordination and Oxidation State of Fe in (001)-Oriented BFO Films

^{57}Fe Mößbauer spectra were recorded to investigate the local coordination geometries and oxidation states of the iron species (only for films on (001)-oriented substrates). With respect to the latter, the chemical shifts of all components are significant for the presence of only Fe^{3+}, showing that the composition of the film can indeed be adjusted to $BaFeO_{2.5}$ after the Ar annealing procedure [136]. Apart from oxidation states, Mößbauer Spectroscopy can yield information about the coordination geometry. Regarding the coordination geometries of the Fe polyhedra, the reader should be familiar with the following considerations:

Within a perovskite-type structure ABX_{3-y} with a cubic close packing (ccp) of the AX_{3-y} layers (i.e., which structure can be derived from the aristotype structure with space group *Pm*-3*m* (a~4 Å)), the coordination number of the anion X (here O) to the cation B (here Fe) can vary between 1 and 2, whereas the coordination number of the B cations usually varies between 4 and 6, dependent on the detailed concentration y of the anion vacancies [137]. For any fully vacancy ordered perovskite compound ABX_{3-y} where y = m/n (m, n being integer numbers, m ≤ n), the compositional formula can be rewritten as $A_nB_nX_{3n-m}$. This formula can also be rewritten to indicate the local coordination schemes of the different cations and anions. To exemplify, the coordination scheme of the monoclinic bulk structure of $BaFeO_{2.5}$ [28] is $Ba_{14}(FeO_{4/2})_2(FeO_{3/2}O_{1/1})_6(FeO_{5/2})_4(FeO_{6/2})_2$ = $Ba_{14}Fe_{14}O_{2*(4/2)+6*(3/2+1/1)+4*(5/2)+2*(6/2)}$ = $Ba_{14}Fe_{14}O_{35}$ = $BaFeO_{2.5}$. Here, the sum of red numbers for each iron atom gives its coordination number, and the blue numbers are the coordination number of the respective oxygen ion to iron ions. In contrast, bulk powder of the brownmillerite-type structure of $SrFeO_{2.5}$ [138] shows a coordination scheme of $Sr_2(FeO_{6/2})Fe(O_{4/2})$ = $Sr_2Fe_2O_{6/2+4/2}$ = $Sr_2Fe_2O_5$ = $SrFeO_{2.5}$, and the coordination scheme of bulk $CaMnO_{2.5}$ [139] is again different $Ca(MnO_{5/2})$ = $CaMnO_{2.5}$.

The Mößbauer signals for tetrahedrally coordinated Fe^{3+}(High Spin) species are usually significantly different to the ones of octahedrally (6-fold) and square-pyramidally (5-fold) coordinated Fe^{3+}(HS) species; tetrahedrally coordinated species possess lower chemical shifts as well as lower magnetic hyperfine fields as compared to the higher coordinated species (in our experience the distinction between 5- and 6-fold coordinated species from the chemical shift and magnetic hyperfine fields strongly depends on the quality of the spectra [28]). Summing up, the Mößbauer spectra of $SrFeO_{2.5}$ and $BaFeO_{2.5}$ can therefore be in principle distinguished from the relative areas of the signals which correspond to 4-fold and higher coordinated Fe species (50:50 vs. ~60:40), whereas only a single signal would be expected for an Fe compound being isotypic to $CaMnO_{2.5}$ (all Fe cations with 5-fold coordination).

Although the resolution of the CEMS spectrum of the annealed $BaFeO_{2.5}$ film (BFO1) of this study is low, it is not possible to fit the spectrum with a single sextet. Instead, at least two sextets, one belonging to 4-fold and one belonging to 5/6-fold coordinated Fe with an approximate intensity ratio of ~1:1 and one doublet are needed to fit the pattern. In the fit model the 4-fold coordinated sites are assigned to the well-defined sextet with the smaller hyperfine splitting (Figure 5.18a, green fit) of about 39 T (see appendix for the full set of obtained fitting parameters), in agreement with earlier results [28]. However the second very broad sextet shows a larger hyperfine field and a strong asymmetric broadening, which indicates a distribution of both hyperfine splitting and chemical shifts (Figure 5.18a, blue fit). It is thus reasonable to assign this subspectrum to the 5/6 fold coordinated sites. Here it is represented with a histogram distribution of magnetic hyperfine fields, which are linearly correlated with the chemical shift, in this way the number of fit parameters is minimized.

Figure 5.18b,c present the obtained histogram distributions and the clearly observable three maxima are indicating that the local structure is similar to the case of bulk monoclinic $BaFeO_{2.5}$ [28]. Although straining appears to be overall prohibitive for adopting the monoclinically distorted structure of $BaFeO_{2.5}$ a principle similarity of the local coordination geometries can still be assumed. Clearly, general 5-fold coordination of Fe ions can be ruled out. To investigate the influence of water uptake on the oxidation state of Fe the CEMS spectrum of a hydrated sample (BFO2) was recorded for comparison. Due to the low quality of the spectra no statement in terms of a difference curve can be made at this point. However the chemical isomer shifts and obtained hyperfine parameters indicate that the oxidation state of Fe is not substantially altered and trivalent Fe is the only species found after hydration.

From both measurements it can be concluded that Fe is present in the 3+ oxidation state, according to the isomer shifts. The corresponding magnetic hyperfine fields indicate 4-fold and 5/6-fold coordinated Fe sites. Upon hydration small changes in the fitting parameters can be observed (see Table A 1 and Table A 2), which indicate changes in the local structure due to the uptake of water. However these changes are not further analyzed due to the quality of the signal. As indicated by studies on bulk powders, the principle ordering of vacancies of $BaFeO_{2.5}$ is quite stable up to higher temperatures, and requires temperatures above 900 °C to result in statistical distribution of oxygen sites [140]. When such vacancy ordering is released, the Mößbauer spectra give only a single signal for the iron site [141]. The fact that more than one Fe signal can be observed within the films indicates strong localization of the oxygen ions and vacancies, which might result in a low mobility.

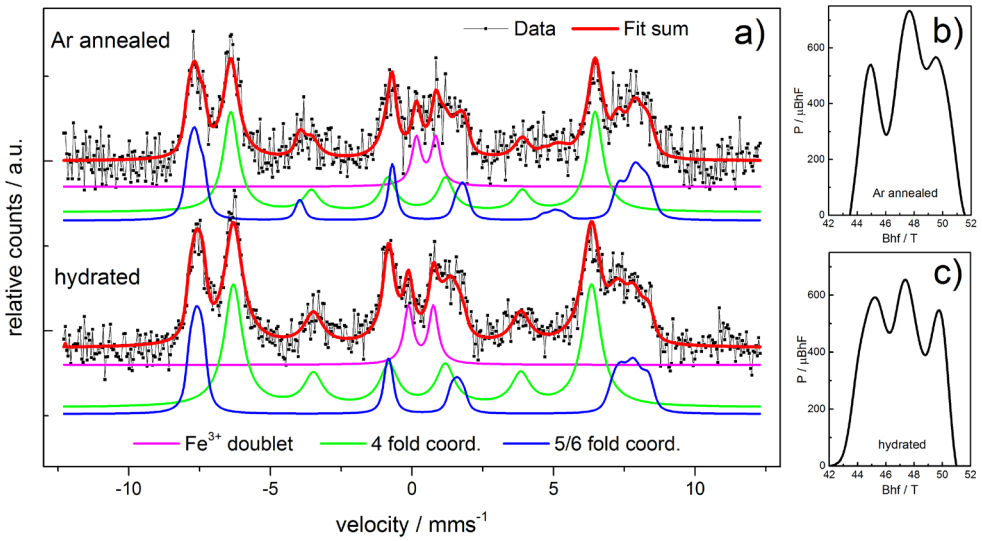

Figure 5.18. a) CEMS spectra of Ar annealed samples before and after hydration and the corresponding histogram distributions of magnetic hyperfine fields for **b)** before and **c)** after hydration.

Furthermore, the oxidation behavior of $BaFeO_{2.5}$ is well known, showing that the material cannot be significantly oxidized under argon atmosphere (with low $p(O_2) \sim 10^{-6}$ bar, estimated from the purity of the gas used). This is in agreement with our observations comparing the heating of the films under different reaction atmospheres. Additionally, the volume changes of the film are low, which is in agreement with relatively small changes of the Mößbauer spectra, and consistent with the presence of local ordering. One additional feature of the spectra is the strong suppression of the second and the fifth line of the sextet. This indicates a spin arrangement in out-of-plane direction of the film, which is related to magnetocrystalline anisotropy, similarly observed for bulk powders of monoclinic $BaFeO_{2.5}$ where the magnetic moments are aligned along the *c*-axis within the G-type antiferromagnetic structure [28].

5.5. X-ray Photoelectron Spectroscopy Analysis of (001)-Oriented BFO Films

When used as an air electrode in a solid oxide electrolysis cell the material is exposed to air at elevated temperatures. As was suggested by Sukkurji et al., little amounts of oxygen impurities could cause oxidation of Fe [115]. With Fe present in Fe^{3+}/Fe^{4+} mixed oxidation states the mechanism of conduction can fundamentally change, which was shown for ultrathin films compared to bulk powders [21,115]. In addition Lee investigated the change in electrochemical impedance response in different atmospheres and correlated the results with the Fe^{4+} ratio contained in the bulk samples [22]. With respect to these findings the measurements in this study were conducted on (001)-oriented BFO films in oxidizing (air) and inert (Ar) atmospheres, as well as under wet and dry conditions. In order to evaluate the chemical composition of the film surfaces and oxidation states (especially of Fe) X-ray Photoelectron Spectroscopy (XPS) was used. Figure 5.19 shows a typical survey spectrum recorded for all samples along with core level detail spectra.

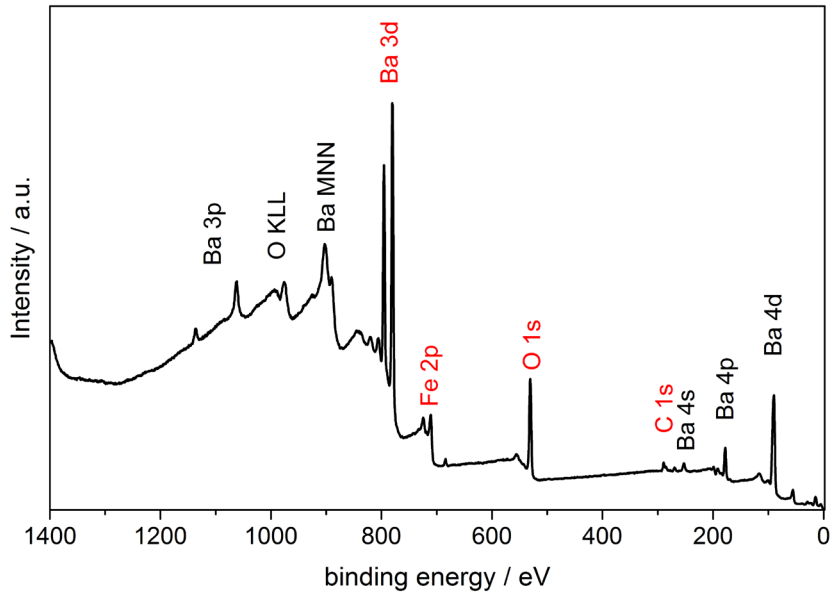

Figure 5.19. Survey spectrum of an as-deposited BFO film. The detail spectra, which are examined in this chapter, are highlighted in red.

Core level detail spectra were recorded for C *1s*, O *1s*, Ba *3d* and Fe *2p* before (after Ar/O_2 heat treatment) and after EIS measurements (indicated in red in Figure 5.19). To compare the composition and changes in oxidation state the individual samples were also measured right after deposition. Figure 5.20 displays samples BFO1 (heated and measured in Ar) and BFO5 (heated in O_2 and measured in air), as well as a sample after deposition. The as-deposited sample as well as the sample heated in oxygen (BFO5) are analyzed in more detail but the de-convolution of the spectra in principle also applies to the other samples, not considering the emerging Sr signal (see 5.6).

The C *1s* core level of the as-deposited sample displays three components at 284.8 eV, 286.2 eV and 288.9 eV respectively, with the first (C-C bonds) and second (C-O bonds) component being the carbon contamination due to air exposure (adventitious carbon). The third component at 288.0 eV can be attributed to carbonate groups. Correspondingly the O *1s* and Ba $3d_{3/2}$ emission lines both show an additional component towards higher binding energy at 531.2 eV and at 780.0 eV, respectively. Both the Ba $3d_{3/2}$ component as well as the O *1s* component have been previously associated with Ba in a non-perovskite environment,

namely in $BaCO_3$ [142–144]. In correcting the integrated peak areas by atomic sensitivity factors (ASF) the presence of $BaCO_3$ is confirmed within the detectable information depth and the entailed quantitative error. The components on the low binding energy side for both the O *1s* at 528.6 eV and for Ba $3d_{3/2}$ at 778.9 eV are characteristic for O^{2-} and Ba^{2+} in the respective perovskite lattice. The fourth component in the O *1s* emission line at 530.3 eV is likely to arise from defects such as oxygen vacancies in the crystal structure and in that way is related to less electron-rich oxygen species [145,146].

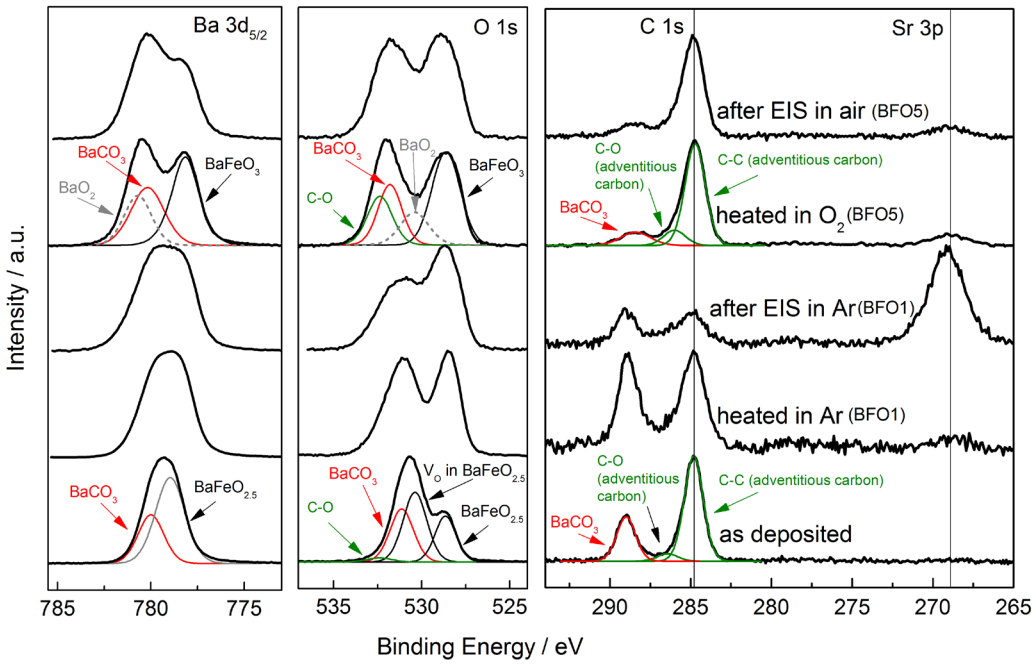

Figure 5.20. Background corrected XPS spectra of BFO thin films: Ba $3d_{5/2}$, O *1s* and C *1s* (Sr *3p*), including fits for two samples.

After the deposition samples BFO1 and BFO5 were heated in Ar and O_2, respectively. Both were then measured by EIS in the respective atmospheres (Ar/Air). The XPS measurements after both heat treatments reveal an emerging Sr *3p* emission line, which increases after the EIS measurements (clearly visible for BFO1 after EIS measurement). In this respect a minor contribution of $SrCO_3$ is suspected to be present in addition to $BaCO_3$ for all samples except for the as deposited. Since the only possibility of Sr on the film surface is due to diffusion/migration from the substrate, an atom probe field ion microscope was used to atomically resolve the composition across the entire film thickness (see Supplementary Materials). The incorporation of Sr throughout the film might decrease the total conductivity since e.g., $SrFeO_3$ and $SrFeO_{2.5}$ are known to be insensitive towards hydration [25]. The implications and possible reasons for the presence of Sr throughout the film, e.g., concerning the conductivity, will be further discussed in section 5.7.

As was already shown in section 5.2 heating sample BFO5 in oxygen oxidizes Fe, which leads to the uptake of oxygen and thereby a drastic decrease of the oxygen vacancies in the perovskite structure. As a result the O *1s* emission line of BFO5 does not show the component, which was previously attributed to defects such as oxygen vacancies. Instead additional components on the high binding energy side of Ba *3d* (580.7 eV) and in the O *1s* spectrum at 530.4 eV are observed. These binding energies agree well with previously reported values of BaO_2 [147] and are supported by the fact that the conditions for the formation of BaO_2 are met during the heat treatment under oxygen (500 °C) [148]. Furthermore, the signal of the C-

O groups attributed to oxygen bonded to adventitious carbon is stronger leading to a broadening of the O *1s* emission line on the high binding energy side. For clarification the reader is informed that the adventitious carbon signal, to which the C *1s* spectra are normalized (except for BFO1 after EIS in Ar), varies to some extent depending on the sample.

Figure 5.21 shows the Fe *2p* emission line for samples BFO1 and BFO2, after the EIS measurement in dry Ar and after hydration and EIS measurement in wet Ar, respectively. The measurement of an untreated sample (only Ar annealing) is added for comparison. By qualitatively comparing the shapes of the Fe *2p* emission lines, changes related to the oxidation state can be deduced. This is possible because ions of a higher positive valence state in a similar chemical environment will have a higher binding energy due to an increase in coulombic interaction of the electron cloud and the ion core [149]. For that reason the Fe $2p_{3/2}$ doublets were normalized and shifted to 710 eV. The emission line of the untreated sample is sharper in comparison, indicating that before any treatment or EIS measurement the Fe exists in its trivalent oxidation state (in agreement with Mößbauer measurements reported in Section 3.2). Strong broadening of the emission lines on the high binding energy side can only be observed in the case of measurement under wet conditions (BFO2). Additionally, the satellite structure of the Fe $2p_{1/2}$ peak is more pronounced. In agreement with other previous results, the change of these features suggests an oxidation of Fe and thus the presence of mixed oxidation states on the surface [150,151]. Alternatively the formation of e.g., FeOOH or Fe_2O_3, which would correspond to a similar change of the shape, cannot be ruled out for the hydrated samples [152]. The phenomenon of surface oxidation due to hydration was already observed previously and suggested to be caused by minor oxygen impurities [115].

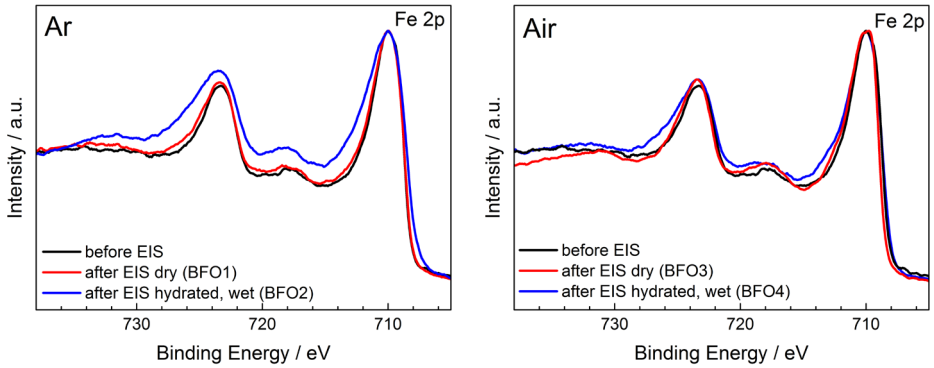

Figure 5.21. Comparison of Fe *2p* spectra after EIS measurements in **a)** Ar and **b)** air. All Fe 2p spectra have been shifted to 710 eV for the purpose of being able to compare the emission line shapes.

Sample BFO1 on the other hand only shows very little broadening, which is to be expected for measurements conducted in inert Ar atmosphere. Figure 5.21b shows samples BFO3 and BFO4, which were both measured in air and consequently both show broadening on the high binding energy side, confirming a partial oxidation of Fe. In light of the probable presence of mixed Fe^{3+}/Fe^{4+} valence states on the surface of BFO2, BFO3 and BFO4 an electronic contribution to the total conductivity has to be considered in the analysis of the EIS measurements (see Section 3.4). However all XPS measurements are surface sensitive and have a penetration depth, which is in the order of a few monolayers depending on the mean free path and the takeoff angle [153]. In this way the above conducted elaborations cannot be directly applied to the bulk of the film. The oxidation state of Fe, which is representative for the bulk of the films, was already analyzed using CEMS in 5.4 and did not indicate the presence of the tetravalent species.

5.6. Atom Probe TOF Mass Spectroscopy Performed on (001)-Oriented BFO Films

Due to the Sr signal detected on the surface during XPS analysis in 5.5, atom probe tomography was used on sample BFO1 after the second EIS measurement to determine the composition as a function of growth direction. Figure 5.22a shows the atomic concentrations of Ba, Fe, Sr and O plotted over the thickness of the film. No other elements, such as Ti or Nb were detected, proving that only Sr migrated/diffused from the substrate. The average atomic concentration of Sr is 10 %, which confirms the assumption of diffusion/migration throughout the complete thickness of the film. Additionally the Ba content is on average 2 % lower than the Fe content, so that as suggested in section 5.5 the replacement of Ba^{2+} by Sr^{2+} is likely to occur. As was already discussed in Section 5.5, XPS analysis also revealed Sr diffusion in connection with annealing procedures and especially EIS measurements.

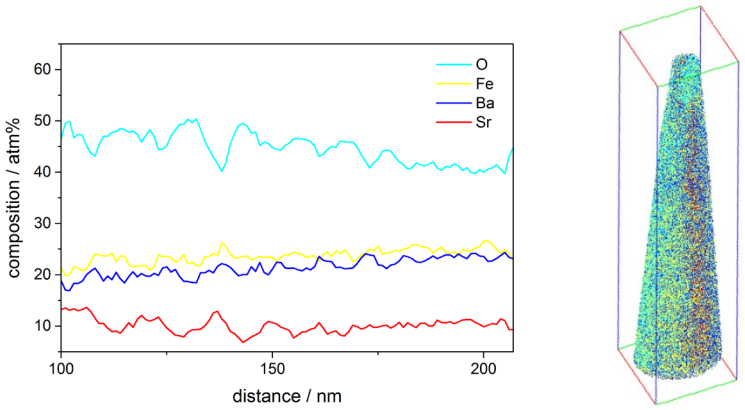

Figure 5.22. a) Composition of BFO1, determined via APT analysis after second EIS measurement (in dry Ar) b) 3-dimensional atom map, 200 nm x 50 nm x 50 nm.

Gupta et al. studied Sr diffusion from STO substrates into $YBa_2Cu_3O_{7-x}$ epitaxial thin films as a function of temperature, ranging from 700 °C to 950 °C [154]. Using ^{85}Sr radioisotopes they traced the diffusive movement throughout the whole film. Considering these results the diffusion process seems likely to be thermally activated whenever the samples are subject to high temperature (during annealing at 700 °C) or a combination of high temperature and applied voltage (during EIS measurements). Additionally the presence of oxygen in the measurement atmosphere can influence the diffusion of Sr^{2+}. The reason for the influence of oxygen is twofold. On one hand it has been observed that the tendency for oxidation of $SrFeO_{3-\delta}$ ($SrFeO_3$ is the prototype Fe(IV) oxide) is greater than for $BaFeO_{3-\delta}$ and on the other hand the oxidation of BFO films on Nb:STO leads to a reduction in lattice strain (see 5.2.1), which is facilitated by incorporating Sr^{2+} with its smaller diameter (compared to Ba^{2+}) [138]. During the diffusion in BFO films the A-site cation, Ba^{2+} is replaced by Sr^{2+} implying that no charge compensation occurs. Furthermore, the incorporation of Sr would lead to a lattice distortion since the ionic radius of Sr (144 pm) is smaller than for Ba (161 pm) [120]. The composition can be described in the form of $Ba_{1-x}Sr_xFeO_{2.5+\delta}$. According to the phase diagram for $BaFeO_3$ – $SrFeO_3$ [155] the estimated composition (~10 atm% of Sr) of $Ba_{0.9}Sr_{0.1}FeO_{2.5+\delta}$ would favor a hexagonal structure (depending on the oxygen partial pressure) but as the XRD data in 5.2.1 clearly shows, no structural changes occur, after any measurement or annealing treatment. In anticipation of the proton conductivity, which is discussed in 5.7 some considerations concerning the incorporation of Sr are elaborated at this point. Although $SrFeO_{3-\delta}$ shows semiconducting behavior [156] and can also be a mixed ionic (oxygen

ion/electronic) conductor at high temperatures (>600 °C), it does not incorporate water and does not enable proton conduction. Empirical findings have shown that Ba containing perovskites (e.g. doped $BaCeO_3$) show higher proton conductivity as compared to Sr containing perovskites (e.g. doped $SrCeO_3$) [61]. For this reason it can be assumed that chemical as well as structural parameters are of importance, when Ba is replaced by Sr. Since in perovskite structured materials (ABO_3) the A and O ions build a close cubic packing, in which one quarter of the octahedral positions are filled with by B ions, the lattice constant is greatly influenced by the sizes of the respective ions (see Table 8). Similar to what was explained in 5.2.1 (Figure 5.6) about the effects of lattice distortion (strain) on proton conductivity it has been postulated that a deviation from the ideal cubic perovskite structure (e.g. orthorhombic distortion) and thereby a lowering of the lattice symmetry as well as a decrease in molar volume impede the formation of protonic defects and lower the saturation limit [61]. Additionally the activation energy of the proton transport is influenced if different oxygen sites are created in the lattice (e.g. following Sr incorporation into the lattice) leading to new conductive pathways (see 5.2.1.)

5.7. Elechtrochemical Impedance Analysis

5.7.1. Temperature Dependent Conductivity Study of Epitaxial BFO on (001)-Oriented Nb:STO

As was found in a previous study the protonic contribution to the absolute conductivity in ultrathin BFO films (~20 nm) cannot be estimated since the overall influence of the contribution of electronic charge carriers could not be determined precisely [115]. The electronic charge carriers are induced by minor oxidation reactions, which can occur on the film surface, e.g., during hydration or measurement in air. We also proposed that epitaxial strain and thereby the activation energy related to proton transport might be strongly affected in such ultrathin films. In contrast, the strain reduction in the thicker films deposited in this work makes the film more comparable to bulk $BaFeO_{2.5}$ (also supported by the Mößbauer studies, see section 5.4), and could therefore induce a more significant contribution of protons as charge carriers. To determine this contribution and to investigate possible effects of different gas atmospheres the films were measured at elevated temperatures in pure Ar and air, respectively. The complex-impedance plane plots of all measurements show two distinct semicircles at temperatures higher than 250 °C (see also Figure 3.7). At lower temperatures (~200 °C) a single semicircle with blocking electrode behavior is observed.

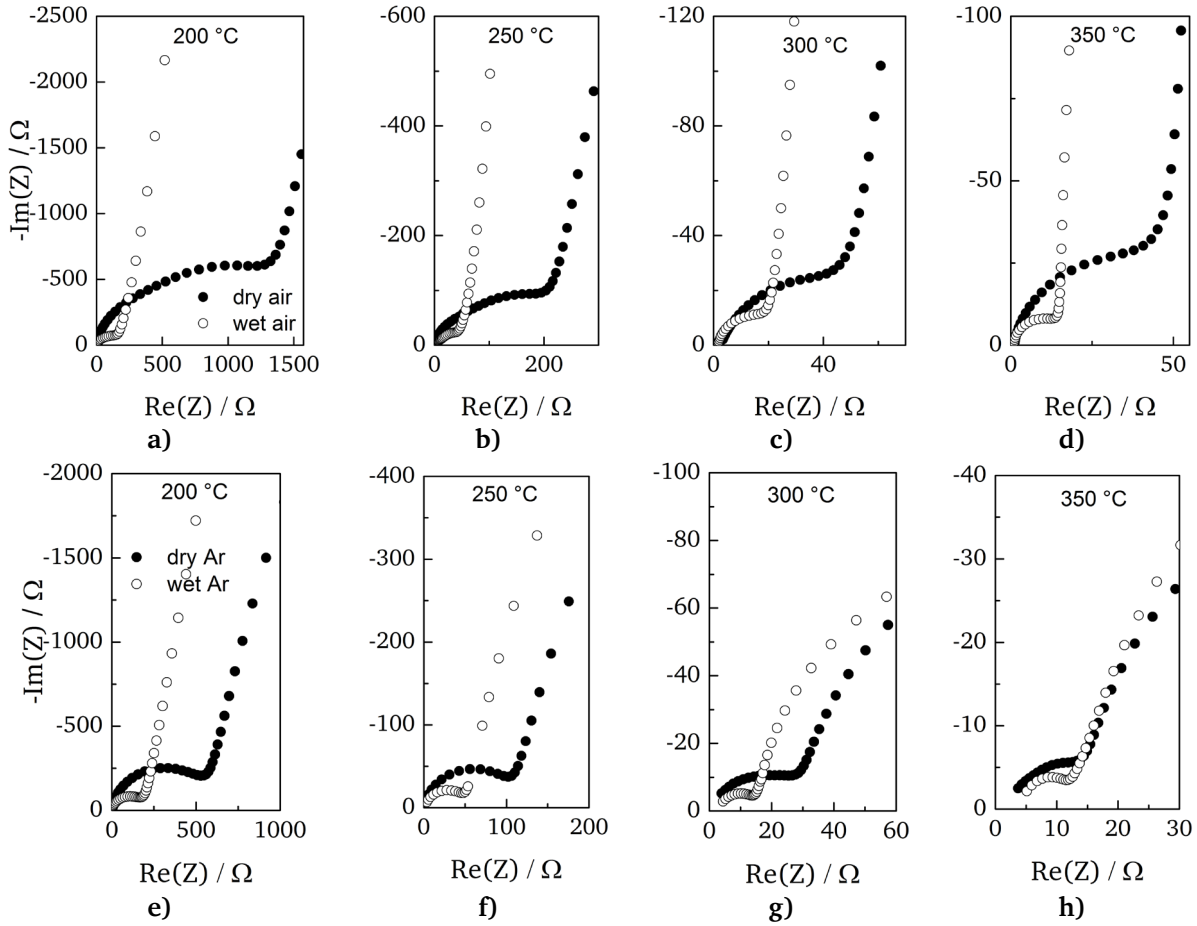

Figure 5.23. Nyquist plots (displaying only the first, high-frequency semicircle) measured in dry (BFO3) and wet (BFO4) air at a) 200 °C b) 250 °C, c) 300 °C and d) 350 °C and measured in dry (BFO1) and wet (BFO2) Ar at e) 200 °C f) 250 °C, g) 300 °C and h) 350 °C.

Since the temperature range between 200 °C and 350 °C was especially important concerning the proton conductivity, (as will be shown later on) the Nyquist plots (only high-

frequency arcs are shown), which were recorded for measurements in air and Ar, are shown in Figure 5.23. Clearly, for all depicted temperatures, the resistance is higher when measured in dry conditions, as opposed to wet conditions. In addition the resistance for both atmospheres and conditions drops considerably with increasing temperature as is to be expected for an ionic conductor. The semicircles were fitted using the model described in Section 3.1.2. From the resistance values of the CPE1 semicircle the conductivities were calculated and activation energies were extracted from ln(σ*T) vs. 1/T plots.

Table 16. Electrochemical parameters extracted from EIS data: Effective capacitance C_{eff}, relative permittivity ε_r, conductivity at 300 °C σ, activation energy E_a (±0.01 eV).

Sample (Measured in)	C_{eff} */F cm^{-1}	ε_r	σ_{tot} at 300 °C/S cm^{-1}	E_a/eV	E_a/eV 2nd cycle
BFO1 (dry Ar)	7.8×10^{-12}	88.1	4.7×10^{-6}	0.63	0.73
BFO2 (wet Ar)	4.3×10^{-12}	48.6	8.3×10^{-6}	0.59(I)/0.55(II)*	-
BFO3 (dry Air)	1.9×10^{-11}	214.6	2.5×10^{-6}	0.69	0.74
BFO4 (wet Air)	1.7×10^{-11}	192.0	5.7×10^{-6}	0.45	-

* two linear regimes with slightly different E_a. (I) from 200 to 300 °C and (II) above 300 °C.

The conductivities measured in Ar atmosphere are shown in Figure 5.24. The measurements in dry atmospheres were conducted twice (while heating up) to track possible changes occurring in the sample due to temperature, atmosphere or applied voltage during measurement. Between 200 °C and 300 °C the hydrated sample (BFO2) exhibits increased conductivity suggesting that around 300 °C water is released from the sample resulting in a decrease of the proton concentration. This is in agreement with the water release temperature observed for $BaFeO_{2.33}(OH)_{0.33}$ under transformation to $BaFeO_{2.5}$, which coincides well with this temperature [21]. Over the remainder of the temperature range the hydrated and non-hydrated (BFO1) samples exhibit a very similar trend up to 500 °C, which is an indication that the conductivity is not dominated by a protonic contribution in this temperature range. The activation energy of 0.63 eV extracted for BFO1 in dry Ar atmosphere is comparable to the activation energy of BFO2 between 300 °C and 475 °C (E_A(I) = 0.55 eV). For temperatures lower than the water release temperature, the activation energy is 0.59 eV, which is similar to what was observed for other perovskite-based proton conductors [11].

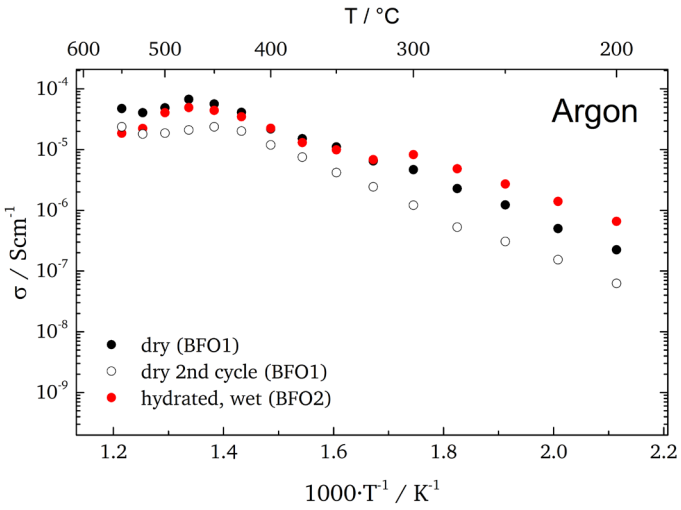

Figure 5.24. Arrhenius plots (only bulk contribution) for samples measured in dry/wet Ar during heating. BFO1 was measured twice to observe the effects of possible diffusion from the substrate.

The second measurement of BFO1 shows a decrease by half an order of magnitude in conductivity as compared to the first measurement, indicating a change in structure, oxidation state or composition at the highest heating temperatures. Since neither a change in crystal structure nor a change in the oxidation state of Fe could be observed after the EIS measurements ceteris paribus, the probable cause is to be found in compositional changes.

The surface analysis presented in section 5.5 clearly revealed that Sr was present on the sample surfaces after post-deposition treatments as well as after EIS measurements. Gupta et al. studied Sr diffusion from STO substrates into $YBa_2Cu_3O_{7-x}$ epitaxial thin films as a function of temperature [154]. Considering the literature reports of Sr diffusion from STO substrates at temperatures >600 °C the diffusion process seems likely to be thermally activated whenever the samples were subject to elevated temperature (during annealing at 700 °C) for extended periods of time. Furthermore, a combination of high temperature and applied voltage (during EIS measurements) might even enable Sr diffusion at lower temperatures. Since the A-site cation, Ba^{2+} is replaced by Sr^{2+} no charge compensation is necessary, which is why no additional defects need to be created within the lattice. However, the incorporation of Sr would lead to a lattice distortion (and thereby a symmetry lowering) because the ionic radius of Sr (144 pm) is smaller than for Ba (161 pm) [120]. The strain induced by the lattice distortion in turn could lead to an increase of the activation energy as observed for the second EIS measurement of BFO1 (0.72 eV) as well as to a decrease in conductivity.

Figure 5.25 shows the Arrhenius plots of the samples measured in air (BFO3/BFO4). As for the measurements under Ar atmosphere, the conductivity of the hydrated sample (BFO4) is significantly higher than for the sample measured in dry air (BFO3). As in the case of Ar, the conductivity of the hydrated sample (BFO4) approaches the conductivity of the dry sample (BFO3), however the conductivity values do not coincide. This is an indication that oxidative reactions take place to a different extent in wet and dry atmosphere (see Section 3.3). The hydrated sample (BFO4) shows a plateau at 350 °C, which is usually attributed to the maximum proton conductivity observed under wet conditions, proving successful hydration and indicating proton conduction [157]. The activation energy over the linear range between 200 and 300 °C is calculated assuming Arrhenius-like behavior and amounts to E_a = 0.45 eV, which is typical for proton conductors [11]. Under dry conditions (BFO3) the total conductivity is lower and the activation energy in the same temperature range is higher (0.74 eV).

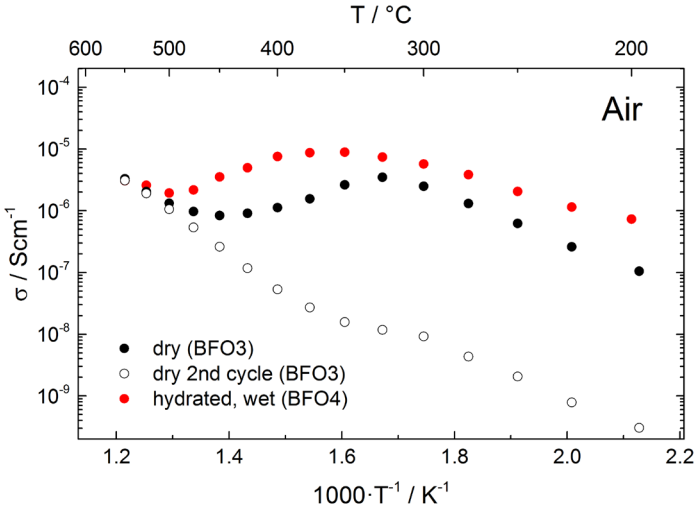

Figure 5.25. Arrhenius plots (only bulk contribution) for samples measured in dry/wet Air during heating. BFO3 was measured twice to observe the effects of possible diffusion from the substrate.

The higher conductivity under wet than under dry conditions coincides with the assumption that in wet atmosphere there is a significant contribution of protons to the total conductivity, in a similar way as for BFO1/BFO2 in Ar. The subsequent second measurement in dry air yields a decreased conductivity of around two orders of magnitude. The reason for this sudden decrease of conductivity can be characteristic for a proton contribution, which is lost at high temperatures above 300-500 °C due to dehydration or the effects of Sr diffusion, as was previously described.

Since the protonic contribution to the total conductivity is significant, a comparison of the conductivity for the samples measured under different conditions is shown in Figure 5.26. It is important to keep in mind that different materials release incorporated water at different temperatures and that above these temperatures the conductivity is mainly due to electronic or ionic contributions.

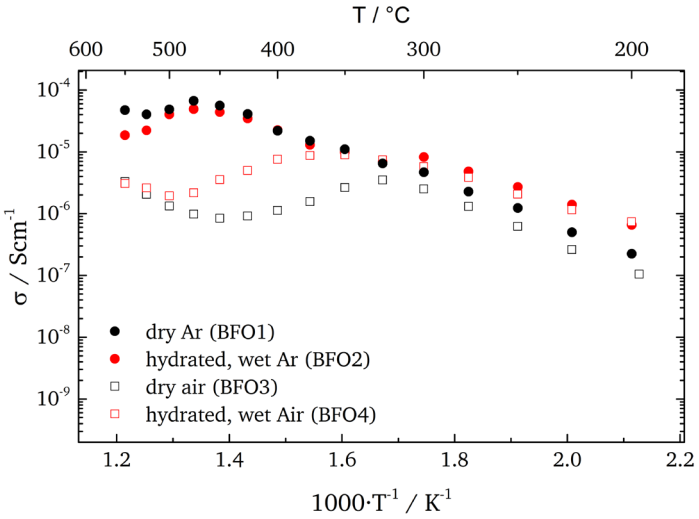

Figure 5.26. Arrhenius plots (only bulk contribution) under different measurement conditions.

In general the total conductivity is given by the sum of the partial conductivities such as electronic σ_{el} and ionic σ_{ion} conductivity. σ_{ion} can be divided into oxygen ionic σ_{oxy} and protonic σ_{prot} conductivity according to:

$$\sigma_{tot}^{Ar} = \sigma_{el}^{Ar} + \sigma_{ion}^{Ar} = \sigma_{el}^{Ar} + \sigma_{oxy}^{Ar} + \sigma_{prot}^{Ar} \tag{5.8}$$

Since the difference in conductivity between wet and dry conditions (between 200 °C and 300 °C) in an inert atmosphere will mainly be due to water uptake and hydration of the film, the following relationship can be used to estimate the protonic contribution to the total conductivity:

$$\sigma_{H^+} \approx \sigma_{tot}^{Ar,wet} - \sigma_{tot}^{Ar,dry} \tag{5.9}$$

In oxygen containing atmospheres this assumption can be used only in first approximation because oxidation may influence σ_{oxy} and σ_{el}. The differences in conductivity are plotted in Figure 5.27 for both air and Ar atmospheres. Only temperatures between 200 °C and 300 °C are considered since water release occurs between 300 °C and 325 °C. To estimate the water release temperature the difference in conductivity of dry and wet atmospheres can be used. The temperature at which the conductivities coincide indicates that most of the water has been released from the sample.

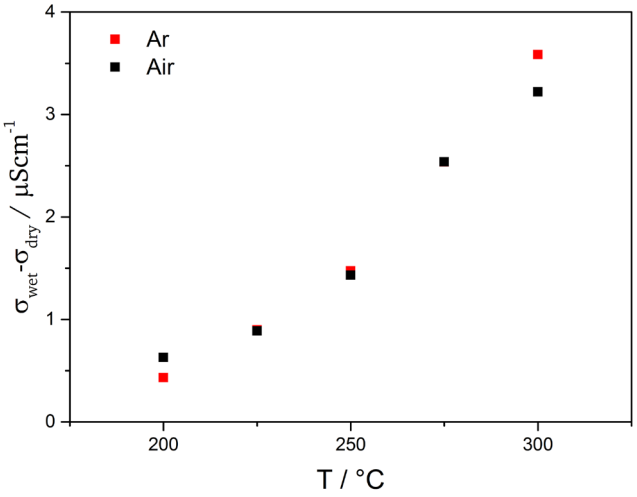

Figure 5.27. Estimation of the protonic contribution to the total conductivity for measurements in Ar and air.

Overall, one can conclude that there is a significant proton conductivity in $BaFeO_{2.5}$ under wet atmospheres, although the absolute value between ~0.5 μS cm^{-1} at 200 °C to ~3.5 μS cm^{-1} at 300 °C is small compared to other known pure proton conductors such as Y-doped $BaZrO_3$ [40]. However since BFO is not a pure proton conductor but can also be a good electronic conductor under certain conditions, the results here suggest principle suitability as an electrode catalyst. Merkle et al. found that already for moderate proton conductivity ($\sigma_{H^+} \geq 10^{-6}\, Scm^{-1}$) the bulk path (only bulk conduction, no triple phase boundaries involved) is expected to dominate for thin film electrodes, meaning that the oxygen reduction reaction could be sufficiently run [158]. The conductivity in most mixed ionic-electronic conductors is dominated by the electronic component (usually at least one or two magnitudes higher [159]).

In $BaFeO_{3-\delta}$ the electronic component is mainly caused by p-type small polaron-hopping [52,53]. Hombo et al. correlated the Fe-O-Fe distance in their hexagonal structure of $BaFeO_{3-\delta}$ and their cubic structure of $SrFeO_{3-\delta}$ with the mobility and thereby with the total conductivity of the hopping transport [23]. Following their reasoning the samples in this work with $c_{out} \geq 4.11$ Å in a tetragonally distorted perovskite structure show longer Fe-O-Fe distances (by 0.1 Å) as compared to the ones reported, and can consequently show a much lower electronic conductivity. Therefore and due to the fact that the samples in this investigation were annealed under Ar at 700 °C before EIS measurement (in that way reducing Fe^{4+} content and polaron hopping to a minimum) the electronic component and thereby the total conductivity is smaller by several orders of magnitude as compared to other literature reports. At this point, the reader should be aware that the reduction of the electronic component in this study is of crucial importance in order to allow for the determination of the protonic contribution to the total conductivity. Accordingly the protonic contribution displayed in Figure 5.27 constitutes a successful first determination of the bulk proton conductivity of (001)-oriented $BaFeO_{2.5}$ in wet atmospheres. From the conclusions drawn in chapter 5.2.1 it is furthermore estimated that the water-uptake and thereby the proton conductivity might be reduced by a factor of ~13, due to the limited volume expansion in thin films (upon hydration). When considering this factor the conductivity in this study is comparable to values, which would be expected based on earlier measurements on bulk powders [21]. For temperatures higher than 300 °C there is no discernible difference between wet and dry measurements in Ar and therefore the protonic contribution is considered to be very small.

5.7.2. Temperature Dependent Conductivity Study of Epitaxial BFO on (111)-Oriented Nb:STO

Since the migration of ions through the crystal lattice strongly depends on the transport mechanisms and local energetics many materials experience anisotropic behavior in their conductive properties. The investigation of anisotropy may allow systematic tuning of the conductive properties in a similar way as can be achieved by applying strain [160], changing the crystallinity [161] or crystal structure [162]. One method of examining the directional dependence of conductivity in materials is to deposit thin epitaxial films on differently oriented substrates and thereby creating specific pathways for the ion migration. For example $Ba_2In_2O_5$, which crystallizes in the orthorhombic brownmillerite structure (until 925 °C, when a phase transition to tetragonal occurs), was investigated in terms of oxygen ion and proton conductivity based on three different substrate orientations [(001), (011) and (111)] [163]. Both oxygen ion and proton conductivity were found to be anisotropic. The reason for anisotropy of the oxygen ion conductivity was explained in relation to the ordering of oxygen ions in the brownmillerite structure, e.g. the one dimensional vacancy channels, which are present along the (101) planes. The proton conduction was found to be anisotropic mostly due to the fact of changes in the pre-exponential factor σ_0 (proportional to the number of free sites, which a proton can hop to) along different directions, while the activation energy E_a did not vary significantly. A conclusion, which can be helpful in the present study, is therefore that a deviation from the cubic structure might not greatly affect the energy barriers but that ordering of protons can restrict the number of available sites for jumps and lead to an anisotropy in σ_0 and the total conductivity. However these results cannot be directly related to the study at hand because the measurements were conducted in an in-plane geometry, which implies that the ionic transport occurred in different crystallographic directions.

To investigate potential anisotropy of the proton transport in BFO, sample BFO7 (see. page 62), which was deposited on (111)-oriented Nb:STO, was electrochemically characterized. The same equivalent circuit model as for the (001)-oriented films (see section 3.1.2) could be used and yielded good fit results as displayed in Figure 5.28.

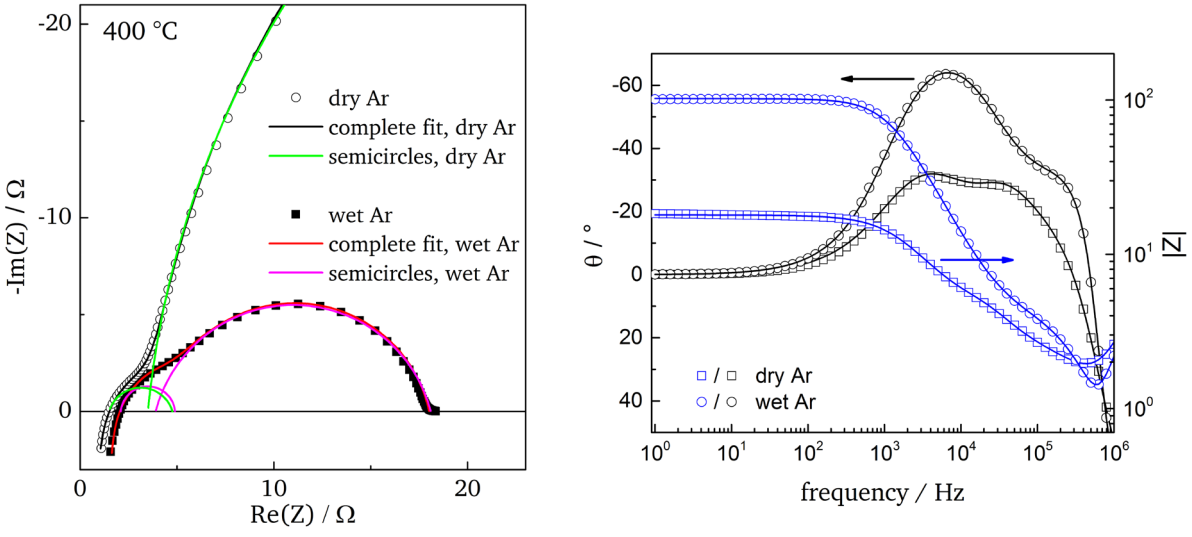

Figure 5.28. **a**) Characteristic Nyquist plots for a measurements in wet and dry Ar, including Zview fits (using the model in Figure 3.5). In addition to the complete fits, the individual semicircles corresponding to bulk and sample-electrode interface are displayed (modeled by simple parallel R-CPE circuits). **b**) The corresponding bode plots for a measurement at 400 °C (Ar atmosphere). Both measurements were performed on the same sample.

Due to time constraints only a single sample (BFO7) could be examined. BFO7 was first measured in wet Ar (after having been hydrated) and subsequently in dry Ar. The second measurement can therefore not reliably be treated in the same way since in 5.7.1 it was found that upon repeated measurement the conductivity drops significantly (most likely due to Sr diffusion). Nevertheless both electrochemical impedance measurements were used to calculate the electrical conductivity, which is plotted in Figure 5.29a. The conductivity for the measurement in wet Ar increases linearly in the Arrhenius plot until 275 °C. Above 275 °C a deviation in the form of a further increase can be observed. The resulting plateau is indicative for the water uptake and resulting proton conduction similar to what was found to be the case for BFO2 and BFO4 in Figure 5.26. This assumption is confirmed by the fact that the measurement in dry Ar shows no sudden increase between 300 °C and 375 °C. In addition to the conductivity Figure 5.29b shows the transference number for proton conduction (t_{H^+}) in wet Ar, which can be calculated according to:

$$t_{H^+} = \frac{\sigma_{H^+}}{\sigma_{tot}^{Ar,wet}} \tag{5.10}$$

The transference number for a good proton conductor would ideally be ~1 signifying that all transported charge carriers are protons. At the water release temperature this value would start to drop until reaching 0. The values for BFO7 indicate, that the conductivity is not purely protonic, and that a sudden increase in proton conduction occurs above 275 °C (see 5.7.4), which drops after water release at 350 °C.

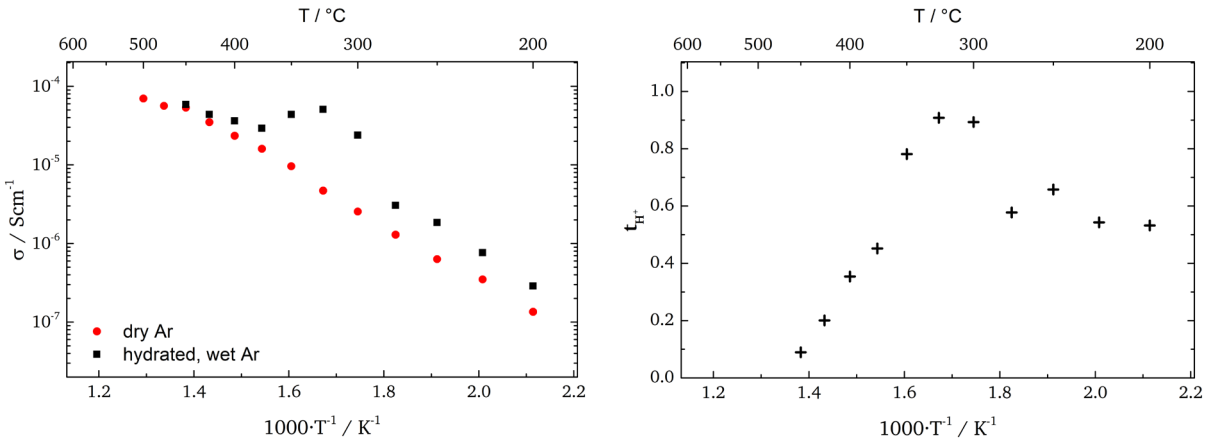

Figure 5.29. a) Arrhenius plots (only bulk contribution) for sample measured in dry/wet Ar during heating. Both measurements were performed on (BFO7). b) Transference number for proton conduction wet Ar.

The electrochemical parameters, which were extracted from the Arrhenius plots in Figure 5.29 are summarized in Table 17. The activation energy extracted from both measurements is similar around 0.6 eV. It is unclear whether the repeated measurement on the same sample (and thereby Sr diffusion) critically influenced the results. However there does not seem to be systematic lowering of the conductivity, since at high temperatures the values of both measurements are almost identical. Considering this uncertainty the actual purely protonic contribution, which was determined in 5.7.1 according to equation (5.9), could not be calculated in the same manner as for BFO7. The absolute conductivity between 300 °C and 375 °C, on the other hand, is high compared to the thin films on (001)-oriented STO, which is why the absolute conductivity in wet Ar will be compared to samples with different substrate

orientation and crystallinity in 5.7.4. The calculated capacitances are smaller than the capacitances of the films deposited on (001)-oriented Nb:STO but are indicative for a bulk contribution.

Table 17. Electrochemical parameters extracted from EIS data: Effective capacitance C_{eff}, relative permittivity ε_r, conductivity at 300 °C σ, activation energy E_a (±0.01 eV).

Sample (Measured in)	C_{eff}*/F cm^{-1}	ε_r	σ_{tot} at 300 °C/S cm^{-1}	E_a/eV
BFO7 (dry Ar)	1.3×10^{-11}	154	2.5×10^{-6}	0.65
BFO7 (wet Ar)	2.0×10^{-11}	187	2.4×10^{-5}	0.63*

*excluding the temperatures from 300 °C until 375 °C

5.7.3. Temperature Dependent Conductivity Study of Polycrystalline BFO on (001)-Oriented Nb:STO

In section 5.2.3 the examination of sample BFO8 showed several reflections, indicating that after annealing the amorphous structure at least partially crystallized to a film with several crystallographic orientations, which exhibited no cracking. However, even though BFO8 remained free of cracks both measurements in wet and dry Ar had to be performed on the same sample. Similar to the measurements in 5.7.2 the measurement in wet Ar (with previous hydration) was performed first. This was done to obtain reliable values for the measurement in wet Ar, since it was found that upon repeated measuring of the same sample a decrease in conductivity can be expected (due to Sr diffusion). As the purpose of the investigation of polycrystalline films is the investigation of the grain boundaries and their respective conductivity, special attention was paid in the evaluation of the impedance data. According to the brick-work layer model (a detailed description of the theoretical aspects of the brick-work layer model can be found in literature [79,164]) a third semicircle (characterized by a capacitance ranging between 10^{-8} F and 10^{-11} F, see Table 3) should appear in the Nyquist plot in addition to bulk and sample/electrode semicircles. Figure 5.30a shows a typical Nyquist plot of measurements in wet and dry Ar at a temperature of 400 °C. The absence of a third semi-circle is obvious, even before fitting the data. For the fitting procedure the same equivalent circuit model, which was already employed for the epitaxial films, could be used without restrictions. The corresponding Bode plots in Figure 5.30b only contain two maxima in the frequency vs. phase angle plot, which is another clear indication that no third semi-circle and therefore no discernable grain-boundary contribution can be extracted.

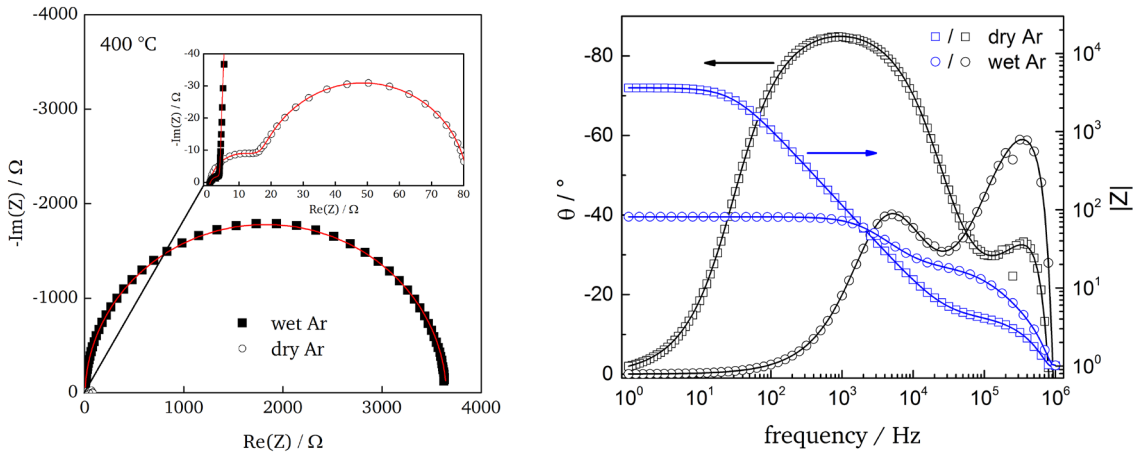

Figure 5.30. a) Characteristic Nyquist plots for a measurements in wet and dry Ar, including Zview fits (using the model in Figure 3.5) with the corresponding **b**) bode plots for a measurement at 400 °C (Ar atmosphere). Both measurements were performed on the same sample (BFO8).

The conductivity, which was extracted from the EIS measurements in dry and wet Ar, is displayed in Figure 5.31. The capacitance values, which are listed in Table 18 were extracted from the first semicircle and calculated according to equation (3.8). The values are in good agreement with values typical for bulk capacitance and similar to values in 5.7.1 and 5.7.2. The activation energies are extracted from the indicated temperature range in Figure 5.31. With 0.9-0.99 eV the activation energies are higher than for all other deposited films, making proton transport less likely.

Table 18. Electrochemical parameters extracted from EIS data: Effective capacitance C_{eff}, relative permittivity ε_r, conductivity at 300 °C σ, activation energy E_a (±0.01 eV).

Sample (Measured in)	C_{eff}*/F cm^{-1}	ε_r	σ_{tot} at 300 °C/S cm^{-1}	E_a/eV
BFO9 (dry Ar)	6.89×10^{-12}	77	8.5×10^{-7}	0.90
BFO9 (wet Ar)	8.9×10^{-12}	101	6.0×10^{-6}	0.99

*activation energies are extracted from the temperature range indicated in Figure 5.31

The conductivities measured in dry and wet Ar show a difference over the complete temperature range (systematic lowering of the total conductivity), which is an indication that during the second measurement (dry Ar) the conductivity dropped due to Sr diffusion. Although the conductivity is quite high around 300 °C, the activation energy for both measurements is considerably higher than for all other films. The values of 0.99 and 0.90 eV are usually indicative for the transport of oxygen ions and not for protons. Therefore the purely protonic contribution can be expected to be low, compared to the absolute conductivity. The slight plateau-like region, which is observed between 275 °C and 350 °C for the measurement in wet Ar, is an indication that proton transport could be present to some extent. However, since both measurements were performed on the same sample the proton contribution cannot be calculated in the same way as for the epitaxial films on (001)-oriented Nb:STO (see equation (5.9)).

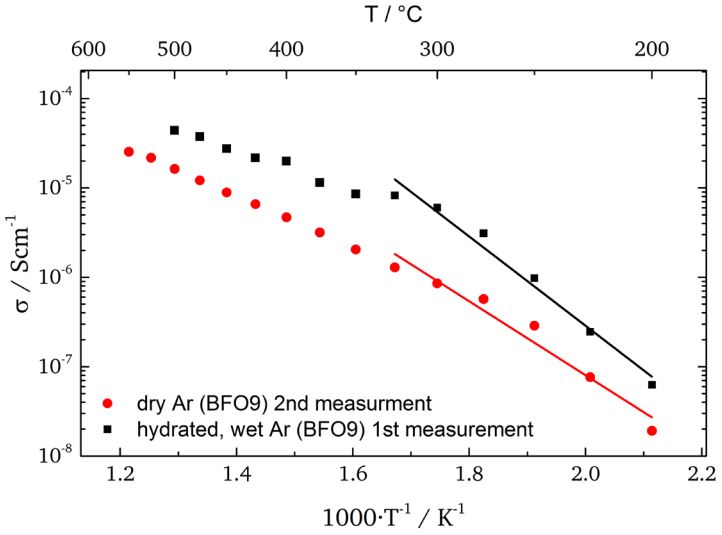

Figure 5.31. Arrhenius plots (only bulk contribution) for sample measured in dry/wet Ar during heating. Both measurements were performed on (BFO9).

5.7.4. Comparison of Different Sample Types and Classification within Comparable Literature

In 5.7.1 to 5.7.3 the conductivity of films with different crystallinity and different substrate orientations was investigated. Especially the expitaxial films on (001)-oriented Nb:STO were examined in detail, including different atmospheres. For the films with several crystallographic orientations on (001)-oriented Nb:STO (BFO9) and the epitaxial films on (111)-oriented STO (BFO7) measurements were only conducted in Ar atmosphere. Figure 5.32 shows a comparison of the conductivities between samples of different crystallinity and substrate orientation in wet and dry Ar. As was already mentioned before BFO7 and BFO9 were measured in wet Ar first and subsequently in dry Ar, which might have led to a decrease in conductivity during the second measurement. For this reason only the absolute values of conductivity, which are shown in Figure 5.32, can be compared.

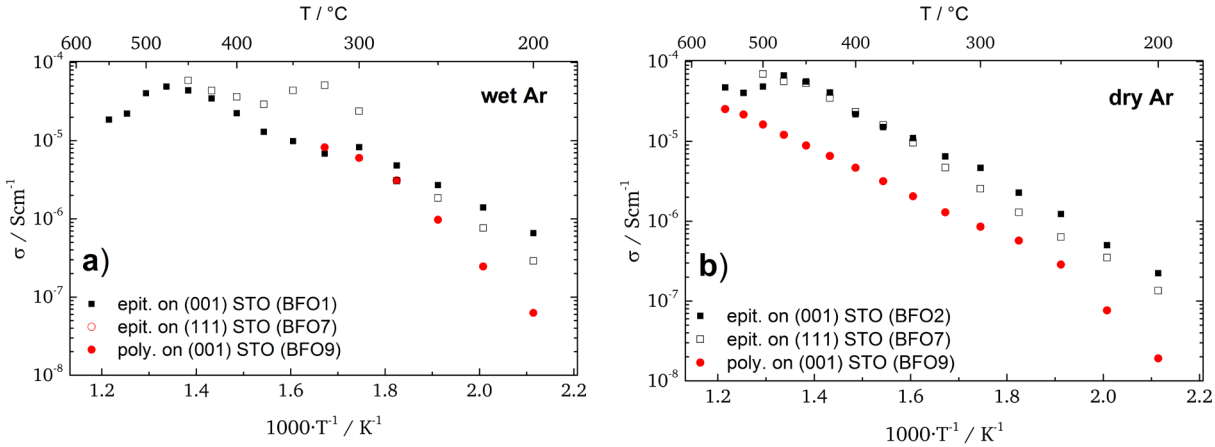

Figure 5.32. Comparison of conductivity between samples of different crystallinity and substrate orientation measured in a) wet Ar and b) measured in dry Ar. Sample BFO9 is designated polycrystalline although not all crystallographic orientations (as is characteristic for a polycrystalline film) showed up in the diffractogram.

In dry Ar atmosphere only sample BFO2 was measured reliably (measurement on a sample, which was not measured previously – "fresh"). Although the conductivity of BFO7 in dry Ar was not measured on a "fresh" sample most of the measured data points coincide approximately with the measured conductivity of BFO2. This is an indication that the measurement data was not strongly influenced by Sr diffusion and that up to a certain degree proton conductivity is present between 200 °C and 275 °C, as for epitaxial BFO on (001)-oriented Nb:STO (BFO1). Additionally above 275 °C sample BFO7 shows a sudden and considerable increase in conductivity. The conductivity in this temperature region excels the values of both other samples (BFO1, BFO9) in wet Ar atmosphere.

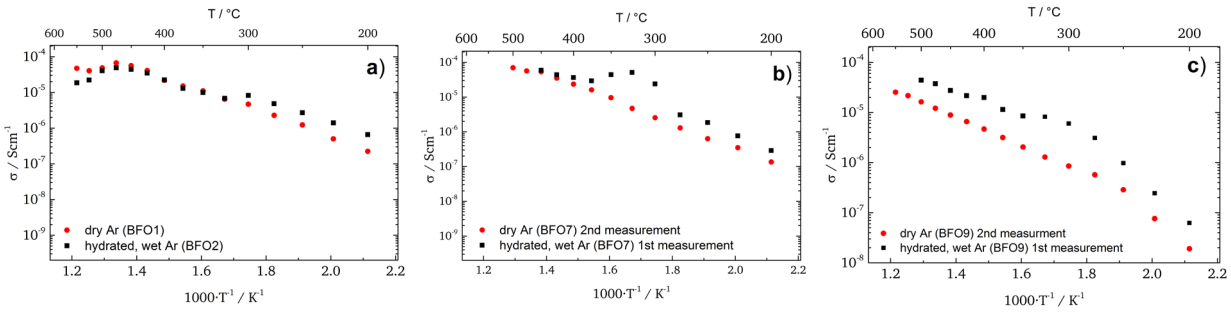

Figure 5.33. Comparison of conductivity measurements of **a)** epitaxial BFO on (001)-oriented STO (BFO1/BFO2) b) epitaxial BFO on (111)-oriented STO (BFO7) and c) polycrystalline BFO on (001)-oriented STO (BFO9) in wet and dry Ar. In (b) and (c) the data points at 475 °C and 500 °C could not be extracted from the EIS data, because the semi-circles could not be reliably separated.

The fact that the total conductivity increases can either be attributed to an increase of the protonic contribution to the total conductivity over the range between 300 °C and 400 °C or alternatively be caused by a higher mobility of the protons along the [111] direction. The total conductivity of BFO7 is higher than the conductivity in BFO1, suggesting that a stabilization of protons is facilitated in the given structural arrangement between 300 °C and 350 °C. Therefore a comparison of the structural differences of BFO1 and BFO7 might help in explaining the difference in conductive behavior. BFO1 on the one hand was epitaxially grown along the [001] direction as a single tetragonally distorted phase in a perovskite structure. BFO7 on the other hand was found to grow in a pseudocubic perovskite-type structure along the [111] direction, following the orientation of the substrate. Previous studies have indicated, that by controlling the amount of vacancies and therefore the amount of water that can be inserted into the structure, the conductivity can be greatly influenced [157,162]. Since the amount of vacancies and therefore the amount of water in this study is not controlled by doping (as in [157,162]), but is rather kept constant by controlling the oxidation state of iron, the influence of compositional changes can be excluded as a possible reason for the high conductivity. It is rather likely that in the present structural arrangement more favorable conductive pathways exist, due to structural changes (bond angles, bond lengths and in general similar effects as in Figure 5.6) associated with the film growth and the internal strains/stresses of the film. In addition the annealing in Ar caused relaxation effects, which could influence the conductivity. However these relaxation effects completely disappeared after the sample was hydrated (see Figure 5.34). Therefore the cause of the increased conductivity must be of different origin.

Based on the diffractograms, which are shown in Figure 5.9, the lattice spacing d_{111} of BFO7 (on 111-oriented Nb:STO) was found to expand during hydration for both components of the film, relaxed (2.338 Å to 2.345 Å) and strained (2.384 Å to 2.387 Å). This expansion is not exceptionally high but on the contrary smaller in magnitude compared to BFO2 and does not explain the increased conductivity. However, in addition to the strained and relaxed components, which are indicated by “r” (relaxed) and “s” (strained) in Figure 5.34, another phase (here called “hydrated phase”) marked by * is clearly visible after hydration. After EIS measurements in Ar the relaxation effects are visible again, while the “hydrated phase” has shifted to lower diffraction angles.

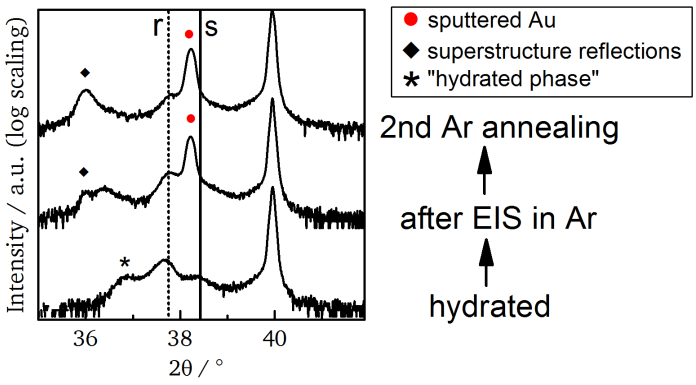

Figure 5.34. Magnified angular range from Figure 5.9, highlighting the “hydrated phase”, which occurred when BFO7 was hydrated.

Further annealing of the sample in Ar causes the “hydrated phase” to completely disappear with the relaxed BFO phase increasing in intensity. It can therefore be concluded that the hydrated phase occurs due the effects of water incorporation and is only visible while water is

retained in the film. During the 2nd annealing in Ar the hydrated phase completely disappears. It follows that the additional hydrated phase might influence the conductivity in BFO7 to some extent, although its phase fraction is small (log scaling in diffractoram). In summary the high conductivity of BFO7 between 300 °C and 400 °C can either be caused by energetically favorable conductive pathways, a higher mobility of the protons along the [111] direction or due to increased water uptake, but most likely by a combination of all effects. Compared to BFO7 and BFO2, the conductivity of BFO9 is low in wet and in dry Ar (see Figure 5.32). Especially between 200 °C and 350 °C, where the proton conductivity was expected to occur, no major indications are visible as compared to BFO7 and BFO2, which both show clear signs of proton conductivity. Even though there is a considerable difference between the conductivity in wet and dry Ar, as is shown in Figure 5.33c, the difference is present over the complete measurement range, indicating a systematic lowering of conductivity as was shown to be the case upon repeated measurements due to Sr diffusion (e.g. comparing Figure 5.24). Therefore a direct comparison between the three sample types is not necessarily significant. However, it is important to notice that for the epitaxial films the proton conductivity could be determined. Moreover it is relevant that the proton conductivity was indeed found to be anisotropic for different substrate orientations.

To conclude the study about the electrochemical behavior of the BFO films it is of importance to correlate the findings presented here with results from previous research conducted on compacted powders of hydrated BFO [21] and on ultrathin films of BFO [115]. When comparing the proton conductivities of the aforementioned samples (displayed in Figure 5.35) certain aspects (experimental and sample related) have to be kept in mind:

1. The compressed powders as well as the ultrathin films were measured using a cryostat in dry Helium atmosphere. Therefore since the measurements were not performed in wet and dry atmospheres, an electronic contribution is possibly present in addition to the ionic conductivity and the determination of the pure protonic contribution was not possible.

2. The second issue with not using a wet measurement atmosphere is that the protonic contribution to the total conductivity might be lowered, because water from the sample is lost faster to the surroundings, due to a larger water pressure gradient.

3. The water incorporation in thin films (determined from the volume expansion) is limited due to the lateral clamping caused by the substrate (see 5.2.1). Therefore and because of the fact that the conductivity σ is directly proportional to the number of charge carriers n (σ~n), the amount of water incorporated into the material must be taken into account when comparing the conductivities of powders to the ones of films.

4. The stress state is different in all of the compared samples. Additionally the compacted powders also differ structurally from the thin films.

5. The experimental setups had different measurement geometries (contact shape, contact materials) leading to a different charge distribution and possibly a different electrode response.

Nevertheless a comparison between the different samples and sample types is useful in order to correlate the different findings and obtain a better understanding of the conductive properties of the material system. An extrapolation of the compacted powder conductivities (Figure 5.35) to a higher temperature (200 °C) results in values, which are comparable to the ones measured on the thin films in this study (taking into account the limited volume expansion – factor 14, see Table 10): σ_{powder} (extrapolated to 200 °C) = 7×10^{-5} S/cm vs. $\sigma_{250\ nm}$(200 °C) × 14 = 1×10^{-5} S/cm. This is an indication that the conductivity values, obtained in the study on compacted powders [21], might have indeed been dominated by the bulk conductivity within the pellet.

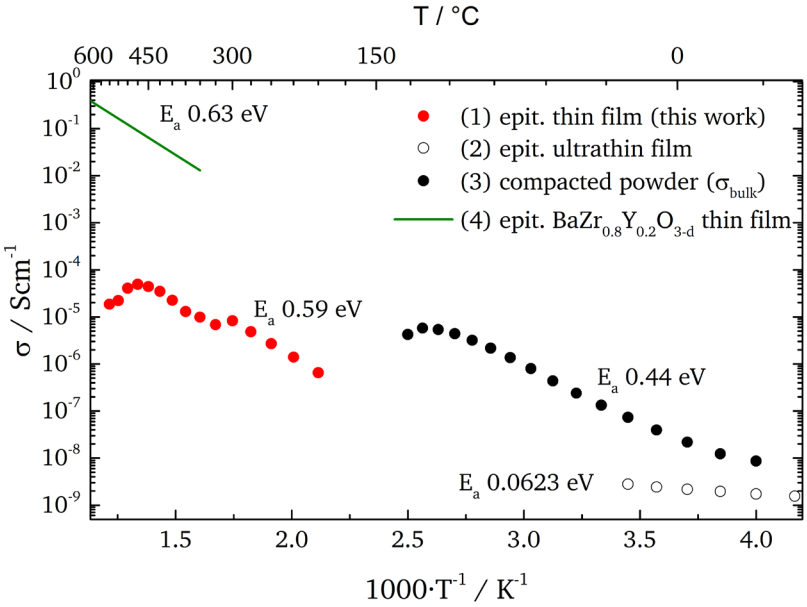

Figure 5.35. Comparison between the electrical conductivity and activation energies of (1) epitaxial BFO thin films on (001)-oriented Nb:STO (hydrated, measured in wet Ar, this work), (2) epitaxial ultrathin BFO films on (001)-oriented Nb:STO (hydrated, measured in dry He, [115]), (3) the bulk contribution of isostatically compacted $BaFeO_{2.33}(OH)_{0.33}$ powder (non-sintered, hydrated, measured in dry He, [21]) and (4) epitaxial $BaZr_{0.8}Y_{0.2}O_{3-\delta}$ thin films on (100)-oriented MgO (measured in wet 5% H_2 in Ar, [40]).

Figure 5.35 also shows that in comparison to all other measurements the epitaxial ultrathin BFO films present the lowest activation energy and conductivity. The much lower conductivity can be explained by the fact that proton transport seemed to be impeded by strong lattice strain, which occurred as a result of the substrate-film lattice mismatch. The activation energy on the other hand is an indication that the charge transport in these films was dominated by an electronic contribution. This electronic contribution was assumed to be caused by oxidative reactions, due to minor oxygen impurities (which weigh stronger for thinner films), leading to mixed Fe oxidation states. Upon comparing the conductivity as well as the activation energy of the ultrathin films with the thicker films deposited in this work it can clearly be stated, that the lattice strain was successfully reduced and that proton transport was enabled.

In order to classify the obtained results for BFO films in the broader context of proton conductors Figure 5.35 also displays the measurement of an epitaxial thin film of $BaZr_{0.8}Y_{0.2}O_{3-\delta}$ [165], which is currently one of the best proton conductors. Although the conductivity of this epitaxial thin film is extraordinarily high (highest proton conductivity in an oxide material to date) and is normally not reached in polycrystalline samples, due to the detrimental effect of grain-boundaries (further information on the effect of space charge in grain boundaries can be found in [113,166,167]), it serves well to set a bar and to compare

bulk conductivities. In the measured temperature range it is obvious that the conductivity of the BFO thin film is still 3 orders of magnitude lower (~2 orders when, considering the limited volume expansion). Even when extrapolating the conductivities of the compacted powder samples to higher temperatures the conductivity is still one order of magnitude lower than the BZY sample. As was previously explained the limited volume expansion related to the clamping effect of the film reduced the possible protonic contribution in this study of BFO films on Nb:STO substrates. The same should also hold true for BZY films but upon closer examination this problem is not as relevant as for the films in this work. The MgO substrate (a=4.21 Å) used for the deposition of BZY thin films matches extremely well with the lattice constant of BZY (a=4.21 Å) and conclusively only causes a minimal lattice mismatch. In addition also the calculated out-of-plane lattice parameter yielded only a minimal deviation (a=4.23 Å). Therefore and due to the fact the in-plane lattice parameter is basically not reduced in any significant way it can be concluded that the BZY thin films remained in an almost stress and strain free condition for the in-plane directions. This stands opposed to the calculations, which were conducted in 5.2.1 for the BFO films (several GPa compressive stress acting on the BFO film in x and y direction), and proves that the limitation on volume expansion is of far greater detrimental influence in this work for the combination BFO film-Nb:STO substrate. However as was already mentioned above, even without any limited volume expansion and stresses acting on the sample, the conductivity of BFO would still be lower as compared to BZY.

A possible explanation might be that the local vacancy ordering, which has shown to be present up to 900 °C [140], leads to different basicities of the ions. This can be visualized in terms of local symmetry lowering of the structure, due to the presence of different oxyen ion sites (oxygen ions are not only part of octahedral coordination but depending on the site might also be involved in tetrahedral coordination). To show the nonequivalence of oxygen ion sites this concept can also be extended in terms of bond valence sums (BVS) as was pointed out in [21]. In principle the above elaborations are valid for bulk powder samples and cannot necessarily be applied to thin films. However, the Mößbauer results suggest a similar distribution of [4]-fold and [6]-fold coordinated Fe, for which reason the application of these concepts is justified. Furthermore as was already pointed out in 2.3.2, empirical observations suggest that protons are easier stabilized in oxides with high basicity. The basicity of the oxygen ion is higher in BZY than in BFO since the atomic radius of Fe^{3+}/Fe^{4+} is smaller than the atomic radius of Zr^{4+} (higher charge density around the oxygen ion). Additionally the difference in electronegativity of the A and B site is smaller for BZY, which has been correlated with high negative hydration enthalpies [61]. The combination of these points indicates that based on the correlations, which are nowadays considered to lead to high proton conductivity, BFO can be expected to exhibit lower conductivities as compared to BZY, as confirmed by this study.

5.8. Summary & Conclusions Chapter 5

In summary, epitaxially grown (001) oriented $BaFeO_{2.5+\delta}$ films (250 nm) were structurally and electrochemically characterized in different atmospheres. Upon hydration an expansion of the out-of-plane lattice parameter of BFO was observed. Aside from examining the oxidation state and local coordination geometries Mößbauer spectroscopy also indicated changes in the local structure of Fe, which are related to uptake of water. Although the structural integrity of the samples was kept intact after undergoing post-deposition treatments and EIS measurements in different atmospheres, examination of the surface by XPS and SEM indicated changes in composition, oxidation state and microstructure. However SEM micrographs also revealed that all films grown on (001)-oriented Nb:STO remained dense and crack-free, making them suitable for examination by EIS. By comparing the conductivity in wet and dry atmospheres a protonic contribution to the total conductivity could be estimated. The protonic contribution, which is present in addition to an electronic contribution stresses that the films investigated here are structurally more relaxed allowing for facilitated proton transport, as compared to ultrathin films [115].

To the best of the author's knowledge this is the first report of bulk proton conductivity in $BaFeO_{2.5+\delta}$ thin films. The corresponding activation energies of all samples measured in wet atmospheres in the temperature range below 300 °C, coincide well with previously reported values on proton transport [11]. The temperature range above 400–500 °C (for samples measured in air) deviates from Arrhenius-like behavior due to a combination of oxidation, Sr diffusion, water loss between 300 °C and 400 °C and possibly due the influence of the EIS measurement itself. The Sr diffusion was investigated by XPS and atom probe tomography. Although XRD indicates that the crystal structure is not affected by this diffusion process a substitution of Ba^{2+} by Sr^{2+} in the form of $Ba_{1-x}Sr_xFeO_{2.5+\delta}$ is likely. The negative effect of Sr incorporation on the total conductivity and the process of hydration was investigated and confirmed by repeated EIS measurements. However for practical applications in SOEC devices the problem of Sr diffusion would not impose a strong problem as long as no Sr containing materials systems are utilized. In that way further investigations could focus on the study of BFO films on different substrates (e.g., $BaTiO_3$) to lower A-cation interdiffusion and allow for a better understanding of film characteristics at higher temperatures.

The directional dependence of conductivity and activation energy was investigated by comparing BFO films grown on (001) and (111)-oriented substrates. The films were grown along the (111) direction following the substrate orientation, without any secondary phases. As opposed to the films deposited on (001)-oriented Nb:STO, the films deposited on (111)-oriented Nb:STO showed effects of relaxation, which manifested in XRD-reflections from a 3x3x3 superstructure, during post-deposition treatments and EIS measurements. Since the EIS measurement for wet and dry atmosphere had to be conducted on the same sample, the proton contribution could not reliably be separated from the total conductivity. Surprisingly, a direct comparison of the absolute conductivities showed that the conductivity of the film, deposited on (111)-oriented Nb:STO, was higher between 300 °C and 400 °C. This was attributed to a combination of energetically favorable conductive pathways, a higher mobility of the protons along the [111] direction or due to increased water uptake by a phase, which was only visible while the film was hydrated. The exact nature of this hydrated phase remained unknown.

The magnitude of the proton bulk conductivity (thin films and compacted powders) was compared to one of the best proton conductors ($BaZr_{0.8}Y_{0.2}O_{3-\delta}$), which is known to date,

showed that the material can be within the range of good proton conductors (when not hindered in volume expansion). As was stated by Merkle et al. the proton conductivity, which was determined here, would suffice ($\sigma_{H^+} \geq 10^{-6}\ Scm^{-1}$) so that the charge transport in a thin film electrode could be dominated by the bulk path and the oxygen reduction reaction could be sufficiently run [158]. In combination with good electronic conductivity BFO could therefore function as an air electrode material or electrode catalyst. Although BFO is known to exhibit good electronic conduction when oxidized [21], the separation of ionic and electronic conductivity remains to be determined. Therefore in a more likely scenario BFO could be combined with another material system, namely $BaCoO_{3-\delta}$, which has recently shown very promising results [168]. $BaCoO_{3-\delta}$ was found to have a much higher conductivity than BFO, which was however determined to mainly be of electronic nature, even though the hydrated phase of $BaCoO_{3-\delta}$ ($BaCoO_{1.80}(OH)_{0.86}$) took up more water than BFO [168]. By investigating aspects of this material class it has become obvious that many more questions need to be answered and many more problems need to be solved. However, there is a large potential for these Ba-containing perovskite-type structures to fulfill the necessary requirements of good electrode catalysts for H-SOFC/SOEC.

6. A Perspective on New Synthesis Techniques for Y-Doped $BaZrO_3$

6.1. Introduction and Motivation

Out of the known proton-conducting solid oxide electrolytes, doped $BaZrO_3$ has been the most promising material due to its exceedingly high proton conductivity, its negligibly small electronic conductivity and its chemical stability towards CO_2 [5,13,40]. As opposed to BFO, the oxygen vacancies, which are necessary for water uptake (proton loading), are created by introducing aliovalent B-site dopants thereby creating charge compensating defects in the form of oxygen vacancies (see equation (2.8)). Literature involving $BaZrO_3$ has studied a wide range of trivalent acceptor-dopants such as Y, In, Gd, Yb, Sc etc [61,169] to determine the highest proton conductivity. In the field of proton conductors $BaZr_{1-x}Y_xO_{3-\delta}$ is one of the most investigated material systems and has shown the highest (bulk) proton conductivity (even significantly larger than the conductivity of the best oxygen-ion conductors, in the investigated temperature range) [40], especially at a doping level of 15-20 mol% Yttrium. However, due to the refractory nature of $BaZrO_3$ (melting point ~2600 °C), processing of powders to form dense large grained pellets is difficult and usually requires very high sintering temperatures ranging from 1500 °C to 1800 °C (up to temperatures as high as 2200 °C [170]) and long sintering times (30 h) [171].

Generally, when Y-doped $BaZrO_3$ is synthesized using solid state reactions at high sintering temperatures (up to 1800 °C), dense but small grained polycrystalline materials with a large area of highly resistive grain boundaries are obtained. These grain boundaries inhibit proton transfer and cause depletion of mobile charge carriers due to the segregation of charged defects, creating a space charge region with a potential barrier [33]. To overcome this problem several approaches and synthesis methods have been studied, with the goal of enhancing grain growth, since conductivity increases with decreasing number density of grain boundaries [172]. One way of enhancing both densification and uniform grain growth at lower sintering temperatures, is the addition of small amounts of sintering aids such as Al_2O_3, Bi_2O_3 and selected first row transition metals such as Zn, Co, Fe or Ti [173]. However the usage of sintering aids goes along with a reduction in conductivity, thus eliminating the advantage over oxygen-ion-conducting oxides. Due to these problems the application of $BaZr_{1-x}Y_xO_{3-x/2}$ as a proton-conducting electrolyte material for SOFC/SOEC is still limited.

One approach, which is proposing to reduce the ohmic resistance of the electrolyte by decreasing its thickness, conclusively leads to the investigation of thin films. The requirements for such films are gas tightness, sufficiently smooth surfaces and as few grain boundaries as possible. Recent approaches working on the deposition of thin films of $BaZr_{1-x}Y_xO_{3-x/2}$ have shown promising results in terms of reducing grain boundary area and electrolyte thickness. A wide variety of thin film deposition methods have proven to produce hundreds of nanometer-thick films of high crystallinity and quality. Namely, thin films of $BaZr_{1-x}Y_xO_{3-x/2}$ have been successfully deposited using physical vapor deposition methods, such as sputter deposition [174,175] and pulsed laser deposition [40,176–178] but also chemical methods such as spray deposition [179–181], chemical solution deposition (spin-coating) [182,183] and chemical

vapor deposition [184]. In this respect the largest proton conductivity reported so far, was measured on a grain-boundary-free epitaxial thin film [40]. Since the aforementioned thin film was deposited using pulsed laser deposition, a technique which is not upscaleable and merely useful on a laboratory basis, many other thin-film deposition techniques are topic of current research. Due to their potential for easy large scale production chemical methods are of special interest. Figure 6.1 shows a general classification of the chemical methods, which can be used to deposit thin films. In this respect this chapter serves as a digression into new thin film deposition methods for $BaZr_{1-x}Y_xO_{3-x/2}$ as an electrolyte material.

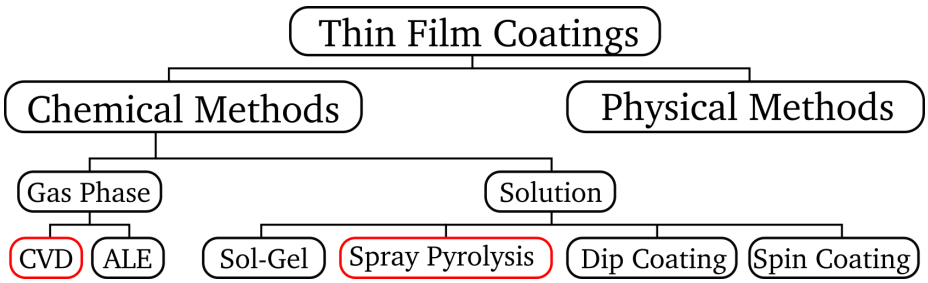

Figure 6.1. Classification of chemical thin film deposition methods. In this work chemical vapor deposition and spray pyrolysis are investigated in more detail.

As a starting point $BaZr_{1-x}Y_xO_{3-x/2}$ was synthesized by conventional solid state reactions in order to obtain reference samples, which could be compared to the thin films. Subsequently several thin film deposition techniques, namely aerosol assisted chemical vapor deposition (pneumatic and ultrasonic atomization), which is an MOCVD-derived spray pyrolysis method, and laser assisted chemical vapor deposition (LA-CVD) were investigated as potentially new possibilities for the deposition of $BaZr_{1-x}Y_xO_{3-x/2}$ thin films. Through the variation of deposition parameters, optimization of the films in terms of structure, composition and microstructure was attempted.

6.2. Synthesis and Analysis of $BaZr_{1-x}Y_xO_{3-\delta}$ Reference Samples

$BaZr_{1-x}Y_xO_{3-x/2}$ powders were synthesized by means of solid state reactions using oxide and carbonate precursors. The method of preparation which was chosen to produce the reference samples involved mixing and milling the precursors in order to decrease the grain size. With smaller initial particle size the final obtained density increases and the grain coarsening is faster due to high surface energy of the particles. Since the composition $BaZr_{0.8}Y_{0.2}O_{2.9}$ was previously found to exhibit the highest proton conductivity [40], this composition in addition to pure $BaZrO_3$ was synthesized as dense pellets and is presented in the following.

Table 19. Sample synthesis parameters for solid state $BaZr_{1-x}Y_xO_{3-x/2}$ pellets. Not all synthesis steps such as milling or grinding are included in this table. For detailed information on the synthesis of samples BZY1 to BZY6 see 4.4.

Sample Name	Y-doping content	Calcination temperature / °C	Sintering temperature / °C	$\frac{\rho_{geo}}{\rho_{theo}}$ / %	a / Å (±0.001 Å)
BZY1	5 mol%	1300 (12 h)	1500 (15 h)	69	
BZY2	5 mol%	1300 (12 h)	1550 (15 h)	78	
BZY3a	5 mol%	1300 (12 h)	1600 (15 h)	81	
BZY3b	5 mol%	1300 (12 h)	1600 (15 h)*	81	
BZY4	0 mol%	1300 (12 h)	1700 (15 h)*	90	4.192
BZY5	10 mol%	1300 (12 h)	1700 (15 h)*	85	4.196/4.216
BZY6	20 mol%	1300 (12 h)	1700 (15 h)*	90	4.223

* samples were covered in $BaZrO_3$ powder to prevent BaO evaporation

Initially BZY1 to BZY3 were calcinated at 1300 °C for 12 h and then pressed into pellets. As was already mentioned in 6.1 the refractory nature of $BaZrO_3$-based ceramics leads to the necessity of high sintering temperatures. To observe the change in density and grain growth BZY1 to BZY3 were sintered at temperatures ranging from 1500 °C to 1600 °C for 15 h. As expected the density (geometrical density) increased with increasing temperature, as is listed in Table 19. With increasing sintering temperature the color of the pellet changes noticeably from a very light to a dark green, as can be seen in Figure 6.2.

Figure 6.2. BZY (5 mol%) pellets sintered at a) 1500 °C (left side) b)1550 °C (middle) and 1600 °C (right side) in atmospheric air.

This indicates that a surface reaction is taking place. Literature has commonly reported that BaO evaporation is the cause of these surface changes during sintering at high temperatures, leading to a Ba deficiency. The resulting vacancy formation on the A-sites of the ABO_3 perovskite structure then preferably allows dopant substitution on the A-site according to [185,186]

$$2Ba_{Ba}^{x} + Y_2O_3 + V_O^{\bullet\bullet} \Leftrightarrow 2Y_{Ba}^{\bullet} + O_O^{x} + 2BaO\uparrow \qquad (6.1)$$

In terms of conductivity this would lead to a drop in the protonic contribution because the oxygen vacancies are reduced and less water can be incorporated into the material.

Structurally the Ba-deficiency has been known to cause the formation of YSZ and $BaZrO_3$ impurity phases. For these reasons the loss of Ba has to be avoided during sintering. A workaround that is commonly applied to prevent the evaporation of BaO involves the covering of pellets in calcinated $BaZrO_3$ powder. Alternatively the surface layer can be removed mechanically until no further impurity phase is detected by XRD. Figure 6.3 displays the diffractograms of BZY3a and BZY3b. BZY3a was sintered in air without being covered by additional powder. As a result several reflections, which resemble YSZ can be attributed to a Ba-deficient phase.

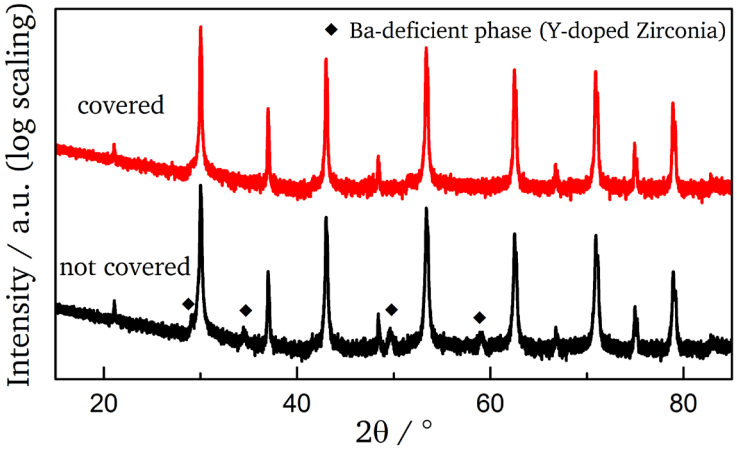

Figure 6.3. BZY (5 mol% Y) pellets sintered at 1600 °C in air. BZY3b was covered in $BaZrO_3$ powder to prevent BaO evaporation. BZY3a was not covered and showed a Ba-deficient phase (Y-doped Zirconia) after sintering.

BYZ3b on the other hand was covered with a mixture of $BaZrO_3$ and $BaCO_3$. Clearly the diffractorgram of BYZ3b (Figure 6.3) does not show any signs of an impurity phase but rather phase pure cubic Y-doped $BaZrO_3$. The following samples (BZY4 to BZY6) were therefore all covered with the same mixture of $BaZrO_3$ and $BaCO_3$ during sintering. The sintering temperature was set to 1700 °C, which yielded densities (ρ_{geo}/ρ_{theo}) between 85 % and 90 % as listed in Table 19.

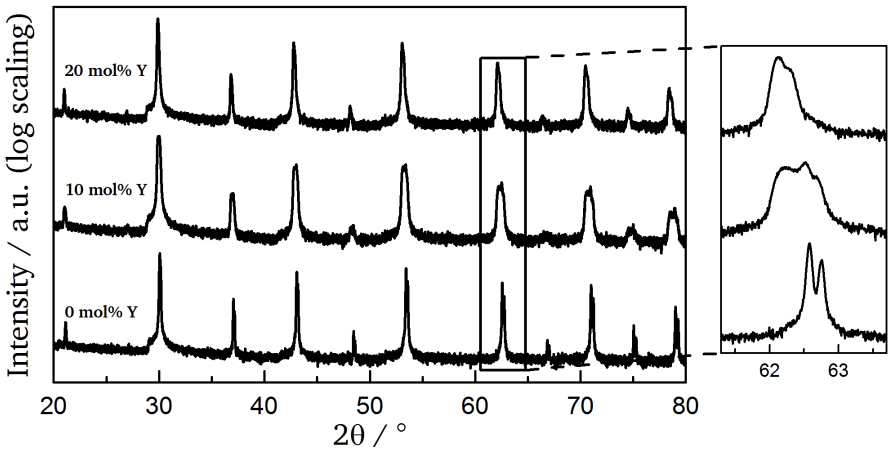

Figure 6.4. X-Ray diffractograms of BZY4 (0 mol% Y_2O_3), BZY5 (10 mol% Y_2O_3) and BZY6 (10 mol% Y_2O_3) sintered at 1700 °C.

The diffractograms in Figure 6.4 show that with increasing Y-content the lattice parameter increases from 4.192 Å (0 mol% Y_2O_3) to 4.223 Å (20 mol% Y_2O_3) as was to be expected, due to the higher ionic radius of Y^{3+} (90 pm) as compared to Zr^{4+} (72 pm) [185]. However sample BZY5 (10 mol% Y_2O_3) does not present a single phase but rather two cubic perovskite

phases with lattice parameters of 4.196 Å and 4.216 Å. As the excerpt in Figure 6.4 already leads to believe, instead of a single phase material of BZY with 10 mol% Y_2O_3, a mixture of undoped and more strongly doped BZY (similar to 20 mol% Y) is present in sample BZY5. Upon examination of the micrographs in Figure 6.5, it can be confirmed that also from a microstructural point of view BZY5 shows two phases, whereas BZY4 and BZY6 only display a single phase. Furthermore the micrographs of BZY5 (Figure 6.5c,d) also confirm the lower density, which was estimated to be 85 %, as opposed to BZY4 and BZY6 (both 90 %).

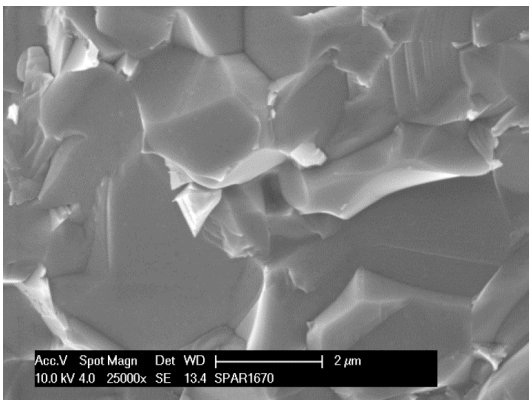

a) BZY4 (0 mol% Y_2O_3) cross-section

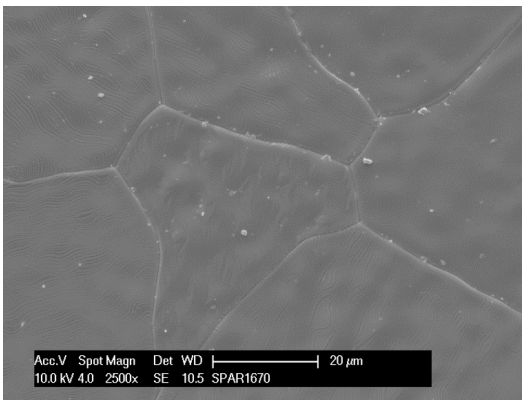

b) BZY4 (0mol% Y_2O_3) surface

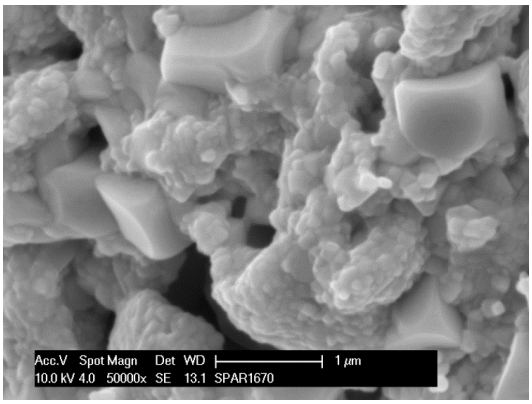

c) BZY5 (10 mol% Y_2O_3) cross-section

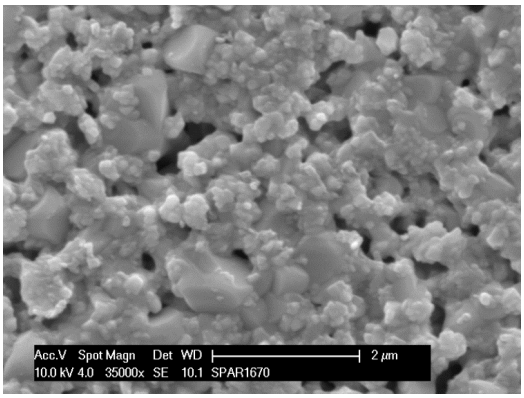

d) BZY5 (10 mol% Y_2O_3) surface

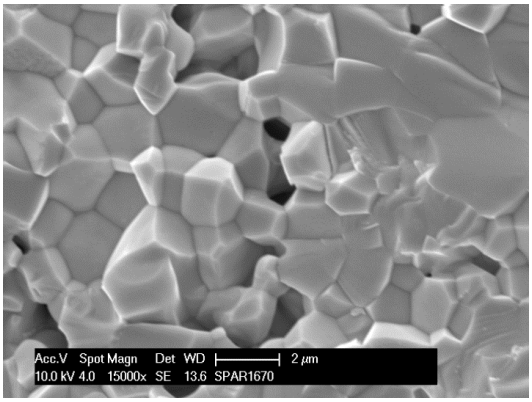

e) BZY6 (20 mol% Y_2O_3) cross-section

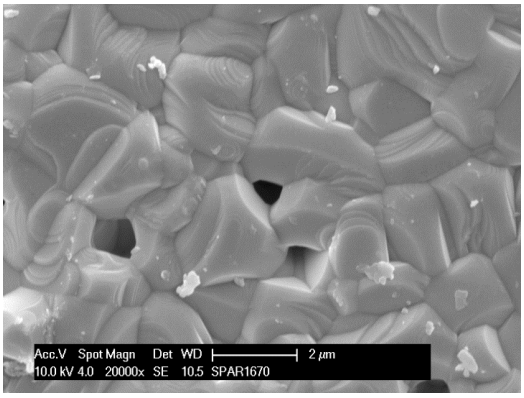

f) BZY6 (20 mol% Y_2O_3) surface

Figure 6.5. SEM micrographs, showing the microstructure of cross-section and surface of samples a,b) BZY4 c,d) BZY5 and e,f) BZY6.

Macroscopically all three samples were clearly distinguishable as is shown in Figure 6.6. Upon breaking all pellets revealed the same color as on the surface, confirming that no surface layers were present (as was already expected from the diffractograms in Figure 6.4).

Figure 6.6. BZY pellets sintered at 1700 °C with 0 mol%, 10 mol% and 20 mol% of Y-doping

In summary it can be concluded that the reference samples of pure $BaZrO_3$ and $BaZr_{0.8}Y_{0.2}O_{2.9}$ (20 mol% Y_2O_3) were successfully synthesized as dense and single-phased pellets. $BaZr_{0.9}Y_{0.1}O_{2.95}$ (10 mol% Y_2O_3) could not be synthesized in a single phase but instead contained two cubic perovskite phases. However this composition was not intended to be used further in terms of reference sample for thin films, because the maximum conductivity was expected to be measured for 20 mol% Y-doping.

6.3. Laser-Assisted Chemical Vapor Deposition

6.3.1. Advantages of LA-CVD and Selection of Precursor Materials

As was introduced in 6.1, the idea of investigating new methods for the deposition of $BaZr_{1-x}Y_xO_{3-\delta}$ has become a popular subject of research in recent years. Among the published literature articles only very few have successfully produced $BaZrO_3$ and Y-doped $BaZrO_3$ by chemical vapor deposition, which is mainly due to the thermal instability and low vapor pressures of certain precursors (e.g. Ba, Sr and rare earth metals [187]). However chemical vapor deposition and especially metal-organic chemical vapor deposition offer a number of useful advantages as compared to physical vapor deposition methods. While physical vapor deposition techniques usually produce very high quality films, they are rather limited to laboratory-scale production.

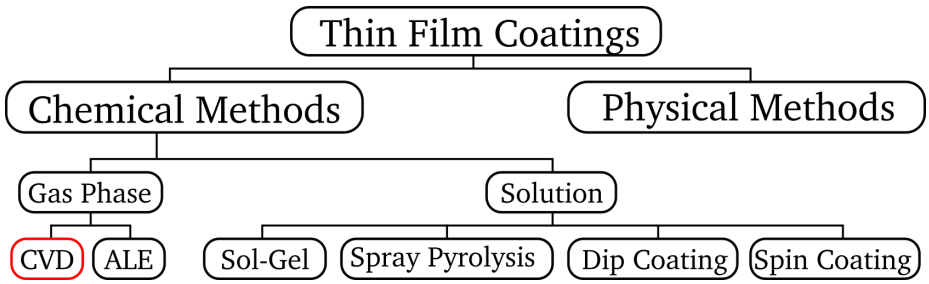

Figure 6.7. Classification of chemical thin film deposition methods. Metal-organic chemical vapor deposition, a subgroup of classical chemical vapor deposition is used for thin film deposition in this chapter.

Moreover the precursor reactions in CVD can be arranged to be more selective in terms of location, favoring deposition only in certain regions of the substrate and at the same time cover rough surfaces uniformly (according to the morphology of the substrate). With the purpose of tackling the problems of conventional CVD, such as high heat load and low precursor vapor pressure, a new precursor delivery method, namely CO_2 laser-assisted chemical vapor deposition, has recently provided promising results [188–190]. LA-CVD exploits the fact that selected metal-organic precursors (i.e. the organic groups) absorb energy in the micrometer range of the electromagnetic spectrum (CO_2-Laser wavelength: 10.6 μm) and can thereby be evaporated simultaneously at comparatively low temperatures ($\sim$ 150 °C). Apart from common factors, which play a role in precursor selection, such as stability (during evaporation and towards air/moisture), adequate decomposition behavior (sufficiently large temperature window between evaporation and decomposition) low toxicity and cost, the focus was put on the precursor's ability to absorb energy and evaporate (low volatility) in the required spectral range [191].

In Figure 6.8 the transmittance of the tested metal-organic precursors is plotted over the spectral range in question, using. The grey bar indicates the range around which the CO_2 laser causes excitation (details about the operating principle of a CO_2 laser as well as the underlying physics can be found elsewhere [192,193]). Most of the precursors show a local minimum in transmittance, within the excitation range of the CO_2 laser, meaning that absorption and subsequently evaporation of the precursor is possible. Using the values of transmittance obtained from the local minima, the evaporation rates of the different precursors could in theory be calculated with respect to each other. However this might not necessarily be correct to the exact extent for the material amounts arriving at the substrate,

which is why empirical adjustments and optimization, not only of the process parameters but also of the precursor ratios are necessary.

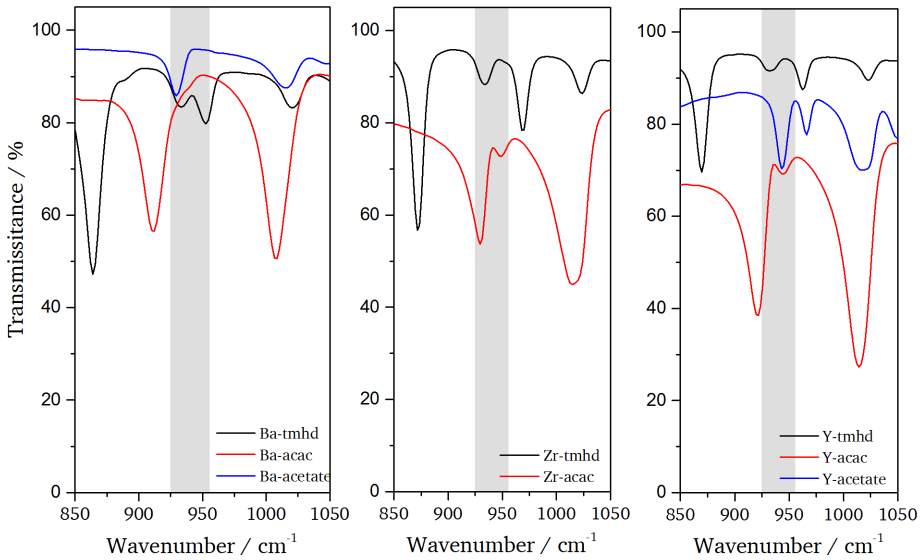

Figure 6.8. FTIR spectra of several different metal-organic precursors used for film growth in LA-CVD setup. The grey bar indicates the excitation range of the CO_2-laser.

Two of the metal-organic precursors, which were investigated in terms of absorption behavior in Figure 6.8, are metal β-diketonates. This class of compounds meets most of the above mentioned criteria such as low volatility and stability. In contrast to other classes such as alkyls they can be handled with ease, due to low toxicity. Most importantly however their chemical and physical properties can be tailored by adapting the functional groups [191]. In Figure 6.9 the β-diketonates, which are used in this project, are displayed with R_1 and R_2 representing the functional groups. When replacing R_1 and R_2 with the respective ligands 2,4-pentanedionate (acetylacetonate, acac) and 2,2,6,6-tetramethyl-3,5-heptanedionate (tmhd) are obtained. A third type of precursor, Barium/Yttrium acetate, was tested in addition, but was rather added for the purpose of comparison at this point.

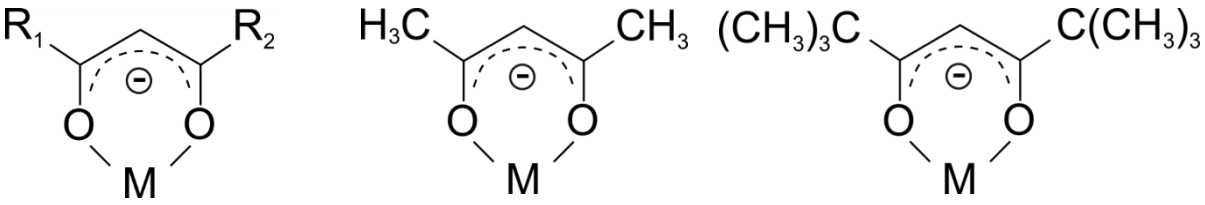

a) Metal (M) β-diketonate **b) Pentane-2,4-dionate (acetylacetonate, acac)** **c) 2,2,6,6-tetramethylheptane-3,5-dionate (thmd)**

Figure 6.9. a) General chemical structure of a metal (M) β-diketonate with the substituents R_1 and R_2 (representing functional groups). R_1 and R_2 highly influence the the properties of the precursor. b) Pentane-2,4-dionate, also called acetylacetonate (acac), where R_1 and R_2 replaced by methyl groups. c) 2,2,6,6-tetramethylheptane-3,5-dionate (tmhd), where R_1 and R_2 are replaced by tert-butyl groups.

The good volatility of the above mentioned precursors in conjunction with the low thermal load, to which the precursors are exposed during irradiation by the CO_2 laser (only a small portion of precursor is exposed to local heating), should enable a continuous and controllable delivery rate of stable precursor molecules to the reaction zone. Furthermore this implies that as opposed to thermal evaporation in conventional CVD the process of evaporating is less

selective in LA-CVD and provides an important improvement in delivering undecomposed precursor molecules to the substrate. The most crucial advantage however is that all solid precursors can be evaporated simultaneously, because the evaporation rate does not depend on the vapor pressures but instead on absolute absorbance and evaporation temperature. Summing up LA-CVD can potentially alleviate major problems of conventional CVD and therefore provide a reasonable basis for the deposition and investigation of $BaZr_{1-x}Y_xO_{3-x/2}$ thin films. All of the precursors, which were tested in terms of their transmittance in Figure 6.8, were also used to deposit films. However, for the purpose of this thesis only the most important results are presented in the following chapter, which include only the following precursors:

Table 20. Precursor materials used for BZY film deposition in chapter 6.3.

Precursor	Supplier	Purity
$Ba(acac)_2 \bullet 2H_2O$	Sigma Aldrich	98.0
$Zr(acac)_4$	Sigma Aldrich	97.0
$Y(acac)_3 \bullet H_2O$	Sigma Aldrich	99.9

6.3.2. Optimization of Thin Films of $BaZrO_3$

In order to establish a basis for the various deposition parameters the simpler system of $BaZrO_3$ was targeted in the beginning. The parameters, which are specific to the experimental setup and not of utmost importance in the beginning, (e.g. temperature in various parts of the setup, gas flow rates or rotation speed of the precursor plate) are not discussed here because they were not varied in the present chapter (see 4.2 for experimental setup). Although investigated, the influence of two parameters, namely CO_2 laser power and pressure within the chamber, is not further elaborated in this thesis, since the results proved to be of minor relevance. The process parameters, which were extensively varied to obtain stoichiometric thin films with the correct structure, were substrate temperature and the ratio of mixed precursors (excess of Ba and Y, ie the deviation from stoichiometric mixing ratio). Table 21 lists the thin film samples (including several sample details), which were deposited and examined in this chapter. For the first deposition standard parameters, which were established for other materials systems [190], were used for chamber pressure (5 mbar), CO_2 laser power (28 W), gas flow rates and substrate temperature. (100)-oriented Si substrates were used for all samples unless stated otherwise. In terms of precursor ratio it was reported in previous investigations that Ba is required in excess of the stoichiometric composition in the precursor mixture (Ba:Ti – 4:1) [194,195] during laser assisted chemical vapor synthesis. A starting ratio of Ba to Zr precursors of 2:1 was chosen (BZY7) as a starting point.

Table 21. Deposition parameters for $BaZrO_3$ thin films deposited using LACVD. Precursor excess refers to the precursor that was added in excess of the stoichiometric ratio. All samples were deposited on (100)-oriented Si substrates. Additional deposition parameters can be found in experimental details in 4.2.

Sample	Precursor ratio (Ba/Zr)	Target composition	Substrate temperature (deposition) / °C	Phase fraction $BaZrO_3$ / %
BZY7	2.0 (100 % Ba excess)	$BaZrO_3$	700	77
BZY8	1.7 (70 % Ba excess)	$BaZrO_3$	700	89
BZY9	1.5 (50 % Ba excess)	$BaZrO_3$	700	96
BZY10	1.2 (20 % Ba excess)	$BaZrO_3$	700	98

The structural refinement, which was subsequently performed on BZY7 and is resolved in more detail in Figure 6.10b, clearly shows that several phases are present in addition to the cubic perovskite phase of $BaZrO_3$ (77 % phase fraction). $BaCO_3$, which would be expected in the case of too much Ba precursor, was detected as well as ZrO_2 and ZrO. Therefore the Ba to Zr ratio in the precursor mixture was successively reduced in the following depositions. With decreasing Ba:Zr ratio the amount of impurity phases also decreased until at Ba/Zr 1.2 (BZY10), only a minor amount of impurity phase remained. As opposed to the results for $BaTiO_3$ the excess of Ba precursor is lower, even close to the stoichiometric ratio. As is shown in Table 21 the $BaZrO_3$ phase fraction of BZY10 is very close to 100 %, making the film almost phase pure. Therefore, following the structural characterization of BZY7 to BZY10 the surface of BZY10 was examined using XPS (the XPS spectra can be found in Figure A 1). Within the accuracy limits of the technique (10 % - 20 %), the ratio of Ba/Zr was found to be close to the expected ratio of 1:1 for stoichiometric $BaZrO_3$ (19 atm% Ba to 18 atm% Zr) with minor amounts of $BaCO_3$.

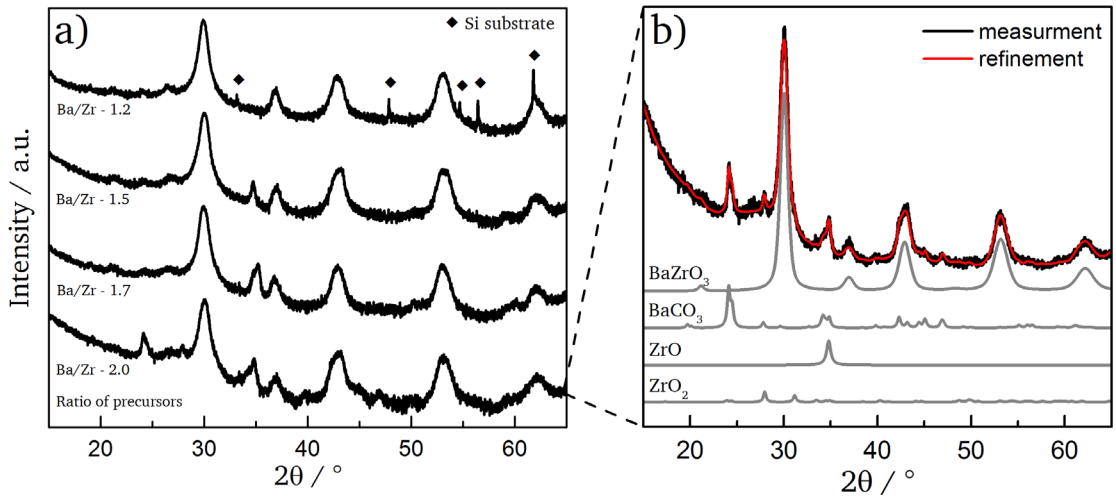

Figure 6.10. X-ray diffractograms of a) BZY thin films with different initial precursor ratios ranging from Ba/Zr – 2.0 (BZY7) to Ba/Zr – 1.2 (BZY10). Si substrate reflections are indicated by w Additionally the refinement of BZY7 including the different phases is shown in b). In a) log(x) was applied to the intensity values to better show the low intensity features. Subsequently all spectra in a) were normalized and plotted.

Although the structure and ratio of Ba/Zr were verified to be conformal with solid state $BaZrO_3$ the scanning electron micrographs in Figure 6.11 show that the morphology was not optimized yet. The film can be estimated to have an approximate thickness of 2 μm. No surface roughness measurements were performed but judging by the micrographs the cauliflower-like structures on the surface are of varying size. Since the film is neither dense nor has a homogeneous smooth surface the morphology is still unfit for electrochemical investigation. Due to time constraints, the morphology of undoped $BaZrO_3$ was not further optimized but instead Y-doped $BaZrO_3$ films (BZY11-BZY18) were investigated in the following.

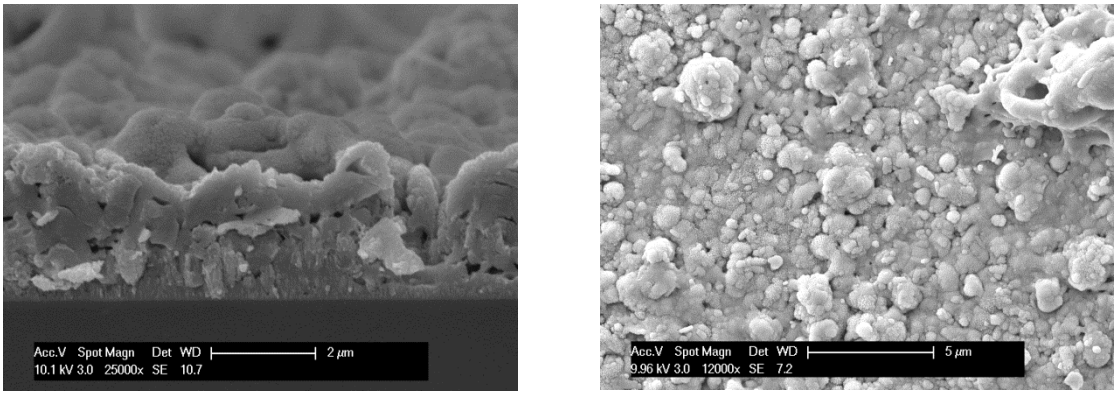

a) BZY10 (Ba/Zr – 1.2) cross-section **b) BZY10 (Ba/Zr – 1.2)**

Figure 6.11. SEM micrographs, showing the microstructure of a) the cross-section and b) the surface of BZY10.

However the investigations on BZY7-BZY10 showed that undoped perovskite type $BaZrO_3$ could be successfully deposited with correct stoichiometry using LACVD (with a Ba excess of 20 % in the precursor mixture). Due to the difference in absorbance of the different precursor materials (shown in Figure 6.8) the precursor ratio is likely to change, when adding $Y(acac)_3$ to the precursor mixture. A first attempt to deposit $BaZr_{0.9}Y_{0.1}O_{2.95}$ by using a similar precursor ratio as for pure $BaZrO_3$ proved to be unsuccessful. The initial precursor ratio was chosen, based on the optimal Ba/Zr ratio of 1.2 (BZY10). Since for the deposition of BZY there are

three precursors involved the concept of precursor ratios is unpractical. For this reason the relative precursor amounts, which were used for the following samples, are presented in terms of excess of the stoichiometric composition. E.g. the precursor ratio of Ba/Zr of 1.2 would correspond to 20 % of Ba excess.

Therefore, the initial precursor mixture used for the deposition of Y-doped $BaZrO_3$ contained a Ba excess of 20 % and an Y excess of 10 %. Figure 6.12 displays the influence of adding $Y(acac)_3$ to the precursor mixture in order to obtain Y-doped $BaZrO_3$. The resulting structure shows no traces of the expected cubic perovskite structure but instead an almost pure Y-doped ZrO_2 phase. XPS confirmed that only minimal amounts of Ba could be found on the film surface.

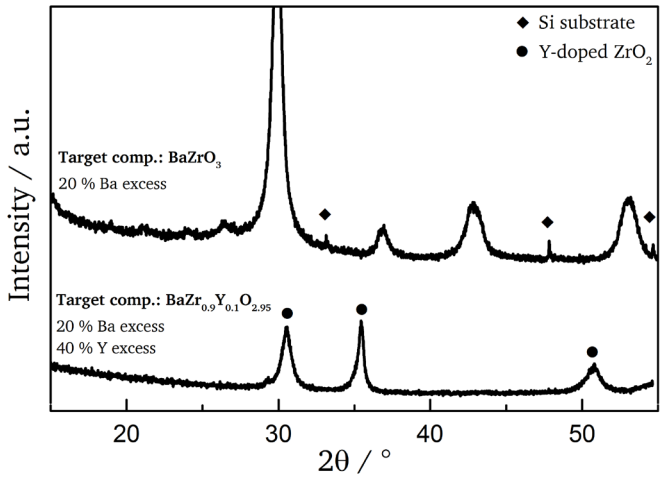

Figure 6.12. Comparison of optimized $BaZrO_3$ (BZY10) with 20 % Ba excess in the precursor mixture, and $BaZr_{0.9}Y_{0.1}O_{2.95}$ (target composition) containing 20 % Ba excess and 10 % Y excess (BZY11) in the precursor mixture. Substrate reflections are marked by Wand the Y-doped ZrO_2 phase by •. Both samples were deposited under the same process conditions.

Based on the obtained structure and the absence of Ba on the film surface it seems that the addition of $Y(acac)_3$ to the precursor mixture impedes the incorporation of Ba during the film formation. It is well known that Ba, Sr and rare earth metal precursors possess low vapor pressures and therefore require high vaporization temperatures (~200 – 250 °C). This however is not likely to be the problem here because the evaporation rate proved to be sufficient for pure $BaZrO_3$. Consequently, in order to obtain stoichiometric films of $BaZr_{0.9}Y_{0.1}O_{2.95}$ the Ba excess was increased successively. Although many samples are not shown or named in this thesis because they provided no additional useful information (adjusting the precursor ratios), Table 22 lists the most important samples. The Ba excess was increased (along with the Y excess) from 20 % (BZY11) up to 460 % (BZY16). Samples BZY12 to BZY16 turned out to be close to the optimal precursor ratio. In fact BZY13 and BZY15 showed the best results, even though the precursor ratios differed slightly. The respective diffractograms with varying precursor ratio are shown in Figure 6.13a. The refinement of BZY13, which also displays the individual phases present in the film, is magnified in Figure 6.13b.

Table 22. Deposition parameters for Y-doped $BaZrO_3$ thin films deposited using LACVD. Precursor excess refers to the precursor that was added in excess of the stoichiometric ratio. All samples were deposited on (100)-oriented Si substrates. Additional deposition parameters can be found in the experimental details section 4.2. Phase fractions were only determined for relevant samples (diffractograms in Figure 6.13).

Sample	Precursor excess / %		Target composition	Substrate temperature (deposition) / °C	Phase fraction $BaZrO_3$ / %
	Ba	Y			
BZY11	20	10	$BaZr_{0.9}Y_{0.1}O_{2.95}$	700	-
BZY12	380	250	$BaZr_{0.9}Y_{0.1}O_{2.95}$	650	85
BZY13	390	250	$BaZr_{0.9}Y_{0.1}O_{2.95}$	650	92
BZY14	400	250	$BaZr_{0.9}Y_{0.1}O_{2.95}$	650	64
BZY15	420	300	$BaZr_{0.9}Y_{0.1}O_{2.95}$	650	93
BZY16	460	320	$BaZr_{0.9}Y_{0.1}O_{2.95}$	650	61
BZY17	390	250	$BaZr_{0.9}Y_{0.1}O_{2.95}$	550	-
BZY18	390	250	$BaZr_{0.9}Y_{0.1}O_{2.95}$	600	-
BZY19	390	250	$BaZr_{0.9}Y_{0.1}O_{2.95}$	700	-

The phase fraction of, which can be attributed to the cubic perovskite phase of $BaZrO_3$, has an overall volume fraction of 92 % and a lattice parameter of 4.22 Å. This lattice parameter is similar to the values, which were obtained for the samples in 6.2 (solid state synthesis) and is therefore an indication that Yttrium was successfully incorporated into the film. Further variation of the precursor ratio did not lead to a single phase film of $BaZrO_3$.

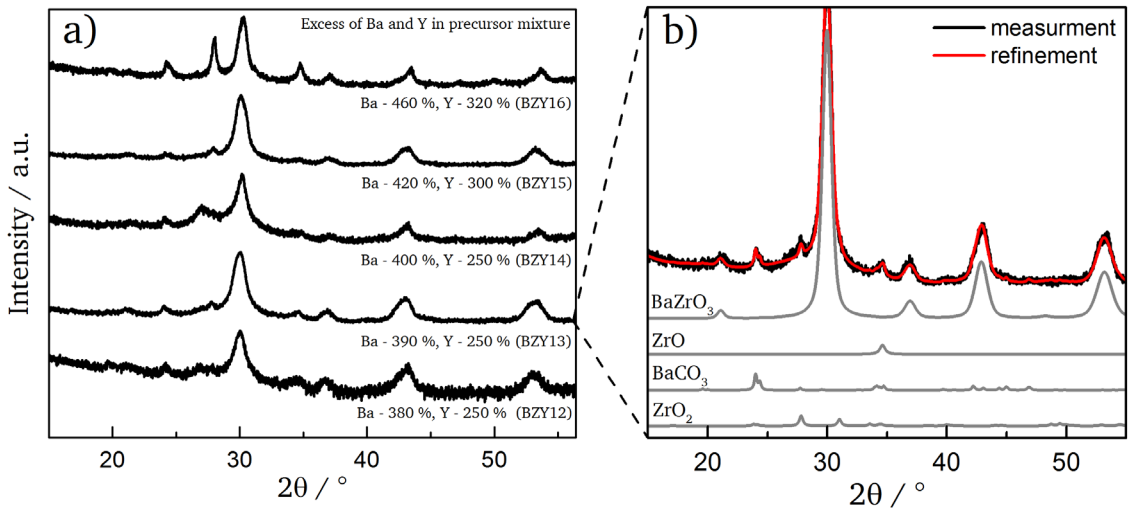

Figure 6.13. X-ray diffractograms of a) BZY thin films with different initial precursor ratios. Additionally the refinement of BZY13 including the individual phases is shown in b). The deposition temperature was kept constant at 650 °C for all samples.

Similarly a modification of the deposition temperature did not improve any structural features. As is apparent from the diffractograms in Figure 6.14, a lowering of the substrate temperature leads to an amorphous or partially amorphous crystal structure. Increasing the substrate temperature on the other hand only leads to the formation of an Y-doped ZrO_2 phase. Conclusively a variation of precursor ratio and substrate temperature did not result in a pure and single-phase of Y-doped $BaZrO_3$ for any of the examined samples.

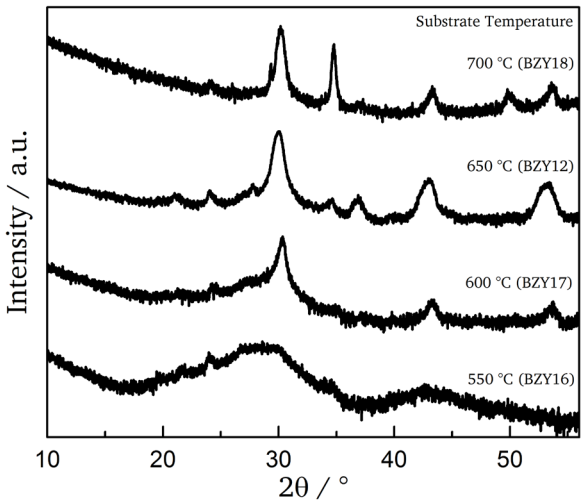

Figure 6.14. X-ray diffractograms of a) BZY thin films with initial precursor ratios of 380 % Ba excess and 250 % Y excess. The deposition temperature was varied between 550 °C and 700°C.

The reasons why the Y-doped $BaZrO_3$ could not be deposited are therefore more complex than changing the composition of the precursor mixture or the substrate temperature. A closer investigation of the films proved that the phase distribution was very inhomogeneous. Macroscopically, all deposited films present with a white spot/streak, indicating that an unusually high amount of precursor deposits at this location. To examine the white spot BZY12 was cut into two pieces, so that the white powdery deposition could be separated. Diffractograms of both pieces were recorded, as indicated in Figure 6.15.

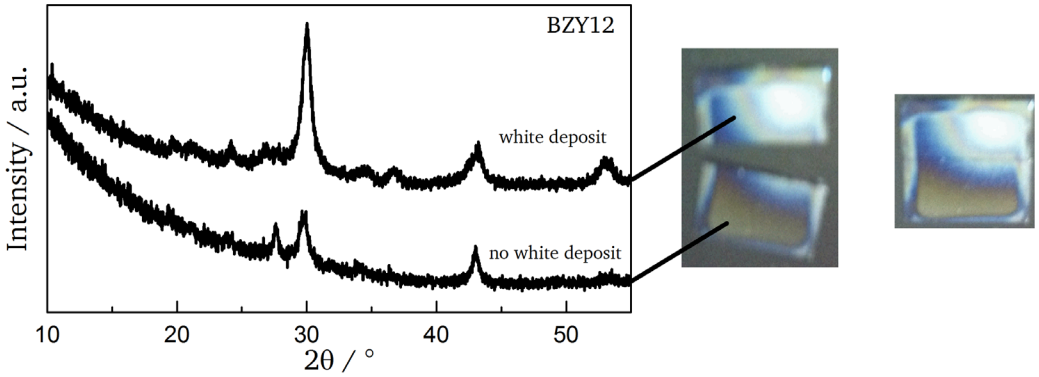

Figure 6.15. X-ray diffractograms of BZY12 broken into two pieces. The two separate pieces (one containing the white spot) are displayed on the right.

The structural differences are drastic, proving that the desired cubic perovskite phase is mostly deposited on the part of the sample, which includes the white spot. The thin film, which is deposited on the side, that does not include the macroscopic deposit, shows the same reflections but with lower intensity. Yet, the surface analysis indicated that across this part of the substrate only small amounts of Ba were present as compared to large amounts of Zr and Y. Therefore the distribution of the perovskite phase across the substrate is very inhomogenous and mostly related to the white deposit. The phenomenon of this white streak/spot-like deposit is suspected to be caused by solid precursor molecules, which are dragged along into the gas phase and to the substrate during the laser evaporation process. Loho et al. found that the amount and occurrence of the white streak depends on the precursor materials and the material system, respectively [196]. E.g. in the case of $LiCoO_2$ no such feature was observed but in the case of $Li_7La_3Zr_2O_{12}$ [196] a white streak-like feature

occurred. Although the detailed mechanism and origin are unknown, a number of possible solutions to remove this feature were suggested and tested [196]. However this investigation (involving physical changes to the LA-CVD setup) were only conducted after the experiments presented in this thesis were already concluded and could therefore not be tested for the BZY material system due to time constraints.

To assess if any of the films, deposited in the investigation at hand, can be useful for the further investigations by EIS, the morphology was investigated using SEM (Figure 6.16). It is important that the microstructure and morphology of the films are dense with a smooth and homogeneous surface (in terms of structure and composition). These attributes are of absolute necessity for the electrochemical investigation of the BZY films because a number of problems are encountered, if these criteria are not met. Namely, high porosity, uneven thicknesses and other undesired surface attributes (outgrowths, sintering necks) could lead to short circuits, bad electrical contact and high local impedances. In addition it would be very difficult to find and analyze meaningful equivalent circuit models for the interpretation of this measurement data. Therefore even though some parts of the films contain the correct phase and a closer examination of general film morphology is needed.

Figure 6.16 displays a photograph of BZY13, displaying a streak-like white pattern across the middle part. In order to examine the morphology across various locations of the film the characteristic sample was broken into two parts along the red line. The SEM micrographs in Figure 6.16 show cross-sections and the surface at different locations of the sample. Location 2 and 4 are representations for the morphology and microstructure around and on the white streak.

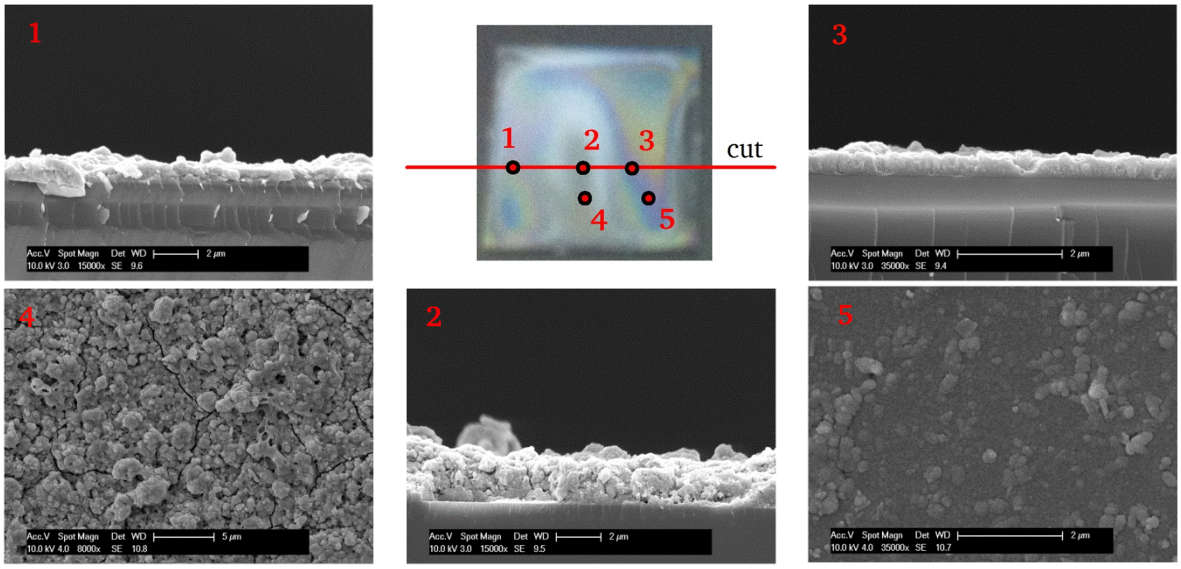

Figure 6.16. SEM micrographs of BZY13 recorded at different locations of the sample, indicated by numbers. The sample was cut along the red line and micrographs of the surface were recorded at locations 4 and 5. Cross-sections were recorded at locations 1, 2 and 3.

The cross-section shows that the deposit is not a well-connected film, but instead shows great porosity. Additionally the surface is cracked and contains a large amount of differently sized irregular shapes. These observations lead to the conclusion that the white deposit is most-likely caused by solid precursor hitting the substrate and subsequently reacting to form powdery particles, which agglomerate afterwards. The micrographs recorded at positions 2, 3 and 5 display the microstructure next to the white deposit. Micrograph 3 shows that away from the white deposit a film with a dense and continuous microstructure is deposited.

Similarly the features on the surface are less numerous and without any visible cracks. The microstructure as it was found around the white deposit is well suited for further investigation of the films. However, as was shown in Figure 6.15 the desired structure would only form within the deposit therefore creating a discrepancy. On the one hand the white deposit reacts to form the correct phase and stoichiometry but on the other hand the film's microstructure and morphology are not suitable. Since variation of different parameters such as temperature, precursor composition, total pressure and oxygen partial pressure did not lead to meaningful improvements concerning the above mentioned problems, no further investigation was conducted using LA-CVD. Due to the non-ideal morphology and phase distribution the films were found to be completely unsuited for a further examination by impedance spectroscopy.

In the following the possible reasons for the problems of BZY formation and microstructure will be elaborated and examined. In light of the obtained results the problems can be divided into several problem categories, which might have different origins:

1) **Inhomogeneous film deposition:** Reasons for the inhomogeneous deposition of the film, with a streak-like deposit are likely to be found in the gas flow and the precursor delivery, respectively. In general the gas flow pattern is of immense importance for the uniform growth of films, especially at high pressures since the mean free path of the gas molecules and thereby the diffusivity increases, causing better intermixing of the precursor molecules. The gas flow behavior can be categorized into two different regimes, which are defined by the Reynolds number R_e (in a tube with diameter D)

$$R_e = \frac{\rho u D}{n} \tag{6.2}$$

where ρ is the mass density of the gas, u the variation in axial flow velocities and n the coefficient of viscosity of the gas. A high Reynolds number (>2000) is said to cause an irregular flow pattern, which is called turbulent. Since turbulent flow causes particular problems in CVD, high pressures and high gas flow velocities have to be avoided. At lower Reynolds numbers (<1000) the flow can occur in a smooth layered manner and is therefore termed laminar. Normally commercial CVD reactors have very low Reynolds numbers (<100). The probability of inducing turbulent flow increases when changes in gas velocity occur, e.g. by sudden changes in tube diameter (at the beginning and the end of tubes).
The white streak-like deposit, which is believed to be formed due to unreacted precursor being dragged along during the evaporation process, may be a result of non-laminar flow and could therefore be reduced using common methods used for turbulent flow reduction, such as honeycomb structures or screen meshes. It was shown by Loho that porous sintered stainless steel microsieves (Tridelta Siperm GmbH) can be mounted inside the Al_2O_3 tube in front of the sample holder (Figure 4.3) and improve the film quality by blocking the solid precursors and homogenizing the gas flow [196]. The films, which were obtained using the microsieve, did not show the white streak and proved to be an effective solution. However, this solution could not be tested in the frame of this thesis.

2) **Different microstructures and morphology in white streak-like deposit and surrounding film:** As was explained in 1) the inhomogeneous gas flow in combination with unreacted precursor reaching the substrate surface might lead to uneven film

growth and during longer film depositions to a macroscopically visible white streak-like deposit. It was found (see Figure 6.16) that the surrounding film and the white streak-like deposit show very different microstructures and morphologies. The morphology of the deposit is clearly influenced by the amount of material arriving at the specific location of the substrate. On the one hand not all of the solid precursor, which is dragged along towards the substrate might already have completely reacted and broken up into small enough pieces when deposited, so that diffusion and redistribution of the atoms cannot occur fast enough. On the other hand the solid precursor particles, hitting the substrate, are bound to impede the deposition and shadow other parts of the substrate, thereby causing a porous film as shown in Figure 6.11 and Figure 6.16.

3) **Different structures and composition within deposit and surrounding film:** In addition to the inhomogeneous film deposition discussed in 1) and the different morphologies of the streak-like powdery deposit and surrounding film discussed in 2) the structural analysis showed that the white deposit contained large fractions of $BaZrO_3$ while the surrounding film was Ba deficient and only contained Y-doped ZrO_2. As discussed in 1) the white powdery precursor stripe could in general be avoided using turbulence reduction methods. Still, this would not solve nor explain the Ba deficiency throughout the film. To shed light on this circumstance a thermodynamical analysis is conducted in the following. The metalorganic precursors, which are used for the deposition, decompose to form oxides and subsequently the final product $BaZr_{1-x}Y_xO_{3-x/2}$. However in the case of the Ba precursor $BaCO_3$ is likely to be formed first before decomposing into BaO and CO_2. Due to the large size of the Ba ion and its relatively low charge density (compared to other cations with smaller ionic radius – Mg, Ca, Sr in their respective carbonates) the decomposition of $BaCO_3$ requires more energy and therefore high temperatures of 1000 – 1300 °C [197]. Since the deposition temperatures in the LA-CVD setup did usually not exceed 750 °C the formation of $BaZr_{1-x}Y_xO_{3-x/2}$ had to occur according to the following reaction:

$$BaCO_3(s) + Zr_{1-x}Y_xO_{2-x/2}(s) \rightarrow BaZr_{1-x}Y_xO_{3-x/2}(s) + CO_2(g) \tag{6.3}$$

To analyze (6.3) in terms of standard thermodynamic quantities two separate equations have to be defined in order to simplify the calculation. In a first step the formation of pure $BaZrO_3$ is expressed in (6.4).

$$BaCO_3(s) + ZrO_2(s) \rightarrow BaZrO_3(s) + CO_2(g) \tag{6.4}$$

In a second step the incorporation of Y can be expressed by the following hypothetical reaction:

$$BaCO_3(s) + YO_{1.5}(s) \rightarrow BaYO_{2.5}(s) + CO_2(g) \tag{6.5}$$

In order to separate (6.3) into (6.4) and (6.5) certain conditions have to be met in terms of thermodynamics and crystal structure. Of course both equations can be considered individually without restrictions. Yet, when combined, the formation of a solid solution can induce additional contributions to the thermodynamic parameters (enthalpy and entropy of mixing), if the mixing is non-ideal. Since the main objective

of this evaluation is based on a relative comparison of two similar reaction equations (with similar assumptions for both), the mixing is treated as an ideal solid solution in the following. This assumption naturally requires $BaYO_{2.5}$ and $YO_{1.5}$ to crystallize in the same structures as $BaZrO_3$ and ZrO_2, respectively.
As a consequence, by regarding the mixtures as ideal solid solutions, equations (6.4) and (6.5) can be used to obtain equation (6.3). In detail, equation (6.3) is obtained by applying the following operation: (1-x)·(6.4)+x·(6.5). Similarly, the standard enthalpy of reaction as well as Gibbs free energy can be estimated according to

$$\Delta H_r^\circ\{(6.3)\} = (1-x)\Delta H_r^\circ\{((6.4))\} + x\Delta H_r^\circ\{((6.5))\} \tag{6.6}$$

and

$$\Delta G^\circ\{(6.3)\} = (1-x)\Delta G^\circ\{((6.4))\} + x\Delta G^\circ\{((6.5))\} \tag{6.7}$$

For a comparison of the thermodynamic quantities the same procedure can be applied to the case where $BaZr_{1-x}Y_xO_{3-x/2}$ is formed purely from oxides, which is usually the case in solid state synthesis. As in the case of formation from $BaCO_3$ equation (6.8) can be described using the individual equations (6.9) and (6.10).

$$BaO(s) + Zr_{1-x}Y_xO_{2-x/2}(s) \rightarrow BaZr_{1-x}Y_xO_{3-x/2}(s) \tag{6.8}$$

$$BaO(s) + ZrO_2(s) \rightarrow BaZrO_3(s) \tag{6.9}$$

$$BaO(s) + YO_{1.5}(s) \rightarrow BaYO_{2.5}(s) \tag{6.10}$$

The thermodynamic quantities can subsequently be calculated according to (6.6) and (6.7). The necessary data for this calculation is taken from literature and is listed in Table 23.

Table 23. List of standard thermodynamic quantities of compound formation, containing enthalpy of formation and entropy at 298 K

Compound	ΔH_f° / kJ/mol	S° / $Jmol^{-1}K^{-1}$	Reference
BaO	-548.1	72	[198]
ZrO_2	-1100.1	50	[198]
Y_2O_3	-1905.2	99	[199,200]
$BaCO_3$	-1210.9	112	[186]
CO_2	-393.5	213	[198]
$BaZrO_3$	-1762.9	126	[201,202]
BaY_2O_4	-2483.4	164	[203]
$Ba_2Y_2O_5$	-2946.8	258	[203]

The numerical values for several Yttrium doping levels (x=0, 0.1, 0.2) and the individual reactions are shown in Table 24. The graphical results of ΔG° over a wider stoichiometry range are plotted in Figure 6.17. For reaction (6.3) involving $BaCO_3$ the reaction is endothermic for all doping levels (positive reaction enthalpy ΔH_r°). The

Gibbs free energy $\Delta G_{700°C}$, which was calculated at a temperature of 700 °C (in reference to a common deposition temperature of the LA-CVD setup) is slightly negative for a doping level of x=0, implying that the reaction can occur spontaneously in the forward direction. However with increasing Y-content $\Delta G_{700°C}$ becomes less negative and reaches a positive value of 10 kJ/mol at an Y-doping level of x=0.2. These results, although of theoretical nature, indicate that Y-doping is unfavorable for the synthesis of BZY from $BaCO_3$ and that the reaction will not occur spontaneously. For reaction (6.8), the synthesis of BZY from BaO, ΔH_r° indicates an exothermic reaction for all investigated doping levels. As opposed to the reaction from $BaCO_3$ the reaction from BaO clearly shows negative $\Delta G°$ values for all doping levels.

Table 24. List of reaction equations (6.3)-(6.5) and (6.8)-(6.10) with the reaction enthalpies ΔH_r° and Gibbs free energies ΔG° calculated for different $YO_{1.5}$ contents (x=0, 0.1, 0.2) at a temperature of 700 °C (referring to the highest deposition temperature, which was used in the LA-CVD setup).

Reaction	ΔH_r° / kJ/mol			$\Delta G_{700°C}^\circ$ / kJ/mol		
	x=0	0.1	0.2	x=0	0.1	0.2
$xBaCO_3(s) + xYO_{1.5}(s) \rightarrow xBaYO_{2.5}(s) + xCO_2(g)$	0	30	59	0	12	24
$(1-x)BaCO_3(s) + (1-x)ZrO_2 \rightarrow (1-x)BaZrO_3(s) + (1-x)CO_2(g)$	154	139	124	-17	-16	-14
$BaCO_3(s) + Zr_{1-x}Y_xO_{2-x/2}(s) \rightarrow BaZr_{1-x}Y_xO_{3-x/2}(s) + CO_2(g)$	154	169	183	-17	-4	10
$xBaO(s) + xYO_{1.5}(s) \rightarrow BaYO_{2.5}(s)$	0	3	8	0	2	6
$(1-x)BaO(s) + (1-x)ZrO_2 \rightarrow (1-x)BaZrO_3(s)$	-115	-103	-80	-119	-107	-83
$BaO(s) + Zr_{1-x}Y_xO_{2-x/2}(s) \rightarrow BaZr_{1-x}Y_xO_{3-x/2}(s)$	-115	-100	-72	-119	-105	-77

Although ΔH_r° and $\Delta G°$ are all negative, the same trends as for reaction (6.3) can be observed. The calculations highlight the fact that BZY can easily be obtained when BaO is present but not when the main educt is predominantly $BaCO_3$.

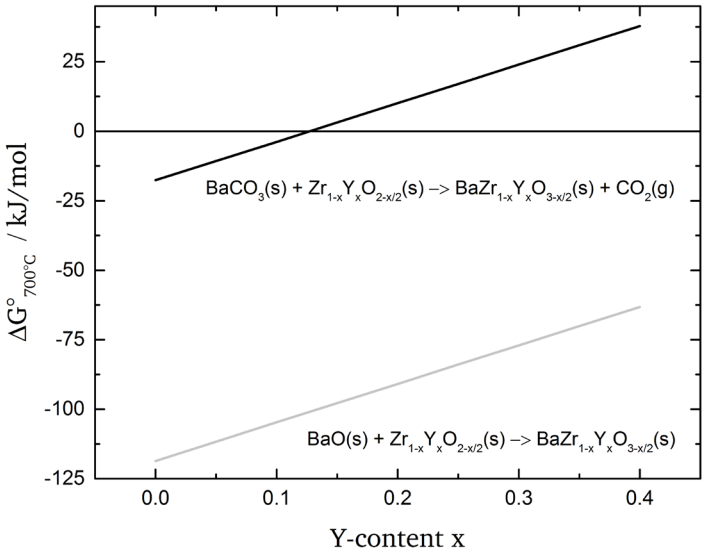

Figure 6.17. Gibbs free energies ΔG° calculated for different $YO_{1.5}$ contents in $BaZr_{1-x}Y_xO_{3-x/2}$ at a temperature of 700 °C. Calculations are based on the thermodynamical data in Table 23.

Furthermore the reaction equilibrium of (6.3) is strongly influenced by the preexisting partial pressures of the gaseous components. Since CO_2 is the only gaseous component, the partial pressure of CO_2 (p_{CO2}) will influence $\Delta G°$ (in equilibrium) according to

$$\Delta G^{\circ}\{(6.3)\} = \Delta H_r^{\circ}\{(6.3)\} - T\Delta S^{\circ}\{(6.3)\} = -RTln(K\{(6.3)\}) = -RTln(p_{CO_2}) \qquad (6.11)$$

where R is the ideal gas constant and K{(5.3)} the equilibrium constant of equation (6.3). Based on (6.11) the relationship between p_{CO2} and the temperature at equilibrium is given by

$$\lg(p_{CO_2}) = -\frac{\Delta H_r^{\circ}\{(6.3)\}}{R \cdot ln10} \cdot \frac{1}{T} - \frac{\Delta S^{\circ}\{(6.3)\}}{R \cdot ln10} \qquad (6.12)$$

and can be used to define the stable region of BZY as shown in Figure 6.18a. Therein the lines separate the thermodynamically stable and unstable region of BZY with respect to p_{CO2} in the temperature range from 200 °C to 1000 °C (for different doping levels x=0, 0.1, 0.2). E.g. at a temperature of 700 °C and a doping content of x=0.2 the $BaZr_{1-x}Y_xO_{3-x/2}$ phase will be stable below p_{CO2}=0.28 atm and unstable above the same value. Since the total pressure within the deposition chamber never exceeded 5 mbar p_{CO2} should not negatively influence the deposition. To further emphasize that p_{CO2} did not crucially influence the formation of BZY, Figure 6.18b displays the stable and unstable regions related to the temperature plotted over the Y-doping content at various p_{CO2}. The lines were calculated by rearranging (6.12). Figure 6.18b shows that the stability region increases with decreasing p_{CO2}.

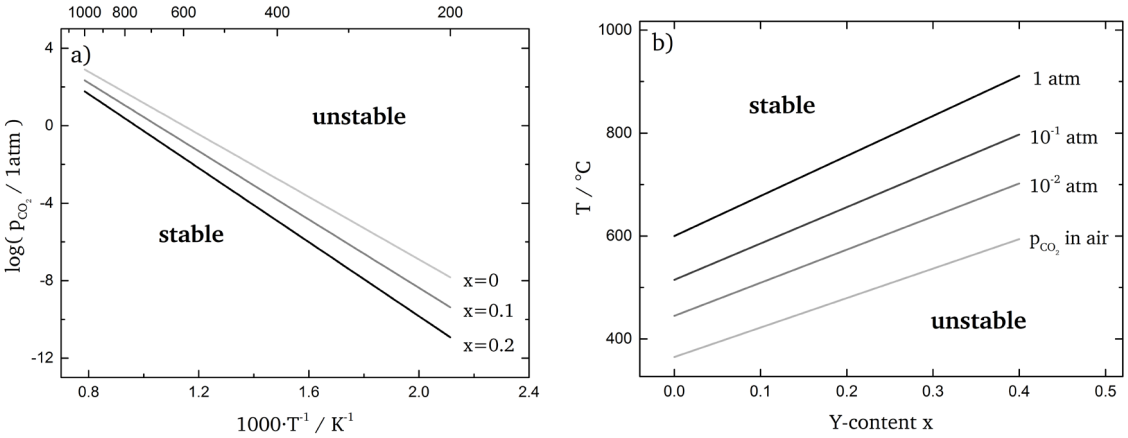

Figure 6.18. a) Temperature and CO_2 partial pressure dependent stability regions of BZY for different Y-doping contents obtained by thermodynamical calculations from equations (6.3)-(6.12). b) Equilibrium temperature depending on the composition of BZY, plotted for several partial pressures, which are indicated at the corresponding lines.

Even though based on Figure 6.18, the CO_2 partial pressure was not found to influence the stability during film deposition in the LA-CVD setup, the thermodynamic considerations support the argument that the reaction involving $BaCO_3$ could have impeded the formation of Y-doped $BaZrO_3$. The positive reaction enthalpy and Gibbs free energy are a strong indication that the problems of Ba incorporation are also of thermodynamical origin. Within the discussed results this assumption is supported by the fact that the deposition of almost phase pure $BaZrO_3$ was possible by adjusting the

process parameters (e.g. BZY10). Furthermore, the fact that, as soon as Y-precursor was added to the precursor mixture (in order to synthesize Y-doped $BaZrO_3$), no more traces of the cubic perovskite phase could be detected under the same process conditions (Figure 6.12), is a strong indication for the increasing thermodynamic reluctance to form BZY. The results of the thermodynamic calculations predict exactly this behavior. Specifically the thermodynamic stability of BZY decreases and the Gibbs free energy increases (positive) with growing Y-content.

Short summary of results obtained for BZY thin films deposited by LA-CVD

In terms of structure and composition undoped films of $BaZrO_3$ were successfully deposited and optimized. Even though the microstructure was not suitable for further electrochemical investigations it was shown for the first time (to the author's best knowledge) that $BaZrO_3$ can be deposited using LA-CVD. However, upon attempting to deposit Y-doped $BaZrO_3$ the cubic perovskite phase could only be obtained with high Ba excess (390 %) in the precursor mixture. In addition, even with high Ba excess the films showed an inhomogenous distribution of phases due to a streak/spot-like white deposit. The white deposit is assumed to be caused by precursor material being dragged along during the laser flash evaporation and subsequently accumulated on the substrate. Since the samples containing the white deposit could not be used for electrochemical investigations and a variation of the process parameters did not alleviate the problem, no electrochemical measurements were performed. However the problems pertaining to the deposition were analyzed and it was found that physical changes to the experimental setup might improve the homogeneity of the film and eliminate the white deposit. Furthermore thermodynamic calculations showed that with increasing Y-doping the formation of the perovskite phase becomes thermodynamically less favorable, which is of special relevance if $BaCO_3$ is involved as an intermediate product. These findings might be a possible reason, which could explain the lack of BZY phase formation. In terms of thermodynamics it can be concluded that depending on the desired doping levels (10 mol% - 20 mol%) a higher substrate temperature of at least 800°C is (theoretically) necessary. Since the diode laser of the LA-CVD setup can reach temperatures of up to 1200 °C, future depositions of BZY can and should be conducted at sufficiently high temperatures (maximum deposition temperature in this work was 800 °C).

6.4. Aerosol-Assisted Metalorganic Chemical Vapor Deposition

6.4.1. Advantages of AA-MOCVD

An aerosol can be defined as a suspension of solid or liquid particles in a gas with the stability ranging from seconds up to years. Although this is no scientific classification but rather corresponds to common usage this description is also accurate enough in most scientific cases. AA-CVD involves the process of atomizing a liquid precursor solution into finely distributed droplets, which are dispersed in a gaseous medium. The subsequent transport to the reaction zone, which includes evaporation and decomposition of the solvent and the precursor, respectively, is explained in 2.4. As opposed to regular CVD the reaction environment for AA-CVD is flexible and the process can even take place in an open atmosphere (to deposit oxides) with inert gases. Similar to the LA-CVD process the precursor delivery is simplified as compared to conventional CVD. The only requirement is that the precursor is liquid or can be dissolved in a solvent. The stoichiometric ratio of precursors is in theory determined by the ratio of the precursors in solution and can be controlled a lot easier as opposed to thermal evaporation. Further advantages of AA-CVD in comparison to conventional CVD are:

- low cost in terms of precursors, due to a wider variety (the common problem of precursor decomposition during thermal evaporation can be avoided) and in terms of experimental setup (e.g. no UHV required)
- high deposition rates due to high mass transport
- advantages for the fabrication of multicomponent films from precursors with poor thermal stability and limited volatility
- inexpensive and environmentally friendly chemicals can be used

Due to all the above mentioned key features AA-CVD is potentially useful for mass production and therefore sparked interest for a variety of research areas such as optics [204], electronics [205], superconductors [206] or solid oxide fuel cells [207] to only name a few. AA-CVD has contributed to broadening the range of applications, for which CVD can be used, by providing a substantial improvement in the delivery of the precursors.

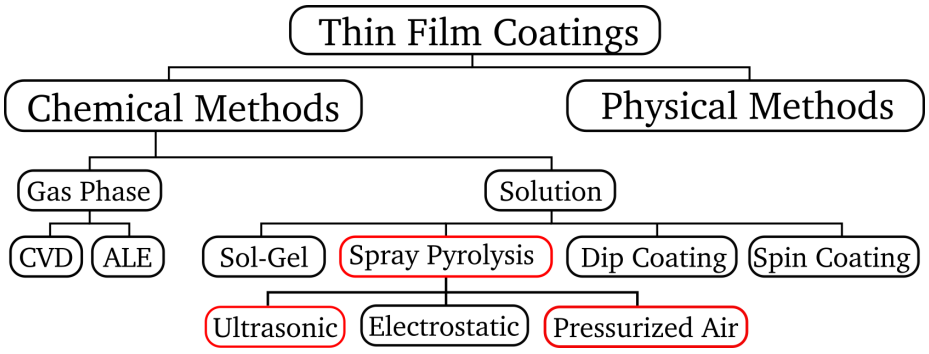

Figure 6.19. Classification of chemical thin film deposition methods. Spray Pyrolysis with pressurized air used for atomization of the precursor solution is used to for the thin film deposition in this chapter.

There are three general methods of atomization used in AA-CVD, namely: Air blast (pressurized air), ultrasonic and electrostatic techniques (Figure 6.19). Due to the ease of use and production, the commercial application has mainly employed pressure atomizers (sometimes called pneumatic aerosol jet [208]). In this thesis a pressurized air gun was used

for atomization due to the simple experimental setup requirements. Additionally the method of ultrasonic aerosol generation was investigated in this thesis using a piezoelectric transducer. The main difference between the three methods of atomization is the rate of atomization, the initial droplet velocity and most importantly the resulting droplet size. The advantage of ultrasonic droplet generation over pneumatic droplet generation is that the created droplets are smaller in size and have a narrower droplet size distribution, which usually leads to an increase in film quality. Since a narrow droplet size distribution as well as a controllable droplet size is one of the most important factors regarding AA-CVD the ultrasonic droplet generation is expected to be superior in term of film quality but slower in terms of deposition rate. Therefore both methods of droplet generation were examined over the course of this work. However, since spray deposition with ultrasonic droplet generation led to the same problem in terms of thermodynamics, as was observed in chapter 6.3.2, the results are not presented in this thesis. To the best of the author's knowledge thin films of $BaZr_{1-x}Y_xO_{3-\delta}$ have so far only been deposited using electrostatic spray deposition [179,209] but neither ultrasonic nor pneumatic methods have successfully been reported.

6.4.2. Pressurized Spray Deposition

Among the chemical methods for thin film coatings (including $BaZr_{1-x}Y_xO_{3-\delta}$), spray pyrolysis is one of the simplest techniques in terms of required hardware. Spray pyrolysis only requires a heated substrate a liquid source (containing precursors) and an atomizer (as was already explained more detailed in 4.3). Spray deposition is therefore very cost effective in terms of operational cost (ambient operation conditions) and only requires very simple facilities. Further advantages are the potential for mass production (up to 100 nm/s [210]) combined with good reproducibility and large surface area coverage. As was explained in Figure 2.9 (chapter 2.4) the deposition mechanism highly depends on the droplet size and the substrate surface temperature. In general it has been found that the highest film quality is achieved when a CVD-like process is dominant (process C in Figure 2.9). However in most spray pyrolysis depositions a CVD-like process cannot be achieved because the deposition temperature is too low for the vaporization of precursors. Therefore, during spray pyrolysis, processes A and B are more likely to occur. The air blast (pressurized air) atomizer makes use of high speed air in order to create an aerosol from the precursor solution, by breaking up the liquid into sheets or jets of liquid. After the aerosol is generated the droplets travel towards the hot substrate (the experimental setup is shown in Figure 4.4). The combination of the parameters temperature, droplet size as well as boiling point and molarity of the precursor solution determine the deposition mechanism. Since the droplet size distributions were unknown for the spray gun (in the micrometer range according to the manufacturer), the general parameters were determined empirically and by using values, which were found to be optimal in other works. The needle tip size, the nozzle tip to substrate distance and the precursor solution flow were optimized empirically, while the air pressure and salt concentration in the precursor solution were adapted from literature. Detailed information about the precursor selection and the solvent composition can be found in the experimental section 4.3. The most suitable set of precursors, which was determined in chapter 4.3 (Set B), is tested in the following by variation of the substrate temperature. In addition different substrates, namely (100)-oriented Si, (100)-oriented MgO and polycrystalline Pt-foil were investigated.

Since the deposition temperatures are low compared to any chemical vapor deposition process the deposition is occurring as droplets spreading on the substrate surface, as described by the droplet evolution (process A) in chapter 2.4. The substrate/deposition temperature is one of the most important parameters in spray pyrolysis because it can effectively control the solvent evaporation rate. The temperature greatly influences whether or not a continuous film can be deposited. Depending on the temperature the evaporation rate of the solvent and thereby the droplet spreading on the substrate surface is influenced. Usually three different situations can be described, depending on the deposition temperature regimes:

1. At lower substrate temperatures, if the droplets still contain too much solvent (when reaching the substrate), the evaporation may occur only after the film deposition on the substrate, resulting in cracks (Figure 6.20a).

2. At intermediate substrate temperatures the droplet deposits as a concentrated liquid with many precipitations, which results in continuous films (Figure 6.20b). Usually a maximum deposition temperature exists above which discontinuous films are formed.

3. Above the maximum deposition temperature (for continuous films) the high evaporation rate of the solvent causes the agglomeration of particles and inhomogeneous film growth (Figure 6.20c).

Besides the substrate temperature the variation of other parameters such as salt concentration, air pressure and flow rate can have similar effects. However, as these parameters were kept constant at values, which were based on previous systematic studies, only the substrate temperature was of importance. These temperature regimes greatly depend on the solvent or solvent mixture, which is used [211].

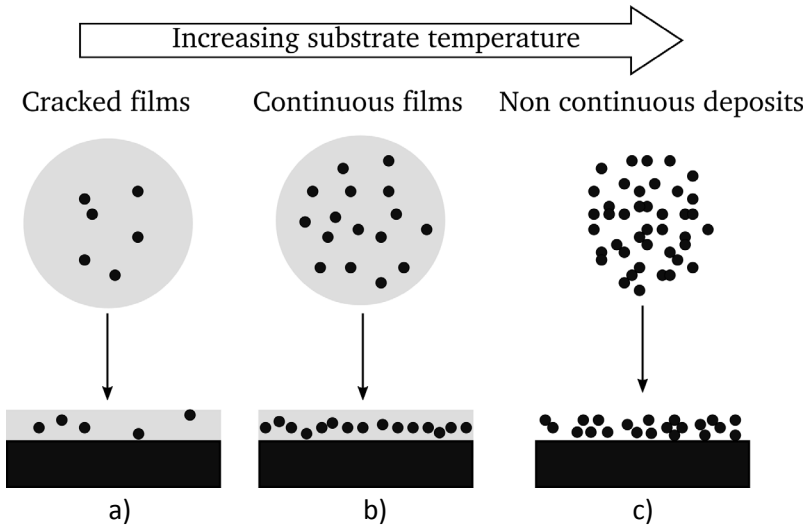

Figure 6.20. Schematic illustration of film formation during pressurized spray deposition a) Low substrate temperature leads to the deposition of a diluted suspension with cracks forming due to the high solvent content during drying and annealing. b) Medium substrate temperature results in a concentrated liquid with many precipitations, leading to continuous films upon drying and annealing. c) High substrate temperature leads to non-continuous deposits. This figure was adapted from [211].

The effect of substrate temperature, which is presented in the following investigation, clearly shows that all three temperature regimes occur. Figure 6.21 shows the micrographs of four as-deposited films at substrate temperatures of 255 °C to 375 °C. The coverage of the substrate (deposition rate) as well as the droplet diameter decrease with increasing temperature, displaying the situation, which is described in Figure 6.20c. To determine the effects of temperature variation on crystal structure and crystallinity, the deposition parameters were chosen so that the substrate surface was always fully covered in the rest of this chapter.

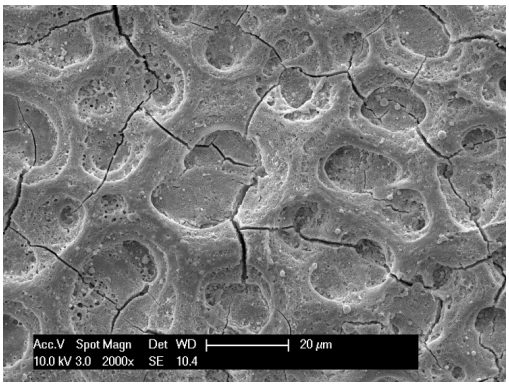

a) deposition at 255 °C

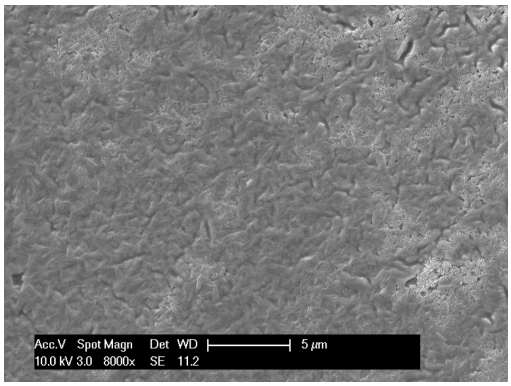

b) deposition at 305 °C

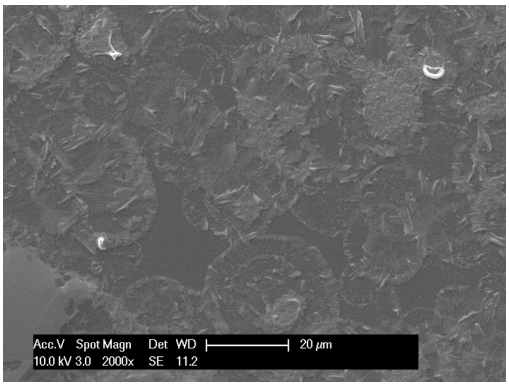

c) deposition at 350 °C

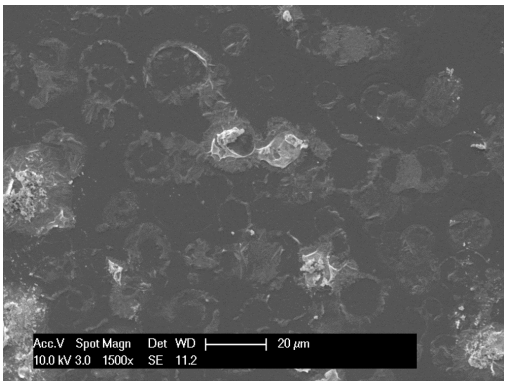

d) deposition at 375 °C

Figure 6.21. Scanning electron micrographs of as-deposited films deposited by PSD (Set B, 30 min) at a) 300 °C, b) 330 °C, c) 350 °C and 375 °C

Samples BZY20-BZY25, which are listed in **Table 25**, were deposited from solution (DI:BC 50:50 and 0.08 mol/l) at different deposition temperatures and subsequently annealed at 1100 °C (10 h) to ensure the complete reaction and decomposition of the precursor materials. The heating and cooling rate was kept low at 2 °C/min to minimize film cracking.

Table 25. Deposition parameters for Y-doped $BaZrO_3$ thin films deposited at different substrate temperatures and subsequently annealed at 1100 °C for 10 h.

Sample	Precursor Set (section 4.3)	Substrate	Substrate temperature (deposition) / °C
BZY2068	Set B	Si	175
BZY2167	Set B	Si	200
BZY2266	Set B	Si	255
BZY2365	Set B	Si	275
BZY2463	Set B	Si	305
BZY2564	Set B	Si	330

The diffractograms in Figure 6.22 were recorded after samples BZY20-BZY25 had been annealed at 1100 °C. Although the content of Y-doped $BaZrO_3$ increases with increasing deposition temperature impurity phases such as $BaCO_3$, ZrO_2 and Y_2O_3 are present. In addition to these phases the high temperature annealing causes silicate formation due to the increased reactivity of Si. Therefore it was not possible to obtain phase pure films on Si substrates.

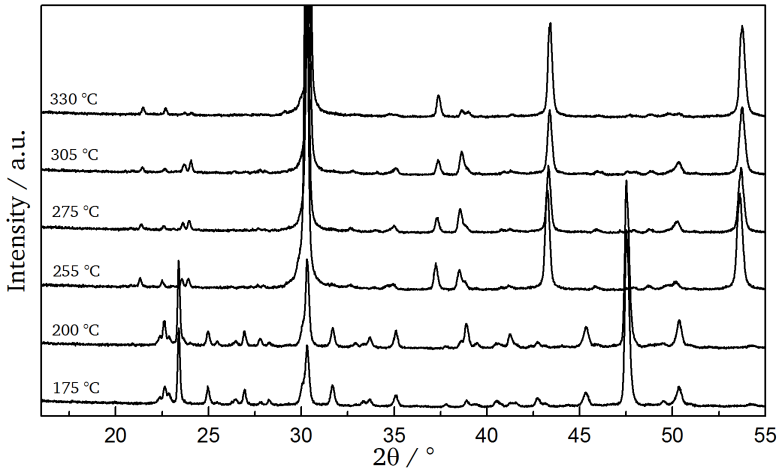

Figure 6.22. X-ray diffractograms of BZY thin films deposited by pressurized spray deposition on Si substrates at different deposition temperatures and subsequently annealed at 1100 °C for 10 h.

Furthermore, the films deposited on Si substrates showed intense cracking when investigated by SEM. Figure 6.23a and b show BZY22 after deposition. The film has a non-uniform thickness of 5-10 um because it is covered with craters (~20 um diameter). Since these craters were not observed during the growth of films deposited at higher temperatures (Figure 6.21a) this might indicate slow solvent evaporation due to low temperatures. Therefore a deposition temperature of 300 °C was chosen for the following experiments to guarantee the deposition of smooth films. In addition the complete film is interspersed with cracks. In spite of these cracks, based on the cross-section in Figure 6.23a, the film appears to be well connected with the substrate.

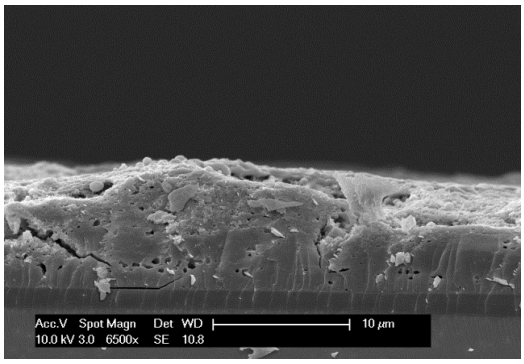

a) cross-section as-deposited

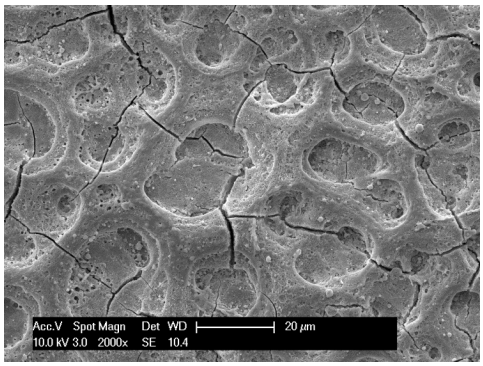

b) surface as-deposited

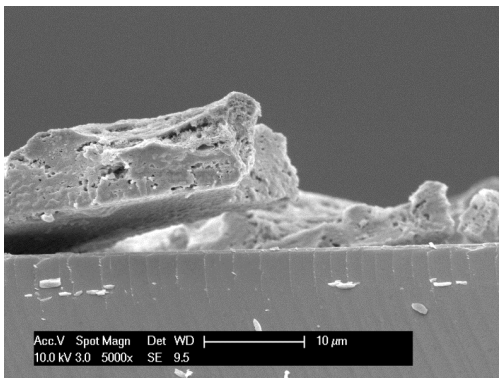

c) cross-section annealed

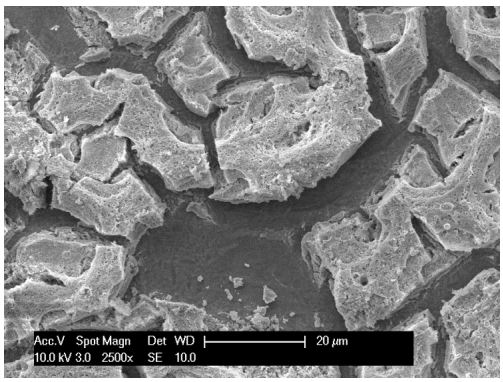

d) surface annealed

Figure 6.23. Scanning electron micrographs of BZY22 (deposition temperature 255°C) of surface and cross-section a), b) as-deposited and c), d) after annealing.

However, during annealing the crystallization and BZY formation reactions cause material shrinkage. As shown in Figure 6.23d the morphology cannot be described in terms of cracks anymore but rather as individual islands of film. Furthermore, the cross-section in Figure 6.23c shows that these islands have delaminated from the substrate and can no longer be described as a film. Due to the reactivity of the Si substrate and the problematic film morphology in combination with the high temperature annealing. Therefore single crystalline MgO and polycrystalline Pt foil were also tested as possible substrates. Figure 6.24 shows a comparison of three films deposited at 300 °C on MgO, Si and Pt. All three films were annealed after the deposition. As opposed to the films deposited on Si substrates the films on MgO and Pt are phase pure following the annealing. On Pt the BZY films were found to be phase pure at deposition temperatures varying from 250 °C to 325 °C. Since these depositions did not yield any new insights they are not shown here but can be found in A Appendix (Figure A 2 and Table A 5).

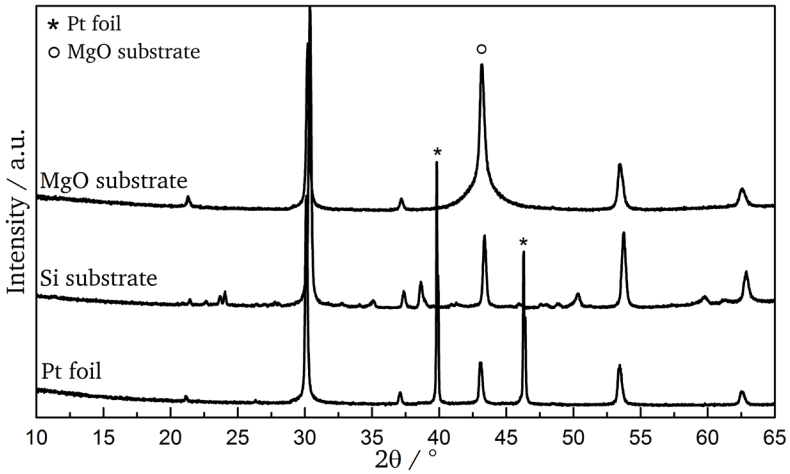

Figure 6.24. BZY films deposited on different substrates by PSD. The substrate reflections for MgO and Pt are indicated. All films were deposited with equal deposition parameters at 300 °C and annealed subsequently.

Although the MgO and Pt substrates led to the deposition of phase pure BZY the annealing created similar problems as were observed for the films deposited on Si. Figure 6.25 shows photographs of the BZY films deposited on the three different substrates. Whiles Figure 6.25a and c show a slight film, MgO already macroscopically confirms that only loose particles remain on the surface after deposition. The SEM micrographs for BZY on Pt confirmed that although the phase was pure a similar problem as for Si occurred.

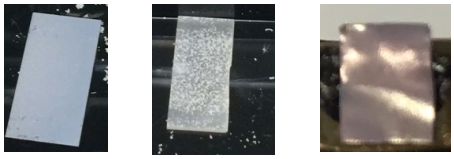

a) **b)** **c)**

Figure 6.25. BZY films deposited on a) Si, b) on MgO and c) on Pt foil.

When comparing the coefficients of thermal expansion (**κ**), which were gathered from literature reports and are summarized in Table 26, the observed problems can be put into perspective. Since the coefficient of thermal expansion for MgO is almost twice as high as that of BZY, the delamination and extreme cracking, which is shown in Figure 6.25b, are to be expected. Si and Pt on the other hand show similar $\Delta \kappa$ and therefore behave similar. However none of the substrates used in this study led to dense and stable films.

Table 26. Coefficients of thermal expansion, for $BaZrO_3$ and the tested substrates.

Material	Temperature range / °C	κ / 10^{-6} K^{-1}	Reference
$BaZrO_3$	500 - 1200	7 – 8	[212]
Pt	500 - 1200	9.5 – 11.5	[213]
Si	500 - 1200	4 – 4.5	[214]
MgO	400 - 1200	12.7 – 15	[215]

Short summary of results obtained for BZY thin films deposited by PSD

By varying the deposition temperature the optimal condition for thin continuous $BaZr_{1-x}Y_xO_{3-d}$ films was determined to be around 300 °C. The other parameters, which were necessary (salt concentration, flow rate, air pressure, spray gun to substrate distance) for the deposition process, were kept constant. The values of these parameters were determined based on systematic studies (which are not presented in this thesis) and literature reports. Although continuous films could be obtained after deposition, they showed cracking after annealing. In addition no phase purity could be obtained for any films deposited on Si substrates. Therefore Pt foil and MgO substrates were used, which both yielded phase purity. However, all films deposited on these substrates showed extensive cracking and disintegration of the film from the substrates after annealing. It is likely that this cracking is due to the very different coefficients of thermal expansion.

7. Conclusions & Outlook

The main findings, which were presented in this thesis, are summarized in the following:

7.1. Conclusions "Investigation of $BaFeO_{2.5+\delta}$"

1. (001)-oriented films of BFO were successfully grown on (001)-oriented Nb:STO. The in-plane orientation relationship was found to be (001) BFO//(001) Nb:STO with cube on cube growth. The occurring stresses and strains were analyzed and could be correlated with the post-deposition treatments. Similarly (111)-oriented films were deposited on (111)-oriented Nb:STO. Post-deposition treatments of these films were found to cause film relaxation, which is assumed to occur in the form of a 3x3x3 superstructure. It can therefore be assumed that the growth of BFO is more favorable on (001)-oriented Nb:STO films. However, both types of films indicated the uptake of water, while retaining their structural integrity. Therefore the films on both types of substrates were found to be well suited for the investigation by EIS.

2. The probing of the local coordination and oxidation state of Fe in BFO films on (001)-oriented Nb:STO was conducted by CEMS. Based on the isomer shifts only the 3+ oxidation state could be detected for both an annealed and a hydrated film. The corresponding magnetic hyperfine fields indicated 4-fold as well as 5/6-fold coordinated Fe sites. The fact that more than one signal are observed indicates strong local ordering of oxygen ions and vacancies, which is similar to what is found in monoclinic $BaFeO_{2.5}$. However, no full ordering could be observed with the films.

3. The surface composition of the films deposited on (001)-oriented Nb:STO was analyzed using XPS. The analysis confirmed a stoichiometric ratio of Ba to Fe on the surface but also showed that depending on the post-deposition treatment $BaCO_3$ and BaO_2 can be detected. Since the samples were exposed to ambient atmosphere the surfaces were also covered with adventitious carbon. Although the Fe *2p* emission lines indicated a change in oxidation state after hydration, this only referred to the surface, as shown by CEMS.

4. A spatially resolved compositional analysis of an Ar-annealed BFO film using AP-TOF mass spectrometry showed that Sr-diffusion occurred from the substrate into the film. The diffusion process is assumed to be thermally activated with the Sr ions replacing Ba ions thereby forming $Ba_{1-x}Sr_xFeO_{2.5+\delta}$. Sr was detected throughout the complete thickness of the film, which coincides with the observations made during XPS surface analysis. This Sr incorporation into the film was found to negatively influence the proton conductivity.

5. The bulk proton conductivity of the BFO films on (001)-oriented Nb:STO could be estimated for the first time. The protonic contribution was obtained by comparing measurements in wet and dry atmosphere and ranged in the order of μScm^{-1} in the range of 200 °C to 300 °C. Since for the film on (111)-oriented Nb:STO EIS

measurements in both atmospheres had to be conducted on the same sample the proton contribution could not be reliably separated from the total conductivity (due to Sr diffusion). Based on literature reports the magnitude of the conductivities determined in this thesis would suffice so that the charge transport in a thin film electrode could be dominated by the bulk path and the oxygen reduction reaction could be sufficiently run [158].

7.2. Conclusions "A perspective on New Synthesis Techniques for Y-Doped $BaZrO_3$"

1. Dense pellets of single phase $BaZrO_3$ and $BaZr_{0.8}Y_{0.2}O_{2.9}$ were obtained by solid state synthesis and could be used as reference samples for thin films.

2. Films of undoped $BaZrO_3$ were successfully deposited and optimized in terms of structure and stoichiometry. Although the microstructure was not suitable for electrochemical investigation it was shown that $BaZrO_3$ could be deposited using LA-CVD for the first time.

3. Y-doped BZY films (deposited by LA-CVD) required very high excess of Ba (390 %) to form a cubic perovskite phase. The desired phase was mostly found in a white streak-like deposit. This white deposit is assumed to be caused by precursor material being dragged along during the laser flash evaporation and subsequently accumulated on the substrate. Due to the deposit and insufficient perovskite phase formation in the surrounding film no EIS measurements could be performed.

4. The problems pertaining to the deposition were analyzed in detail: It was found that physical changes to the experimental setup could block the solid particles and therefore avoid the formation of a white deposit. Furthermore thermodynamic considerations showed that depending on the desired doping level a higher substrate temperature of at least 800 °C is required so that the chemical reaction of BZY formation can occur spontaneously.

5. For the deposition of BZY by PSD the optimum conditions for continuous film growth were determined. However, subsequent annealing caused film extensive film delamination and cracking on all tested substrates (Si, Pt, MgO). The cracking is suggested to be caused by the difference in thermal expansion coefficients.

7.3. Outlook

1. The investigation of the conductive properties of BFO highlighted that the proton conductivity not only depends on the respective atmosphere but also on stress applied to the material as well as on the incorporation of contaminants (e.g. Strontium). Therefore further investigations of BFO could focus on using different substrates, which eliminate the problem of diffusive processes. In terms of the influence of stress and strain on the proton conductivity a similar study as was conducted for Y-doped $BaZrO_3$ (strain engineering through in-situ stress monitoring) [131], could be conducted by using a buffer layer. In addition, it is important to acknowledge that especially the BFO films deposited on (111)-oriented STO:Nb in this thesis were not optimized and that the proton conductivity along this specific crystallographic direction requires further examination and understanding.

2. Concerning the broader context of searching for an air electrode material with sufficient electronic and proton contribution future work might include a combination of BFO and $BaCoO_{3-\delta}$, which was recently found to show a much higher (although electronic) conductivity and take up larger amounts of water than BFO [168]. Furthermore, the integration of these materials into complete devices might enable the investigation of the interfacial polarization resistances, which are known to be a limiting factor in proton conducting SOFCs and SOECs.

3. Since $BaZr_{1-x}Y_xO_{3-\delta}$ or solid solutions of Y-doped $BaZrO_3$ and $BaCeO_3$ are considered to be very promising candidates for functional proton conducting electrolytes, further investigations and research are required. Especially the search for cost-effective thin film deposition methods, which are able to deliver high quality films, is important to promote the development of proton conducting SOFCs and SOECs. Since the applicability of chemical deposition methods proved to be difficult in terms of thermodynamics an approach using physical methods, which are not bound to thermodynamic equilibria, is suggested (e.g. co-sputtering of Y-doped $BaZrO_3$ and $BaCeO_3$).

8. References

1. *World Energy Outlook 2018*; World Energy Outlook; OECD, 2018; ISBN 9789264064522.
2. REN21 *Renewables 2018 Global Status Report*; Paris, France, 2018; ISBN 978-3-9818911-3-3.
3. Forschungsverbund Erneuerbare Energien -FVEE- Energiekonzept 2050 - Eine Vision für ein nachhaltiges Energiekonzept auf Basis von 100 % erneuerbaren Energien. *Berlin* **2010**.
4. Sapountzi, F. M.; Gracia, J. M.; Weststrate, C. J. (Kees-J.; Fredriksson, H. O. A.; Niemantsverdriet, J. W. (Hans) Electrocatalysts for the generation of hydrogen, oxygen and synthesis gas. *Prog. Energy Combust. Sci.* **2017**, *58*, 1–35, doi:10.1016/j.pecs.2016.09.001.
5. Bi, L.; Boulfrad, S.; Traversa, E. Steam electrolysis by solid oxide electrolysis cells (SOECs) with proton-conducting oxides. *Chem. Soc. Rev.* **2014**, *43*, 8255–8270, doi:10.1039/C4CS00194J.
6. Fabbri, E.; Pergolesi, D.; Traversa, E. Electrode materials: a challenge for the exploitation of protonic solid oxide fuel cells. *Sci. Technol. Adv. Mater.* **2010**, *11*, 044301, doi:10.1088/1468-6996/11/4/044301.
7. Carnot, N. L. S. Reflections on the Motive Power of Heat. *Reflections Motiv. Power Heat.* **1897**, doi:10.1016/0043-1354(95)00149-F.
8. Tarancón, A. Strategies for Lowering Solid Oxide Fuel Cells Operating. **2009**, 1130–1150, doi:10.3390/en20401130.
9. Srinivasan, S. *Fuel Cells: From Fundamentals to Applications*; Springer US: Boston, MA, 2006; ISBN 978-0-387-25116-5.
10. Brett, D. J. L.; Atkinson, A.; Brandon, N. P.; Skinner, S. J. Intermediate temperature solid oxide fuel cells. *Chem. Soc. Rev.* **2008**, *37*, 1568–1578, doi:10.1039/b612060c.
11. Kreuer, K. Aspects of the formation and mobility of protonic charge carriers and the stability of perovskite-type oxides. *Solid State Ionics* **1999**, *125*, 285–302, doi:10.1016/S0167-2738(99)00188-5.
12. Münch, W.; Seifert, G.; Kreuer, K. D.; Maier, J. A quantum molecular dynamics study of proton conduction phenomena in $BaCeO_3$. *Solid State Ionics* **1996**, *86–88*, 647–652, doi:10.1016/0167-2738(96)00229-9.
13. Fabbri, E.; Bi, L.; Pergolesi, D.; Traversa, E. Towards the Next Generation of Solid Oxide Fuel Cells Operating Below 600 °C with Chemically Stable Proton-Conducting Electrolytes. *Adv. Mater.* **2012**, *24*, 195–208, doi:10.1002/adma.201103102.
14. Matsuzaki, Y.; Tachikawa, Y.; Somekawa, T.; Hatae, T.; Matsumoto, H.; Taniguchi, S.; Sasaki, K. Effect of proton-conduction in electrolyte on electric efficiency of multi-stage solid oxide fuel cells. *Sci. Rep.* **2015**, *5*, 12640, doi:10.1038/srep12640.
15. Coors, W. G. Protonic ceramic fuel cells for high-efficiency operation with methane. *J. Power Sources* **2003**, *118*, 150–156, doi:10.1016/S0378-7753(03)00072-7.

16. Ni, M.; Leung, M. K. H.; Leung, D. Y. C. Mathematical modelling of proton-conducting solid oxide fuel cells and comparison with oxygen-ion-conducting counterpart. *Fuel Cells* **2007**, *7*, 269–278, doi:10.1002/fuce.200600049.

17. Rao, Y.; Zhong, S.; He, F.; Wang, Z.; Peng, R.; Lu, Y. Cobalt-doped $BaZrO_3$: A single phase air electrode material for reversible solid oxide cells. *Int. J. Hydrogen Energy* **2012**, *37*, 12522–12527, doi:10.1016/j.ijhydene.2012.05.022.

18. Munoz-Garcia, A. B.; Pavone, M. K-doped $Sr_2Fe_{1.5}Mo_{0.5}O_{3-\delta}$ as a bifunctional catalyst for air electrodes in proton- conducting solid oxide electrochemical cells. *J. Mater. Chem. A* **2017**, *5*, 12735–12739, doi:10.1039/C7TA03340K.

19. Kim, J.; Sengodan, S.; Kwon, G.; Ding, D.; Shin, J.; Liu, M.; Kim, G. Triple-Conducting Layered Perovskites as Cathode Materials for Proton-Conducting Solid Oxide Fuel Cells. *ChemSusChem* **2014**, *7*, 2811–2815, doi:10.1002/cssc.201402351.

20. Fan, L.; Su, P. C. Layer-structured $LiNi_{0.8}Co_{0.2}O_2$: A new triple ($H^+/O^{2-}/e^-$) conducting cathode for low temperature proton conducting solid oxide fuel cells. *J. Power Sources* **2016**, *306*, 369–377, doi:10.1016/j.jpowsour.2015.12.015.

21. Knöchel, P. L.; Keenan, P. J.; Loho, C.; Reitz, C.; Witte, R.; Knight, K. S.; Wright, A. J.; Hahn, H.; Slater, P. R.; Clemens, O. Synthesis, structural characterisation and proton conduction of two new hydrated phases of barium ferrite $BaFeO_{2.5-x}(OH)_{2x}$. *J. Mater. Chem. A* **2016**, *4*, 3415–3430, doi:10.1039/C5TA06383C.

22. Lee, E. Characteristics of mixed conducting perovskites $(Ba_{1-x}Nd_x)Fe^{3+}{}_{1-t}Fe^{4+}{}_tO_{3-y}$. *J. Ind. Eng. Chem.* **2008**, *14*, 701–706, doi:10.1016/j.jiec.2008.02.011.

23. Hombo, J.; Matsumoto, Y.; Kawano, T. Electrical conductivities of $SrFeO_{3-\delta}$ and $BaFeO_{3-\delta}$ perovskites. *J. Solid State Chem.* **1990**, *84*, 138–143, doi:10.1016/0022-4596(90)90192-Z.

24. Tilley, R. J. D. *Perovskites: Structure-Property Relationships*; John Wiley & Sons, Ltd: Chichester, UK, 2016; ISBN 9781118935651.

25. Ishihara, T. *Perovskite Oxide for Solid Oxide Fuel Cells*; Ishihara, T., Ed.; Fuel Cells and Hydrogen Energy; Springer US: Boston, MA, 2009; ISBN 978-0-387-77707-8.

26. Jagodzinski, H. Eindimensionale Fehlordnung in Kristallen und ihr Einfluss auf die Röntgeninterferenzen. I. Berechnung des Fehlordnungsgrades aus den Röntgenintensitäten. *Acta Crystallogr.* **1949**, *2*, 201–207, doi:10.1107/S0365110X49000552.

27. Katz, L.; Ward, R. Structure Relations in Mixed Metal Oxides. *Inorg. Chem.* **1964**, *3*, 205–211, doi:10.1021/ic50012a013.

28. Clemens, O.; Gröting, M.; Witte, R.; Perez-Mato, J. M.; Loho, C.; Berry, F. J.; Kruk, R.; Knight, K. S.; Wright, A. J.; Hahn, H.; Slater, P. R. Crystallographic and magnetic structure of the perovskite-type compound $BaFeO_{2.5}$: Unrivaled complexity in oxygen vacancy ordering. *Inorg. Chem.* **2014**, *53*, 5911–5921, doi:10.1021/ic402988y.

29. Grenier, J.-C.; Wattiaux, A.; Pouchard, M.; Hagenmuller, P.; Parras, M.; Vallet, M.; Calbet, J.; Alario-Franco, M. A. Sur le système $BaFeO_{3-y}$ ($0 < y \leq 0.50$). *J. Solid State Chem.* **1989**, *80*, 6–11, doi:10.1016/0022-4596(89)90025-X.

30. Baranovskii, S.; Rubel, O. *Springer Handbook of Electronic and Photonic Materials*; Kasap, S., Capper, P., Eds.; Springer International Publishing: Cham, 2017; ISBN 978-3-319-48931-5.

31. Bockris, J. O.; Reddy, A. K. N. *Modern Electrochemistry 1: Ionics*; 1998; ISBN 0306455552.

32. Maier, J. *Physical Chemistry of Ionic Materials*; 2004; Vol. 1; ISBN 9780470020227.

33. Helgee, E. E.; Lindman, A.; Wahnström, G. Origin of Space Charge in Grain Boundaries of Proton-Conducting $BaZrO_3$. *Fuel Cells* **2013**, *13*, 19–28, doi:10.1002/fuce.201200071.

34. Iwahara, H.; Esaka, T.; Uchida, H.; Maeda, N. Proton Conduction in Sintered Oxides and its Application to Steam Electrolysis for Hydrogen Production. *Solid State Ionics* **1981**, *3/4*, 359–363.

35. Scholten, M. J.; Schoonman, J.; van Miltenburg, J. C.; Cordfunke, E. H. P. The thermodynamic properties of $BaCeO_3$ at temperatures from 5 to 940 K. *Thermochim. Acta* **1995**, *268*, 161–168, doi:10.1016/0040-6031(95)02431-X.

36. Scholten, M. J.; Schoonman, J.; van Miltenburg, J. C.; Oonk, H. A. J. Synthesis of strontium and barium cerate and their reaction with carbon dioxide. *Solid State Ionics* **1993**, *61*, 83–91, doi:10.1016/0167-2738(93)90338-4.

37. Tanner, C. W. Instability of $BaCeO_3$ in H_2O-Containing Atmospheres. *J. Electrochem. Soc.* **1996**, *143*, 1386, doi:10.1149/1.1836647.

38. Yajima, T. Protonic conduction in $SrZrO_3$-based oxides. *Solid State Ionics* **1992**, *51*, 101–107, doi:10.1016/0167-2738(92)90351-O.

39. Hibino, T.; Mizutani, K.; Yajima, T.; Iwahara, H. Evaluation of proton conductivity in $SrCeO_3$, $BaCeO_3$, $CaZrO_3$ and $SrZrO_3$ by temperature programmed desorption method. *Solid State Ionics* **1992**, *57*, 303–306, doi:10.1016/0167-2738(92)90162-I.

40. Pergolesi, D.; Fabbri, E.; D'Epifanio, A.; Di Bartolomeo, E.; Tebano, A.; Sanna, S.; Licoccia, S.; Balestrino, G.; Traversa, E. High proton conduction in grain-boundary-free yttrium-doped barium zirconate films grown by pulsed laser deposition. *Nat. Mater.* **2010**, *9*, 846–852, doi:10.1038/nmat2837.

41. Iwahara, H. Proton Conduction in Sintered Oxides Based on $BaCeO_3$. *J. Electrochem. Soc.* **1988**, *135*, 529, doi:10.1149/1.2095649.

42. Fukui, T.; Ohara, S.; Kawatsu, S. Conductivity of $BaPrO_3$ based perovskite oxides. *J. Power Sources* **1998**, *71*, 164–168, doi:10.1016/S0378-7753(97)02813-9.

43. Cook, R. L. Investigations on $BaTh_{0.9}Gd_{0.1}O_3$ as an Intermediate Temperature Fuel Cell Solid Electrolyte. *J. Electrochem. Soc.* **1992**, *139*, L19, doi:10.1149/1.2069273.

44. Valkenberg, S.; Bohn, H. G.; Schilling, W. The electrical conductivity of the high temperature proton conductor $Ba_3Ca_{1.18}Nb_{1.82}O_{9-\delta}$. *Solid State Ionics* **1997**, *97*, 511–515, doi:10.1016/S0167-2738(97)00051-9.

45. Fujii, H.; Katayama, Y.; Shimura, T.; Iwahara, H. Protonic Conduction in Perovskite-type Oxide Ceramics Based on $LnScO_3$ (Ln= La,. *J. Electroceramics* **1998**, *2*, 119–125, doi:10.1023/A:1009935208872.

46. Shimura, T. Protonic conduction in lanthanum strontium aluminate and lanthanum niobate-based oxides at elevated temperatures. *Solid State Ionics* **2002**, *154–155*, 653–658, doi:10.1016/S0167-2738(02)00514-3.

47. Li, S.; Schonberger, F.; Slater, P. $La_{1-x}Ba_{1+x}GaO_{4-x/2}$: a novel high temperature proton conductor. *Chem. Commun.* **2003**, *44*, 2694–2695.

48. Shimura, T.; Suzuki, K.; Iwahara, H. High temperature protonic conduction in Sr_2TiO_4-based ceramics with K_2NiF_4-type structure. *Solid State Ionics* **1997**, *104*, 79–88, doi:10.1016/S0167-2738(97)00394-9.

49. Animitsa, I.; Norby, T.; Marion, S.; Glöckner, R.; Neiman, A. Incorporation of water in

strontium tantalates with perovskite-related structure. *Solid State Ionics* **2001**, *145*, 357–364, doi:10.1016/S0167-2738(01)00931-6.

50. Glöckner, R.; Neiman, A.; Larring, Y.; Norby, T. Protons in $Sr_3(Sr_{1+x}Nb_{2-x})O_{9-3x/2}$ perovskite. *Solid State Ionics* **1999**, *125*, 369–376, doi:10.1016/S0167-2738(99)00197-6.

51. Zhang, G. B.; Smyth, D. M. Protonic conduction in $Ba_2In_2O_5$. *Solid State Ionics* **1995**, *82*, 153–160, doi:10.1016/0167-2738(95)00199-8.

52. Murugaraj, P. High proton conductivity in barium yttrium stannate $Ba_2YSnO_{5.5}$. *Solid State Ionics* **1997**, *98*, 1–6, doi:10.1016/S0167-2738(97)00102-1.

53. Shimura, T.; Fujimoto, S.; Iwahara, H. Proton conduction in non-perovskite-type oxides at elevated temperatures. *Solid State Ionics* **2001**, *143*, 117–123, doi:10.1016/S0167-2738(01)00839-6.

54. Amezawa, K.; Takahashi, N.; Kitamura, N.; Tomii, Y.; Yamamoto, N. High temperature protonic conduction in $LaBO_3$ with the aragonite-type structure. *Solid State Ionics* **2004**, *175*, 575–579, doi:10.1016/j.ssi.2004.02.079.

55. Shimura, T.; Komori, M.; Iwahara, H. Ionic conduction in pyrochlore-type oxides containing rare earth elements at high temperature. *Solid State Ionics* **1996**, *86–88*, 685–689, doi:10.1016/0167-2738(96)00148-8.

56. Amezawa, K. High temperature protonic conduction in Ca-doped YPO_4. *Solid State Ionics* **2003**, *162–163*, 175–180, doi:10.1016/S0167-2738(03)00223-6.

57. Amezawa, K.; Kitajima, Y.; Tomii, Y.; Yamamoto, N.; Widerøe, M.; Norby, T. Protonic conduction in acceptor-doped LaP_3O_9. *Solid State Ionics* **2005**, *176*, 2867–2870, doi:10.1016/j.ssi.2005.09.017.

58. Norby, T.; Christiansen, N. Proton conduction in Ca- and Sr-substituted $LaPO_4$. *Solid State Ionics* **1995**, *77*, 240–243, doi:10.1016/0167-2738(94)00274-V.

59. Haugsrud, R.; Norby, T. Proton conduction in rare-earth ortho-niobates and ortho-tantalates. *Nat. Mater.* **2006**, *5*, 193–196, doi:10.1038/nmat1591.

60. Kreuer, K. D. Proton Conductivity: Materials and Applications. *Chem. Mater.* **1996**, *8*, 610–641, doi:10.1021/cm950192a.

61. Kreuer, K. D. Proton-Conducting Oxides. *Annu. Rev. Mater. Res.* **2003**, *33*, 333–359, doi:10.1146/annurev.matsci.33.022802.091825.

62. Norby, T.; Widerøe, M.; Glöckner, R.; Larring, Y. Hydrogen in oxides. *Dalt. Trans.* **2004**, 3012–3018, doi:10.1039/B403011G.

63. Kreuer, K.-D.; Rabenau, A.; Weppner, W. Vehikel-Mechanismus, ein neues Modell zur Deutung der Leitfähigkeit schneller Protonenleiter. *Angew. Chemie* **2006**, *94*, 224–225, doi:10.1002/ange.19820940335.

64. Liu, Y.; Tan, X.; Li, K. Mixed Conducting Ceramics for Catalytic Membrane Processing. *Catal. Rev.* **2006**, *48*, 145–198, doi:10.1080/01614940600631348.

65. Samgin, A. L. Lattice-assisted proton motion in perovskite oxides. *Solid State Ionics* **2000**, *136–137*, 291–295, doi:10.1016/S0167-2738(00)00406-9.

66. Münch, W.; Kreuer, K. D.; Seifertli, G.; Majer, J. A quantum molecular dynamics study of proton diffusion in $SrTiO_3$ and $CaTiO_3$. *Solid State Ionics* **1999**, *125*, 39–45, doi:10.1016/S0167-2738(99)00156-3.

67. El-Aiat, M. M.; Kröger, F. A. Hydrogen donors in α-Al_2O_3. *J. Appl. Phys.* **1982**, *53*,

3658–3667, doi:10.1063/1.331150.

68. Okuyama, Y.; Kurita, N.; Futatsu, N. Proton Transport Properties in Single Crystal of α-Alumina. *J. MMIJ* **2009**, *125*, 3–8.

69. Knauth, P.; Di Vona, M. L. *Solid State Proton Conductors Properties and Applications in Fuel Cells*; Knauth, P., Di Vona, M. L., Eds.; John Wiley & Sons Ltd., 2012;

70. Krasnoholovets, V. V.; Tomchuk, P. M.; Lukyanets, S. P. Proton Transfer and Coherent Phenomena in Molecular Structures with Hydrogen Bonds. In; 2003; pp. 351–548.

71. *Membranes for Energy Conversion*; Peinemann, K.-V., Pereira Nunes, S., Eds.; Wiley-VCH Verlag GmbH & Co. KGaA: Weinheim, Germany, 2007; ISBN 9783527622146.

72. Filipovic, L.; Selberherr, S.; Mutinati, G. C.; Brunet, E.; Steinhauer, S.; Anton, K.; Teva, J.; Kraft, J.; Schrank, F. Modeling Spray Pyrolysis Deposition. *Proc. World Congr. Eng.* **2013**, *II*, 6–11.

73. Perednis, D. Thin film deposition by spray pyrolysis and the application in solid oxide fuel cells, 2003.

74. Bryant, W. A. The fundamentals of chemical vapour deposition. *J. Mater. Sci.* **1977**, *12*, 1285–1306, doi:10.1007/BF00540843.

75. Markov, I. V *Crystal Growth for Beginners*; WORLD SCIENTIFIC, 2017; ISBN 978-981-314-342-5.

76. Royer, L. Recherches expérimentales sur l'épitaxie ou orientation mutuelle des cristaux d'espèces différentes, 1928.

77. Darwin, C. G. XXXIV. The theory of X-ray reflexion. *London, Edinburgh, Dublin Philos. Mag. J. Sci.* **1914**, *27*, 315–333, doi:10.1080/14786440208635093.

78. Chaudhuri, J.; Shah, S. Thickness measurement of thin films by x-ray absorption. *J. Appl. Phys.* **1991**, *69*, 499–501, doi:10.1063/1.347691.

79. Barsoukov, E.; Macdonald, J. R. *Impedance Spectroscopy: Theory, Experiment, and Applications*; 2005; ISBN 0471647497.

80. Sinclair, D. C. Characterization of Electro-materials using ac Impedance Spectroscopy. *Ceram. y Vidr.* **1995**, *34*, 55–66.

81. Mulder, W. H.; Sluyters, J. H.; Pajkossy, T.; Nyikos, L. Tafel current at fractal electrodes. *J. Electroanal. Chem. Interfacial Electrochem.* **1990**, *285*, 103–115, doi:10.1016/0022-0728(90)87113-X.

82. Schiller, C. A.; Strunz, W. The evaluation of experimental dielectric data of barrier coatings by means of different models. *Electrochim. Acta* **2001**, *46*, 3619–3625, doi:10.1016/S0013-4686(01)00644-2.

83. Hirschorn, B.; Orazem, M. E.; Tribollet, B.; Vivier, V.; Frateur, I.; Musiani, M. Determination of effective capacitance and film thickness from constant-phase-element parameters. *Electrochim. Acta* **2010**, *55*, 6218–6227, doi:10.1016/j.electacta.2009.10.065.

84. Johnson, D. ZView: a Software Program for IES Analysis 2008.

85. Hsu, C. H.; Mansfeld, F. Technical Note: Concerning the Conversion of the Constant Phase Element Parameter Y_0 into a Capacitance. *CORROSION* **2001**, *57*, 747–748, doi:10.5006/1.3280607.

86. Shoar Abouzari, M. R.; Berkemeier, F.; Schmitz, G.; Wilmer, D. On the physical interpretation of constant phase elements. *Solid State Ionics* **2009**, *180*, 922–927,

doi:10.1016/j.ssi.2009.04.002.

87. Als-Nielsen, J.; McMorrow, D. *Elements of Modern X-ray Physics*; John Wiley & Sons, Inc.: Hoboken, NJ, USA, 2011; ISBN 9781119998365.

88. Song, Y.; Zavalij, P. Y.; Suzuki, M.; Whittingham, M. S.; Zhang, F.; Chen, R.; Greedan, J. E.; Raju, N. P.; Bieringer, M.; Pecharsky, V. K.; Gschneidner, K. A.; Decomposition, F. P.; Structure, C.; Methods, A. I.; Problem, T. I.; Preparation, P.; X-rays, W.; Cell, U.; New, S.; Dictionary, C.; Publ, M. C.; Edition, S.; Crystallographica, A. *Fundamentals of Powder Diffraction and Structural Characterization of Materials*; Springer US: Boston, MA, 2009; Vol. 940; ISBN 978-0-387-09578-3.

89. Birkholz, M. *Thin Film Analysis by X-Ray Scattering*; Wiley-VCH Verlag GmbH & Co. KGaA: Weinheim, FRG, 2005; ISBN 9783527607594.

90. Rietveld, H. M. A profile refinement method for nuclear and magnetic structures. *J. Appl. Crystallogr.* **1969**, *2*, 65–71, doi:10.1107/S0021889869006558.

91. Shirley, D. A. High-resolution x-ray photoemission spectrum of the valence bands of gold. *Phys. Rev. B* **1972**, *5*, 4709–4714, doi:10.1103/PhysRevB.5.4709.

92. Wagner, C. D.; Davis, L. E.; Zeller, M. V.; Taylor, J. A.; Raymond, R. H.; Gale, L. H. Empirical atomic sensitivity factors for quantitative analysis by electron spectroscopy for chemical analysis. *Surf. Interface Anal.* **1981**, *3*, 211–225, doi:10.1002/sia.740030506.

93. Moulder, J. F. *Handbook of X-ray Photoelectron Spectroscopy*; Physical Electronics, 1995;

94. ULVAC-PHI Inc. Operator's PHI MultiPak Software Manual 2010.

95. Thompson, K.; Lawrence, D.; Larson, D. J.; Olson, J. D.; Kelly, T. F.; Gorman, B. In situ site-specific specimen preparation for atom probe tomography. *Ultramicroscopy* **2007**, *107*, 131–139, doi:10.1016/j.ultramic.2006.06.008.

96. Larson, D. J.; Prosa, T. J.; Ulfig, R. M.; Geiser, B. P.; Kelly, T. F. *Local Electrode Atom Probe Tomography*; Springer, 2013;

97. CHOY, K. Vapor processing of nanostructured materials. In *Handbook of Nanostructured Materials and Nanotechnology*; Elsevier, 2000; pp. 533–577.

98. Schick, R. J. Spray Technology Reference Guide: Understanding Drop Size Preface. In *47th Chemical Processing Industry Exposition*; 1997; p. 6.

99. Kelly, A. J. Charge Injection Electrostatic Atomizer Modeling. *Aerosol Sci. Technol.* **1990**, *12*, 526–537, doi:10.1080/02786829008959367.

100. Benes, A.; Molinari, A.; Witte, R.; Kruk, R.; Brötz, J.; Chellali, R.; Hahn, H.; Clemens, O. Proton Conduction in Grain-Boundary-Free Oxygen-Deficient $BaFeO_{2.5+\delta}$ Thin Films. *Materials (Basel)*. **2017**, *11*, 52, doi:10.3390/ma11010052.

101. Benedek, N. A.; Fennie, C. J. Why Are There So Few Perovskite Ferroelectrics? *J. Phys. Chem. C* **2013**, *117*, 13339–13349, doi:10.1021/jp402046t.

102. Benel, C.; Darbandi, A. J.; Djenadic, R.; Evans, A.; Tölke, R.; Prestat, M.; Hahn, H. Synthesis and characterization of nanoparticulate $La_{0.6}Sr_{0.4}CoO_{3-\delta}$ cathodes for thin-film solid oxide fuel cells. *J. Power Sources* **2013**, *229*, 258–264, doi:10.1016/j.jpowsour.2012.11.149.

103. Liu, H.; Yang, X. A brief review on perovskite multiferroics. *Ferroelectrics* **2017**, *507*, 69–85, doi:10.1080/00150193.2017.1283171.

104. Matsui, T.; Taketani, E.; Fujimura, N.; Ito, T.; Morii, K. Magnetic and Dielectric

Properties of Epitaxially Grown $BaFeO_3$ Thin Films on $SrTiO_3$ Single-Crystal Substrates. *Korean Phys. Soc.* **2003**, *42*, 1378–1381.

105. Hayashi, N.; Yamamoto, T.; Kageyama, H.; Nishi, M.; Watanabe, Y.; Kawakami, T.; Matsushita, Y.; Fujimori, A.; Takano, M. $BaFeO_3$: A Ferromagnetic Iron Oxide**. *Angew. Chemie Int. Ed.* **2011**, *50*, 12547–12550, doi:10.1002/anie.201105276.

106. Suga, Y.; Hibino, M.; Kudo, T.; Mizuno, N. Electrochemical Oxidation of $BaFeO_{2.5}$ to $BaFeO_3$. *Electrochim. Acta* **2014**, *137*, 359–362, doi:10.1016/j.electacta.2014.05.162.

107. Parras, M.; Vallet-Regi, M.; González-Calbet, J. M.; Grenier, J. C. Oxygen vacancy distribution in 6H$BaFeO_{3-y}$ ($0.2 \leq y \leq 0$). *J. Solid State Chem.* **1989**, *83*, 121–131, doi:10.1016/0022-4596(89)90061-3.

108. Parras, M.; Vallet-Regi, M.; Gonzalez-Calbet, J. M.; Alario-Franco, M. A.; Grenier, J. C.; Hagenmuller, P. A reassessment of $Ba_2Fe_2O_5$. *Mater. Res. Bull.* **1987**, *22*, 1413–1419, doi:10.1016/0025-5408(87)90306-0.

109. Parras, M.; Fournes, L.; Grenier, J. C.; Pouchard, M.; Vallet, M.; Calbet, J. M.; Hagenmuller, P. Structural aspects and Mößbauer resonance investigation of $Ba_2Fe_2O_5$. *J. Solid State Chem.* **1990**, *88*, 261–268, doi:10.1016/0022-4596(90)90223-K.

110. Mori, K.; Kamiyama, T.; Kobayashi, H.; Otomo, T.; Nishiyama, K.; Sugiyama, M.; Itoh, K.; Fukunaga, T.; Ikeda, S. Mixed magnetic phase in 6H-type $BaFeO_{3-\delta}$. *J. Appl. Crystallogr.* **2007**, *40*, 501–505, doi:10.1107/S0021889807001653.

111. Taketani, E.; Matsui, T.; Fujimura, N.; Morii, K.; Taketani, E.; Matsui, T.; Fujimura, N.; Morii, K. Effect of Oxygen Deficiencies on Magnetic Properties of Epitaxial Grown $BaFeO_3$ Thin Films on (100) $SrTiO_3$ Substrates. *IEEE Trans. Magn.* **2004**, *40*, 2736–2738, doi:10.1109/TMAG.2004.830168.

112. Callender, C.; Norton, D. P.; Das, R.; Hebard, a. F.; Budai, J. D. Ferromagnetism in pseudocubic $BaFeO_3$ epitaxial films. *Appl. Phys. Lett.* **2008**, *92*, 012514, doi:10.1063/1.2832768.

113. Chen, C.-T.; Danel, C. E.; Kim, S. On the origin of the blocking effect of grain-boundaries on proton transport in yttrium-doped barium zirconates. *J. Mater. Chem.* **2011**, *21*, 5435, doi:10.1039/c0jm03353g.

114. Fischer, W. Structural transformation of the oxygen and proton conductor $Ba_2In_2O_5$ in humid air: an in-situ X-ray powder diffraction study. *Solid State Ionics* **1999**, *116*, 211–215, doi:10.1016/S0167-2738(98)00405-6.

115. Sukkurji, P. A.; Molinari, A.; Benes, A.; Loho, C.; Chakravadhanula, V. S. K.; Garlapati, S. K.; Kruk, R.; Clemens, O. Structure and conductivity of epitaxial thin films of barium ferrite and its hydrated form $BaFeO_{2.5-x+\delta}(OH)_{2x}$. *J. Phys. D. Appl. Phys.* **2017**, *50*, 115302, doi:10.1088/1361-6463/aa5718.

116. Nair, A. Unpublished Master Thesis, Technische Universität Darmstadt, 2019.

117. Nowroozi, M. A.; Ivlev, S.; Rohrer, J.; Clemens, O. La_2CoO_4 : a new intercalation based cathode material for fluoride ion batteries with improved cycling stability. *J. Mater. Chem. A* **2018**, *6*, 4658–4669, doi:10.1039/C7TA09427B.

118. Adler, S. B. Chemical Expansivity of Electrochemical Ceramics. *J. Am. Ceram. Soc.* **2004**, *84*, 2117–2119, doi:10.1111/j.1151-2916.2001.tb00968.x.

119. Sander, D.; Tian, Z.; Kirschner, J. Cantilever measurements of surface stress, surface reconstruction, film stress and magnetoelastic stress of monolayers. *Sensors* **2008**, *8*, 4466–4486, doi:10.3390/s8074466.

120. Shannon, R. D. Revised effective ionic radii and systematic studies of interatomic distances in halides and chalcogenides. *Acta Crystallogr. Sect. A* **1976**, *32*, 751–767, doi:10.1107/S0567739476001551.

121. Walsh, A.; Catlow, C. R. A.; Zhang, K. H. L.; Egdell, R. G. Control of the band-gap states of metal oxides by the application of epitaxial strain: The case of indium oxide. *Phys. Rev. B - Condens. Matter Mater. Phys.* **2011**, *83*, 1–4, doi:10.1103/PhysRevB.83.161202.

122. Strasser, P.; Koh, S.; Anniyev, T.; Greeley, J.; More, K.; Yu, C.; Liu, Z.; Kaya, S.; Nordlund, D.; Ogasawara, H.; Toney, M. F.; Nilsson, A. Lattice-strain control of the activity in dealloyed core–shell fuel cell catalysts. *Nat. Chem.* **2010**, *2*, 454–460, doi:10.1038/nchem.623.

123. Li, S.; Ding, X.; Ren, J.; Moya, X.; Li, J.; Sun, J.; Salje, E. K. H. Strain-controlled thermal conductivity in ferroic twinned films. *Sci. Rep.* **2015**, *4*, 6375, doi:10.1038/srep06375.

124. Kilner, J. A. Ionic conductors: Feel the strain. *Nat. Mater.* **2008**, *7*, 838–839, doi:10.1038/nmat2314.

125. Birkholz, M.; Fewster, P. F. High-Resolution X-ray Diffraction. In *Thin Film Analysis by X-Ray Scattering*; Wiley-VCH Verlag GmbH & Co. KGaA: Weinheim, FRG, 2006; pp. 297–341 ISBN 3527310525.

126. Abadias, G.; Chason, E.; Keckes, J.; Sebastiani, M.; Thompson, G. B.; Barthel, E.; Doll, G. L.; Murray, C. E.; Stoessel, C. H.; Martinu, L. Review Article: Stress in thin films and coatings: Current status, challenges, and prospects. *J. Vac. Sci. Technol. A Vacuum, Surfaces, Film.* **2018**, *36*, 020801, doi:10.1116/1.5011790.

127. Frentrup, M.; Hatui, N.; Wernicke, T.; Stellmach, J.; Bhattacharya, A.; Kneissl, M. Determination of lattice parameters, strain state and composition in semipolar III-nitrides using high resolution X-ray diffraction. *J. Appl. Phys.* **2013**, *114*, 213509, doi:10.1063/1.4834521.

128. De Jong, M.; Chen, W.; Angsten, T.; Jain, A.; Notestine, R.; Gamst, A.; Sluiter, M.; Ande, C. K.; Van Der Zwaag, S.; Plata, J. J.; Toher, C.; Curtarolo, S.; Ceder, G.; Persson, K. A.; Asta, M. Charting the complete elastic properties of inorganic crystalline compounds. *Sci. Data* **2015**, *2*, 1–13, doi:10.1038/sdata.2015.9.

129. Kossoy, A.; Wachtel, E.; Lubomirsky, I. On the poisson ratio and XRD determination of strain in thin films of $Ce_{0.8}Gd_{0.2}O_{1.9}$. *J. Electroceramics* **2014**, *32*, 47–50, doi:10.1007/s10832-013-9835-7.

130. Fluri, A.; Schneider, C. W.; Pergolesi, D. In situ stress measurements of metal oxide thin films. In *Metal Oxide-Based Thin Film Structures*; Elsevier, 2018; pp. 109–132 ISBN 9780128111666.

131. Fluri, A.; Marcolongo, A.; Roddatis, V.; Wokaun, A.; Pergolesi, D.; Marzari, N.; Lippert, T. Enhanced Proton Conductivity in Y-Doped $BaZrO_3$ via Strain Engineering. *Adv. Sci.* **2017**, *1700467*, 1700467, doi:10.1002/advs.201700467.

132. Münch, W.; Kreuer, K. D.; Adams; Seifert, G.; Maier, J. The relation between crystal structure and the formation and mobility of protonic charge carriers in perovskite-type oxides: A case study of Y-doped $BaCeO_3$ and $SrCeO_3$. *Phase Transitions* **1999**, *68*, 567–586, doi:10.1080/01411599908224535.

133. Jacobson, A. J. A powder neutron diffraction study of the structure of and oxygen vacancy distribution in 6H $BaFeO_{2.79}$. *Acta Crystallogr. Sect. B Struct. Crystallogr. Cryst. Chem.* **1976**, *32*, 1087–1090, doi:10.1107/S056774087600472X.

134. Wang, Y.; Zhang, M.; Meletis, E. On the Novel Biaxial Strain Relaxation Mechanism in Epitaxial Composition Graded $La_{1-x}Sr_xMnO_3$ Thin Film Synthesized by RF Magnetron Sputtering. *Coatings* **2015**, *5*, 802–815, doi:10.3390/coatings5040802.

135. Gregori, G.; Lupetin, P.; Maier, J. Huge Electrical Conductivity Changes in $SrTiO_3$ upon Reduction of the Grain Size to the Nanoscale. *ECS Trans.* **2012**, *45*, 19–24, doi:10.1149/1.3701289.

136. Menil, F. Systematic trends of the 57Fe Mößbauer isomer shifts in (FeOn) and (FeFn) polyhedra. Evidence of a new correlation between the isomer shift and the inductive effect of the competing bond T-X (→ Fe) (where X is O or F and T any element with a formal posit. *J. Phys. Chem. Solids* **1985**, *46*, 763–789, doi:10.1016/0022-3697(85)90001-0.

137. Anderson, M. T.; Vaughey, J. T.; Poeppelmeier, K. R. Structural Similarities among Oxygen-Deficient Perovskites. *Chem. Mater.* **1993**, *5*, 151–165, doi:10.1021/cm00026a003.

138. Clemens, O.; Haberkorn, R.; Slater, P. R.; Beck, H. P. Synthesis and characterisation of the $Sr_xBa_{1-x}FeO_{3-y}$-system and the fluorinated phases $Sr_xBa_{1-x}FeO_{2F}$. *Solid State Sci.* **2010**, *12*, 1455–1463, doi:10.1016/j.solidstatesciences.2010.06.002.

139. Poeppelmeier, K. R.; Leonowicz, M. E.; Longo, J. M. $CaMnO_{2.5}$ and $Ca_2MnO_{3.5}$: New Oxygen-Defect Perovskite-Type Oxides. *J. Solid State Chem.* **1982**, *44*, 89–98.

140. Parras, M.; Gonzalezcalbet, J.; Valletregi, M.; Grenier, J. A high temperature study of the $BaFeO_{3-y}$ system. *Solid State Ionics* **1993**, *63–65*, 714–718, doi:10.1016/0167-2738(93)90185-6.

141. Fournès, L.; Potin, Y.; Grenier, J.; Demazeau, G.; Pouchard, M. High temperature Mößbauer spectroscopy of some $SrFeO_{3-y}$ phases. *Solid State Commun.* **1987**, *62*, 239–244, doi:10.1016/0038-1098(87)90803-9.

142. Miot, C.; Husson, E.; Proust, C.; Erre, R.; Coutures, J. P. X-ray photoelectron spectroscopy characterization of barium titanate ceramics prepared by the citric route. Residual carbon study. *J. Mater. Res.* **1997**, *12*, 2388–2392, doi:10.1557/JMR.1997.0316.

143. Sosulnikov, M. I.; Teterin, Y. A. X-ray photoelectron studies of Ca, Sr and Ba and their oxides and carbonates. *J. Electron Spectros. Relat. Phenomena* **1992**, *59*, 111–126, doi:10.1016/0368-2048(92)85002-O.

144. Christie, A. B.; Lee, J.; Sutherland, I.; Walls, J. M. An XPS study of ion-induced compositional changes with group II and group IV compounds. *Appl. Surf. Sci.* **1983**, *15*, 224–237, doi:10.1016/0378-5963(83)90018-1.

145. García-Zaldívar, O.; Díaz-Castañón, S.; Espinosa-Beltrán, F. J.; Hernández-Landaverde, M. A.; López, G.; Faloh-Gandarilla, J.; Calderón-Piñar, F. $BiFeO_3$ codoping with Ba , La and Ti : Magnetic and structural studies. *J. Adv. Dielectr.* **2015**, *5*, 1–8, doi:10.1142/S2010135X15500344.

146. Fang, L.; Liu, J.; Ju, S.; Zheng, F.; Dong, W.; Shen, M. Experimental and theoretical evidence of enhanced ferromagnetism in sonochemical synthesized $BiFeO_3$ nanoparticles. *Appl. Phys. Lett.* **2010**, *97*, 242501, doi:10.1063/1.3525573.

147. Chakrabarti, S.; Ginnaram, S.; Jana, S.; Wu, Z.-Y.; Singh, K.; Roy, A.; Kumar, P.; Maikap, S.; Qiu, J.-T.; Cheng, H.-M.; Tsai, L.-N.; Chang, Y.-L.; Mahapatra, R.; Yang, J.-R. Negative voltage modulated multi-level resistive switching by using a Cr/$BaTiO_x$/TiN structure and quantum conductance through evidence of H_2O_2 sensing mechanism. *Sci. Rep.* **2017**, *7*, 4735, doi:10.1038/s41598-017-05059-9.

148. Jensen, W. B. Holleman-Wiberg's Inorganic Chemistry (edited by Wiberg, Nils). *J. Chem. Educ.* **2002**, *79*, 944, doi:10.1021/ed079p944.

149. Siegbahn, C.; Fahlman, A.; Nordberg, R. ESCA: atomic, molecular and solid state structure studied by means of electron spectroscopy. *Nov. Acta Regiae Soc. Sci. Ups.* **1967**, *Series IV*.

150. Yang, Y.; Jiang, Y.; Wang, Y.; Sun, Y. Photoinduced decomposition of $BaFeO_3$ during photodegradation of methyl orange. *J. Mol. Catal. A Chem.* **2007**, *270*, 56–60, doi:10.1016/j.molcata.2007.01.033.

151. Bhargava, G.; Gouzman, I.; Chun, C. M.; Ramanarayanan, T. A.; Bernasek, S. L. Characterization of the "native" surface thin film on pure polycrystalline iron : A high resolution XPS and TEM study. *Appl. Surf. Sci.* **2007**, *253*, 4322–4329, doi:10.1016/j.apsusc.2006.09.047.

152. Grosvenor, A. P.; Kobe, B. A.; Biesinger, M. C.; McIntyre, N. S. Investigation of multiplet splitting of Fe 2p XPS spectra and bonding in iron compounds. *Surf. Interface Anal.* **2004**, *36*, 1564–1574, doi:10.1002/sia.1984.

153. Seah, M. P.; Dench, W. A. Quantitative electron spectroscopy of surfaces: A standard data base for electron inelastic mean free paths in solids. *Surf. Interface Anal.* **1979**, *1*, 2–11, doi:10.1002/sia.740010103.

154. Gupta, D.; Lacey, J. A.; Laibowitz, R. B. Migration of Sr at the $YBa_2Cu_3O_{7-\delta}$ Epitaxial Film and (100) $SrTiO_3$ Substrate Interface. *Defect Diffus. Forum* **1991**, *75*, 79–88, doi:10.4028/www.scientific.net/DDF.75.79.

155. Fuks, D.; Mastrikov, Y.; Kotomin, E.; Maier, J. Ab initio thermodynamic study of (Ba,Sr)(Co,Fe)O_3 perovskite solid solutions for fuel cell applications. *J. Mater. Chem. A* **2013**, *1*, 14320, doi:10.1039/c3ta12874a.

156. Lee, S. H.; Frawley, T. W.; Yao, C. H.; Lai, Y. C.; Du, C. H.; Hatton, P. D.; Wang, M. J.; Chou, F. C.; Huang, D. J. Charge and spin coupling in magnetoresistive oxygen-vacancy strontium ferrate $SrFeO_{3-\delta}$. *New J. Phys.* **2016**, *18*, doi:10.1088/1367-2630/18/9/093033.

157. Bjørheim, T. S.; Rahman, S. M. H.; Eriksson, S. G.; Knee, C. S.; Haugsrud, R. Hydration thermodynamics of the proton conducting oxygen-deficient perovskite series $BaTi_{1-x}M_xO_{3-x/2}$ with M = In or Sc. *Inorg. Chem.* **2015**, *54*, 2858–2865, doi:10.1021/ic503006u.

158. Merkle, R.; Poetzsch, D.; Maier, J. (Invited) Oxygen Reduction Reaction at Cathodes on Proton Conducting Oxide Electrolytes: Contribution from Three Phase Boundary Compared to Bulk Path. *ECS Trans.* **2015**, *66*, 95–102, doi:10.1149/06602.0095ecst.

159. Liu, X.; Zhao, H.; Yang, J.; Li, Y.; Chen, T.; Lu, X.; Ding, W.; Li, F. Lattice characteristics, structure stability and oxygen permeability of $BaFe_{1-x}Y_xO_{3-\delta}$ ceramic membranes. *J. Memb. Sci.* **2011**, *383*, 235–240, doi:10.1016/j.memsci.2011.08.059.

160. Schichtel, N.; Korte, C.; Hesse, D.; Janek, J. Elastic strain at interfaces and its influence on ionic conductivity in nanoscaled solid electrolyte thin films—theoretical considerations and experimental studies. *Phys. Chem. Chem. Phys.* **2009**, *11*, 3043, doi:10.1039/b900148d.

161. Kim, Y. B.; Gür, T. M.; Jung, H. J.; Kang, S.; Sinclair, R.; Prinz, F. B. Effect of crystallinity on proton conductivity in yttrium-doped barium zirconate thin films. *Solid State Ionics* **2011**, *198*, 39–46, doi:10.1016/j.ssi.2011.07.004.

162. Rahman, S. M. H.; Norberg, S. T.; Knee, C. S.; Biendicho, J. J.; Hull, S.; Eriksson, S. G.

Proton conductivity of hexagonal and cubic $BaTi_{1-x}Sc_xO_{3-\delta}$ ($0.1 \leq x \leq 0.8$). *Dalt. Trans.* **2014**, *43*, 15055–15064, doi:10.1039/C4DT01280A.

163. Fluri, A.; Gilardi, E.; Karlsson, M.; Roddatis, V.; Bettinelli, M.; Castelli, I. E.; Lippert, T.; Pergolesi, D. Anisotropic Proton and Oxygen Ion Conductivity in Epitaxial $Ba_2In_2O_5$ Thin Films. *J. Phys. Chem. C* **2017**, *121*, 21797–21805, doi:10.1021/acs.jpcc.7b02497.

164. Song, S.; Placido, F. The influence of phase probability distributions on impedance spectroscopy. *J. Stat. Mech. Theory Exp.* **2004**, *2004*, P10018, doi:10.1088/1742-5468/2004/10/P10018.

165. Duval, S. B. C.; Holtappels, P.; Stimming, U.; Graule, T. Effect of minor element addition on the electrical properties of $BaZr_{0.9}Y_{0.1}O_{3-\delta}$. *Solid State Ionics* **2008**, *179*, 1112–1115, doi:10.1016/j.ssi.2007.11.030.

166. Iguchi, F.; Sata, N.; Tsurui, T.; Yugami, H. Microstructures and grain boundary conductivity of $BaZr_{1-x}Y_xO_3$ (x=0.05, 0.10, 0.15) ceramics. *Solid State Ionics* **2007**, *178*, 691–695, doi:10.1016/j.ssi.2007.02.019.

167. Kjølseth, C.; Fjeld, H.; Prytz, Ø.; Dahl, P. I.; Estournès, C.; Haugsrud, R.; Norby, T. Space–charge theory applied to the grain boundary impedance of proton conducting $BaZr_{0.9}Y_{0.1}O_{3-\delta}$. *Solid State Ionics* **2010**, *181*, 268–275, doi:10.1016/j.ssi.2010.01.014.

168. Waidha, A. I.; Lepple, M.; Wissel, K.; Benes, A.; Wollstadt, S.; Slater, P. R.; Fortes, A. D.; Clemens, O. Synthesis, structure and electrical conductivity of a new perovskite type barium cobaltate $BaCoO_{1.80}(OH)_{0.86}$. *Dalt. Trans.* **2018**, *47*, 11136–11145, doi:10.1039/C8DT01326H.

169. Kreuer, K. D.; Adams, S.; Münch, W.; Fuchs, A.; Klock, U.; Maier, J. Proton conducting alkaline earth zirconates and titanates for high drain electrochemical applications. *Solid State Ionics* **2001**, *145*, 295–306, doi:10.1016/S0167-2738(01)00953-5.

170. Duval, S. B. C.; Holtappels, P.; Vogt, U. F.; Pomjakushina, E.; Conder, K.; Stimming, U.; Graule, T. Electrical conductivity of the proton conductor $BaZr_{0.9}Y_{0.1}O_{3-\delta}$ obtained by high temperature annealing. *Solid State Ionics* **2007**, *178*, 1437–1441, doi:10.1016/j.ssi.2007.08.006.

171. Schober, T. Water vapor solubility and electrochemical characterization of the high temperature proton conductor $BaZr_{0.9}Y_{0.1}O_{2.95}$. *Solid State Ionics* **2000**, *127*, 351–360, doi:10.1016/S0167-2738(99)00283-0.

172. Yamazaki, Y.; Hernandez-Sanchez, R.; Haile, S. M. High Total Proton Conductivity in Large-Grained Yttrium-Doped Barium Zirconate. *Chem. Mater.* **2009**, *21*, 2755–2762, doi:10.1021/cm900208w.

173. Tao, S.; Irvine, J. T. S. Conductivity studies of dense yttrium-doped $BaZrO_3$ sintered at 1325°C. *J. Solid State Chem.* **2007**, *180*, 3493–3503, doi:10.1016/j.jssc.2007.09.027.

174. Arab Pour Yazdi, M.; Briois, P.; Georges, S.; Billard, A. Electrical and structural investigations of perovskite structure reactively sputter deposited coatings. *Solid State Ionics* **2009**, *180*, 1246–1251, doi:10.1016/j.ssi.2009.07.008.

175. Arab Pour Yazdi, M.; Briois, P.; Georges, S.; Shaula, A. L.; Cavaleiro, A.; Billard, A. Comparison of Structural and Electrical Properties of Barium Zirconate Pellets and Thin Films. *J. Electrochem. Soc.* **2010**, *157*, B1582, doi:10.1149/1.3482032.

176. Bae, H.; Lee, Y.; Kim, K. J.; Choi, G. M. Effects of Fabrication Conditions on the Crystallinity, Barium Deficiency, and Conductivity of $BaZr_{0.8}Y_{0.2}O_{3-\delta}$ Films Grown by Pulsed Laser Deposition. *Fuel Cells* **2015**, *15*, 408–415, doi:10.1002/fuce.201400004.

177. Bae, K.; Jang, D. Y.; Choi, S. M.; Kim, B. K.; Lee, J. H.; Son, J. W.; Shim, J. H. Influence

of background oxygen pressure on film properties of pulsed laser deposited Y:$BaZrO_3$. *Thin Solid Films* **2014**, *552*, 24–31, doi:10.1016/j.tsf.2013.12.006.

178. Chang, I.; Paek, J. Y.; Cha, S. W. Parametric study of Y-doped $BaZrO_3$ thin film deposited via pulsed laser deposition. *J. Vac. Sci. Technol. A Vacuum, Surfaces, Film.* **2015**, *33*, 021515, doi:10.1116/1.4905775.

179. Somroop, K.; Pornprasertsuk, R.; Jinawath, S. Fabrication of Y_2O_3-doped $BaZrO_3$ thin films by electrostatic spray deposition. *Thin Solid Films* **2011**, *519*, 6408–6412, doi:10.1016/j.tsf.2011.04.125.

180. Takahashi, T.; Iguchi, F.; Yugami, H.; Esashi, M.; Tanaka, S. Fabrication of Proton-Conductive Bzy-Based Low-Temperature Micro Solid Oxide Fuel Cell. *Measurement* **2009**, 482–485.

181. Somroop, K.; Pornprasertsuk, R. Fabrication of proton conducting Y_2O_3-doped $BaZrO_3$ thin films by electrostatic spray deposition. In *Nanoelectronics Conference (INEC), 2010 3rd International*; 2010; pp. 974–975.

182. Peng, C.; Melnik, J.; Li, J.; Luo, J.; Sanger, A. R.; Chuang, K. T. ZnO-doped $BaZr_{0.85}Y_{0.15}O_{3-\delta}$ proton-conducting electrolytes: Characterization and fabrication of thin films. *J. Power Sources* **2009**, *190*, 447–452, doi:10.1016/j.jpowsour.2009.01.020.

183. Schneller, T.; Schober, T. Chemical solution deposition prepared dense proton conducting Y-doped $BaZrO_3$ thin films for SOFC and sensor devices. *Solid State Ionics* **2003**, *164*, 131–136, doi:10.1016/S0167-2738(03)00308-4.

184. Ganster, R.; Hoffmann-Eifert, S.; Waser, R. Characterization of $BaTiO_3$ --$BaZrO_3$ Solid Solution Thin Films Prepared by MOCVD. *Integr. Ferroelectr.* **2003**, *55*, 795–805, doi:10.1080/10584580390259245.

185. Pornprasertsuk, R.; Kosasang, O.; Somroop, K.; Horprathum, M.; Limnonthakul, P.; Chindaudom, P.; Jinawath, S. Proton conductivity of Y-doped $BaZrO_3$: Pellets and thin films. *Solid State Sci.* **2011**, *13*, 1429–1437, doi:10.1016/j.solidstatesciences.2011.04.015.

186. Gonçalves, M. D.; Maram, P. S.; Muccillo, R.; Navrotsky, A. Enthalpy of formation and thermodynamic insights into yttrium doped $BaZrO_3$. *J. Mater. Chem. A* **2014**, *2*, 17840–17847, doi:10.1039/c4ta03487b.

187. Sénateur, J.-P.; Dubourdieu, C.; Galindo, V.; Weiss, F.; Abrutis, A. Application of Pulsed Injection MOCVD to the Deposition of Oxide Single Layers and Superlattices. In *Innovative Processing of Films and Nanocrystalline Powders*; Published by Imperial College Press and Distributed by World Scientific Publishing Co., 2002; pp. 71–105.

188. Loho, C.; Djenadic, R.; Bruns, M.; Clemens, O.; Hahn, H. Garnet-Type $Li_7La_3Zr_2O_{12}$ Solid Electrolyte Thin Films Grown by CO_2-Laser Assisted CVD for All-Solid-State Batteries. *J. Electrochem. Soc.* **2017**, *164*, A6131–A6139, doi:10.1149/2.0201701jes.

189. Loho, C.; Djenadic, R.; Mundt, P.; Clemens, O.; Hahn, H. On processing-structure-property relations and high ionic conductivity in garnet-type $Li_5La_3Ta_2O_{12}$ solid electrolyte thin films grown by CO_2-laser assisted CVD. *Solid State Ionics* **2017**, *313*, 32–44, doi:10.1016/j.ssi.2017.11.005.

190. Loho, C.; Darbandi, A. J.; Djenadic, R.; Clemens, O.; Hahn, H. CO_2-Laser Flash Evaporation as Novel CVD Precursor Delivery System for Functional Thin Film Growth. *Chem. Vap. Depos.* **2014**, *20*, 152–160, doi:10.1002/cvde.201307089.

191. Jones, A. C. MOCVD of Electroceramic Oxides: A Precursor Manufacturer's Perspective. *Chem. Vap. Depos.* **1998**, *4*, 169–179, doi:10.1002/(sici)1521-

3862(199810)04:05<169::aid-cvde169>3.0.co;2-6.

192. Patel, C. K. N. Continuous-Wave Laser Action on Vibrational-Rotational Transitions of CO_2. *Phys. Rev.* **1964**, *136*, A1187–A1193, doi:10.1103/PhysRev.136.A1187.

193. Uno, K. Longitudinally Excited CO_2 Laser. In *Laser Pulses - Theory, Technology, and Applications*; InTech, 2012; Vol. 2, p. 64 ISBN 9789537619992.

194. Mojić-Lanté, B.; Djenadic, R.; Srdić, V. V.; Hahn, H. Direct preparation of ultrafine $BaTiO_3$ nanoparticles by chemical vapor synthesis. *J. Nanoparticle Res.* **2014**, *16*, 2618, doi:10.1007/s11051-014-2618-5.

195. Mojić-Lanté, B.; Djenadic, R.; Chakravadhanula, V. S. K.; Kübel, C.; Srdić, V. V.; Hahn, H. Chemical Vapor Synthesis of FeO_x-$BaTiO_3$ Nanocomposites. *J. Am. Ceram. Soc.* **2015**, *98*, 1724–1730, doi:10.1111/jace.13531.

196. Loho, C. Advanced Chemical Vapor Deposition Methods for All-Solid-State , Conversion-Type and 3D Li-Ion Battery Concepts, Technische Universität Darmstadt, 2018.

197. Arvanitidis, I.; Siche, D.; Seetharaman, S. A study of the thermal decomposition of $BaCO_3$. *Metall. Mater. Trans. B* **1996**, *27*, 409–416, doi:10.1007/BF02914905.

198. Robie, A. R.; Hemingway, B. S. *Thermodynamic properties of minerals and related substances at 298.15 K and 1 bar (105 pascals) pressure and at higher temperatures*; 1995;

199. Morss, L. R.; Day, P. P.; Felinto, C.; Brito, H. Standard molar enthalpies of formation of Y_2O_3, Ho_2O_3, and Er_2O_3 at the temperature 298.15 K. *J. Chem. Thermodyn.* **1993**, *25*, 415–422, doi:10.1006/jcht.1993.1045.

200. Goldstein, H. W.; Neilson, E. F.; Walsh, P. N. David White: The Heat Capacities Yttrium Oxide(Y_2O_3) Lanthanum Oxide (La_2O_3), and Neodymium Oxide (Nd_2O_3) from 16 to 300°K. *J. Phys. Chem.* **1959**, *63*, 1445–1449, doi:10.1021/j150579a028.

201. Kurosaki, K.; Konings, R. J. M.; Wastin, F.; Yamanaka, S. The low-temperature heat capacity and entropy of $SrZrO_3$ and $BaZrO_3$. *J. Alloys Compd.* **2006**, *424*, 1–3, doi:10.1016/j.jallcom.2005.09.096.

202. Huntelaar, M. E.; Booij, A. S.; Cordfunke, E. H. P. The standard molar enthalpies of formation of $BaZrO_3$(s) and $SrZrO_3$(s). *J. Chem. Thermodyn.* **1994**, *26*, 1095–1101, doi:10.1006/jcht.1994.1127.

203. Pashin, S. F.; Tretyakov, Y. D. Thermodynamics of Y-Ba-Cu-O System and Related Aspects. In *Chemistry of High Temperature Superconductors*; WORLD SCIENTIFIC, 1991; pp. 306–347 ISBN 978-981-02-0805-9.

204. Deschanvres, J. L.; Meffre, W.; Joubert, J. C.; Senateur, J. P.; Robaut, F.; Broquin, J. E.; Rimet, R. Rare earth-doped alumina thin films deposited by liquid source CVD processes. *J. Alloys Compd.* **1998**, *275–277*, 742–745, doi:10.1016/S0925-8388(98)00433-2.

205. Maki, K.; Komiya, N.; Suzuki, A. Fabrication of thin films of ITO by aerosol CVD. *Thin Solid Films* **2003**, *445*, 224–228, doi:10.1016/j.tsf.2003.08.021.

206. Jergel, M. Synthesis of high-T_c superconducting films by deposition from an aerosol. *Supercond. Sci. Technol.* **1995**, *8*, 67–78, doi:10.1088/0953-2048/8/2/001.

207. Song, H. Aerosol-assisted MOCVD growth of Gd_2O_3-doped CeO_2 thin SOFC electrolyte film on anode substrate. *Solid State Ionics* **2003**, *156*, 249–254, doi:10.1016/S0167-2738(02)00688-4.

208. Hou, X.; Choy, K.-L. Processing and Applications of Aerosol-Assisted Chemical Vapor Deposition. *Chem. Vap. Depos.* **2006**, *12*, 583–596, doi:10.1002/cvde.200600033.

209. Pornprasertsuk, R.; Piyaworapaiboon, M.; Jinawath, S. Fabrication of Y-doped barium cerium zirconate thin films by electrostatic spray deposition technique for protonic ceramic fuel cell application. *Ceram. Int.* **2014**, *40*, 9319–9326, doi:10.1016/j.ceramint.2014.01.155.

210. Sun, H.; Wang, C.; Pang, S.; Li, X.; Tao, Y.; Tang, H.; Liu, M. Photocatalytic TiO_2 films prepared by chemical vapor deposition at atmosphere pressure. *J. Non. Cryst. Solids* **2008**, *354*, 1440–1443, doi:10.1016/j.jnoncrysol.2007.01.108.

211. Dubach, D. B. A.; Gauckler, A. R. S. L. J. Spray pyrolysis of $La_{0.6}Sr_{0.4}Co_{0.2}Fe_{0.8}O_{3-\delta}$ thin film cathodes. *J. Electroceramics* **2006**, 221–228, doi:10.1007/s10832-006-6971-3.

212. Goretta, K. C.; Park, E. T.; Koritala, R. E.; Cuber, M. M.; Pascual, E. A.; Chen, N.; de Arellano-López, A. R.; Routbort, J. L. Thermomechanical response of polycrystalline $BaZrO_3$. *Phys. C Supercond.* **1998**, *309*, 245–250, doi:10.1016/S0921-4534(98)00588-7.

213. Kirby, R. K. Platinum - A thermal expansion reference material. *Int. J. Thermophys.* **1991**, *12*, 679–685, doi:10.1007/BF00534223.

214. Okada, Y.; Tokumaru, Y. Precise determination of lattice parameter and thermal expansion coefficient of silicon between 300 and 1500 K. *J. Appl. Phys.* **1984**, *56*, 314–320, doi:10.1063/1.333965.

215. NIELSEN, T. H.; LEIPOLD, M. H. Thermal Expansion in Air of Ceramic Oxides to 2200°C. *J. Am. Ceram. Soc.* **1963**, *46*, 381–387, doi:10.1111/j.1151-2916.1963.tb11756.x.

A Appendix

Mößbauer Fit Data

Table A 1. ^{57}Fe Mößbauer Spectroscopy Parameters (δ chemical isomer shift, ε effective quadrupole interaction parameter, B_{HF} magnetic hyperfine field) for $BaFeO_{2.5}$ determined from the Ar-annealed sample in Figure 5.

Site in Ar annealed sample	δ / mms^{-1}	ε / mm^{-1}	B_{HF} / T	Relative Area / %
Fe^{3+} doublet	0.60	0.68	-	9
4-fold coord.	0.21	-0.13	39.8	50
5/6 fold coord.	0.42	-0.42	48.1	41

Table A 2. ^{57}Fe Mößbauer Spectroscopy Parameters (δ chemical isomer shift, ε effective quadrupole interaction parameter, B_{HF} magnetic hyperfine field) for $BaFeO_{2.5}$ determined from the hydrated sample in Figure 5.

Site in hydrated sample	δ / mms^{-1}	ε / mm^{-1}	B_{HF} / T	Relative Area / %
Fe^{3+} doublet	0.42	0.88	-	9
4-fold coord.	0.20	-0.16	39.2	59
5/6 fold coord.	0.33	-0.31	47.5	32

Determination of Lattice Planes Showing up in Φ-Scan

$$\begin{pmatrix} h_{trig} \\ k_{trig} \\ l_{trig} \end{pmatrix} = \begin{pmatrix} 1 & -1 & 0 \\ 0 & 1 & -1 \\ n/3 & n/3 & n/3 \end{pmatrix} \begin{pmatrix} h_{cubic} \\ k_{cubic} \\ l_{cubic} \end{pmatrix}$$

Table A 3. (110) equivalent lattice planes in the cubic and trigonal crystal system notation for hexagonal (number 1-18) and rombohedral (number 1-12) crystal systems (exemplary for n=6). Number 13-18 are obtained through 60 ° rotations of number 1-12. This symmetry operation does not exist in the rhombohedral crystal system. (hkl), yielding a reflection in the phi-scan (correct angle of 35.2643) are highlighted in bold.

#	$\begin{pmatrix} h_{cubic} \\ k_{cubic} \\ l_{cubic} \end{pmatrix}$	$\begin{pmatrix} h_{trig} \\ k_{trig} \\ l_{trig} \end{pmatrix}$	Angle between $\begin{pmatrix} h_{cubic} \\ k_{cubic} \\ l_{cubic} \end{pmatrix}$ and $\begin{pmatrix} h_{trig} \\ k_{trig} \\ l_{trig} \end{pmatrix}$ / °
1	$\begin{pmatrix} 1 \\ 1 \\ 0 \end{pmatrix}$	$\begin{pmatrix} 0 \\ 1 \\ 4 \end{pmatrix}$	**35.2643**
2	$\begin{pmatrix} -1 \\ -1 \\ 0 \end{pmatrix}$	$\begin{pmatrix} 0 \\ -1 \\ -4 \end{pmatrix}$	144.7356
3	$\begin{pmatrix} 1 \\ -1 \\ 0 \end{pmatrix}$	$\begin{pmatrix} 2 \\ -1 \\ 0 \end{pmatrix}$	90,0000
4	$\begin{pmatrix} -1 \\ 1 \\ 0 \end{pmatrix}$	$\begin{pmatrix} -2 \\ 1 \\ 0 \end{pmatrix}$	90,0000
5	$\begin{pmatrix} 1 \\ 0 \\ 1 \end{pmatrix}$	$\begin{pmatrix} 1 \\ -1 \\ 4 \end{pmatrix}$	**35.2643**
6	$\begin{pmatrix} -1 \\ 0 \\ -1 \end{pmatrix}$	$\begin{pmatrix} -1 \\ 1 \\ -4 \end{pmatrix}$	144.7356
7	$\begin{pmatrix} 1 \\ 0 \\ -1 \end{pmatrix}$	$\begin{pmatrix} 1 \\ 1 \\ 0 \end{pmatrix}$	90,0000
8	$\begin{pmatrix} -1 \\ 0 \\ 1 \end{pmatrix}$	$\begin{pmatrix} -1 \\ -1 \\ 0 \end{pmatrix}$	90,0000
9	$\begin{pmatrix} 0 \\ 1 \\ 1 \end{pmatrix}$	$\begin{pmatrix} -1 \\ 0 \\ 4 \end{pmatrix}$	**35.2643**
10	$\begin{pmatrix} 0 \\ -1 \\ -1 \end{pmatrix}$	$\begin{pmatrix} 1 \\ 0 \\ -4 \end{pmatrix}$	144.7356
11	$\begin{pmatrix} 0 \\ 1 \\ -1 \end{pmatrix}$	$\begin{pmatrix} -1 \\ 2 \\ 0 \end{pmatrix}$	90,0000
12	$\begin{pmatrix} 0 \\ -1 \\ 1 \end{pmatrix}$	$\begin{pmatrix} 1 \\ -2 \\ 0 \end{pmatrix}$	90,0000
13	$\begin{pmatrix} 1/3 \\ 4/3 \\ 1/3 \end{pmatrix}$	$\begin{pmatrix} -1 \\ 1 \\ 4 \end{pmatrix}$	**35.2643**

14	$\begin{pmatrix} 1/3 \\ 1/3 \\ 4/3 \end{pmatrix}$	$\begin{pmatrix} 0 \\ -1 \\ 4 \end{pmatrix}$	**35.2643**
15	$\begin{pmatrix} 4/3 \\ 1/3 \\ 1/3 \end{pmatrix}$	$\begin{pmatrix} 1 \\ 0 \\ 4 \end{pmatrix}$	**35.2643**
16	$\begin{pmatrix} -1/3 \\ -4/3 \\ -1/3 \end{pmatrix}$	$\begin{pmatrix} 1 \\ -1 \\ -4 \end{pmatrix}$	144.7356
17	$\begin{pmatrix} -1/3 \\ -1/3 \\ -4/3 \end{pmatrix}$	$\begin{pmatrix} 0 \\ 1 \\ -4 \end{pmatrix}$	144.7356
18	$\begin{pmatrix} -4/3 \\ -1/3 \\ -4/3 \end{pmatrix}$	$\begin{pmatrix} -1 \\ 0 \\ -4 \end{pmatrix}$	144.7356

XPS Measurements on BZY

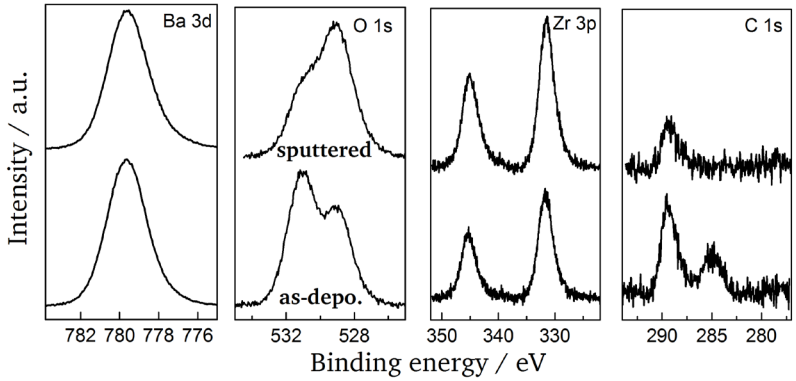

Figure A 1. Background corrected XPS spectra of BZY thin film deposited by LA-CVD: Ba *3d*$_{5/2}$, O *1s* , Zr *3p* and C *1s*. The film was measured as-deposited and after having been sputtered for 600s (2.4 µA at 3 keV).

Table A 4. Relative concentration of Ba and Zr on film surface, calculated with the peak area and the ASFs [93] as-deposited and after sputtering for 600 s. The bulk of the film shows a ratio close to the stoichiometric ratio for $BaZrO_3$. The accuracy of these calculations is between 15-20 % [93].

Sputter time	Emission line	Area	ASF	Area/ASF	Ratio Ba/Zr
0	Ba $3d_{5/2}$	28767	7.343	3917	1.83
0	Zr $3p$	4088	1.917	2133	
600	Ba $3d_{5/2}$	27413	7.343	3733	1.14
600	Zr $3p$	6245	1.917	3258	

BZY Films Deposited by PSD on Pt

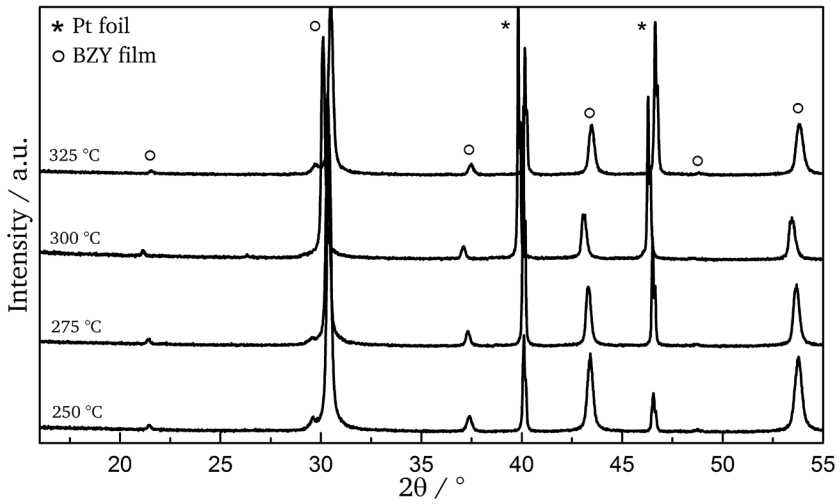

Figure A 2. X-ray diffractograms of BZY thin films deposited by pressurized spray deposition on Pt substrates at different deposition temperatures and subsequently annealed at 1100 °C for 10 h.

Table A 5. Deposition parameters for Y-doped $BaZrO_3$ thin films deposited by PSD at different substrate temperatures on Pt and subsequently annealed at 1100 °C for 10 h.

Sample	Precursor Set	Substrate	Substrate temperature (deposition) / °C
BZY26106	Set B	Pt	250
BZY27102	Set B	Pt	275
BZY28101	Set B	Pt	300
BZY29105	Set B	Pt	325

B List of Abbreviations

AACVD	Aerosol-assisted Chemical Vapor Deposition
AC	Alternating Current
APT	Atom Probe Tomography
ASF	Atomic Sensitivity Factors
BFO	$BaFeO_{3-\delta}$
BZY	$BaZr_{1-x}Y_xO_{3-x/2}$
CCP	Cubic Close Packed
CEMS	Conversion Electron Mößbauer Spectroscopy
CPE	Constant Phase Element
DAISY-Bat	Darmstadt Integrated System for Battery Research
DC	Direct Current
EIS	Electrochemical Impedance Spectroscopy
FWHM	Full Width at Half Maximum
GIXRD	Grazing Incidence X-Ray Diffraction
HS	High Spin
LA-CVD	CO_2 Laser Assisted Chemical Vapor Deposition
MO-CVD	Metal Organic Chemical Vapor Deposition
MFC	Mass Flow Controller
Nb:STO	Nb doped $SrTiO_3$
PLD	Pulsed Laser Deposition
PSD	Pressurized Spray Depostion
RHEED	Reflection High Energy Electron Diffraction
SEM	Scanning Electron Microscopy
SOEC	Solid Oxide Electrolysis Cell
SOFC	Solid Oxide Fuel Cell
TOF	Time Of Flight
UHV	Ultra High Vacuum
XPS	X-ray Photoelectron Spectroscopy
XRD	X-Ray Diffraction
XRR	X-Ray Reflectivity
YSZ	Yttria-Stabilized Zirconia

C List of Symbols

α	Constant phase element exponent
$a_{p.c.}$	Pseudocubic lattice parameter
a	Lattice parameter
A	Area
c_i	Charge carrier density
c_{out}	Lattice parameter in c-direction
C	Capacitance
C_{eff}	Effective capacitance
d	Distance
d_{hkl}	Spacing between lattice planes
D	Diffusivity
D_0	Preexponential factor of diffusion
ε	Strain
ε_0	Permittivity of free space
ε_r	Permittivity of material
E_a	Activation energy
E	Electric field
g_{hkl}	Lattice spacing in reciprocal space
G	Goldschmidt tolerance factor
ΔG	Electric energy demand
ΔH	Total energy
ΔH_f°	Enthalpy of formation
ΔH_r°	Enthalpy of reaction
I	Current
J	Current density
κ	Thermal expansion coefficient
k	Wave vector
k_b	Boltzmann constant
λ	Wavelength
m	Lattice mismatch
n	Coefficient of viscosity
L	Inductivity
η	Efficiency
μ	Mobility
φ	Phase angle
q	Charge
Q	Fit parameter of the constant phase element
R	Resistance
R_e	Reynolds number
R_x	Ionic radii
S°	Entropy
θ	Scattering angle

ρ	Mass density
τ	Time constant of RC element
t	Time
t_{H^+}	Transference number for protons
T	Temperature
ω	Frequency
u	Variation in axial flow
V	Voltage
$V_{f.u.}$	Volume per formula unit
X	Electronegativity
Z	Impedance
Z’	Real impedance part
Z’’	Imaginary impedance part
σ	Conductivity
Σ	Stress

D List of Figures

E List of Tables

F List of Publications

06.2018	Waidha, A.; Lepple, M.; Wissel, K.; Benes, A. et al. Synthesis, structure and electrical conductivity of a new perovskite type barium cobaltate $BaCoO_{1.80}(OH)_{0.86}$. *Dalton Transactions* **2018**, 47 (32), 1113
05.2018	Wissel, K.; Dasgupta, S.; Benes A.; Schoch R. et al. Developing intercalation based anode materials for fluoride-ion batteries: topochemical reduction of $Sr_2TiO_3F_2$ via a hydride based defluorination process. *J. Mater. Chem. A* **2018**, 6 (44), 22013
01.2018	Benes, A.; Molinari A.; Witte R.; Krug, R. et al. Proton Conduction in Grain-Boundary-Free Oxygen-Deficient $BaFeO_{2.5+\delta}$ Thin Films. *Materials* **2018**, 11 (1), 52
02.2017	Sukkurji, P.; Molinari, A.; Benes, A.; Loho, C. et al. Structure and conductivity of epitaxial thin films of barium ferrite and its hydrated form $BaFeO_{2.5-x+\delta}(OH)_{2x}$. *J. Phys. D: Appl. Phys*. **2017**, 50 (11), 115302

G Danksagung

An dieser Stelle möchte ich allen ganz herzlich danken, die entweder direkt an der erfolgreichen Vollendung dieser Dissertation beteiligt waren oder mir durch ihre Unterstützung zur Seite gestanden haben.

Allen voran möchte ich mich bei Herrn Prof. Dr. Horst Hahn für die Ermöglichung dieses Projektes in seiner Arbeitsgruppe, sowie seine fortwährende Unterstützung danken. Dazu gehören auch die Freiheiten und das mir entgegengebrachte Vertrauen, das maßgeblich zum Erfolg dieser Arbeit beigetragen hat. Herrn Prof. Dr. Oliver Clemens danke ich für seine intensive Betreuung über den kompletten Verlauf meiner Promotion und die Übernahme des Erstgutachtens. Die Vielzahl an Diskussionen und seine Denkanstöße haben mir nicht nur geholfen neue Sichtweisen in Bezug auf viele Zusammenhänge zu verinnerlichen, sondern auch zu einer äußerst aufregenden und spannenden Zeit geführt. Auf dem manchmal steinigen Weg zum Abschluss dieser Arbeit bedanke ich mich auch für seine ständige Verfügbarkeit und die Hingabe zu meinem Thema.

Des Weiteren bedanke ich mich bei Frau Prof. Dr. Barbara Albert für die Übernahme des Zweitgutachtens. Herrn Prof. Dr. Ensinger und Herrn Prof. Dr. Donner möchte ich zum einen für ihr Mitwirken als Prüfer in meiner Prüfungskommission danken und zum anderen für ihr unentwegt offenes Ohr bei Fragen seit Beginn meines Studiums 2007.

Mein großer Dank gilt außerdem allen Mitgliedern des Gemeinschaftslabors Nanomaterialien und der Gruppe Materialdesign durch Synthese. Ganz besonders bedanke ich mich bei Cahit Benel, Miriam Botros, Ruzica Djenadic, Christoph Loho und Abhishek Sarkar, die mir nicht nur bei zahllosen Problemen im Labor und bei wissenschaftlichen Diskussionen immer zur Seite standen, sondern auch für alle Späße und spontane Aktionen immer zu haben waren. An diese lustige und schöne Zeit mit Euch werde ich mich immer erinnern, egal ob es im Labor, im Büro, auf Konferenzen oder in einer Bar war. Natürlich nicht zu vergessen ist Renate Hernichel, die unseren Laden immer mit einem Blick auf die Finanzen am Laufen gehalten hat. Vielen Dank für die viele Organisation und deine moralische Unterstützung!

Außerdem möchte ich mich bei allen Kollegen aus Karlsruhe bedanken. Vor allem Alan Molinari danke ich für seine Hilfe und Einführung in die wichtigste Abscheidemethode dieser Arbeit, das Laserstrahlverdampfen. Ebenso danke ich Ralf Witte für die Mößbauer-Spektroskopie Messungen und seine Hilfe und Expertise bei der Auswertung selbiger. Für die Durchführung und Analyse der Atomsondentomographie Messungen danke ich Reda Chellali.
Auch an der TU Darmstadt danke ich meinen Kollegen für ihre Hilfe. Darunter insbesondere Christoph Loho (Einführung LA-CVD), Lukas Zeinar (Röntgendiffraktometriemessungen) und Joachim Brötz (Röntgendiffraktometriemessungen). Mein spezieller Dank gilt den Mitarbeitern der feinmechanischen Werkstatt unter der Leitung von Jochen Rank, sowie Michael Weber aus der Elektrowerkstatt (Hochtemperaturimpedanzspektroskopieaufbau und viele weitere Hilfestellungen). Zusätzlich danke ich der finanziellen Unterstützung durch die Darmstädter Exzellenz-Graduiertenschule für Energiewissenschaft und Energietechnik.

Zum Schluss möchte ich mich bei meiner Familie und meinen Freunden für ihre Unterstützung und ihr großes Verständnis, welches sie mir in zahllosen Situationen entgegengebracht haben, bedanken. Ohne euch und euren mentalen sowie emotionalen Beistand wäre dieses Unterfangen unmöglich gewesen.

Erklärung zur Dissertation

Hiermit versichere ich, die vorliegende Dissertation ohne Hilfe Dritter nur mit den angegebenen Quellen und Hilfsmitteln angefertigt zu haben. Alle Stellen, die aus Quellen entnommen wurden, sind als solche kenntlich gemacht. Diese Arbeit hat in gleicher oder ähnlicher Form noch keiner Prüfungsbehörde vorgelegen.

Darmstadt, den

(Alexander Benes)